

e - ISSN 2586-9396

Current Applied Science and
Technology



Vol. 20 No. 1

January - April 2020

Advisory Board

Prof. Dr. Suchatvee Suwansawat

President of King Mongkut's Institute of Technology Ladkrabang, Thailand

Prof. Dr. Wanlop Surakamponton

College of Advanced Manufacturing
Innovation, King Mongkut's
Institute of Technology Ladkrabang, Thailand
Faculty of Engineering, King Mongkut's
Institute of Technology Ladkrabang, Thailand

Prof. Dr. Monai Krairiksh

Current Applied Science and Technology or CAST, formerly KMITL Science and Technology Journal, has been established since its inception as KMITL Science Journal published by King Mongkut's Institute of Technology Ladkrabang (KMITL) in 2001. The journal has been dedicated to publishing advanced and applied knowledge in the form of high-quality research and review articles covering the main areas of Biotechnology, Environmental Science, Agricultural Technology and other fields related to Applied Science and Technology. Special issues devoted to important topics in advanced science and technology will occasionally be published.

The journal is an open access peer-reviewed and double blinded journal using Online Journal System (OJS) publishing online academic research and review articles. Previously, articles were published in print on a regular basis (two issues per year) since 2001 and since 2010 onward the articles have been published both in print and electronic forms starting from volume 10. In 2017, the journal title has been changed from *KMITL Science and Technology Journal* to *Current Applied Science and Technology* (CAST) (e-ISSN 2586-9396) to be more identifiable to the international scientific community according to the suggestion of Thai-Journal Citation Index Centre. The journal has been published online only since volume 17(2) (July-December, 2017). In addition, the journal has attracted researchers from other countries more than 22% according to the data. Because of more demands on publication in CAST, the editorial board has decided to publish online original academic research and review articles three issues per year (April, August and December) from 2018 onward.

Furthermore, the advisory board and editorial board comprises honorable and well-known members from around the world in which 50% of editorial board members are from various countries like U.K., Norway, Japan, India, China, Canada, Estonia and Egypt. Only 25% of Thai editorial board members are from the publisher organization and 25% from other publisher organizations. Most of advisory and editorial board members have high H-index according to SCOPUS.

The journal is also committed to maintaining the high level of integrity in the content published and has a Conflict of Interest policy in place. The journal uses plagiarism detection software to screen the submissions. The journal has been working closely with Thai-Journal Citation Index Centre to ensure that the journal complies with international standard of SCOPUS.

Electronic Journal Managing Editor Asst. Prof. Dr. Vorapat Sanguanchaipaiwong
Assistant Managing Editors

Ms. Nathawee Chainork
Ms. Jermaroon Autaijamsripon
Ms. Mongkutkarn Udompongsuk

Current Applied Science and Technology (CAST)

(formerly KMITL Science and Technology Journal)

Editor

Dusanee Thanaboripat

King Mongkut's Institute of Technology Ladkrabang, Thailand

Editorial Board

Keiichi Ishihara	Kyoto University, Japan
Chaliceemalapalli K. Jayasankar	Sri Venkateswara University, India
Bjorn Kristiansen	GlycaNova, Norway
Hidegori Mimura	Shizuoka University, Japan
Yang Qian	Harbin Institute of Technology, PR China
Mike Mattey	University of Strathclyde, UK
Minoru Tanaka	Tokai University, Japan
Mohamed Yacout	Alexandria University, Egypt
He Yawen	Shanghai Jiao Tong University, PR China
Rajeev Bhat	Estonian University of Life Sciences, Estonia
Brian J.B. Wood	University of Strathclyde, UK
Serge Belloncik	Institut Armand- Frappier, Canada
Soottawat Benjakul	Prince of Songkla University, Thailand
Krisana Kraisintu	Krisana Kraisintu Foundation, Thailand
Somboon Tanasupawat	Chulalongkorn University, Thailand
I-Ming Tang	King Mongkut's University of Technology Thonburi, Thailand
Arinthip Thamchaipenet	Kasetsart University, Thailand
Rattikorn Yimnirun	Vidyasirimedhi Institute of Science and Technology, Thailand
Anuwat Jangwanitlert	King Mongkut's Institute of Technology Ladkrabang, Thailand
Chamroon Laosinwattana	King Mongkut's Institute of Technology Ladkrabang, Thailand
Wisnu Pecharapa	King Mongkut's Institute of Technology Ladkrabang, Thailand
Puntani Pongsumpun	King Mongkut's Institute of Technology Ladkrabang, Thailand
Chanboon Sathitwiriyawong	King Mongkut's Institute of Technology Ladkrabang, Thailand

CONTENTS

	Page
Research Articles:	
Effect of Crude Ethanolic Extracts from Bottle Brush (<i>Callistemon viminalis</i>) against Leaf Spot Fungi and Their Phytotoxicity on Lettuce (<i>Lactuca sativa L.</i>)	1
Suriyasit Somnuek, Tanimnun Jaenaksorn and Chamroon Laosinwattana	
The Design and On-sky Results of the Prototype of a Low-Resolution Spectrograph for the Thai National Telescope	15
Jitsupa Paenoi, Christophe Buisset, Kajpanya Suwansukho, Wichit Sirichote, Piyamas Choochaler, Suparerk Aukkaravittayapun, Griangsak Thummasorn, Surin Ngernsujja, Anuphong Inpun, Pimol Kaewsamoeta, Suchinno Kanthum, Apichat Leckngam, Wayne Orchiston, Krittidas Chaniworawit, Saran Poshajinda and Boonrucksar Soonthornthum	
Shelf-life Prediction of Micro-encapsulated Shrimp Oil in Different Packages using Empirical Models	30
Sirima Takeungwongtrakul, Soottawat Benjakul, Supachai Pisuchpen, Pensiri Kaewthong and Sitthipong Nalinanon	
Visible-light-driven Photodegradation of Commercial Dyes by the Cooperation of Co-doped TiO₂ Material	43
Russameeruk Noonuruk and Chakkaphan Wattanawikkam	
Effects of Seven Plant Essential Oils on Mortalities of Chicken Lice (<i>Lipeurus caponis L.</i>) Adult	52
Jarongsak Pumnuan, Ammorn Insung and Ampon Klompanya	
Geographic Information System-based Analysis to Identify the Spatiotemporal Patterns of Road Accidents in Sri Racha, Chon Buri, Thailand	59
Narong Pleerux	

Effect of Surface Treatment on Electrical Properties of Polydimethylsiloxane Based Triboelectric Nanogenerator	71
Parinya Panprom, Naratip Vittayakorn and Chanisa Nawanol	
Resistance to Quinone-outside Inhibitor (QoI) Fungicides in <i>Colletotrichum</i> Species Isolated from Anthracnose Disease Occurring in Thailand	79
Pornprapa Kongtragoul, Kazuumi Imamoto and Hideo Ishii	
Semi-Automated Method to Extract Urban Areas from Barren Land/ Bare Soil, Case Study: Idku, Nile Delta Coast, Egypt	90
Hanady H. Khalil and Mahmoud Hassaan	
Physiological and Metabolic Modifications in Response to Nanocarbon in Callus of Indica Rice Cultivar	106
Thanawat Sutjaritvorakul and Sutee Chutipaijit	
Genotypic Variation of Seed Oil Content in Twelve Genotypes of <i>Citrullus colocynthis</i> from Morocco	117
Saïd El Madidi and Abedlhamid Benmoumou	
Fabrication of Activated Carbon Pouch Cell Supercapacitor: Effects of Calendering and Selection of Separator-Solvent Combination	124
Gladis Aros Safitri, Khanin Nueangnoraj, Paiboon Sreearunothai and Jedsada Manyam	
Adsorbents Based on Keratin for Lead and Cadmium Removal	136
Viktoriia Havryliak, Vasylyna Mykhaliuk, Romana Petrina, Olena Fedorova, Vira Lubenets and Volodymyr Novikov	
Application of TOPSIS Method to Green Supplier Selection for a Thai OTOP Producer	144
Walailak Atthirawong	

Review Article:

**Recent Evaluations and Applications of a Cassava Model
in Thailand: A Review**

156

Benjamas Kumsueb and Attachai Jintrawet

Instructions for Authors

I

Effect of Crude Ethanolic Extracts from Bottle Brush (*Callistemon viminalis*) against Leaf Spot Fungi and Their Phytotoxicity on Lettuce (*Lactuca sativa L.*)

Suriyasit Somnuek*, Tanimnun Jaenaksorn and Chamroon Laosinwattana

Department of Plant Production Technology, Faculty of Agricultural Technology,
King Mongkut's Institute of Technology Ladkrabang, Bangkok, Thailand

Received: 6 August 2019, Revised: 25 September 2019, Accepted: 2 October 2019

Abstract

In response to the public concern about environmental problems as well as fungicide residues on agricultural produces especially leaf vegetables, we investigated the potential use of crude extracts from bottle brush (*C. viminalis*) leaves against leaf spot fungi and their phytotoxicity on lettuce grown in hydroponics. Yield, total phenolic and flavonoid contents of the extract were also evaluated. Regarding the *in vitro* antifungal assay using poisoned food technique, 3×3 factorial in Completely Randomized Design (CRD) was employed with three replicates. Factor A was 3 crude extracts (50% ethanol, 70% ethanol and 95% ethanol crude extract) while factor B was the 3 concentrations (0, 5,000 and 50,000 ppm) of crude extracts. Results showed that all three crude extracts were significantly effective in inhibiting the mycelial growth and sporulation of leaf spot fungi (*Alternaria* sp. and *Curvularia* sp.). There was a significant interaction between all extracts and their concentration regarding inhibition percent. Increase in crude extract concentrations resulted in a marked increase in their inhibition. The concentration of 50,000 ppm gave the highest effectiveness. For phytotoxicity test, all tested crude extracts did not give any negative effects either on seed germination or growth of lettuce grown in hydroponics. Interestingly, growth promotion about 30 percent was achieved on this regard. Based on quantitative assay, the highest yield of crude extract was obtained from 95% ethanol solvent. Highest total phenolic and flavonoid contents were detected at the highest concentration of all crude extracts.

Keywords: bottle brush extract, phytotoxicity, antifungal activity, leaf spot fungi, *Alternaria*, *Curvularia*

DOI 10.14456/cast.1477.1

1. Introduction

Lettuce (*Lactuca sativa L.*), an annual plant, is commercially grown worldwide as leafy vegetable. In Thailand, lettuce is widely consumed as fresh vegetable meanwhile its production in soil and hydroponic cultivation has been increasing due to great market demand and health concern. Leaf spot diseases of vegetable crops caused by fungi such as *Alternaria* sp., *Cercospora* sp., *Curvularia* sp., and *Septoria* sp. are commonly found throughout the world and have significant impact on quantity, quality and commercial value of crops [1]. In southern Thailand, *Curvularia aeria* and *C. lunata* were reported to be causal agents of leaf spot diseases on lettuce and cabbage grown in field, respectively [2-4]. In general, most *Alternaria* species are mainly saprophytic fungi. However, some species have acquired pathogenic capacities collectively causing a range of diseases with

*Corresponding author: Tel.: +66 89-794-2595

E-mail: suriyasitsom@gmail.com

economic impact on a large variety of important agronomic host plants including vegetables [5]. For example, *A. dauci*, the carrot pathogen, can cause a disease on lettuce and celery grown in the field [6].

Chemical fungicides have often been used to control these diseases, but this conduct is associated with negative impacts on ecosystems, harmful effects on human health and deposition of residue on agricultural produces. Hence, there is a great demand for developing safer alternative and effective measures, such as treatment with natural agents like plant extracts, which are capable of preventing or controlling such diseases to reduce dependency on synthetic fungicides.

At present, much attention has been paid towards plant extract having an inhibitory effect on plant pathogens with none or less negative impacts on growing plants, human and the environment. *Callistemon viminalis*, commonly known as bottle brush tree, belongs to the family Myrtaceae which is a common ornamental small tree with pendulous foliage [7-9]. This plant is on the plant lists of the “Plant Genetic Conservation Project” under the Royal Initiative of Her Royal Highness Maha Chakri Sirindhorn, Thailand. Various parts of this plant used in traditional and folk medicine have been reported to have antibacterial activities [7-9]. However, a few studies have been focused on its antifungal properties for plant disease control especially on leafy vegetables.

Therefore, this research was conducted to evaluate the possible antifungal activities of crude extracts from *C. viminalis* leaves (using solvents with different ethanolic percentages and different extract concentrations) as well as its phytotoxicity on lettuce in order to obtain the safer effective method for disease control.

2. Materials and Methods

2.1 Pathogenicity test

The pathogenicity test was carried out using detached leaf test. The fungi tested in this experiment, i.e., *Alternaria* sp. and *Curvularia* sp. were isolated from lettuce leaves showing leaf spot symptom. The lettuce leaves were washed in tap water and left air-dried. Then, the leaf was inoculated by 5 mm dia mycelial agar plug (7 days old). The PDA agar plug without pathogen was used as a control. The inoculated leaves were kept into the moist plastic box at room temperature. Disease index was rated up to 4 levels of lesion sizes as: 0 = no infection; 1 = 1-5 mm; 2 = 5.1-10 mm; 3 = 10.1-15 mm; and 4 = >15 mm at 3 and 5 days after inoculation (DAI). Disease incidence (DI) and disease severity (DS) of tested lettuce were calculated by the equations:

$$\text{where } \% \text{ DI} = (\text{Number of infected leaves} / \text{Number of total leaves}) \times 100$$

$$\% \text{ DS} = \frac{\sum (\text{Number of infected leaves} \times \text{Disease index})}{\text{Number of total leaves} \times \text{The highest disease index}} \times 100$$

2.2 Preparation of *Callistemon viminalis* extract and evaluation of its total phenolic and flavonoid contents

The disease free and fresh leaves of *C. viminalis* were collected from Ladkrabang district area, Bangkok, Thailand. The samples were washed thoroughly with water for 3 times and left air-dried. Then, approx. 1.5 kg of air-dried leaves were dried in hot air oven at 45°C for 3 days. Dried plant leaves were ground and soaked into 95, 70 and 50% ethanol solvent with the ratio of 1:10 (w/v) for 3 days. The extracts were filtered through double-layered cheesecloth and one layer of Whatman No.1 filter paper. The filtrates were collected and concentrated at 40°C under reduced pressure using

rotary evaporator. All the extracts were then transferred into airtight vials and stored at 4°C for further use.

The total phenolics and flavonoids of the crude extract were analyzed by Folin-Ciocalteu method [10] and the aluminum chloride method [11], respectively. For total phenolic contents, the 300 μ l of extract was mixed with 2.25 ml of Folin-Ciocalteu reagent (10% dilution) and kept for 5 min at room temperature. Then, 2.25 ml of sodium carbonate solution was added to the mixture for 90 min at room temperature. The mixture and absorbance were detected at 750 nm using a spectrophotometer. Gallic acid was used as standard and total phenolic contents were expressed as gallic acid equivalent per milliliter (mg GAE/ml). For flavonoid contents, the 0.5 ml of extract was mixed with 2.25 ml of distilled water. Afterwards, 0.15 ml of 5% NaNO₂ solution was added and kept at room temperature for 6 min. Then, 0.3 ml of 10% AlCl₃ solution and 1 ml of 1 M NaOH were added and shaken. The mixture and absorbance were measured at 510 nm using a spectrophotometer. Quercetin was used as standard and flavonoid contents were calculated as mg quercetin equivalent per milliliter (mg QE/ml).

2.3 Antifungal activity of *C. viminalis* crude ethanolic extracts

The antifungal activity of crude ethanolic extracts from *C. viminalis* was *in vitro* tested against two foliar fungal pathogens of lettuce, namely *Alternaria* sp. and *Curvularia* sp., using poisoned food assay method. The experiment was carried out in a CRD with a 3×3 factorial arrangement plus one positive control (using 50 ppm carbendazim). Factor A was 50, 70 and 95% ethanolic extracts where factor B was 0, 5,000 and 50,000 ppm. The extract was incorporated into the molten PDA at a desired final concentration and mixed well. Then, the medium was poured into Petri dish. After overnight pre-incubation, the inoculation was done by a mycelial disc of 5 mm dia, which was deposited in the center of the agar plate. After further incubation at 25 °C, the diameters of fungal growth in control and treatment plates were measured and the antifungal effect was estimated by the following formula:

$$\text{Antifungal activity (\%)} = (D_c - D_t) / D_c \times 100$$

where D_c was the diameter of growth in control plate.

D_t was the diameter of growth in the plate containing tested extract.

Sporulation was determined at the end of incubation according to Islam *et al.* [12] with slight modification. Six discs (5 mm dia) were randomly taken from each Petri dish of fungal culture and macerated in 10 ml of sterile water. Spore suspensions obtained were filtered and homogenized. Spores were then counted under microscope using a haemacytometer. Assay was carried out in three replicates. The percent reduction or stimulation by each extract was determined.

2.4 Phytotoxicity of *C. viminalis* crude ethanolic extracts on lettuce

Phytotoxic effects of the extracts were assessed on seed germination and growth of lettuce in hydroponics as follows:

Seed germination: Phytotoxicity of *C. viminalis* crude ethanolic extract was determined on lettuce seed germination. The dry crude extracts were dissolved into the required concentrations in 10% dimethyl sulfoxide (DMSO). Then, lettuce seeds were soaked into the prepared extract for 15 min. Afterwards, 25 treated seeds of lettuce were placed on sterilized germination paper in 9 cm Petri dishes containing 5 ml sterilized water. The dish was maintained at 25 °C, 12 h photoperiod in the growth chamber. The experiment was carried out by 3×4 factorials in CRD with 4 replications.

Factor A was 3 crude extracts (50%, 70%, and 95% ethanol crude extract) while factor B was 4 concentrations of crude extracts (0, 5,000, 25,000 and 50,000 ppm). Ten percent of DMSO without the extract was used as control. Seed germination, hypocotyl and radicle length were recorded.

Growth of lettuce in hydroponics: The effect of foliar sprayings of *C. viminalis* crude ethanolic extract was evaluated on lettuce grown in Dynamic root floating technique (DRFT) with nutrient solution (EC = 1.6-1.8 mS/cm, pH= 5.8-6.2). The experiment was laid out as 3×4 factorials in CRD with 3 replications (3 plants per replication). Factor A and B were set as same as in the seed germination test whereas foliar sprayings of 2 ml of the extract were made on leaf of 15 days old lettuce. Phytotoxicity was determined as the occurrences of necrosis and discoloration. Plant growth parameters such as leaf greenness (by SPAD value using a portable chlorophyll meter, SPAD-502, Konica Minolta Sensing, Inc., Japan), leaf size and numbers were weekly monitored after treatment whereas the fresh and dry weight of shoot and root were recorded at the end of the cultivation.

3. Results and Discussion

3.1 Isolation and pathogenicity test

The pathogenicity test on detached leaf test revealed that both tested fungi (*Alternaria* sp. and *Curvularia* sp.) were the causal pathogen of the leaf spot disease of lettuce, showing 100% DI with 85% and 40% DS, respectively at 5 DAI (Table 1). Regarding the symptom, brown circular leaf spots and yellow halo were found on both fungal inoculations. *Alternaria* sp. caused large necrotic and chlorosis symptoms (about 23 mm dia) while *Curvularia* sp. caused small lesion (about 6.6 mm dia) (Table 1). Our findings are in agreement with many researchers who reported that both fungi were leaf and seed-borne pathogen of leafy vegetable crops and especially *Alternaria* sp. leaf spot is a common disease and particularly problematic for plant in the cabbage family [2-3, 13].

3.2 Extract yield, total phenolic and flavonoid contents

Extract yields of *C. viminalis* were shown in Table 2. It was shown that 50% ethanolic extract of *C. viminalis* (50% EECV), 70% ethanolic extract of *C. viminalis* (70% EECV) and 95% ethanolic extract of *C. viminalis* (95% EECV) yielded 4, 6 and 13%, respectively, based on oven dry weight of the leaves (300 g). It can be seen that percentage crude yield of extract increased along with an increase of alcohol percentage in the solvent, i.e., 95% ethanol shown to be the best extraction solvent in terms of crude yield (13%). However, in some cases reported in Salem *et al.* [14], extract yield of *C. viminalis* using methanolic solvent was much higher as 23%. In 2012, Krishna *et al.* [15] reported that the extract yield of *C. citrinus* about 1.75% based on oven dry weight of the leaves (400 g) was obtained by using ethanol solvent.

The total phenolic and flavonoid contents were presented in Table 3. The result revealed a significant interaction between all extracts and their concentrations regarding total phenolic and flavonoid contents. The highest concentration (50,000 ppm) of all tested extracts gave the highest phenolic contents about 1.16-1.23 mg GAE/ml. With regard to flavonoid contents, the 50,000 ppm of 70% EECV significantly exhibited higher content about 3.31 mg % QUE/ml followed by 95%

Table 1. Pathogenicity test of *Alternaria* sp. and *Curvularia* sp. on lettuce leaf.

Treatment	Incidence (%)		Severity (%)		Symptom 5 DAI
	3 DAI ^{1/}	5 DAI	3 DAI	5 DAI	
Control	0c ^{1/}	0c	0c	0c	
<i>Alternaria</i> sp.	100a	100a	75a	85a	
<i>Curvularia</i> sp.	60b	100b	12b	40b	

^{1/}Values are means of three replicates .Values in each column followed by the same letter are not significantly different according to Duncan's Multiple Range Test (P>0.05). Scale bar = 10 mm.

^{2/}DAI= Day after inoculation

Table 2. Extract details of *Callistemon viminalis* leaves.

Plant part	Solvent	Solvent volume (ml)	Extract weight (g)	Yield (%)
Leaf (300g)	50% Ethanol	3000	12	4
Leaf (300g)	70% Ethanol	3000	18	6
Leaf (300g)	95% Ethanol	3000	39	13

Table 3. Total phenolic and flavonoid contents of *Callistemon viminalis* leaves.

Extract name	Conc ⁿ (ppm)	Total phenolic (mg GAE/ml)	Total flavonoid (mg QUE/ml)
50%EECV	0	0.00f	0.00h
	5,000	0.48c	1.19fg
	25,000	0.92b	1.96e
	50,000	1.16a	3.01b
70%EECV	0	0.00f	0.00h
	5,000	0.20d	1.20f
	25,000	1.00b	2.17d
	50,000	1.23a	3.31a
95%EECV	0	0.00f	0.00h
	5,000	<1e	1.11g
	25,000	1.08b	1.93e
	50,000	1.22a	2.92c
C.V. (%)		2.44	3.67
Value of factor A ^{2/}		**	**
Value of factor B ^{3/}		**	**
A×B		**	**

^{1/}Values are means of three replicates .Values in each column followed by the same letter are not significantly different according to Duncan's Multiple Range Test (P>0.05).

^{2/}Factor A is the ethanol concentration for extraction

^{3/}Factor B is the concentration of crude extracts

EECV and 50% EECV about 3.01 and 2.92 mg % QUE/ml, respectively (Table 3). Our results are in agreement with the previous findings [14, 16] who reported that the qualitative phytochemical analysis revealed the presence of different phytochemicals including flavonoids and phenolics in methanol and ethanol crude extract of *C. viminalis*. *Callistemon viminalis* was a rich source of phenolic compounds whereas higher amount of phenolics (about 88.83 mg GAE/g DW), flavonoids (about 65.48 mg GAE/g DW) was found in its ethanol extract [16]. The 44.3 mg GAE/g extract of total phenolics and 45.36 mg GAE/g extract of total flavonoids were detected in methanol crude extract [14]. In addition, its aqueous leaf extract was also reported to contain about 48.35 µg GAE mg⁻¹ tissue phenolics [17]. Flavonoid and phenolic contents were also reported to be present in other species of *Callistemon* [18]. Regarding our result on high flavonoids content in 70% EECV, it was in line with Bimakr *et al.* [19] who mentioned that the higher concentrations of more bioactive flavonoid compounds were detected with 70% ethanol due to its higher polarity than pure ethanol. It is worth noted that numerous biological activities (such as antimicrobial activity, antioxidant capacity and so on) of phenolic compounds and flavonoids have been demonstrated by Hasan *et al.* [16], therefore the quantity of the two phytochemical compounds of our crude extracts could play an important role on such biological activities.

3.3 Antifungal activity of *C. viminalis* crude ethanolic extracts

In vitro antifungal activity of the extracts obtained from *C. viminalis* leaves, using different solvents and concentrations, against the tested fungi was shown in Table 4. The growth inhibition of each fungus was presented in Figure 1. All three crude extracts at 5,000 and 50,000 ppm were found to be significantly effective against mycelial growth of the tested fungi at 3 and 5 DAI (Table 4) and at 7 DAI (Figure 1). In addition, there was an interaction between solvent type and extract concentration level on their effects on inhibition percentage of the growth of the two tested fungi. As the concentration level of the crude extracts increased, the percent growth inhibition also increased.

Table 4. Effect of different concentrations of ethanolic extracts from *C. viminalis* leaves on mycelial growth of leaf spot fungi at 3 and 5 DAI.

Factor A	Factor B	Growth inhibition (%)			
		<i>Alternaria</i> sp.		<i>Curvularia</i> sp.	
		3 DAI	5 DAI	3 DAI	5 DAI
50%EECV	0 ppm	0.0e ^{1/}	0.0d	0.0f	0.0g
	5000 ppm	38.4d	31.4c	71.6c	67.0d
	50000 ppm	89.9a	89.6a	86.1b	83.7b
70%EECV	0 ppm	0.0e	0.0d	0.0f	0.0g
	5000 ppm	50.8c	43.4b	67.3d	61.9e
	50000 ppm	84.8b	84.4a	85.5b	80.1c
95%EECV	0 ppm	0.0e	0.0d	0.0f	0.0g
	5000 ppm	53.5c	47.9b	58.5e	49.2f
	50000 ppm	89.1a	88.7a	94.4a	91.8a
C.V. (%)		5.32	7.73	2.40	3.46
Value of factor A		**	*	*	**
Value of factor B		**	**	**	**
A×B		**	**	**	**

^{1/}Values are means of three replicates .Values in each column with in each pathogen followed by the same letter are not significantly different according to Duncan's Multiple Range Test (P>0.05).

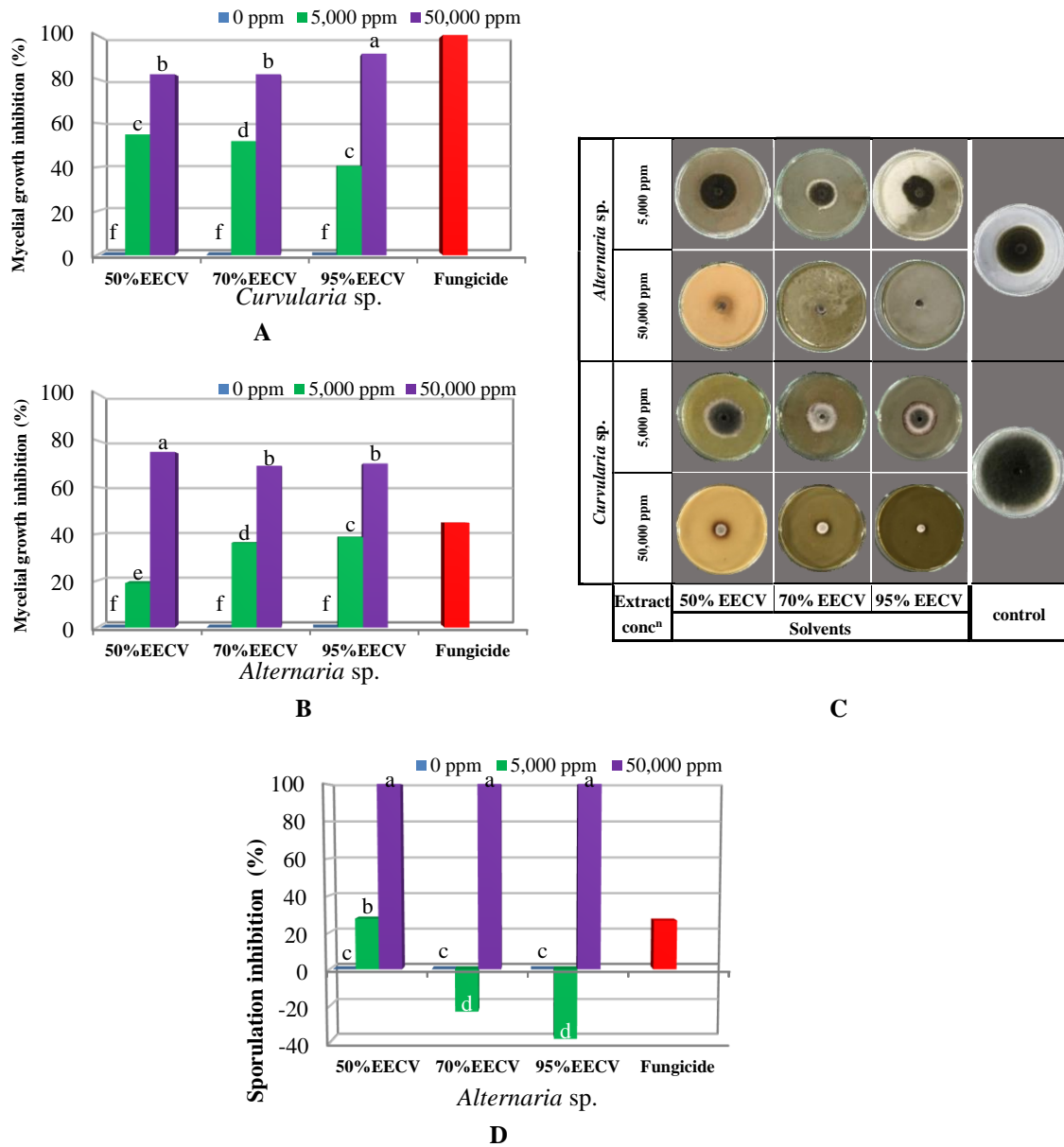


Figure 1. Growth inhibition of *Alternaria* sp. and *Curvularia* sp. by crude ethanolic extract from *C. viminalis* leaves at 7 DAI. Values are means of three replicates. Values followed by the same letter are not significantly different according to Duncan's Multiple Range Test ($P>0.05$)
A) Mycelial growth inhibition of *Curvularia* sp. (%), B) Mycelial growth inhibition of *Alternaria* sp. (%), C) Colony morphology of *Curvularia* sp. and *Alternaria* sp. grown on PDA with crude extracts, and D) Sporulation inhibition or stimulation of *Alternaria* sp. (%)

At 7 DAI, the highest concentration (50,000 ppm) of the 50% EECV showed the greatest inhibitory effect (about 75%) on growth of *Alternaria* sp., followed by 95% and 70% EECV (about 70%) whereas only 44.8 % growth inhibition was recorded from positive control (50 ppm carbendazim) (Figures 1A, 1C). Unlike *Alternaria* sp., 95% EECV was shown to be the most significantly effective against *Curvularia* sp. (about 91%) at the same concentration of 50,000 ppm followed by 50% and 70% EECV (about 82%), while 50 ppm carbendazim completely inhibited fungal growth (Figures 1B, 1C). In regard to sporulation assessment, only *Alternaria* sp. has been conducted since the growth of *Curvularia* sp. was almost completely inhibited by the extract. The result showed that its sporulation was totally inhibited at the highest concentration (50,000 ppm) of the tested extracts whereas it was stimulated at 5,000 ppm of 70% EECV and 95% EECV (Figure 1D).

From the result on *Alternaria* sp., this fungus seemed to be less sensitive to carbendazim fungicide (only 44.8% inhibition) but more sensitive to the extracts (about 75% inhibition) (Figure 1A). This finding was in agreement with the reports in USA and France [20-21] mentioning that *Alternaria* spp. were insensitive to many classes of fungicides recently recovered from fields. From our findings, it would be noted that a marked antifungal activity of the all tested crude extracts of *C. viminalis* leaves was observed which may be attributed to the presence of phenolics and flavonoids contents. *Callistemon viminalis*, especially its flowers are rich in polyphenols, flavonoids, saponins, steroids contents which possess good antibacterial and antifungal activities [8, 22]. A number of studies [8, 12, 23-24] reported that phytochemical extracts of *C. viminalis* leaves exhibited strong to moderate antibacterial effects and methanol extracts in some cases showed a stronger effect than ethanolic extract, which could be explained by the differences in the compounds between these two extracts. However, we have still focused on using ethanolic solvents for the safety reason [25]. In terms of antifungal activity of *Callistemon* plant, Nguefack *et al.* [26] reported that 70% ethanol extract from *C. citrinus* leaf proved to be effective against *Alternaria padwickii* and *Bipolaris oryzae* under both laboratory and field conditions.

Stimulation of *Alternaria* sporulation observed at 5,000 ppm of 70% EECV and 95% EECV was in line with the finding of Tiaiba *et al.* [27] who reported that the fungus *Ascochyta pisi* could sporulate on the medium containing 1.5% of plant extracts at levels sometimes exceeding the control.

3.4 Effect of *C. viminalis* crude ethanolic extracts on lettuce

Phytotoxicity of *C. viminalis* crude ethanolic extracts was assessed on seed germination (by seed treatment) and growth of lettuce (by foliar spray). With regard to the assessment of phytotoxic effects on lettuce seed germination, it revealed that the crude extracts at all tested concentrations did not have any significant adverse effect on seed germination at 2, 3 and 5 DAT compared to control (Table 5). On the contrary, especially the lowest concentration (5,000 ppm) of all tested ethanolic extracts (50% EECV, 70% EECV and 95% EECV) significantly stimulated the germination to 100% at 5 DAT compared to control showing about 91%. There was no interaction between the three extracts and their concentrations on percent seed germination. In addition, the 50,000 ppm of all the extracts as well as all 3 concentrations of 95% EECV significantly increased the seedling length compared to control (Table 5 and Figure 2).

Table 6 presented the effect of crude ethanolic extract of *C. viminalis* on lettuce growth. The result was in line with that of seed germination trial. Importantly, phytotoxicity (necrosis and discoloration) was rarely detected on lettuces treated with the extracts except for the concentration of 25,000 and 50,000 ppm of 50% EECV which showing only few necrotic lesions on the young leaf. Overall, the extracts did not give any negative effects on lettuce growth throughout the experiment. On the other hand, the extracts seemed to exhibit the positive effect such as stimulation

Table 5. Effect of different concentrations of ethanol extracts on seed germination and seedling growth of lettuce

Factor A	Factor B	Seed germination (%)			Seedling length (mm)	
		2 DAT ^{2/}	3 DAT	5 DAT	Radicle	Hypocotyl
50%	0 ppm	91.8ab ^{1/}	91.8c	91.8b	24.4e	13.0ef
EECV	5000 ppm	92.0ab	96.0abc	100.0a	32.7cd	12.1f
	25000 ppm	97.8a	100.0a	100.0a	33.3bcd	13.3e
	50000 ppm	92.0ab	96.0abc	96.0ab	31.2d	14.8d
70%	0 ppm	91.8ab	91.8c	91.8b	24.4e	13.0ef
EECV	5000 ppm	92.0ab	96.0abc	100.0a	33.8bcd	12.9ef
	25000 ppm	96.0ab	98.0ab	98.0ab	33.7bcd	15.0d
	50000 ppm	96.0ab	100.0a	100.0a	36.0ab	16.5ab
95%	0 ppm	91.8ab	91.8c	91.8b	24.4e	13.0ef
EECV	5000 ppm	90.0b	96.0abc	100.0a	34.7bc	17.2a
	25000 ppm	90.0b	96.0abc	96.0ab	37.5a	16.1bc
	50000 ppm	93.8ab	94.0bc	93.9ab	37.7a	15.1cd
C.V. (%)		3.51	2.26	2.66	14.74	13.10
Value of factor A		ns	ns	ns	**	**
Value of factor B		ns	**	**	**	**
A×B		ns	ns	ns	**	**

^{1/}Values are means of three replicates. Values in each column followed by the same letter are not significantly different according to Duncan's Multiple Range Test (P>0.05).

^{2/}DAT= Day after treatment

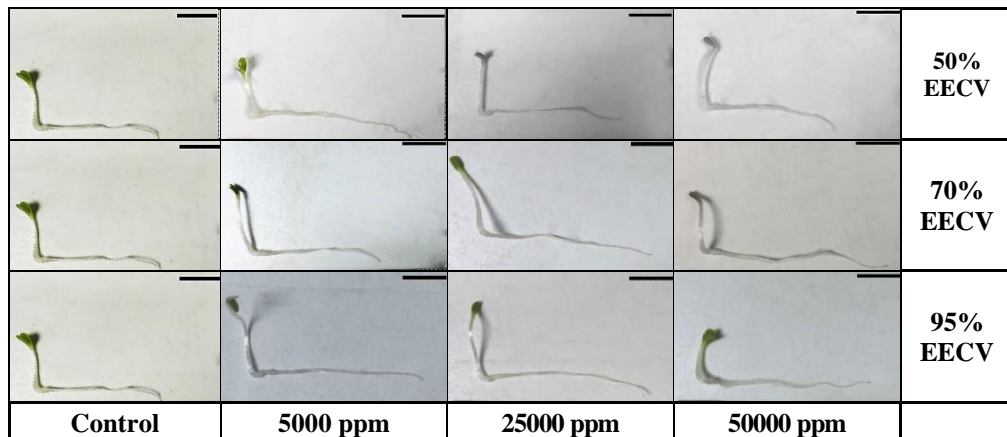


Figure 2. Effect of crude ethanolic extract from *C. viminalis* leaves on lettuce seedling at 5 DAT
Scale bar = 10 mm

Table 6. Effect of crude ethanolic extracts from *C. viminalis* leaves on lettuce growth in hydroponics

Factor A	Factor B	Phytotoxicity				Plant parameters					
		3 DAT ¹		7 DAT 21 DAT		Leaf number		Leaf size (cm)		SPAD value	
		Necrosis	Discoloration	7 DAT	21 DAT	7 DAT	21 DAT	7 DAT	21 DAT	7 DAT	21 DAT
50% EECV	0 ppm	-	-	8.4ab ²	16.6b	9.2d	17.3a	36.3d	35.1ab		
	5000 ppm	-	-	8.4ab	19.3ab	11.8a	18.3a	37.3cd	33.6b		
	25000 ppm	+++	-	8.0b	17.6ab	11.2ab	17.7a	39.2b	35.6ab		
	50000 ppm	+++	-	9.0a	19.6a	9.6cd	16.4a	41.9a	34.8ab		
70% EECV	0 ppm	-	-	8.4ab	16.6b	9.24d	17.3a	36.3d	35.1ab		
	5000 ppm	-	-	8.2ab	20.0ab	11.1ab	17.7a	38.5bc	35.2ab		
	25000 ppm	-	-	8.5ab	20.3a	11.9a	18.3a	38.0bc	36.4ab		
	50000 ppm	-	-	8.4ab	19.6a	10.1bcd	18.4a	38.5b	36.7ab		
95% EECV	0 ppm	-	-	8.4ab	16.6b	9.2d	17.3a	36.3d	35.1ab		
	5000 ppm	-	-	9.0a	19.0ab	10.8abc	18.3a	38.7bc	34.7b		
	25000 ppm	-	-	8.8a	19.3ab	10.2bcd	18.5a	39.4b	36.4ab		
	50000 ppm	-	-	8.8a	19.0ab	9.6cd	18.7a	38.4bc	38.5a		
C.V. (%)				8.81	7.41	12.83	19.98	3.62	12.62		
Value of factor A				ns	ns	ns	ns	ns	ns		
Value of factor B				ns	**	ns	ns	**	ns		
A ₁ × B ₁				ns	ns	ns	ns	**	ns		

¹Values are means of three replicates .Values in each column followed by the same letter are not significantly different according to Duncan's Multiple Range Test (P>0.05).

²DAT= Day after treatment

on some growth parameters and yield. At 21 DAT, the extracts were shown to increase the leaf numbers, while a significant increase was recorded at 50% EECV (5,000 ppm) having 19.6 leaves and 70% EECV (25,000 and 50,000 ppm) having 20.3 and 19.6 leaves compared to control (16.6 leaves). Leaf size and leaf greenness expressed by SPAD values were not significantly affected by the extracts (Table 6).

With regard to lettuce yield, fresh and dry weights of stem and root of the treated lettuces were significantly greater than control (Figures 3 and 4). The extract at 5,000 ppm of 70% EECV significantly stimulated lettuce growth in terms of stem fresh weight over control about 30 percent. The enhancing effect on some growth parameters and yield was probably due to phenolic compound present in the extract. Our findings were in accordance with Bali *et al.* [17] who reported that no phytotoxic effect of 1% and 2% aqueous leaf extract of *C. viminalis* was observed on rice whereas its growth and yield attributes increased, probably due to the release of allelochemicals (mainly phenolics). On the contrary, the aqueous leaf extract of *C. viminalis* still exhibited phytotoxicity as well as inhibited germination and growth of rice weed [17]. In addition, quite a number of reports mentioning that seed germination, growth and yield attributes of lettuce crop were not affected by negative effects of the plant extracts such as clove, colander and cinnamon extracts [28]; orange, mango, jabuticaba and guava leaf extracts [29]; *Ocimum tenuiflorum* leaf extract [30]. In regard to *C. viminalis*, our results seemed to contradict with earlier finding of Oliveira *et al.* [31] which stating on allelopathic activity of *C. viminalis* and negative effect of its essential oil on lettuce seedlings and causing a reduction in the length of shoots and root system. This contradiction result was probably due to the differences between phytochemical compounds in essential oil and ethanolic crude extract which were responsible for growth-enhancing or growth-retarding effect.

Overall, our results seem to be very promising as the crude ethanolic extracts from *C. viminalis* showed significant inhibition against the two tested fungal pathogens. The extracts showed no adverse effect on lettuce seed germination, less or no phytotoxicity on lettuce leaves with significant growth-enhancing effect on the lettuce grown in hydroponics about 30% above control.

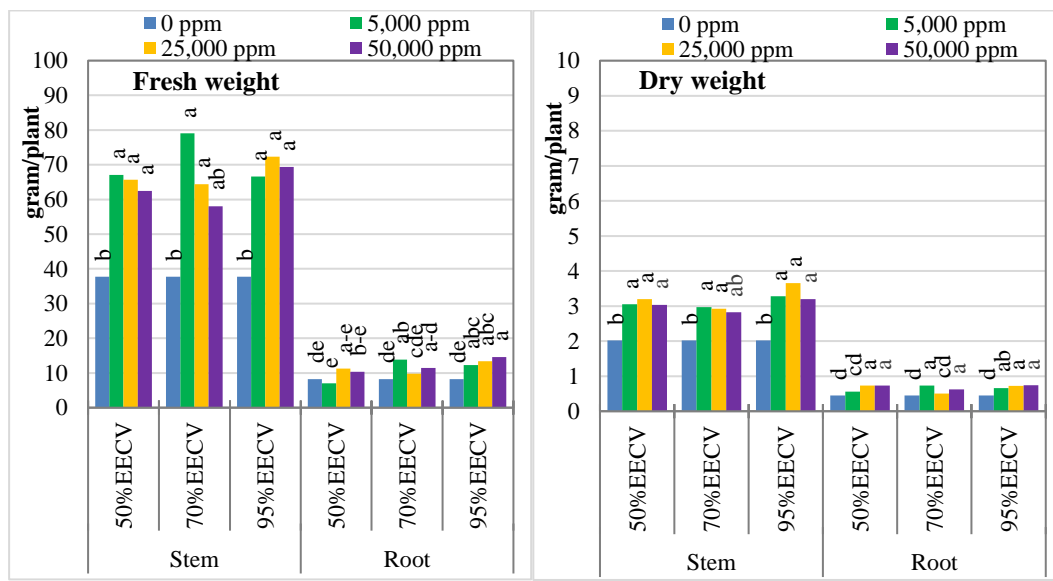


Figure 3. Yield of lettuce grown in hydroponics treated with ethanolic extract from *C. viminalis* leaves. The same letter on column bar is not significantly different according to Duncan's Multiple Range Test ($P > 0.05$)

Control	Extract concentration			Extract name	
	5000 ppm	25000 ppm	50000 ppm		
				50%EECV	
				70%EECV	
				95%EECV	
A					B

Figure 4. Effect of crude ethanolic extracts from *C. viminalis* leaves on yield of lettuce grown in hydroponics. A = Representative of lettuce treated with crude ethanolic extract from *C. viminalis* leaves, B= All treated lettuce grown in hydroponics

4. Conclusions

In conclusion, crude extracts from *C. viminalis* leaf (using 50%, 70% and 95% ethanol as solvent) were found to have high antifungal activities against *in vitro* mycelial growth and sporulation of leaf spot fungi (*Alternaria* sp. and *Curvularia* sp.). The highest concentration (50,000 ppm) of 50% and 95% ethanol crude extracts gave the strongest inhibitory effect. No phytotoxicity of crude extract was noted either during seed germination or growth of tested lettuce in hydroponics. Interestingly, foliar spraying of the extracts induced positive effects on the growth and yield of lettuce in hydroponics more than control treatment. For quantitative assay of crude extract, its highest yield was obtained from 95% ethanol solvent. Highest total phenolic and flavonoid contents were detected at the highest concentration of the tested crude extracts.

Our findings provided evidence that *C. viminalis* crude extract could be a new potential source for the development of an alternative natural fungicide to manage some plant pathogenic fungi. Further research would be necessary to precisely identify the chemical substances in the extract responsible for antifungal activity as well as plant growth-enhancing effect.

References

- [1] Pegg, K., Duff, J. and Manners, A., 2014. *Alternaria diseases in production nurseries*. [online] Available at: https://www.ngia.com.au/Attachment?Action=Download&Attachment_id=1838
- [2] Pornsuriya, C., Shin-Ishi, I. and Sunpapao, A., 2018. First report of leaf spot on lettuce caused by *Curvularia aeria*. *Journal of General Plant Pathology*, 84, 296-299.
- [3] Wonglom, P., Ito, S. and Sunpapao, A., 2018. First report of *Curvularia lunata* causing leaf spot of *Brassica rapa* subsp. *pekinensis* in Thailand. *New Disease Reports*, 38, 15.
- [4] Baiyee, B., Ito, S. and Sunpapao, A., 2019. *Trichoderma asperellum* T1 mediated antifungal activity and induced defense response against leaf spot fungi in lettuce (*Lactuca sativa* L.). *Physiological and Molecular Plant Pathology*, 106, 96-101.
- [5] Thomma, B.P.H.J., 2003. *Alternaria* spp.: From general saprophyte to specific parasite. *Molecular Plant Pathology*, 4(4), 225-236.
- [6] Koike, S.T., Smith, R.F., Cahn, M.D. and Pryor, B.M., 2017. Association of the carrot pathogen *Alternaria dauci* with new diseases, *Alternaria* leaf speck of lettuce and celery in California. *Plant Health Progress*, 18, 136-143.
- [7] Cowan, M.M., 1999. Plant products as antimicrobial agents. *Clinical Microbial Research*, 12, 564-582.
- [8] El-Batran, S.A., Mahmoud, S.S., Moharram, F.A., Marzouk, M.S. and Mohamed, M.I., 2002. Evaluation of some pharmacological effects of *Callistemon viminalis* and *Callistemon lanceolatus* extracts. *Journal of Union of Arab Biologists Cairo*, 17, 17-28.
- [9] Srivastava, S.K., Ahmad, A., Syamsunder, K.V., Aggarwal, K.K. and Khanuja, S.P.S., 2003. Essential oil composition of *Callistemon viminalis* leaves from India. *Flavour and Fragrance Journal*, 18(5), 361-363.
- [10] Singleton, V.L., Orthofer, R. and Lamuela-Raventós, R.M., 1999. Analysis of total phenols and other oxidation substrates and antioxidants by means of folin-ciocalteu reagent. *Methods in Enzymology*, 299, 152-178.
- [11] Hassan, M.M., Oyewale, A.O., Amupitan, J.O., Abdulla, M.S. and Okonkwo, E.M., 2004. Preliminary Phytochemical and antibacterial investigation of crude extracts of the root bark of *Detarium microcarpum*. *Journal of Chemical Society of Nigeria*, 29, 26-29.
- [12] Islam, M.R., Alam, S., Rahman, M.Z., Chowdhury, S.P., Begum, M.F., Akhter, N., Alam, M.S., Han, K.D. and Lee, M.W., 2003. Effects of plant extracts on conidial germination, mycelial growth and sporulation of fungi isolated from poultry feed. *Mycobiology*, 31(4), 221-225.
- [13] Rotem, J., 1994. *The Genus Alternaria: Biology, Epidemiology, and Pathogenicity*. Minnesota : The American Phytopathological Society.
- [14] Salem, M.Z.M., Ali, H.M., El-Shanherey, N.A. and Abdel-Megeed, A., 2013. Evaluation of extracts and essential oil from *Callistemon viminalis* leaves: antibacterial and antioxidant activities, total phenolic and flavonoid contents. *Asian Pacific Journal of Tropical Medicine*, 6 (10), 785-791.
- [15] Krishna, K.V.V.S., Surendra, G., Anjana, M., and Siva Nagini, K.S.K., 2012. Phytochemical screening and antimicrobial activity of *Callistemon citrinus* (L.) leaves extracts. *International Journal of Pharmacological Technology and Research*, 2, 700-704.
- [16] Hasan, N., Mamun, A., Belal, H., Rahman, A., Ali, H., Tasnin, N., Ara, T., Rabbi, A.R., Asaduzzaman, M. and Islam, A., 2016. A report on antioxidant and antibacterial properties of *Callistemon viminalis* leaf. *International Journal of Pharmaceutical Science and Research*, 1(7), 36-41.

- [17] Bali1, A.S., Batish, D.R. Singh, H.P., Kaur, S. and Kohli, R.P., 2017. Phytotoxicity and weed management potential of leaf extracts of *Callistemon viminalis* against the weeds of rice. *Acta Physiologiae Plantarum* 39, 25. <https://doi.org/10.1007/s11738-016-2313-5>
- [18] Das, A., Zaman, K. and Singh, A.V., 2008. Antimicrobial and antioxidant activities of *Callistemon linearis* DC leaf extract. *Pharmacology*, 3, 875-881.
- [19] Bimakr, M., Abdul Rahman, R., Saleena Taip, F., Ganjloo, A., Md Salleh, L., Selamat, J. and Zaidul, I.S.M., 2011. Comparison of different extraction methods for the extraction of major bioactive flavonoid compounds from spearmint (*Mentha spicata* L.) leaves. *Food and Bioproducts Processing*, 89, 67-72.
- [20] Grimmer, M.K., Bosch F., Powersb, S.J. and Paveley, N.D., 2013. Evaluation of a matrix to calculate fungicide resistance risk. *Pest Management Science*, 70(6), 1008-1016.
- [21] Rosenzweig, N., Hanson, L.E., Pratt, D., Stewart, J. and Somohano, P., 2017. First report of QoI resistance in *Alternaria* spp. infecting sugar beet (*Beta vulgaris*). *New Disease Report*, 36, 5. <http://dx.doi.org/10.5197/j.2044-0588.2017.036.005>
- [22] Salem, M.Z.M., El-Hefny, M., Nasser, R.A., Ali, H.M., El-Shanshorey, N.A. and Elansary, H.O., 2017. Medicinal and biological values of *Callistemon viminalis* extracts: History, current situation and prospects. *Asian Pacific Journal of Tropical Medicine*, 10(3), 229-237.
- [23] Delahaye, C., Rainford, L., Nicholson, A., Mitchell, S., Lindo, J. and Ahmad, M., 2009. Antibacterial and antifungal analysis of crude extracts from the leaves of *Callistemon viminalis*. *Journal of Medical and Microbiological Sciences*, 3(1), 1-7.
- [24] Sharma, D., Thakur, N., Vashist, J., and Bisht, G.S., 2018. Antibacterial evaluation of cuprous oxide nanoparticles synthesized using leaf extract of *Callistemon viminalis*. *Indian Journal of Pharmaceutical Education and Research*, 52(3), 449-455.
- [25] Liu, H., 2010. Extraction and isolation of compounds from herbal medicines. In: Liu, W.J.H., ed. *Traditional Herbal Medicine Research Methods: Identification, Analysis, Bioassay, and Pharmaceutical and Clinical Studies*. John Wiley & Sons, Inc. Wiley Online Books, pp 81-138.
- [26] Nguefack, J., Wulff, G.E., Dongmo, J.B.L., Fouelefack, F.R., Fotio, D., Mbo, J. and Torp, J., 2013. Effect of plant extracts and an essential oil on the control of brown spot disease, tillering, number of panicles and yield increase in rice. *European Journal of Plant Pathology*, 137, 871-882.
- [27] Tiaiba, A., Derbali, M. and Bendahmane, B.S., 2018. *In vitro* effect of crude extracts from eight Algerian steppe plants on mycelial growth and sporulation of *Ascochyta pisi* Lib. *Anales de Biología*, 40, 115-120.
- [28] Carmello, R. and Cardoso, J.C., 2018. Effect of extracts and sodium hypochlorite on lettuce germination and inhibition of *Cercospora longissimi* *in vitro*. *Scientia Horticulturae*, 234, 245-249.
- [29] Teixeira, M.F.F., Pinheiro, D.T., Junior, H.C.S., Alves, E.C., Barros, T.V., Freitas, M.A.M. and Dias, D.C.F.S., 2018. Allelopathic influence of some fruit tree leaf extracts on germination and seedling development of different weeds and vegetable crops. *Australian Journal of Crop Science*, 12(5), 726-730.
- [30] Islam, A.K.M.M. and Kato-Noguchi, H., 2014. Phytotoxic activity of *Ocimum tenuiflorum* extracts on germination and seedling growth of different plant species. *The Scientific World Journal*. <http://dx.doi.org/10.1155/2014/676242>.
- [31] Oliveira, C.M., Cardoso, M.G., Figueiredo, A.C.S., Carvalho, M.L.M. Miranda, C.A.S.F., Albuquerque, L.R.M., Nelson, D.L., Gomes, M.S., Silva, L.F., Santiago, J.A.S., Teixeira, M.L. and Brandão, R.M., 2014. Chemical composition and allelopathic activity of the essential oil from *Callistemon viminalis* (Myrtaceae) blossoms on lettuce (*Lactuca sativa* L.) seedling. *American Journal of Plant Sciences*, 5, 3551-3557.

The Design and On-sky Results of the Prototype of a Low-Resolution Spectrograph for the Thai National Telescope

Jitsupa Paenoi^{1*}, Christophe Buisset², Kajpanya Suwansukho¹, Wichit Sirichote¹,
Piyamas Choochalerm², Suparerk Aukkaravittayapun², Griangsak Thummasorn², Surin
Ngernsujja², Anuphong Inpun², Pimol Kaewsaengta², Suchinno Kanthum², Apichat
Leckngam², Wayne Orchiston², Krittidas Chaniworawit^{2,3},
Saran Poshyajinda² and Boonrucksar Soonthornthum²

¹Physics Department, Faculty of Science, King Mongkut's Institute of
Technology Ladkrabang, Bangkok, Thailand

²National Astronomical Research Institute of Thailand (Public Organization),
Chiang Mai, Thailand

³Astronomy Department, University of Florida, Florida, USA

Received: 6 June 2019, Revised: 18 August 2019, Accepted: 3 October 2019

Abstract

The objectives of the research project presented in this paper are to design and develop a Low Resolution Spectrograph for the 2.4 m Thai National Telescope. The Low Resolution Spectrograph will deliver a spectrum in the spectral range (440 - 740 nm), with a resolution of R approximately equals to 1,000 at the central wavelength, λ_c , of 600 nm, while observing through a slit with a width of 0.9 arcsecond wide (in long-slit mode) or during slit-less observations. The Low Resolution Spectrograph was designed to have a total weight of less than 20 kg and a maximum displacement due to gravity of less than 6 μm during a 360° rotation of the instrument cube. We have installed a prototype of the Low Resolution Spectrograph on the Thai National Telescope in December 2018. We have tested its performance on stellar objects during a one-night observing run. During these observations, we calibrated the instrument using a Thorium-Argon spectral calibration lamp and a Tungsten lamp and recorded the spectrum of the planetary nebula NGC 2392 in both slit-less and long-slit modes. We measured a spectral resolution of 800-1,300 over the wavelength range 440-740nm, thus demonstrating that the on-sky performance of the prototype was in agreement with the theoretical specifications.

Keywords: low resolution spectrograph, long-slit spectroscopy, slitless spectroscopy, opto-mechanical design, Thai National Telescope

DOI 10.14456/cast.1477.2

1. Introduction

The National Astronomical Research Institute of Thailand (NARIT) and the King Mongkut's Institute of Technology Ladkrabang (KMITL) are currently developing a compact and cost-effective Low-Resolution Spectrograph (LRS) with high throughput for the 2.4 m Thai National Telescope (TNT). This Rickey-Crétiens telescope is NARIT's main facility for astronomical observations

*Corresponding author: Tel : +66 83-011-2900
E-mail: jitsupapaenoi@gmail.com

in the optical domain. The TNT is located at the Thai National Observatory (TNO), near the summit of Doi Inthanon (latitude of 18.56° N and longitude of 98.46° E), the highest mountain in Thailand (elevation of 2,457m). At this site, the median seeing is 0.9 arcseconds, while the sky brightness is equal to 22.5 and 21.9 magnitude per square arcsecond in the B and V bands, respectively [1]. The TNT is currently equipped with the ULTRASPEC camera, a 4K camera, and a Medium Resolution Spectrograph (MRES). ULTRASPEC is a high-precision photometer that contains a $1k \times 1k$ electron-multiplying CCD with a field of view (FOV) of 7 arcminutes and a plate scale of 0.45"/pixel. This instrument is specified to work over the spectral range 330-1,000 nm and has been used to measure rapidly varying phenomena such as transits, flares and outbursts. The 4K camera comprises a cryogenically cooled thin CCD with $4k \times 4k$ pixels. NARIT is currently developing a focal reducer to image a circular FOV of 14 arcminutes on this camera with an image quality close to the seeing limit over the B, V, R and I spectral bands [2]. The Medium Resolution Echelle Spectrograph is a single object fiber-fed medium resolution spectrograph with a spectral resolution close to 15,000 over the spectral band 400- 800 nm. This instrument has been used to measure the spectra of stars down to a limiting magnitude close to 13 and record their radial velocities.

Within this framework, the main objective of the LRS currently being developed at NARIT is to provide spectra of faint point sources (unresolved objects) and extended objects, whose sizes smaller than 3 arcminutes. The spectral resolution of this instrument at the wavelength λ is defined as $R = \delta\lambda/\lambda$ where $\delta\lambda$ is the minimum spectral element that can be resolved by the instrument. The spectral resolution is thus a dimensionless quantity. Our objective is to reach a spectral resolution equal to 1,000 at the wavelength equal to 600 nm. This instrument is designed to complete the observing capabilities of the TNT for the following scientific applications: exoplanet detections and atmosphere characterization and the spectroscopic investigation of transit phenomenon.

The second objective of this project is to develop the human capacity to design, manufacture, assemble, align and commission spectrographs in Thailand. Although the optical design of this spectrograph was provided by Professor John Meaburn from the University of Manchester, staff from NARIT and KMITL developed the optomechanical design of the LRS, procured the optical components, manufactured the mechanical parts, and assembled, aligned, and installed the instrument on the TNT. To our knowledge, this is the first time that such a spectrograph has been fully developed and tested in Thailand and our objective is to use this knowledge and the skills acquired during this project to build more spectrographs for astronomical observations, atmospheric studies and space-based remote sensing applications.

Between 2017 and 2019 we developed a prototype of the LRS. Our objectives were to test this prototype on-sky with the TNT, to show that the spectral resolution and field of view of the instrument were in line with specifications and to identify the potential optimizations that will be implemented in the final system.

In this paper, we discuss the specifications of the LRS and present the optical design of the prototype. The mechanical design of the LRS, including the interface with the TNT are described. The results of the Finite Element Analyses are presented to show that the maximum error induced by gravity and thermoelastic effects would be equal to a few μm . The on-sky results obtained in December 2018 during a one-night observing run with the TNT would be reported. The spectrum of the planetary nebula NGC 2392 obtained in long-slit mode over the spectra range of 450-750 nm showing that the spectral resolution, R , was 900 at a wavelength, λ , of 650 nm would be analyzed.

2. Materials and Method

2.1 Specifications and optical design

2.1.1 Specifications

The specifications of the new NARIT Low Resolution Spectrograph (LRS) are presented in Table 1. This spectrograph is specified to deliver a spectrum over the wavelength range of 400-800 nm that covers the visible spectrum and to reach a spectral resolution of R equal to 1,000 at a wavelength equal to 600 nm. The spectrograph provides two observing modes, i.e. the long-slit mode and the slitless mode.

Table 1. Specifications of the Low Resolution Spectrograph developed for the 2.4 m Thai National Telescope.

Parameter	Specification
Spectral domain	400-800 nm
Observing mode	Slitless and Long-slit
Spectral Resolution	$R \approx 1000$ at $\lambda \approx 600$ nm
Slit mechanical length	20 mm
Slit on-sky angular length	3 arcminutes
Slit mechanical width	100 μm
Slit on-sky angular width	0.9''
Dispersion	180 $\text{\AA}/\text{mm}$
Plate scale	37 arcsec/mm
Detector format	2000 \times 500 pixels

The long-slit observations were made by placing the 20 mm slit on the TNT image plane which corresponded to an angular size projected on-sky of 3 arcminutes. This was necessary in order to be able to measure the spectra of (i) extended sources of a few arcminutes, or (ii) two stars (e.g. a science star and a reference star) separated by a few arcminutes.

The slit width, w_s , is equal to 100 μm , which corresponds to an angular size of 0.9 arcseconds. This value is equal to the seeing at the TNO in median conditions [1]. The full spectral domain was then imaged on a detector with a dispersion length, $L_{\text{Dispersion}}$, of 22 mm. The plate scale was specified to be equal to 37 arcsecond/mm and the full 3 arcminutes FOV was imaged along the FOV direction equal to L_{FOV} of 5 mm. The width of the slit image, w_{Slit} , was 23 μm . The dispersion was specified to be equal to 180 $\text{\AA}/\text{mm}$. So, we deduced that the spectral resolution limited by the slit width was 1,500, well above the specified spectral resolution.

The detector was specified to have a pixel size of 10 μm so that the slit image covered 2 pixels, which was close to the Nyquist frequency criterion. Thus, the detector format to cover the specified spectral domain and the specified FOV was equal to 2,000 \times 500 pixels.

2.1.2 Prototype design

Figure 1 shows the side-view of the spectrograph optical design and the left panel in Figure 2 represents the top-view propagation of the beam of light inside the LRS prototype during scientific observations. This prototype was mounted on the TNT which included the rotating mirror M4. The orientation of this mirror was adjusted during the observations to select the instrument mounted on the instrument cube. In the case of observations with the LRS, mirror M2 reflected the beam of light coming from the TNT towards the spectrograph.

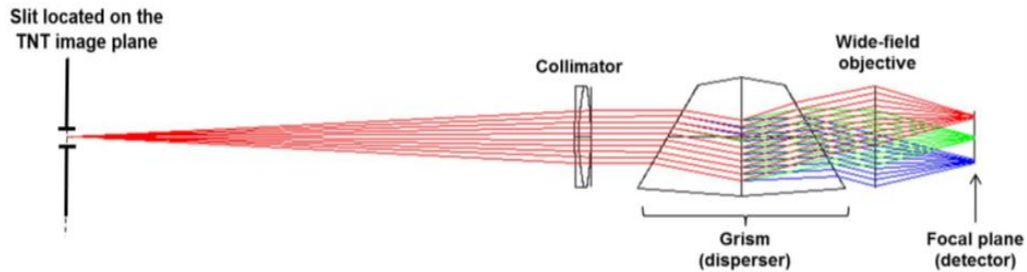


Figure 1. Side-view of the spectrograph optical design [3]

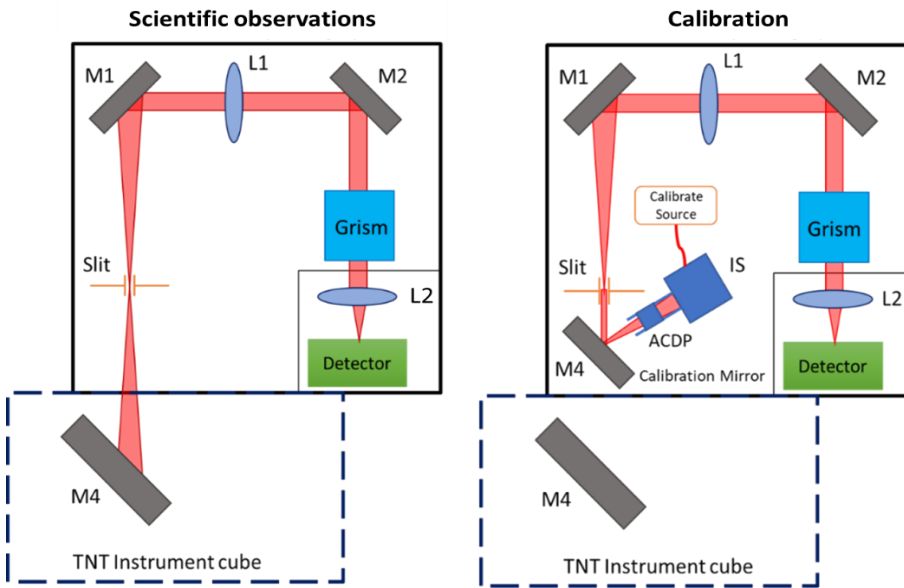


Figure 2. Left-hand panel: Scheme representing the top-view propagation of the light beam inside the spectrograph prototype during the scientific observations. Right-hand panel: Scheme representing the top-view propagation of the light beam inside the spectrograph prototype during the calibration of the instrument

The LRS slit was located in the TNT image plane. The slit selected one linear section of the incident FOV with a length of 3 arcminutes and a width of 0.9 arcseconds. The beam transmitted by the slit was collimated by lens L1 and directed towards the mirrors M1 and M2. These mirrors reflected the beam towards the grism located in the pupil plane. The grism comprised a Volume Phase Holographic (VPH) grating immersed between two prisms. The grism performed the spectral dispersion of the incident beam and transmitted it without any deviation of the central wavelength, λ_c equal to 600 nm. The beam transmitted by the grism was imaged by the lens L2 on the detector.

During the calibration of the spectrograph (Figure 2, right panel), we placed mirror M4 (mounted on a translating stage) in front of the entrance slit. We also injected the light emitted by some flat-field and spectral calibration lamps inside an Integrating Sphere (IS) by using a multi-mode fiber. The IS output face was imaged on the entrance slit via the achromatic doublet ACDP and mirror M4. After reflection by mirror M4, the optical path of the calibration beam emitted by the IS was identical to the optical path of the scientific beam coming from the TNT.

The slit is a 25 mm long 100 μm wide chrome slit, and was manufactured by Ealing. The collimator is a 50.8 mm achromatic doublet with a focal length of 250 mm, made by Thorlabs. This doublet was optimized for the spectral domain 400-700 nm, which is the specified spectral domain of the LRS. The grism was manufactured by Kayser, and the VPH has 930 lines/mm and the angles of the prisms are 30°. The wavelength λ_G not deviated by the grism is equal to 605 nm. The diffraction efficiency is more than 50% over the LRS specified spectral domain, and is more than 90% over the wavelength range of 500-600 nm. The faces of the grisms are coated with an anti-reflective coating that has a reflectivity of less than 1.5% over the specified spectral range of the LRS. The lens L2 is made of one commercial objective manufactured by the company Nikon model Noct-Nikkor AI-s. The focal length of this objective is equal to 58 mm f/1.2, its diameter is equal to 74 mm, and its angle of view is equal to 40.8°.

The detector used in the prototype is a commercial STF-8300 camera manufactured by Diffraction Limited. This camera has a 5.4 μm CCD with 3326×2504 pixels. The dimensions of the detector are thus equal to $18 \times 13 \text{ mm}^2$, which limits the width of the spectral interval detectable with this prototype to $\Delta\lambda = 330 \text{ nm}$.

Hence, the results provided by this prototype and presented in Section 3 cover the spectral interval 440-740 nm. This is not compliant with the specified interval for the LRS but has been considered as an acceptable value to verify the behavior of the full instrument and to check that the spectral performance is acceptable.

One advantage of the slitless mode is to be able to observe multiple and fainter targets within a single pointing with the trade-off of coarser spectral resolution, which is highly dependent on the seeing and the size of the object. This mode is suitable for a quick confirmation of objects with broad and prominent spectral features, such as confirming the natures of emission line galaxies or active galactic nuclei, or obtaining the slope of the spectral energy distribution to determine the ages of the underlying stellar populations of galaxies or globular cluster. On the other hand, the long-slit mode provides a constant spectral resolution that is independent of seeing and size of an object. By adjusting the slit width, one can adjust the resolution needed for a specific observation goal.

However, in the long-slit mode, one can only observe up to two objects in a single pointing. This mode is suitable for studying the chemical components, metallicities, and ionization levels of bright objects such as stars and parts of nearby galaxies via their series of absorption and emission features, and for observing the radial motions of binary stars via the doppler shifts of their absorption lines. Thus, the decision to choose between slitless and long-slit modes is based on the scientific goal of each observation program.

2.2 Prototype mechanical design and simulation analyses

2.2.1 Mechanical design

The LRS prototype comprises 24 commercial parts from the Thorlabs catalog and 32 parts that were designed using SolidWorks [4] and manufactured in the NARIT Precision Mechanical Workshop using Computer Numerical Control (CNC) machines.

Figure 3 represents the box of the LRS prototype. This box comprises 8 rectangular panels denoted A, B, C, D, E, F, G and H made of 6061 alloy, the properties of which are described in Table 2.

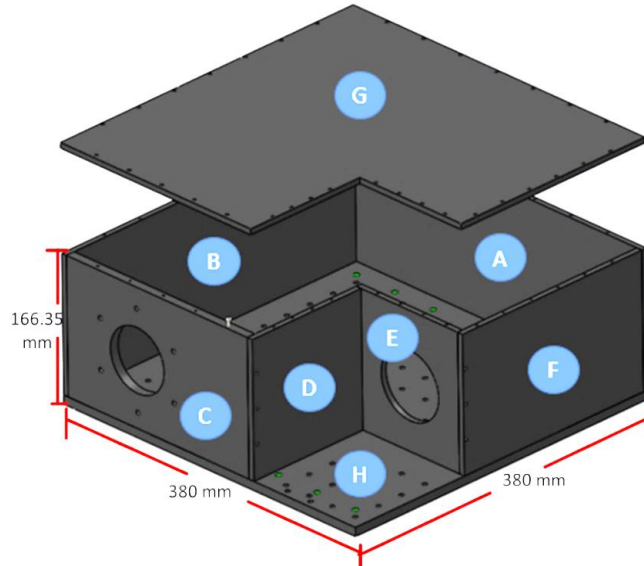


Figure 3. Size of the Low Resolution Spectrograph prototype. Width, length and height are in millimeters. A, B, C, D, E and F are side panels; G is the top panel that covers the spectrograph; and H is the optical breach board

The optical breach H holds the optomechanical components. The side panel components A, B, C, D, E and F are connected to the optical bench H and are covered on the top by the plate G. Panel C has a 70 mm center hole that corresponds to the LRS entrance face placed in front of the TNT instrument cube flange. Panel E has a 70 mm hole where the optical beam from the grism is transmitted to the camera objective (see Figure 4).

The width and the length of the LRS box are both 380 mm and the height is equal to 166.35 mm. The total weight of this structure is equal to 9.99 kg, as shown in Table 2.

Figure 4 represents all the optical and mechanical components of the prototype mounted inside the spectrograph box. Figure 5 show the SolidWorks model of the prototype mounted on the TNT. Several items have weights lower than 500 g and do not contribute significantly to the total weight of the instrument. The heaviest components are (i) the Grism and the CCD camera with the individual weights of both equal to 0.82 kg; (ii) the Linear Step Motor (LSM) that translates the entrance slits (1.60 kg); and (iii) the adapter of the box for the instrument cube.

Table 2. The mass, size and material type of each panel of the LRS prototype box

Name	Mass (g)	Size (mm)	Material
A	974.89	$380 \times 150 \times 6.35$	6061Alloy
B	958.72	$373.65 \times 150 \times 6.35$	6061Alloy
C	845.72	$245.56 \times 150 \times 10$	6061Alloy
D	361.75	$125 \times 150 \times 6.35$	6061Alloy
E	261.55	$121.74 \times 150 \times 6.35$	6061Alloy
F	595.41	$248.65 \times 150 \times 6.35$	6061Alloy
G	2151.12	$380 \times 380 \times 6.35$	6061Alloy
H	3847.07	$380 \times 380 \times 10$	6061Alloy
Total	9996.26	$380 \times 380 \times 166.35$	6061Alloy

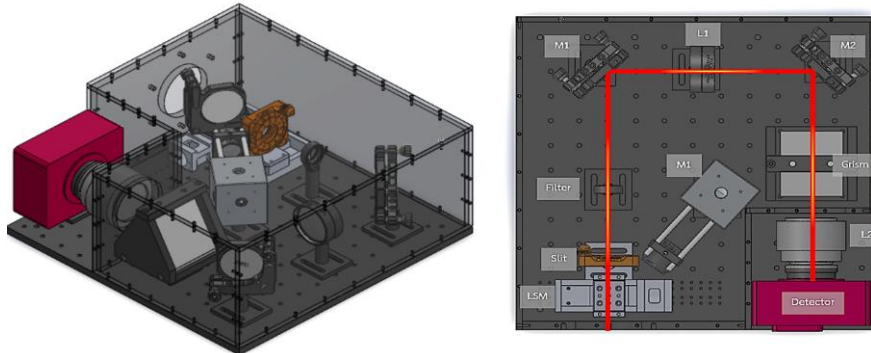


Figure 4. Left-hand panel: Side interior 3D sketch view of the Low Resolution Spectrograph prototype. Right-hand panel: Schematic top-view of the Low Resolution Spectrograph prototype. The red line represents the optical axis of the spectrograph.

The total weight of this prototype is equal to 18.91 kg, which is particularly low for a spectrograph dedicated to a 2 m class telescope. The LRS prototype is thus a light weight and compact instrument. Two advantages of the prototype are that i) it is possible to install the LRS on the TNT and remove it very easily, and ii) the balance of the instrument cube does not need to be adjusted after installing the LRS. It is thus possible to easily install the spectrograph on the TNT for only a few hours of observations and remove it from the instrument cube.

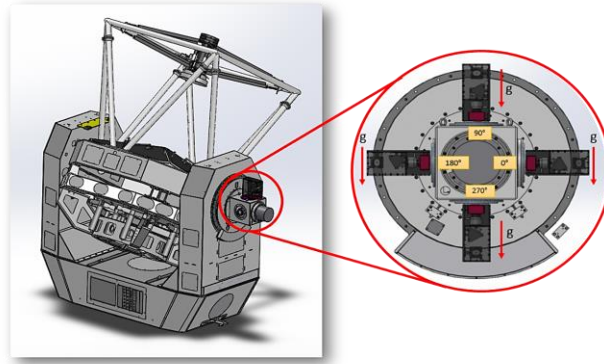


Figure 5. Left-hand panel: 3D view of the Low Resolution Spectrograph prototype mounted on the 2.4 m Thai National Telescope at the Nasmyth focus (SolidWorks model). Right-hand panel: Close-up of the spectrograph mounted on the instrument cube, with the interface between the LRS and the instrument cube shown in purple

2.2.2 Simulation analyses of Finite Element

The Low Resolution spectrograph is mounted on the TNT located inside the dome of the Thai National Observatory. During the night-time, the minimum temperature inside the dome is higher than 0°C while the maximum temperature is lower than 25°C. For these reasons, we decided to perform the thermos-elastic simulations over the temperature range equal to [0°C, 25°C].

During the observations, the Low Resolution Spectrograph rotates slowly around the instrument cube at a maximum angular speed equal to 15°C/h. Thus, we neglect the force due to this rotation and consider gravity to be the only force asserted on the spectrograph.

Figure 6 represents the assumptions used to perform the simulation. We have assumed that the spectrograph is interfaced with the instrument cube via the item “Fixture”. We also assumed that gravity is the only force that is applied to the spectrograph box and to each opto-mechanical component (integrating sphere, collimator, focusing lens). For example, in Figure 6, left-panel, we have represented the direction of gravity for the orientation and the direction of gravity at the orientation is equal to 180°.

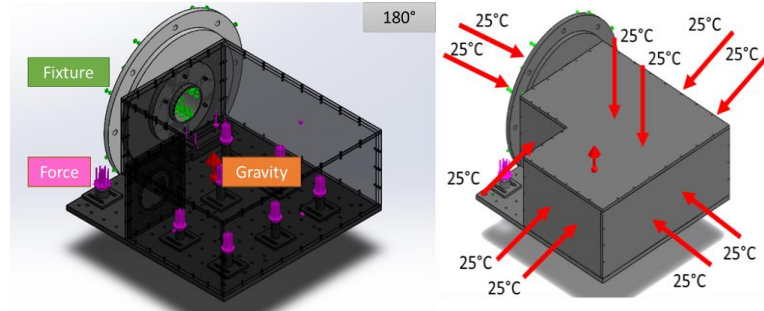


Figure 6. Left-hand panel: Assumptions used for the calculation of the mechanical deformations induced by the gravity of the spectrograph at the orientation equal to 180°.

Right-hand panel: Schematic of the assumption made on the environment temperature for the calculation of the deformations induced by the thermos-elastic effect

3. Results and Discussion

3.1 Simulation results

3.1.1 Gravity effect simulation results

During the observations, the orientation of the instrument cube can be fully adjusted between 0° and 360° . This is in order to adjust the orientation of the slit on the observed object and to compensate for the rotation of the field of view. Thus, we performed Finite Element Analyzes (FEA) to simulate the deformations induced by gravity on the LRS box only and to verify that these deformations will not misalign our optical system. These simulations were performed by using the simulation module in the SolidWorks software.

As a first step, we created a mesh element of the LRS prototype. We specified the mesh type to be a standard Solid Mesh, with 4 Jacobian points. The element size was 11.5 mm, with a tolerance of 0.6 mm. With these parameters, we used 492385 nodes and 296275 numbers of elements to model the prototype.

As a second step, we studied the gravitational displacement of the box. For example, in Figure 7 we have represented the deformation of the LRS prototype by assuming that gravity was acting on the base of the prototype box. This corresponds to an orientation θ of the instrument cube equal to 180° .

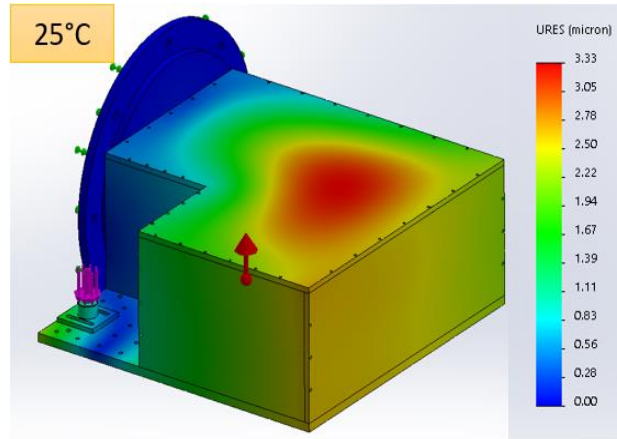


Figure 7. Results of the displacement simulation of the Low Resolution Spectrograph in SolidWorks at the instrument cube orientation θ equal to 180° . The simulation included the following fundamental physical effects: acceleration due to gravity ($|g|$ equal to 9.81 m/s^2), action force with the post, and fixtures in geometry mode.

In this case, we estimated that the maximum displacement value was less than $6 \mu\text{m}$. We repeated these simulations for the following orientations of the instrument cube: θ equal to 0° , 90° , 180° and 270° . We found that the maximum displacement of the box was equal to $3 \mu\text{m}$, which was obtained at θ equal to 180° . In this case, gravity is perpendicular to the optical bench.

We deduced that the maximum deformation of the box during a 360° rotation of the instrument cube is less than $6 \mu\text{m}$. This corresponds to approximately 1 pixel of the camera.

The maximum deformation caused by gravity and simulated using the SolidWorks model is considered acceptable since the prototype will be used to produce spectra during relatively short observing sessions (typically 1 h) that will be compatible with a small variation in the spectrum position on the camera.

3.1.2 Thermal expansion simulation results

We simulated the deformation of the box due to the effect of thermal expansion under the expected range of working temperatures of the Low Resolution Spectrograph (i.e., 0-25°C). This was done by using the SolidWorks model of the spectrograph described in the previous Section.

As a first step, we selected the orientation of the instrument cube as θ equal to 270°. At this orientation, gravity is perpendicular to the optical bench. As a second step we calculated the deformation due to both thermal expansion and gravity at a temperature T equal to 0 °C. The results are represented in Figure 7. As a third step, we repeated the simulation at a temperature T equal to 25°C. The results obtained at this temperature are also represented in Figure 7.

We noticed that the deformations in Figures 7 were identical despite the wide change of temperatures, from 0°C to 25°C. Based on these results, we estimated that the deformation of the box due to thermal variations should be less than 1 μm and is therefore negligible.

Thus, we concluded that the LRS prototype design is robust for the typical thermal variations experienced during operational conditions at the TNO. We also concluded that the prototype could be aligned in the laboratory at a temperature close to 20°C and then installed on the TNT without needing any realignment.

3.2 Prototype results obtained during on-sky observations with the TNT

3.2.1 Installation on the TNT and the Observing Procedure

We installed the LRS on the TNT during the engineering night of 22 December 2018. Figure 8 represents the LRS prototype before installation on the TNT (left panel) and after installation on the instrument cube (left-panel). The objectives of this observing run were:

- i) To verify that the full system can be operated in real observing conditions, including calibration of the system, pointing and scientific observations.
- ii) To verify that the performance of the prototype was in line with the specifications under operational conditions. This would be done by measuring the performance on celestial objects during real observations with the TNT.

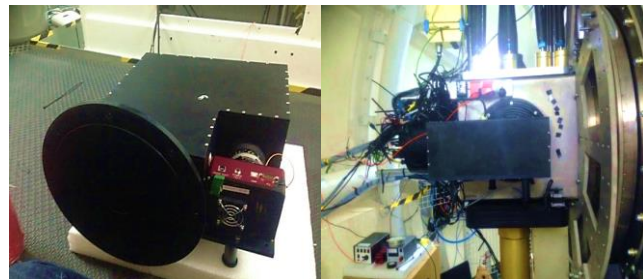


Figure 8. Left-hand panel: The Low Resolution Spectrograph prototype before installation on the TNT. On the left part of the box, there is a large black circular plate that constitutes the interface between the spectrograph and the TNT. Right-hand panel: The LRS prototype mounted on the TNT instrument cube.

It is important to mention that the prototype was aligned at the NARIT Optical Laboratory located in Chiang Mai. We therefore assumed that any misalignment introduced by i) transportation to the TNO, and ii) the pressure and temperature variations between the laboratory and the TNO would only cause a minor variation in the focus.

The procedure for testing the spectrograph involved four steps: focus adjustment; calibration; pointing; and measurement of the spectra. These are now described.

First, we placed the mirror M4 in front of the slit, injected inside the IS the light emitted by a Thorium-Argon spectral calibration lamp, and then recorded the spectrum measured by the detector. This lamp emits light at specific wavelengths and the spectral image comprises several lines, as represented in Figure 9. Each line corresponds to an image of the slit at a given wavelength. The focus adjustment was performed by varying the focus of the wide-field objective L2 and by measuring simultaneously the Full Width at Half-Maximum (FWHM) of the slit image. After adjusting the focus, we measured a FWHM equal to $32.4 \mu\text{m}$ (2 detector pixels) at the wavelength $\lambda = 5740 \text{ \AA}$ that corresponds to a spectral resolution of $R = 1,043$.

Second, we recorded the images of the spectrum provided by the spectrograph while injecting in the IS the light emitted by the Thorium-Argon spectral calibration lamp (Figure 9). We used these images to calculate the relationship between the pixel number and the wavelength by using Isis software [5, 6].

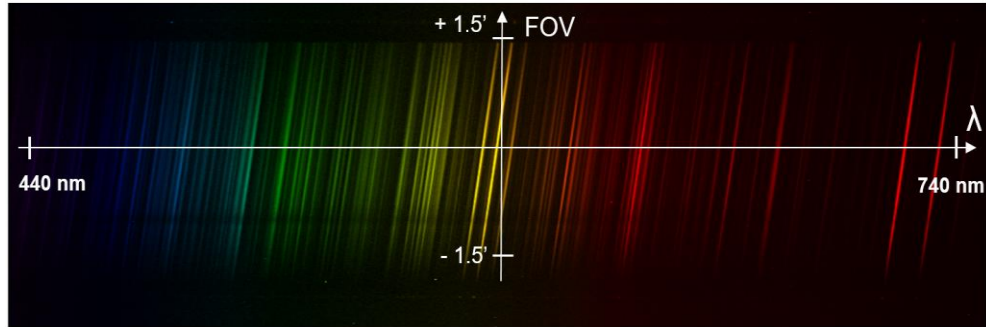


Figure 9. False-color image of the spectrum measured by the spectrograph during the calibration by injecting the light emitted by the Thorium-Argon (ThAr) lamp on the IS. The sloping emission lines correspond to the image of the spectrograph entrance slit at each emission line of the ThAr lamp

Third, we injected the light emitted by a Tungsten lamp inside the IS and we recorded the images of the spectrum provided by the spectrograph. In Figure 10, we noticed that the spectrum measured on the detector fully covers the specified FOV over the spectral interval 440-740 nm. These data confirm the possibility of calculating the spectrograph's instrumental response and pixel-to-pixel variations of the detector response over the FOV and the spectral domain covered by the LRS prototype.

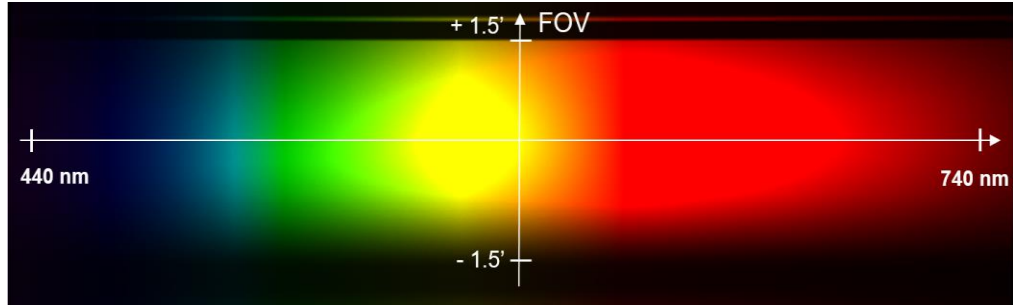


Figure 10. False-color image of the spectrum measured by the spectrograph during the calibration by injecting the light emitted by one tungsten lamp on the IS

The spectrograph response (Figure 11) was calculated as the ratio between the signal detected on the detector and the theoretical spectral irradiance of the source provided by Thorlabs, the supplier of the Tungsten lamp [7]. In Figure 11, we noticed that the normalized response of the spectrograph is more than 0.8 over the spectral interval 500-650 nm and reached a maximum at a wavelength near 560 nm. This is close to the spectral domain 500-600 nm over which the grating diffraction efficiency is maximal. At wavelengths less than 460 nm and more than 720 nm, the response of the instrument was between 0.2 and 0.4 and the limitation was due to the grating efficiency. Over this spectral range the transmission of the spectrograph is very low, and the measurement of the spectrum can be done only on very bright objects.

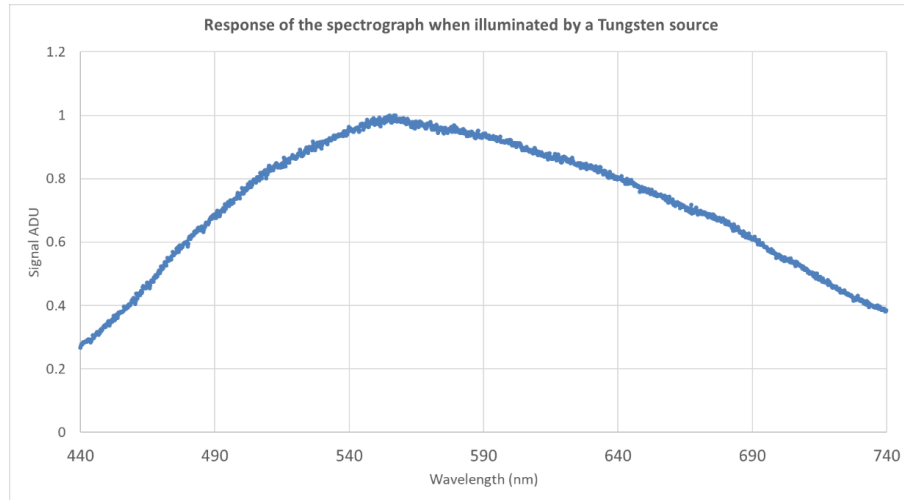


Figure 11. The normalized spectral response of the spectrograph calculated as the ratio between the signal measured on the central line of the detector and the theoretical spectral irradiance of the Tungsten source. The normalization was done to the maximum of the response of the spectrograph.

3.2.2 The Spectrum of NGC 2392

NGC 2392 (the Eskimo Nebula) is a moderately evolved, morphologically complex high-excitation double-shell planetary nebula [1] with a right ascension of 07h 29m 10.77 and declination of $+20^{\circ} 54' 42.5''$, and a magnitude of 9.68. Its elevation at the time of the test, between 23:00 and 01:00 local time, varied between $64^{\circ} 10' 59.5''$ and $78^{\circ} 49' 08.3''$.

We selected the Eskimo Nebula to test on-sky the performance of the spectrograph. Indeed, the size of this nebula is equal to 0.47 arcminutes, and making it possible to verify the image quality of the spectrograph over a part of the FOV. This planetary nebula has some specific emissions lines at the wavelengths equal to 486.13 nm, 495.8 nm, 500.7 nm and 656.28 nm, wavelengths which cover the prototype spectral domain. These emission lines were thus used to observe the replica of the nebula and to measure the spectral resolution at these wavelengths.

We used an integration time of 10 seconds for the 4K camera and the LRS in slitless and LRS longslit modes, as illustrated in Figures 12 and 13. We measured the signal-to-noise ratio of NGC 2392 with the 4K camera as 325.2, and for the LRS in longslit mode as 102.317 and in slitless mode as 92. We normalized the spectrum of NGC 2392 and calculated the spectral resolution. For H β it was 801; for OIII 826; for OIII (second line) 845; for HeI 1,097; and for NII 1,224, as illustrated in Figure 14.

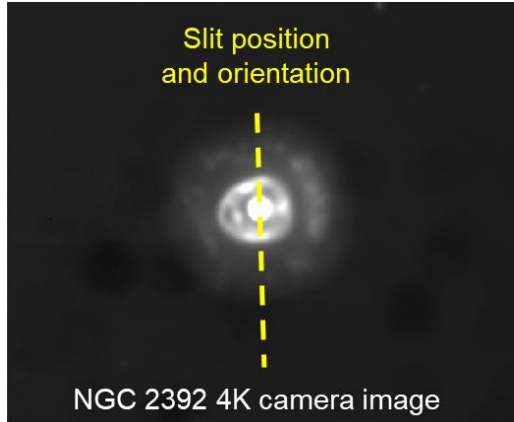


Figure 12. The image of NGC 2392 obtained with the 4K camera mounted on the TNT instrument cube. Integration time equal to 10 s, scale: signal min equal to 8649(0.2) ADU, signal max equal to 45000(1) ADU

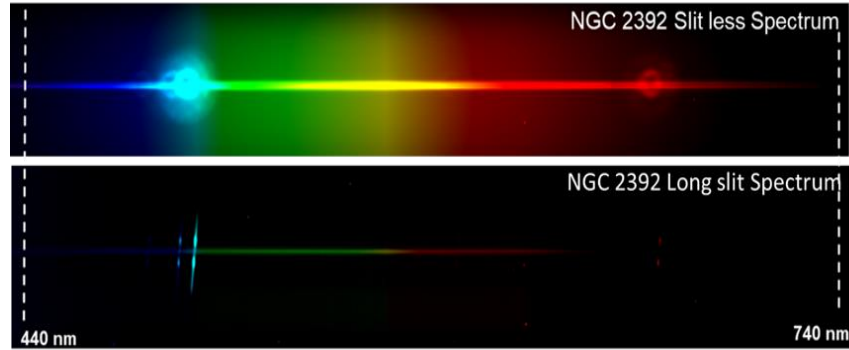


Figure 13. The top panel shows NGC 2392 in slit-less mode. Integration time equal to 10 s, scale: signal min equal to 4537(0.15) ADU, signal max equal to 30000(1) ADU. The bottom-panel shows NGC 2392 in long-slit mode. Integration time equal to 10 s, scale: signal min equal to 1500(0.67) ADU, signal max equal to 2194(1) ADU

We compared the extracted one-dimensional spectrum obtained from the LRS prototype mounted on the Thai National Telescope with one published spectra of NGC-2392 observed with a spectrograph mounted on the 2.16 m Beijing Astronomical Observatory [8] (Figure 14). We noticed in Figure 14 that the location and the shape of the emission lines of the H-alpha, H-beta, NII-doublets, and OII-doublets, as measured with the TNT LRS and as per the already published example, were in good agreement. However, we notice that the continuum measured with the TNT is slightly higher. The potential origins of this difference could be the differences between the calibration method used to process the dataset and the spectral resolution of the spectrographs used to make the observations.

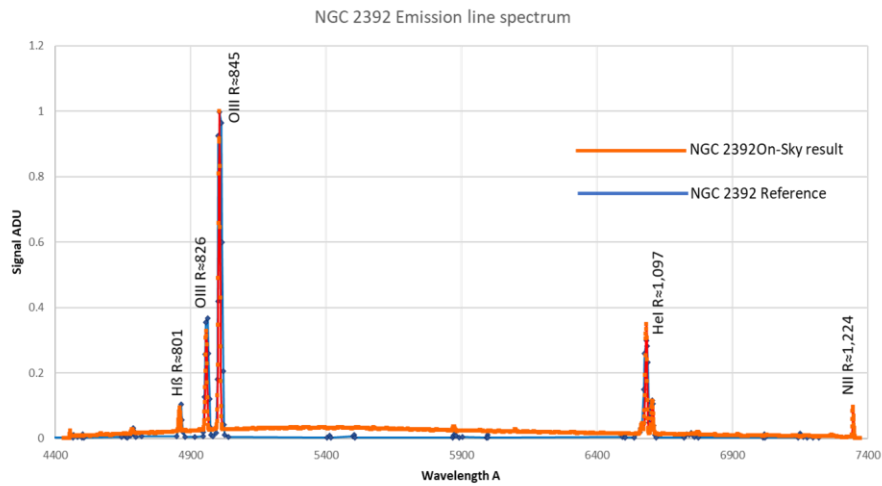


Figure 14. The normalized spectrum of NGC 2392 On-Sky result of LRS prototype for Thai National Telescope (orange curve) compared with published observed spectra of NGC 2392 (blue curve)

4. Conclusions

In this paper, we have presented the design development and on-sky results of the prototype of a Low-Resolution Spectrograph built for the 2.4 m Thai National Telescope. In the next step, we plan to develop a final version of the Low Resolution Spectrograph for the TNT, and build a LRS for the 0.7 m telescope at NARIT's regional observatory at Chachoengsao (Thailand).

References

- [1] Dhillon, V.S., Marsh, T.R., Atkinson, D.C., Bezawada, N., Bours, M.C.P., Copperwheat, C.M., Gamble, T., Hardy, L.K., Hickman, R.D.H., Irawati, P., Ives, D.J., Kerry, P., Leckngam, A., Littlefair, S.P., McLay, S.A., O'Brien, K., Peacocke, P.T., Poshyachinda, S., Richichi, A., Soonthornthum, B. and Vick, A., 2014. ULTRASPEC: a high speed imaging photometer on the 2.4-m Thai National Telescope. *Monthly Notices of the Royal Astronomical Society*, 4009-4021.
- [2] Buisset, C., Deboos, A., Lépine, T., Poshyachinda, S., and Soonthornthum, B., 2016. Design and performance estimate of a focal reducer for the 2.3 m Thai National Telescope. *Optics Express*, 1416-1430.
- [3] Buisset, C., Poshyachinda, S., Soonthornthum, Prasit, B.A., Alagao, M.A., Choochalerm, P., Wanjaroen, W., Lépine, T., Rabbia, Y., Aukkaravittayapun, S., Leckngam, A., Thummasorn, G., S. Ngernsujja, S., Inpan, A., Kaewsamoeta, P., Lhospice, E., Meemon, P., Artsang, P., Suwansukho, K., Sirichote, W. and Paenoi, J., 2018. Activity status and future plans for the Optical Laboratory of the National Astronomical Research Institute of Thailand. *Proceedings of the Third International Conference on Photonics Solutions*, 10714. ICPS2017.SPIE.
- [4] Dassault Systèmes Solidworks Corp., 1997. SolidWorks. USA 25.0.0.5021.
- [5] Nagasawa, D., Marshall, J., DePoy, D., and Mondrik, N., 2014. Conceptual design of a low resolution spectrograph for the Astronomical Observatory of C'ordoba. Ground-based and Airborne Instrumentation for Astronomy V, SPIE 9147.
- [6] Ammler-von Eiff, M., Sebastian, D., Guenther, E., Stecklum, B. and Cabrera, J., 2015. The power of low-resolution spectroscopy: On the spectral classification of planet candidates in the ground-based CoRoT follow-up. *Astronomische Nachrichten* 336(2), 134-144.
- [7] Shelyak, Ins., 2006. Thorium-Argon bulb. [online] Available at: <https://www.shelyak.com/description-eshel/?lang=en>
- [8] Wu, C., Li, J., Chang, Z., Lin, C., Hu, J. and Ip, W., 2001. Chemical Abundances of the Planetary Nebulae NGC 2392 and NGC 3242. *ASPC*, 246, 339.

Shelf-life Prediction of Micro-encapsulated Shrimp Oil in Different Packages using Empirical Models

Sirima Takeungwongtrakul^{1*}, Soottawat Benjakul², Supachai Pisuchpen³,
Pensiri Kaewthong⁴ and Sithipong Nalinanon⁴

¹ Department of Agricultural Education, Faculty of Industrial Education,
King Mongkut's Institute of Technology Ladkrabang, Bangkok, Thailand

² Department of Food Technology, Faculty of Agro-Industry,
Prince of Songkla University, Songkhla, Thailand

³ Department of Material Product Technology, Faculty of Agro-Industry,
Prince of Songkla University, Songkhla, Thailand

⁴ Faculty of Agro-Industry, King Mongkut's Institute of Technology Ladkrabang,
Bangkok, Thailand

Received: 3 May 2019, Revised: 10 September 2019, Accepted: 7 October 2019

Abstract

Micro-encapsulated shrimp oil (MSO) can be used to fortify food products and may be especially useful in the development of new functional foods. The shelf-life of packaged MSO was studied and sorption isotherms were examined. Moisture sorption isotherms and moisture sorption kinetics of MSO were evaluated at 30°C for water activity (a_w) values ranging from 0.113 to 0.923 by a static gravimetric method. Empirical models were determined to predict the experimental data. The initial stage of moisture sorption by the MSO was relatively rapid and it decreased with time. All the sorption curves were found to be type III. The most suitable model for predicting the moisture sorption isotherm of MSO was the GAB model because it had the lowest percentage root mean square error (RMSE). The shelf-life of MSO packaged in polypropylene (PP), Nylon/linear low density polyethylene (Nylon/LLDPE) and metalized polyethylene terephthalate (metalized PET) pouches stored at 30°C and either 75% or 80% relative humidity (RH) was predicted by the GAB equation and the longest shelf-life of MSO (507 days in 80% RH and 725 days in 75% RH) was found in metalized PET packages. The empirical models can be useful for predicting the shelf-life of MSO.

Keywords: micro-encapsulated shrimp oil, moisture sorption isotherm, empirical model, shelf-life, packaging
DOI 10.14456/cast.1477.3

*Corresponding author: Tel.: +66 89-657-0887 Fax: +66 2-329-8435
E-mail: sirima.ta@kmitl.ac.th

1. Introduction

Hepatopancreas is a by-product generated from the manufacturing of hepatopancreas-free whole shrimp. Shrimp oil from hepatopancreas is one of the major sources of polyunsaturated fatty acids (PUFAs) such as eicosapentaenoic acid (EPA) and docosahexaenoic acid (DHA) and it also contains the antioxidant astaxanthin. PUFAs are known for their health benefits, which include their ability to prevent lipotoxicity, cardiovascular diseases, human breast cancer, inflammatory diseases and Alzheimer's disease [1]. The use of shrimp oil in food products has been limited owing to the high susceptibility of PUFAs to oxidation. Encapsulation can be used to delay or inhibit oxidation and mask unpleasant flavors and odors in the resulting products [2] and the micro-encapsulation of oil can be achieved by spray drying [3]. Good quality microcapsules, with low water activity (a_w) and ease of storage and handling, can protect the active material against undesirable reactions. However, many food ingredients that are added in the form of powders tend to have sticking and caking problems due to moisture adsorption during storage. Water molecules permeate into the package, leading to an increase in moisture content and a decrease in the product stability and dispersibility over time [3]. Moisture sorption isotherms are related to the hydration of food products [4] and represent a correlation between a_w and equilibrium moisture content (EMC) in food products at a constant temperature [5]. Therefore, moisture sorption isotherms are a useful means of monitoring the drying process of products and the shelf-life stability of packaged products. They are usually classified into Types I, II, III, IV and V [6]. In general, dried food products have Type II or III isotherms [7]. Sorption isotherms have previously been described by mathematical models validated by statistical methods. Theoretical mathematical models were developed to describe sorption mechanisms. Some mathematical models are just empirical, or simplifications of more elaborate models [7, 8]. There are some semi-empirical equations with two or three fitting parameters to describe moisture sorption isotherms [7]. The BET equation, the GAB model, the Peleg model, the Lewicki model, the Oswin model and the Smith model are widely used to describe sorption in food products. Thus, it is a requirement to choose a suitable equation of moisture sorption isotherm for a specific product. This study aimed to investigate moisture sorption kinetics in order to select an empirical model for the moisture sorption isotherm and to evaluate the shelf-life of micro-encapsulated shrimp oil (MSO) packaged in bags made from three materials; (polypropylene (PP), nylon/linear low density polyethylene (Nylon/LLDPE) and metalized polyethylene terephthalate (metalized PET)).

2. Materials and Methods

2.1 Materials

Sodium caseinate was procured from Vicchi Enterprise Co., Ltd. (Bangkok, Thailand). Fish skin gelatin (bloom strength of 230-250 g) was procured from Lapi Gelatine S.p.A. (Milano, Italy). Glucose syrup was obtained from Charoenworrakit Co., Ltd. (Samut Prakan, Thailand). All the plastic bags were purchased from a supermarket. Polypropylene (PP), Nylon/linear low-density polyethylene (Nylon/LLDPE) and metalized polyethylene terephthalate (metalized PET) bags with the dimension of 3.0 cm × 2.0 cm were used.

2.2 Preparation of micro-encapsulated shrimp oil (MSO)

The shrimp oil was extracted from the digestive gland (hepatopancreas) of Pacific white shrimp (*Litopenaeus vannamei*) using a mixture of isopropanol and hexane as per the method of Takeungwongtrakul *et al.* [9]. Fish gelatin, sodium caseinate and glucose syrup were mixed at a ratio of 1:1:4 (w/w/w) in deionised water, to prepare the “wall materials” according to the method of Takeungwongtrakul and Benjakul [3]. Shrimp oil was added into the solution at a core/wall material ratio of 1:4 (v/v). The mixtures were homogenised at a pressure level of 4,000 psi for 4 passes. A SD-06A spray-dryer (LabPlant Ltd., Huddersfield, UK) was used to produce micro-encapsulated shrimp oil (MSO) following the method of Takeungwongtrakul *et al.* [9]. Four grams of MSO was packaged in the different bags as described above and heat-sealed.

2.3 Determination of initial and critical moisture content

Initial moisture content (IMC) was determined following the method of AOAC [10], and the critical moisture content (CMC) of MSO was determined by placing MSO into water desiccators at 30°C until MSO was assessed as being at an unacceptable level by 10 trained panelists. The panelists were trained to evaluate the appearance of MSO. Prior to the evaluation, the panelists were trained three times a week. They were trained with standards for two sessions using a scale of 0-15, where 0 and 15 represented dry and wet MSO, respectively. The appearance of MSO was the initial quality that was used to judge the acceptability of MSO.

MSO was evaluated for moisture content (% dry weight basis) every hour until MSO samples reached their CMC. The CMC was identified as the point at which the deterioration of MSO reached an unacceptable level. The CMC was reached when the MSO particles stuck together to a level at which it was rejected by the panelists.

2.4 Moisture sorption characteristics

2.4.1 Moisture curve and rates

The sorption isotherm was determined by a static gravimetric technique, using different saturated salt solutions [11]. MSO was pre-dried in a desiccator over phosphorus pentoxide (P_2O_5) and kept in separated desiccators with different saturated salt solutions. The desiccators were then kept in an electric oven at $30 \pm 1^\circ C$, which gave equilibrated environments in the desiccators. All saturated salt solutions ($MgCl_2$, KI , KCl , $NaCl$ and K_2NO_3) were selected to produce a broad range of a_w (0.324-0.923) [12]. The a_w of storage conditions were confirmed by means of a humidity meter (HM70, Vaisala, Helsinki, Finland). Weight of MSO was determined as a function of time. Moisture content (g H_2O /100 g dry sample) of MSO was determined by placing samples in an oven at $105^\circ C$ for 3 h. Water activity (a_w) was measured using an AquaLab Series 3 water activity meter (Decagon Devices, Inc., Pullman, WA, USA). The moisture adsorption data were fitted into Peleg's equation [12]:

$$M_t = M_0 + t / (k_1 + k_2 t) \quad (1)$$

where M_t represents the moisture content after designated time of storage (% dry weight), M_0 represents the initial moisture content (% dry weight), k_1 represents the constant of Peleg rate (h/g water/g solids) and k_2 represents the constant of Peleg capacity (g solids/g water).

2.4.2 Sorption isotherm

The moisture sorption isotherm of MSO was determined for the a_w range of 0.113-0.923 using different saturated salt solutions in the desiccators as described above. The salt solutions were K_2NO_3 , KCl , $NaCl$, KI , $Mg(NO_3)_2$ and $MgCl_2$ at the following a_w of 0.923, 0.836, 0.751, 0.679, 0.514 and 0.324, respectively. Sample weights, as a function of time, were determined until they reached equilibrium. The moisture contents (% dry weight basis) in the samples were measured at 105 °C for 3 h using an oven. The a_w was evaluated using an Aqua-Lab Water Activity Meter. The percentage of the equilibrium moisture content (EMC) in the samples at each specific a_w was determined using equation 2 [13]:

$$\% EMC = (W_e / W_i) \times (M_i + 1) - 1 \quad (2)$$

where W_e represents total weight (dry weight + water) at equilibrium (g), W_i represents the initial weight (g) and M_i represents the initial moisture content (g/g). Thus, a sorption isotherm was constructed by plotting between a_w and % EMC.

2.4.3 Moisture sorption isotherm modeling of MSO

The models of the sorption isotherms of MSO were expressed as shown in Table 1. The model parameters were derived from the experimental results. The root mean square error (RMSE) is the predicting capability of a model in relation to the number of data points. The RMSE was calculated using equation 9.

Table 1. Moisture sorption models for fitting experimental data

Model names	Model equations	Equation number	References
BET	$M = m_o Ca_w / [(1 - a_w) + (C - 1)(1 - a_w) a_w]$	3	Brunauer <i>et al.</i> [14]
GAB	$M = m_o C k a_w / [(1 - k a_w)(1 - k a_w + C k a_w)]$	4	Van Den Berg [15]
Peleg	$M = a_w^b + c \cdot a_w^d$	5	Peleg [16]
Lewicki	$M = [F/(1 - a_w)^G] - [F/(1 + a_w^H)]$	6	Lewicki [17]
Oswin	$M = k[a_w/(1 - a_w)]^c$	7	Oswin [18]
Smith	$M = C_1 + C_2 \ln(1 - a_w)$	8	Smith [19]

$$RMSE = \sqrt{\frac{\sum[(M_{exp} - M_{cal})/M_{exp}]^2}{N}} \times 100 \quad (9)$$

where M_{exp} is the equilibrium moisture content determined from the experimental data and M_{cal} is the equilibrium moisture content predicted using the mathematical models; N is the number of experimental points.

2.5 Shelf -life prediction of the packaged MSO

MSO (4 g) was packed in the different plastic bags (PP, Nylon/LLDPE and metallized PET) and the bags were heat sealed. MSO is very sensitive to changes in % RH. A small change in RH affects the amount of water in MSO. Thus, the packaged MSO samples were stored at 30°C and either 75% RH or 80% RH for 13 weeks in an environmental chamber (WTB Binder, Tuttlingen, Germany). Water vapour permeability (WVP) was determined by a modified ASTM method [20] and calculated using equation 10:

$$WVP \text{ (g m}^{-1} \text{ s}^{-1} \text{ Pa}^{-1}) = w l A^{-1} t^{-1} (P_2 - P_1)^{-1} \quad (10)$$

where w is the weight gain of the cup (g); l is the film thickness (m), A is the exposed area of film (m^2), t is the time of gain (s), $(P_2 - P_1)$ is the vapor pressure difference across the film (Pa). Three films were used for WVP testing.

The simplest shelf-life calculation is when the isotherm is treated as a linear function in the linear model [21]. The model can be calculated using equation 11:

$$t = [(l \cdot w_d \cdot \beta) / (P \cdot A \cdot p_s)] \cdot \ln [(a_{wo} - a_{w,t=0}) / (a_{wo} - a_{w,t=t})] \quad (11)$$

where w_d (g) represents the dry weight in the packaged food, l (cm) represents the film thickness, P represents the water vapour permeability coefficient ($\text{g water.cm/cm}^2.\text{sec.cm Hg}$), A represents the package surface area (cm^2), p_s represents the saturated vapour pressure of water at the storage temperature (cm Hg), a_{wo} represents the water activity of storage conditions, $a_{w,t=0}$ represents the initial water activity of product, $a_{w,t=t}$ represents the critical water activity of product at time = t , and β represents a slope of the moisture sorption isotherm.

Shelf-life calculation was verified by using the actual package product storage test. The MSO in a bag rendering the highest shelf-life was studied. The samples were regularly examined for the EMC. The value of RMSE was used to evaluate the goodness of fit between the experimental and the predicted moisture content. The lower value of RMSE indicates the better fit.

2.6 Statistical analysis

Experiments were performed in triplicate and data were subjected to analysis of variance (ANOVA) and mean comparison by Duncan's Multiple Range Test using the Statistical Package for Social Science (SPSS for windows, SPSS Inc, Chicago, IL, USA). The parameters of the different models were obtained from the regression curves by statistical tools using Microsoft Excel 2007.

3. Results and Discussion

3.1 Moisture content and a_w of MSO

MSO initially had a moisture content of $1.13 \pm 0.01\%$ (dry basis), which corresponded to a low a_w (0.35 ± 0.01). The CMC and critical a_w were $7.78 \pm 0.07\%$ (dry basis) and 0.71 ± 0.02 , respectively. MSO readily adsorbs moisture from the surrounding atmosphere and is considered a moisture sensitive food. A high a_w in food products leads to shorter storage life because high free water promotes biochemical reactions that are associated with deterioration [22].

3.2 Moisture sorption kinetics

The sorption kinetic curves of MSO are given in Figure 1. Moisture sorption rapidly increased during the initial stage, while less moisture was adsorbed as storage time progressed and moisture content plateaued, which was likely to be the equilibration a_w in each condition. At a_w of 0.324-0.923, the time required to reach each equilibrium a_w increased when the a_w increased. Baucour and Daudin [23] reported that mass transfer is very slow at high a_w , indicating that it is difficult to reach equilibrium at a_w of 0.9-1.0. The sorption kinetics of MSO under experimental situation were predicted with Peleg's equation (Eq. 1), which is associated with the hydration behavior of MSO. The coefficient of determination was found to be high in all cases ($R^2 > 0.99$), which represented a desired fit to the experimental data. The constants of Peleg's rate (k_1) and capacity

(k_2) are shown in Table 2. Food products generally kept at a higher RH have lower values of k_1 and k_2 [24]. Turhan *et al.* [25] reported that k_1 is associated with mass transfer. It means that a lower value of k_1 indicates a higher degree of initial moisture adsorption rate. The results indicated that a decrease in k_1 of MSO was also found when a_w was increased, which was in accordance with an increase in initial rate of water adsorption. The k_2 is associated with the maximum water adsorption capacity. The lower constant value of k_2 indicates a higher adsorption capacity [25]. The k_2 decreased as a_w increased from 0.324 to 0.923, meaning that the water adsorption capacity of MSO increased with increasing a_w . From the values of k_1 and k_2 , MSO adsorbed faster and kept more water when stored in an environment with high a_w .

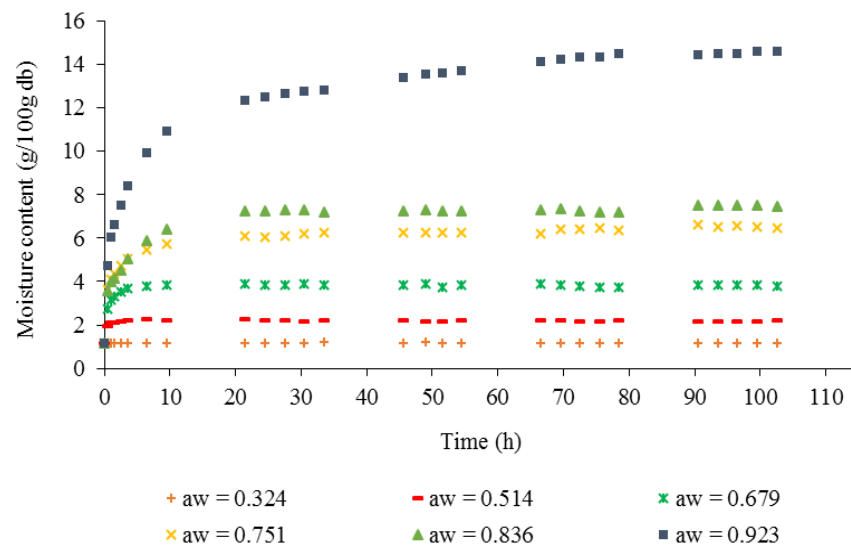


Figure 1. Moisture sorption curves of MSO at various water activities as a function of time

Table 2. Sorption kinetic model constants and coefficients of determination for MSO

Water activity	MSO		
	k_1	k_2	R^2
0.324	7.1160	18.1690	0.9917
0.679	0.4091	0.9534	0.9996
0.751	0.3255	0.1875	0.9998
0.836	0.2546	0.1537	0.9991
0.923	0.2217	0.0728	0.9996

k_1 = the constant of Peleg rate, k_2 = the constant of Peleg capacity, R^2 = the coefficient of determination

3.3 Moisture sorption isotherm of MSO

Changes in the experimental and predicted equilibrium moisture content (EMC) of MSO for a_w range of 0.324-0.923 are given in Figure 2. The results indicated that the EMC increased at higher a_w . The sorption isotherms obtained in this study are type III isotherms (J shape). Foods containing high-sugar levels typically show Type III isotherms and they adsorb relatively small amounts of water at low a_w and large amounts of water at high a_w , especially beyond 0.60 [26]. In this study, the EMC of MSO dramatically soared above $a_w = 0.514$. For a_w lower than 0.514, a slight increase in EMC with increasing a_w was found. This might have been due to the fact that adsorption of water occurs only at the surface of wall materials. For higher a_w ($a_w > 0.514$), the dissolution of soluble wall materials caused the increase in moisture content. Water molecules penetrate the pore structure of wall materials and are mechanically trapped in the void spaces of wall materials, especially at higher a_w . The uptake of water at higher a_w could be affected by the stability of the microporous structure [27]. The results reconfirmed that the constituents of the wall materials (fish gelatin, sodium caseinate and glucose syrup) were able to interact directly with the water molecules, which affected the moisture sorption ability of MSO. Type of isotherm (Type III isotherm) was similar to that reported for beta glucan-rich biscuits [28] and freeze-dried and spray-dried passion fruit pulp powders [29]. Panjagari *et al.* [28] reported that the sugar component of the product rendered the most significant influence on the sorption behavior. Barreiro *et al.* [30] reported that the EMC of barley malt sharply increased at higher a_w of 0.5, mainly at higher amounts of sugars.

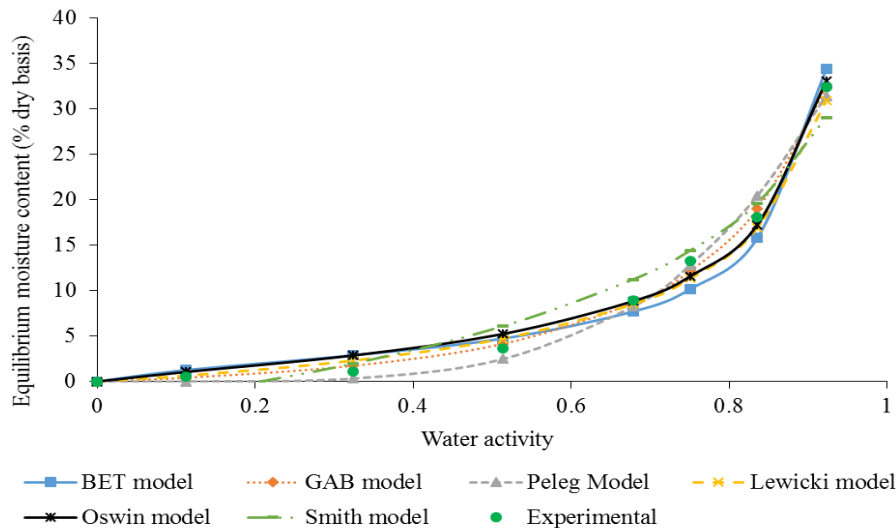


Figure 2. Experimental data and empirical models of moisture sorption isotherms for MSO at 30°C

3.4 Modeling of sorption isotherms

Various researchers have described the sorption isotherms for several products. Some of these models were empirical, others were semi-empirical. In this study, the sorption isotherms were predicted using six sorption isotherm equations: the BET, GAB, Peleg, Lewicki, Oswin and Smith models. These common mathematical equations used for describing moisture sorption in food

products are shown in Table 1. Those models have the parameters of two, three and four partial regression coefficients. The researchers correlated the experimental data with these moisture sorption isotherm models in order to identify the model of best fit. The isotherm models, equation constants and root mean square error (RMSE) for each model of MSO are summarized in Table 3. The goodness-of-fit of the experimental and predicted EMC values for the different sorption isotherm models were evaluated by RMSE, and lower values of RMSE pointed to the most suitable fit. The results showed that all investigated models gave a good description of the isotherms of spray-dried MSO at 30°C. However, the GAB model had the minimum values for RMSE (0.64) when used to predict the moisture sorption isotherm of spray-dried MSO at 30°C. It was found that the GAB model presented a good fitting for the spray-dried MSO at 30°C, and it was followed in increasing RMSE order of best-fit by the Smith, BET, Lewicki, Peleg and Oswin models, respectively. A similar result was reported by Zammouri *et al.* [31] for Hypril (pharmaceutical compounds). Zammouri *et al.* [31] found that the GAB model, Peleg model and the Oswin model fitted well with the water sorption isotherms of Hypril, but it was the Oswin model that presented the best fit. Referring to the GAB model, the monolayer moisture content (m_o) value of that model shows the amount of adsorbed water in a monolayer on the adsorbent surface. It is also used to measure the availability of active sorption sites in spray-dried MSO. It is a crucial quality factor for the planning of optimal storage conditions. The parameter C represents the stronger bonds between water molecules at monolayer and the binding sites on the adsorbent surface. In addition, k is a correction parameter for multilayer molecules relative to the bulk liquid. When k is 1, the molecules beyond the monolayer act as pure water [32]. Heat evaporation of the multilayer molecules is the same as pure water ($k = 1$) [33]. Sormoli and Langrish [34] used the GAB model to fit the moisture sorption data and found it to be more effective than other models they tried. The ability of the GAB model to fit the moisture sorption isotherms of foods with a wide range of a_w values was documented by Timmermann [35]. The monolayer moisture content shows the maximum shelf-life of dried products with a_w values between 0.2 and 0.3, and lipid oxidation can be initiated above this moisture content [36]. Changes in factors such as stickiness and caking of food powders occurred at a range of a_w from 0.35 to 0.5 [34]. However, the CMC of

Table 3. Sorption isotherm model constants and percentage of root mean square error for MSO

Sorption isotherm model	Constant	RMSE
BET	$m_o = 2.69$ $C = 5.53$	1.14
GAB	$m_o = 12.14$ $k = 0.87$ $C = 0.29$	0.64
Peleg	$a = 22.24$ $b = 4.34$ $c = 22.24$ $d = 4.34$	1.90
Lewicki	$F = 52.29$ $G = 0.38$ $H = 0.28$	1.21
Oswin	$k = 5.01$ $c = 0.76$	2.12
Smith	$C_1 = -2.93$ $C_2 = -12.47$	0.90

food products in regard to microbial growth terms was recommended to be 0.6 [36]. Thus, the appropriate a_w for MSO should be at $a_w < 0.3$ and moisture content of lower than 12.14% (on a dry weight basis) was recommended (Table 3). The Smith model provides the sorption isotherm of biological substances. Al-Muhtaseb *et al.* [37] reported that the Smith model gave a good fit for experimental data between a_w values of 0.35 and 0.9. The BET model could be used to estimate the monolayer water content in the food products, and it was applicable at a_w range of 0.1-0.5 [38]. Nevertheless, the Lewicki model was applicable to a high range of a_w levels. The water content goes to infinity as a_w reaches 1.0 [17]. The Oswin model expressed the moisture isotherms throughout all the ranges of a_w [18]. Nonetheless, this present study found that the maximum RMSE value was predicted by the Oswin model. The non-sigmoidal and sigmoidal isotherms could be predicted using the Peleg model [16], since this model could predict the moisture sorption isotherm more effectively than the GAB model. The RMSE data from the Peleg model were higher than those of GAB model. The experimental and the predicted models of moisture sorption isotherms for spray-dried MSO are shown in Figure 3. Validation of the established model was evaluated by comparing the predicted moisture contents with their experimental counterparts in spray-dried MSO. The predicted data usually banded around the straight line, suggesting the mathematical model was suitable to describe the sorption behavior of spray-dried MSO.

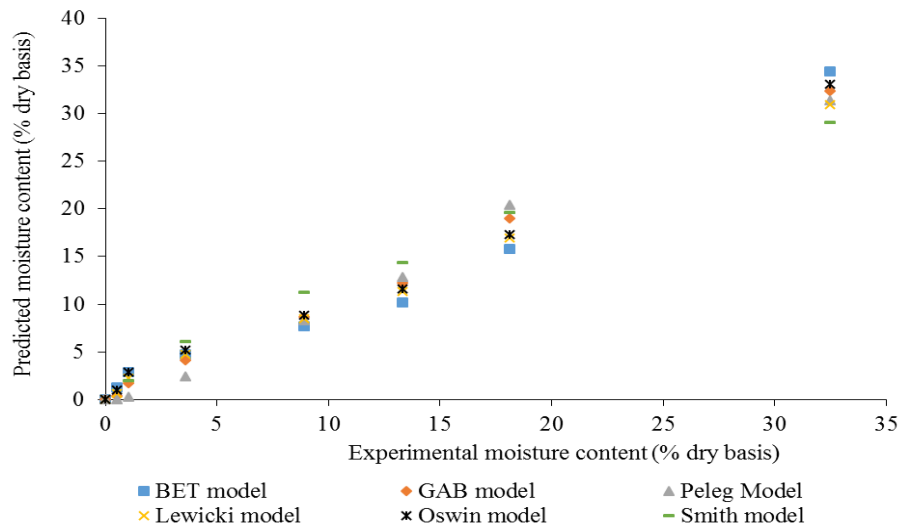


Figure 3. Comparison between experimental moisture content and predicted moisture content of MSO by various sorption models

3.5 Shelf-life prediction of MSO

The predicted shelf-life of spray-dried MSO in different commercial bags (PP, Nylon/LLDPE and metalized PET bags) at 30°C and either 75% or 80% RH is shown in Table 4. The shelf-life of

Table 4. Thickness and permeability coefficients of films and predicted shelf-life of MSO in different bags under 75% and 80% RH at 30°C

Package	Thickness (μm)	WVP (×10 ⁻³ g.mm/day.m ² .mmHg)	Relative humidity (%)	Predicted shelf-life (days)
PP	89 ± 0.00a	6.09 ± 0.37b	75	722
			80	505
Nylon/LLDPE	82 ± 1.59c	9.31 ± 1.60a	75	436
			80	305
Metalized PET	85 ± 0.00b	5.76 ± 1.06b	75	725
			80	507

Data are expressed as mean ± SD (n=3), Lowercase letters in the same column indicate significant difference ($p < 0.05$).

spray-dried MSO is limited by moisture uptake. It is important to study the water vapour barrier properties of packaging materials. The moisture uptake of food products during storage depends on the moisture sorption isotherms of foods, the WVP of packaging film and environmental RH [12]. Table 4 shows that the average thickness of the PP, Nylon/LLDPE and metalized PET bags was found to be 89±0.00, 82±1.59 and 85±0.00 μm, respectively. The WVP of the bags was 6.09, 9.31 and 5.76×10^{-3} g.mm/day.m².mmHg for PP, Nylon/LLDPE and metalized PET bags, respectively. The results indicated that Nylon/LLDPE film bags had a higher WVP than the other two ($p < 0.05$), which was more likely related to its lower thickness (Table 4). However, there was no significant difference ($p > 0.05$) in WVP between metalized PET and PP films. Therefore, the commercial metalized PET and PP films had better water vapour barrier properties than the commercial Nylon/LLDPE film. The water vapour barrier property of film is an important parameter for estimating the shelf-life of food products. In this study, the shelf-life estimation of MSO depends on the critical limits used, initial product conditions, packaging conditions and environmental conditions. Equation 11 was used to calculate and predict the shelf-life of MSO in different commercial bags. The results indicated that the commercial metalized PET and PP bags extended the shelf-life of MSO more efficiently than the commercial Nylon/LLDPE bag at all % RH. However, the shelf-life of MSO packaged in PP bags was slightly lower than that of metalized PET bags. So, the different bags showed the influence of WVP on the shelf-life of MSO. For the same packaging, the results showed that MSO stored at 75% RH had longer shelf-life than MSO stored at 80% RH because of a lower moisture gradient between the storage environment and inside the packaging. The water molecules passed through the packaging film and the moisture content of dry food increased at a rapid pace at this early stage. Afterwards, the gradient of RH between the inside and outside of the packaging gradually decreased while the moisture content of dry food increased slowly until equilibrium with environmental RH was reached [39]. In conclusion, the longer shelf-life of MSO was calculated as 507 days in 80% RH and 725 days in 75% RH when MSO was packaged in metalized PET bags. The verification of shelf-life for MSO packaged in metalized PET bag was performed at 30°C, 75% RH. The EMC of MSO from the experiment was compared with the EMC from the prediction. The RMSE value of this equation was 0.711. In a similar study, Pisuchpen [40] reported that the experimental and the predicted values of EMC for hot curry cube in Nylon/LLDPE bags had the RMSE values of 1.88. The low RMSE value indicates the small difference between the experimental and predicted values. Thus, this equation could be considered a reliable tool for predicting the EMC with time for MSO in the metalized PET bag.

4. Conclusions

The isotherms and moisture sorption kinetics of MSO were made using various types of saturated salt solutions. The initial stage of the moisture sorption kinetics of MSO occurred relatively rapidly. However, the amount of water adsorbed decreased with time. MSO exhibited a Type III isotherm. The GAB model was the most appropriate model to estimate the moisture sorption isotherms of MSO. The predicted shelf-life of packaged MSO in metalized PET bags at 30°C and 75% RH fitted well with the actual shelf-life. Thus, the empirical models can be useful for predicting the shelf-life of MSO.

5. Acknowledgements

This work was financially supported by KMITL Research Fund under Researcher Development Grant for Project No. KREF016103 to Dr. SirimaTakeungwongtrakul. The authors would also like to thank Professor Dr. Anthony Keith Thompson, Visiting Professor at Faculty of Agro-Industry under Visiting Research Scholar granted by KMITL Research Fund, for invaluable suggestions and corrections.

References

- [1] Martinez, P.P., Jimenez, F.P., Miranda J.L., 2010. N-3 PUFA and lipotoxicity. *Biochimica et Biophysica Acta*, 1801(3), 362-366.
- [2] Tonon, R.V., Grosso, C.R. and Hubinger, M.D., 2011. Influence of emulsion composition and inlet air temperature on the microencapsulation of flaxseed oil by spray drying. *Food Research International*, 44(1), 282-289.
- [3] Takeungwongtrakul, S., and Benjakul, S., 2016. Effect of glucose syrup and fish gelatin on physicochemical properties and oxidative stability of spray-dried micro-encapsulated shrimp oil. *Journal of Food Processing and Preservation*, 41(3), 1-12.
- [4] Bahloul, N., Boudhrioua, N., and Kechaou, N., 2008. Moisture desorption-adsorption isotherms and isosteric heats of sorption of Tunisian olive leaves (*Olea europaea* L.). *Industrial Crops and Products*, 28(2), 162-176.
- [5] Abramović, H., and Klofutar, C., 2006. Water adsorption isotherms of some gellan gum samples. *Journal of Food Engineering*, 77(3), 514-520.
- [6] Basu, S., Shrivhare, U., and Mujumdar, A., 2006. Models for sorption isotherms for foods: a review. *Drying Technology*, 24(8), 917-930.
- [7] Yan, Z., Sousa-Gallagher, M.J., and Oliveira, F.A.R., 2008. Sorption isotherms and moisture sorption hysteresis of intermediate moisture content banana. *Journal of Food Engineering*, 86(3), 342-348.
- [8] Foster, K.D., Bronlund, J.E., and Paterson, A.T., 2005. The prediction of moisture sorption isotherms for dairy powders. *International Dairy Journal*, 15(4), 411-441.
- [9] Takeungwongtrakul, S., Benjakul, S., Santoso, J., Trilaksani, W., and Nurilmala, M., 2015. Extraction and stability of carotenoid-containing lipids from hepatopancreas of Pacific white shrimp (*Litopenaeus vannamei*). *Journal of Food Processing and Preservation*, 39(1), 10-18.
- [10] AOAC, 2000. *Official Methods of Analysis*. Washington, DC: Association of Official Analytical Chemists.
- [11] Greenspan, L., 1977. Humidity fixed points of binary saturated aqueous solutions. *Journal of Research of the National Bureau of Standards*, 81(1), 89-96.

- [12] Peleg, M., 1988. An empirical model for the description of moisture sorption curves. *Journal of Food Science*, 53(4), 1216-1217.
- [13] Rachtanapun, P., 2007. Shelf life study of salted crackers in pouch by using computer simulation models. *Chiang Mai University Journal of Science*, 34(2), 1-10.
- [14] Brunauer, S., Emmett, P.H., and Teller, E., 1938. Adsorption of gases in multimolecular layers. *Journal of the American Chemical Society*, 60(2), 309-319.
- [15]. Van den Berg C., 1984. Description of water activity of foods for engineering purposes by means of the GAB model of sorption, In: B.M. McKenna ed. *Engineering and Food*. Elsevier Applied Science: New York, pp. 311-321.
- [16] Peleg, M., 1993. Assessment of a semi-empirical four parameter general model for sigmoid moisture sorption isotherms. *Journal of Food Process Engineering*, 16(1), 21-37.
- [17] Lewicki, P.P., 1998. A three parameter equation for food moisture sorption isotherms. *Journal of Food Process Engineering*, 21(2), 127-144.
- [18] Oswin, C., 1946. The kinetics of package life. III. The isotherm. *Journal of Chemical Technology and Biotechnology*, 65(12), 419-421.
- [19] Smith, S.E., 1947. The sorption of water vapor by high polymers. *Journal of the American Chemical Society*, 69(3), 646-651.
- [20] ASTM., 1989. *Annual Book of ASTM Standards*. Philadelphia: American Society for Testing and Materials.
- [21] Azanha1, A.B., and Faria, J.A.F., 2005 Use of mathematical models for estimating the shelf-life of cornflakes in flexible packaging. *Packaging Technology and Science*, 18, 171-178.
- [22] Quek, S.Y., Chok, N.K., and Swedlund, P., 2007. The physicochemical properties of spray-dried watermelon powders. *Chemical Engineering and Processing: Process Intensification*, 46(5), 386-392.
- [23] Baucour, P., and Daudin, J., 2000. Development of a new method for fast measurement of water sorption isotherms in the high humidity range validation on gelatine gel. *Journal of Food Engineering*, 44(2), 97-107.
- [24] Kulchan, R., Boonsupthip, W., and Suppakul, P., 2010. Shelf life prediction of packaged cassava-flour-based baked product by using empirical models and activation energy for water vapor permeability of polyolefin films. *Journal of Food Engineering*, 100(3), 461-467.
- [25] Turhan, M., Sayar, S., and Gunasekaran, S., 2002. Application of Peleg model to study water absorption in chickpea during soaking. *Journal of Food Engineering*, 53(2), 153-159.
- [26] Cervenka, L., Rezkova, S., and Kralovsky, J., 2008. Moisture adsorption characteristics of gingerbread, a traditional bakery product in Pardubice, Czech Republic. *Journal of Food Engineering*, 84(4), 601-607.
- [27] Zomorodian, A., Kavosi, Z., and Momenzadeh, L., 2011. Determination of EMC isotherms and appropriate mathematical models for canola. *Food and Bioproducts Processing*, 89(4), 407-413.
- [28] Panjagari, N.R., Singh, A.K., Ganguly, S., and Indumati, K.P., 2015. Beta-glucan rich composite flour biscuits: modelling of moisture sorption isotherms and determination of sorption heat. *Journal of Food Science and Technology*, 52(9), 5497-5509.
- [29] Catelam, K.T., Trindade, C.S.F., and Romero, J.T., 2011. Water adsorption isotherms and isosteric sorption heat of spray-dried and freeze-dried dehydrated passion fruit pulp with additives and skimmed milk. *Ciência e Agrotecnologia*, 35(6), 1196-1203.
- [30] Barreiro, J.A., Fernández, S. and Sandoval, A.J., 2003. Water sorption characteristics of six row barley malt (*Hordeum vulgare*). *LWT - Food Science and Technology*, 36(1), 37-42.
- [31] Zammouri, A., Ben Zid, M., Kechaou, N. and Boudhrioua Mihoubi, N., 2018. Thermodynamic properties and moisture sorption isotherms of two pharmaceutical compounds. *21st International Drying Symposium Proceedings*. 449-456. Editorial Universitat Politècnica de València.

- [32] Quirijns, E.J., Van Boxtel, A.J., Van Loon, W.K. and Van Straten, G., 2005. Sorption isotherms, GAB parameters and isosteric heat of sorption. *Journal of the Science of Food and Agriculture*, 85(11), 1805-1814
- [33] Samaniego-Esguerra, C.M., Boag, I.F. and Robertson, G.L., 1991. Comparison of regression methods for fitting the GAB model to the moisture isotherms of some dried fruit and vegetables. *Journal of Food Engineering*, 13(2), 115-133.
- [34] Sormoli, M.E. and Langrish, T.A., 2015. Moisture sorption isotherms and net isosteric heat of sorption for spray-dried pure orange juice powder. *LWT-Food Science and Technology*, 62(1), 875-882.
- [35] Timmermann, E., 2003. Multilayer sorption parameters: BET or GAB values? *Colloids and Surfaces A: Physicochemical and Engineering Aspects*, 220(1-3), 235-260.
- [36] Labuza, T.P. and Altunakar, B., 2007. Water activity prediction and moisture sorption isotherms. *Water Activity in Foods: Fundamentals and Applications*, 1, 109-154.
- [37] Al-Muhtaseb, A., McMinn, W. and Magee, T., 2004. Water sorption isotherms of starch powders: part 1: mathematical description of experimental data. *Journal of Food Engineering*, 61(3), 297-307.
- [38] Kaymak-Ertokin, F., and Sultanoğlu, M., 2001. Moisture sorption isotherm characteristics of peppers. *Journal of Food Engineering*, 47(3), 225-231.
- [39] Hao, F., Lu, L., and Wang, J., 2016. Finite element simulation of shelf life prediction of moisture-sensitive crackers in permeable packaging under different storage conditions. *Journal of Food Processing and Preservation*, 40(1), 37-47.
- [40] Pisuchpen, S., 2008. Shelf life analysis of hot curry cubes. *Asian Journal of Food and Agro-Industry*, 1(1), 43-50.

Visible-light-driven Photodegradation of Commercial Dyes by the Cooperation of Co-doped TiO₂ Material

Russameeruk Noonuruk and Chakkaphan Wattanawikkam*

Division of Physics, Faculty of Science and Technology, Rajamangala University of Technology Thanyaburi, Pathum Thani, Thailand

Received: 14 March 2019, Revised: 16 August 2019, Accepted: 10 October 2019

Abstract

The Co-doped TiO₂ photocatalysts with various contents of Co were fabricated by co-precipitation method combined with calcinations at 500°C. Two different dyes of rhodamine b and methylene blue were used to evaluate the photocatalytic performance of the prepared samples. The different concentration of Co has significant influence on structural, morphological, optical properties as well as photocatalytic activity of TiO₂ catalyst. The XRD diffraction patterns of all samples exhibit the anatase phase. X-ray photoelectron spectroscopy technique was used to investigate the chemical state of prepared samples. The BET measurement shows larger specific surface area of doped samples than that of pure TiO₂. The incorporation of Co ions into TiO₂ results in the red-shift in photo-absorption of samples toward visible region. The photocatalytic activities on rhodamine b and methylene blue dyes degradation clearly show that the performance of photodegradation highly depends on the concentration of dopant contents and type of organic dyes. The Co-doped TiO₂ sample with 3% of Co dopant concentration exhibited superior photodegradation rate under visible light illumination in both of rhodamine b and methylene blue dyes. The influences of dopant ions and concentration on physical properties, optical absorption and photocatalytic activity on TiO₂ are also discussed.

Keywords: Co-doped TiO₂, Photocatalyst, co-precipitation method

DOI 10.14456/cast.1477.4

1. Introduction

Nowadays, the existence of organic pollutant in waste water is a worldwide topic for researchers and global environmental safety community [1]. Therefore, a complete removal of this toxic and organic dye is mandatory. Photocatalysis treatment has received great attention for removal of these organic toxic substances in aqueous phase.

Titanium dioxide (TiO₂) with anatase phase has been widely reported as the most favorable photocatalyst owing to its outstanding photocatalytic properties, together with an advantage in high photo-efficiency, strong oxidizing power, non-toxicity and low-cost [2-3]. However, pure TiO₂ photocatalyst has a large energy band gap of 3.2 eV, requiring ultraviolet (UV) light source for excitation, along with relatively high recombination rate of electron and hole pair. Thus, the photocatalytic performance of TiO₂ is expected to be inefficient under visible light or solar light irradiation, even with a lower rate of recombination rate. Many studies have been conducted for enhancing photocatalytic performance of TiO₂ by doping with suitable transition metal ions. Transition metal ion dopant can provide new energy levels within a band gap of the semiconductor

*Corresponding author: Tel.: +66 83-874-4045

E-mail: chakkaphan_w@rmutt.ac.th

that would result in lowering the excitation energy for an electron transfer from these levels to conduction band compared with pure TiO_2 catalyst [4]. Numerous types of transition metal ions have been studied as potential dopants, including chromium, manganese, iron, cobalt, nickel, copper and zinc [5-15]. It has been reported that incorporation of selective transition ions into TiO_2 could effectively enhance visible light response and photocatalytic efficiency. Devi *et al.* [16] studied the effect of Mn^{2+} , Ni^{2+} and Zn^{2+} in TiO_2 and their photocatalytic activities on aniline blue under ultraviolet and visible light irradiation. They suggested that Mn dopant could promote the mixing phase of anatase and rutile which showed the enhancement in photocatalytic activity under visible light irradiation. The different dopants of W, V, Ce, Zr, Fe and Cu were also utilized to adjust optical and photocatalytic properties of TiO_2 synthesized by a solution combustion method [17]. The synthesis of Co- and Mn-doped TiO_2 nanoparticles by hydrothermal method was reported for methylene blue dye decomposition under ultraviolet irradiation. Among these transition metal ion dopants, Co^{2+} ions have received much attention due to its suitable radius and energy level. The radius of Co^{2+} (0.078nm) closed to that of Ti^{4+} (0.068nm), indicating Co^{2+} ions easy to incorporate in TiO_2 lattice. Moreover, the cobalt doping has the positive effect through an introduction on catalyst such as an enhancement in invisible light absorption and increasing photo-excited electron-hole life time. Hence, in this study, the main objective was to develop TiO_2 nanoparticles by doping with Co at different contents by using a facile co-precipitation method. The performance of Co-doped TiO_2 to that of the bare TiO_2 for the degradation of rhodamine b (RhB) and methylene blue (MB) solution as a goal pollutant, general dyes used in the textile industry, was also compared.

2. Materials and Methods

Titanium isopropoxide (TTIP) and cobalt nitrate hexahydrate were used as a precursor of Ti and Co, respectively. Ammonia (NH_3) and absolute ethanol were used as a precipitation agent and solvent, respectively. TiO_2 doped with Co was synthesized by co-precipitation method, according to following steps. First, TTIP (14.2 ml) and cobalt nitrate (at 0.5, 1, 3 and 5 mol%) were weighed according to the required stoichiometric proportion and separately dissolved in absolute ethanol (100ml) under magnetic stirring for 20 min. Afterwards, both solutions were mixed together under vigorous stirring. Then, NH_3 solution was slowly loaded by drop-wise into the solution until pH 9 was achieved under stirring. The homogeneous solution was continuously stirred for 3 h. The solution was then aged for 24 h. The powders were washed by DI water to eliminate the impurity phase until the pH became 7. As synthesized powders were dried at 100°C for 24 h, the green powders were finally calcined at 500°C for 2 h.

The structural phase of Co- TiO_2 was studied by X-ray diffractometer (XRD); Rigaku Rint 2100 CMJ using $\text{CuK}\alpha$ ($\lambda=0.15406$ nm). X-ray photoelectron spectroscopy (XPS); JEOL Ltd. model JPS-9010TRX, was used to study chemical composition of all samples. FESEM images were performed with Hitachi Model SU6600 scanning electron microscope. The optical properties were investigated by UV-vis diffused reflectance spectrometer (UV-Vis DRS); Perkin Elmer model Lamda 750s. Typical dyes in the industry, RhB and MB were used as a model to evaluate the photocatalytic activity of prepared catalyst. The amount of catalyst added was 0.08 g in 100 ml of 0.01 mmol concentration of dyes solution. To guarantee the establishment of adsorption/desorption between catalyst and dye, the solution was stirred in the dark system for 20 min. The photocatalytic reaction was conducted at room temperature using Xenon lamp with 390 nm cutoff filter. The photocatalytic performance was determined by RhB and MB dyes degradation by checking the absorbance at $\lambda_{max} = 554$ and 663 nm, respectively, through a UV-Vis DRS.

3. Results and Discussion

The XRD diffraction patterns of Co-doped TiO_2 photocatalyst are shown in Figure 1. Their patterns clearly indicated that the main peak of pure TiO_2 and Co-doping sample located at $2\theta = 25.4, 39.2, 48.0, 54.8$ and 62.2 corresponding to the reflection from (101), (004), (200), (105) and (211). These observed patterns are nicely matched with the standard tetragonal anatase TiO_2 . Furthermore, there is no characteristic peak corresponding to the secondary phases for oxides of dopants metal ions and rutile structure, indicating the good incorporation of Co ion dopant into TiO_2 matrix. Using full width at half maximum of predominant peak and Debye-Scherer formula, the crystalline size was estimated to be approximate value of 320, 239, 221, 215 and 202 nm for 0, 0.5 1, 3 and 5% dopant concentration, respectively. The reduction in crystalline size by increasing of dopant ions was observed in TiO_2 doped with transition metals like Fe and Ni. It is reported that the growth rate of TiO_2 nanocrystals on doping decreased due to the decreasing in the availability of growth sites of Ti ions as a result of the incorporation of dopant atoms. The occupation of specific growth sites of Ti atoms by dopant atoms inhibits further growth of TiO_2 nanoparticles.

X-ray photoelectron spectroscopy was used to determine insight of oxidation states for titanium, oxygen and cobalt metal cations in the samples and to ensure the chemical composition at surface layer of samples. The XPS survey scan (0-1300 eV) of 5 mol% Co- TiO_2 nanoparticles is displayed in Figure 2(a). The rough scanning spectra of doped sample reveal the existence of dopant ion, with main peaks from Co, O and Ti, confirming the chemical composition of major elements of Co-doped TiO_2 samples. For the identification of titanium oxide phase, it is noticed that the splitting of Ti 2p_{3/2} and 2p_{1/2} binding energy located at 458.6 and 464.3 eV, respectively, is observable as seen in Figure 2(b). The separation of splitting binding energy is 5.7 eV, demonstrating a normal state of Ti with 4+ of oxidation state, which is attributed to the spin-orbit splitting of Ti2p_{3/2} and 2p_{1/2} for Ti^{4+} in TiO_2 [12]. The binding energy of O1s is shown in Figure 2(c). The binding energy of samples could be deconvoluted into two constituents, synonymous to oxygen containing chemical bonds of water molecule (H-O-H) at 531.4 eV and hydroxyl (Co-O-H) at 530.1 eV [18]. Compared with bare- TiO_2 [12], the XPS peak position of Ti2p_{3/2} and Ti2p_{1/2} and O1s is at 458.3, 463.8 and 429.9 eV, respectively. It can be seen in current work that the slight shift of peak position after loading Co atoms was obtained. These results confirm the slight changing in TiO_2 structure. The XPS core level spectra of Co in the TiO_2 matrix are illustrated in Figure 2(d). The result demonstrates the binding energy values of Co2p_{3/2} and 2p_{1/2} positioned at 781.1 and 796.9 eV, indicating that the Co elements could be in 2+ state [18].

Figure 3 shows the FESEM image and particle size distributions from several FESEM photographs of pure TiO_2 and Co-doped TiO_2 samples. As seen in micrographs, the powdered particle of pure TiO_2 consists of clusters of nanosized spherical primary particles, with average particle size around 330 nm. Meanwhile, the samples doped with different transition metal ions exhibit slightly smaller particle size at higher percentage of dopant and more agglomeration occurs with increasing doping content. The broaden peak in the particle size distribution increased with increasing of Co-content was observed. The average particle size of doped samples slightly decreases with increasing doping concentration, as a value of 240 - 210 nm. A slight decrease in the particle size and more agglomeration after loading higher Co ions could be due to the presence of an element in the TiO_2 compound. This presence causes a strain on the lattice and thus decrease the

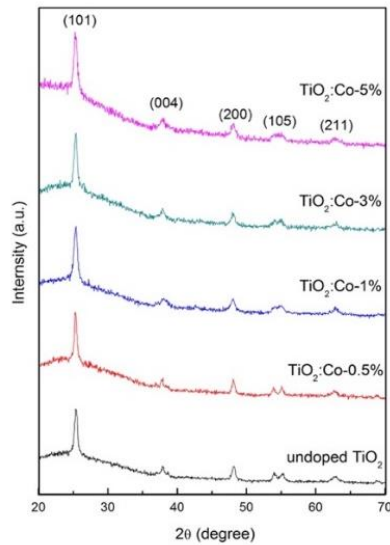


Figure 1. XRD patterns of Co-TiO₂ nanoparticles with various Co concentrations

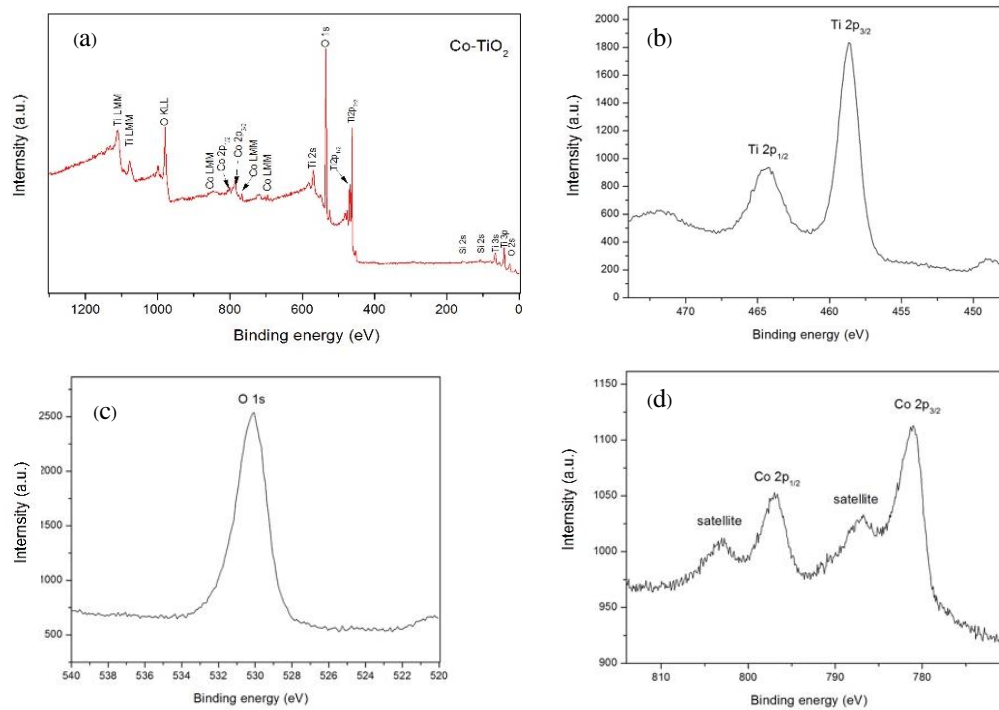


Figure 2. XPS spectrum of Co-TiO₂ with (a) Survey spectrum (b) core level spectrum of Ti, (c) core level spectrum of O and (d) core level spectrum of Co

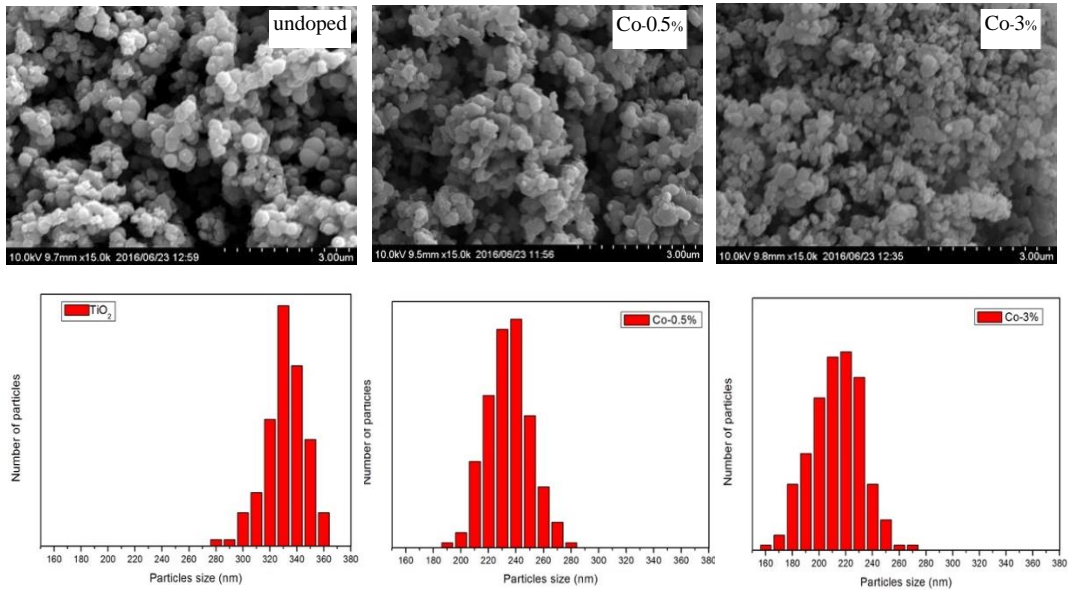


Figure 3. FESEM images and particle size distributions of undoped and Co-TiO₂ nanoparticles

lattice constant. By the smaller particles size, higher relative surface area and larger relative number of surface atoms were observed in the particles. Such surface atoms exhibit unsaturated coordination and each atom has vacant coordination sites. Thus, more bonds need to be formed to each surface atom. This causes an agglomeration in the prepared samples. The FESEM investigation suggests that the primary particle size could be responsible for the specific surface area of the powder. The specific surfaces of all samples were measured by BET technique. The undoped sample shows BET surface area of 48 m²/g. Co-doped TiO₂ samples show their BET surface areas are in a range of 53, 56, 58 and 54 m²/g for 0.5, 1, 3 and 5% of Co-content, respectively. Moreover, the doped samples represent the higher surface area when compared with undoped samples. Co-TiO₂ exhibited higher BET surface area that could result to the enhancement of photocatalytic behavior of the doped samples.

The UV-Vis DRS was used to determine the optical properties of the samples and corresponding spectra in the range of 250-700 nm for P-25 (for comparison), undoped and Co-TiO₂ samples and the results are exhibited in Figure 4. The reflectance spectra of P-25 and undoped sample display strong visible light reflection (>400nm). Meanwhile, the doped samples exhibit lower reflection in visible region; reflection spectra decrease with increasing doping concentration. From these results, it could be deduced that the addition Co-ion in the TiO₂ nanostructure can result in the amelioration in visible absorption. Moreover, the presence of Co-ion dopant may introduce the defect state located between the band gap that may allow TiO₂ to absorb light with lower energy than band gap energy. The incorporation of transition metal provides *d* orbitals below the conduction band that enables the ease of electron transfer from the valence band [9]. Typically, the band gap energy of the sample could be estimated using following equation: $(\alpha h\nu) = A(h\nu - E_g)^{1/2}$; where $h\nu$ is the photon energy, α is the absorption coefficient which can be obtained from the reflectance spectra according to the Kubelka-Munk theory and A is a constant related to type of material. It is clearly noticed that the transition metal ions doped into TiO₂ significantly induce a prominent shift of band edge. The band gap value of Co-doped sample greatly decreases, with a value of 3.21, 3.05, 3.00, 2.75 and 2.95 eV as the doping content increases from 0, 0.5, 1, 3 and 5% of Co-content,

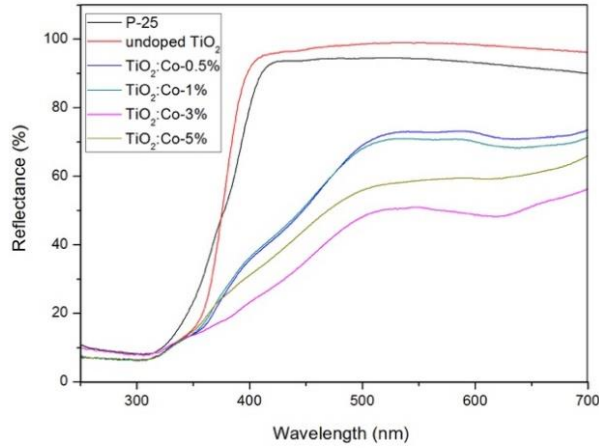


Figure 4. UV-Vis diffuse reflectance spectra of Co-TiO₂ samples with various Co-contents

respectively. It can be seen that the E_g of present work was narrower than the results reported in previous literature, for example $E_g = 2.98, 2.97, 3.08$ eV of Co-doped TiO₂ was claimed by Pirbazari *et al.* [19], Lee *et al.* [20] and Jiang *et al.* [21], respectively.

RhB and MB are representative of organic dyes in the textile effluents as seen in the functional groups in Figure 5 (a). These two organic compounds are often considered as a model contaminant in the photocatalytic decomposition in the waste water. Figures 5 (b) and (c) exhibit the photodegradation of RhB and MB in the presence of commercial sample P-25, undoped and Co-doped TiO₂ samples under visible light irradiation. It can be seen that the undoped samples show RhB degradation activity of ~ 19% in 270 min. In case of doped samples, the highest RhB photodecomposition was found in the 3% of Co-content with 82% of degradation. For the MB, the maximum decolorization of ~ 88% was found in the 3% of Co-content. Under the photocatalytic process, the photodecomposition mechanism can be described that the radicals in the solution attack principally at aromatic chromophore ring, leading to the degradation of RhB and MB structure. It could be deduced that the photocatalytic behavior of the samples highly depends on the dopant concentration. At small doping content, transition metal incorporated into TiO₂ may increase the lifetime of charge carrier resulting in the increasing photocatalytic performance. When the doping content exceeds the certain value, the number of crystal defects could be generated and may act as recombination centers resulting in the decrease of photocatalytic activity. Generally, the photocatalytic activity depends on several parameters such as phase structure, surface area and optical properties and so on. In this present work, the doping ions could induce insignificant change in the crystal structure. This may be attributed to the effect on the impurity levels in the energy band gap of TiO₂ host catalyst. For the other possible reason, the addition of transition metal ion might produce new trapping site which affects the life-time of charge carriers [13]. Moreover, it can be seen that the photocatalytic rate constant of degradation for MB is higher than that of RhB as shown in Figures 5 (d) and (e). This may be attributed to the difference in the chemical structure and nature functional groups of dyes, resulting in the different absorption characteristics and difference in susceptibility to photodegradation. The chemical structure of RhB dye is more complex, making it

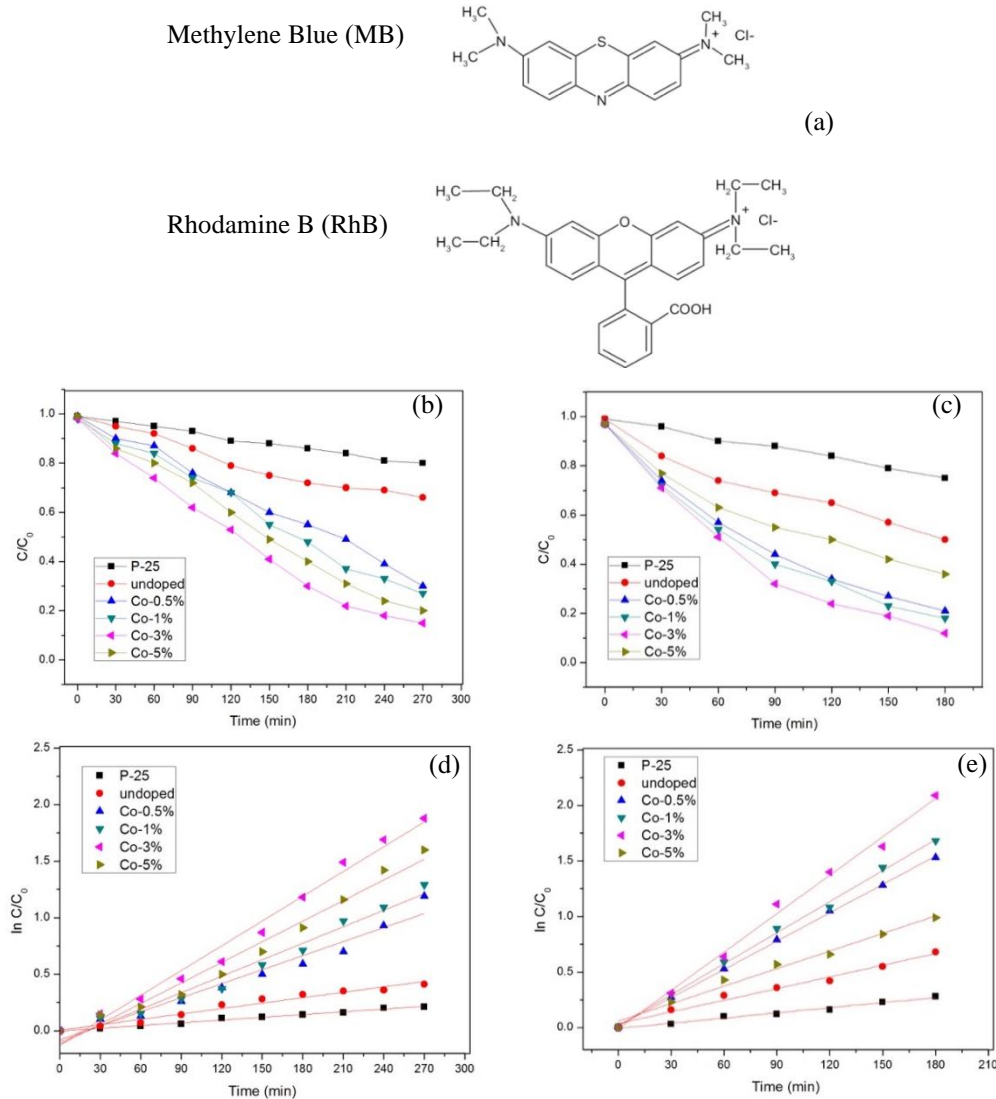


Figure 5. Functional group of MB and RhB dyes (a) with their photodegradation: RhB (b), MB (c) and their rate constant of photodegradation: RhB (d), MB (e) in presence of P-25, undoped and Co-TiO₂ nanoparticles under visible light irradiation and photodegradation

less photodegradable. By comparing to the previous work for transition metal ions doping, it is observed that the results of this work are slightly higher than the prior reported. For example, Pirbazari *et al.* [19] have claimed that the Co/TiO₂ prepared by sol-gel method exhibits 100% and 60% of MB dye degradation within 210 min under UV and visible light irradiation, respectively.

4. Conclusions

The Co-doped TiO₂ catalysts with doping content of 0.5-5 mol% were synthesized via simple co-precipitation method combined with annealing process at 500°C for 2 h. The structural phases of all samples belong to the anatase TiO₂ without impurity phase of oxide compounds. The XPS results exhibit the existence of Co in the host samples, confirming the oxidation state of 4+ and 2+ for Ti and Co, respectively. The Co dopant introduced into TiO₂ catalyst leads to the increase of surface area and visible light optical absorption response. The band gap energies of all samples decrease with increasing doping Co content. The amount of dopant directly affected the photocatalytic efficiency of photocatalyst. Both RhB and MB dyes were highly degraded by TiO₂ doped with 3% of Co. The difference of dopant concentration has strong influence on phase structure, morphology, optical properties and also photocatalytic activity of TiO₂ sample.

5. Acknowledgements

The authors are grateful to Division of Physics, Faculty of Science and Technology, Ragamangala University of Technology Thanyaburi (RMUTT) and Smart Materials Research Unit (SMRU) for supporting the facilities.

References

- [1] Ahmed, S., Rasul, M.G., Brown, R. and Hashib, M.A., 2011. Influence of parameters on the heterogeneous photocatalytic degradation of pesticides and phenolic contaminations and waste water. *Journal of Environmental Management*, 92, 311-330.
- [2] Hoffmann, M.R., Martin, S.T., Choi, W. and Bahnemann, D.W., 1995. Environmental Application of semiconductor photocatalysis. *Chemical Reviews*, 95, 69-96.
- [3] Litter, M.I., 1999. Heterogeneous photocatalysis: Transition metal ion in photocatalytic system. *Applied Catalysis B: Environmental*, 23, 89-114.
- [4] Choi, J., Park H. and Hoffmann, M.R., 2010. Effects of single metal-doping on visible light photoreactivity of TiO₂. *Journal of Physical Chemistry C*, 114, 783-792.
- [5] Ananpattarachai, J. and Kajitvichyanukul, P., 2016. Enhancement of chromium removal efficiency on adsorption and photocatalytic reduction using a bio-catalyst, titania-impregnated chitosan/xylan hybrid film. *Journal of Cleaner Production*, 130, 126-136.
- [6] Chauhan, R., Kumar, A. and Chaudhary, R.P., 2012. Structural and photocatalytic studies of Mn doped TiO₂ nanoparticles. *Spectrochimica Acta Part A: Molecular and Biomolecular Spectroscopy*, 98, 256-264.
- [7] Moradi, H., Eshaghi, A., Hosseini, S.R. and Ghani, K., 2016. Fabrication of Fe-doped TiO₂ nanoparticles and investigation of photocatalytic decolorization of reactive red 198 under visible light irradiation. *Ultrasonic Sonochemistry*, 32, 314-319.
- [8] Junlabut, P., Wattanawikram, C., Phoohinkong, W., Mekprasart, W. and Pecharapa, W., 2016. Effect of cobalt on structural and optical properties of co-precipitated TiO₂ nanopowders. *Key Engineering Materials*, 675/676, 97-100.
- [9] Yadav, H.M., Otari, S.V., Bohara, R.A., Mali, S.S., Pawar, S.H. and Delekar, S.D., 2014. Synthesis and visible light photocatalytic antibacterial activity of nickel-doped TiO₂

nanoparticles against Gram-positive and Gram-negative bacteria. *Journal of Photochemistry and Photobiology A: Chemistry*, 294, 130-136.

- [10] Wattanawikkam, C., Pecharapa, W. and Ishihara, K. N., 2017. X-ray absorption spectroscopy analysis and magnetic properties of M-doped TiO₂ nanoparticles (M=Co, Mn, Ni and Zn) prepared by co-precipitation method. *Ceramics International*, 43, S397-S402.
- [11] Singla, P., Sharma, M., Pandey, O.P. and Singh, K., 2014. Photocatalytic degradation of azo dyes using Zn-doped and undoped TiO₂ nanoparticles. *Applied Physics*, 116, 371-389.
- [12] Reddy, S., Boningari, T. and Suidan, M., 2014. Visible-light-induced photodegradation of gas phase acetonitrile using aerosol-made transition metal ion (V, Cr, Fe, Co, Mn, Mo, Ni, Cu, Y, Ce and Zr) doped TiO₂. *Applied Catalysis B: Environmental*, 114, 333-342.
- [13] Tripathi, A.K., Mathpal, M.C., Kumer, P., Singh, M.K., Soler, M.A.G. and Garwal, A.A, 2015. Structural, optical and photoconductivity of Sn and Mn doped TiO₂ nanoparticles. *Journal of Alloys and Compounds*, 622, 37-47.
- [14] Park, J.Y., Choi, K.I., Lee, J.H., Hwang, C.H., Choi, D.Y. and Lee, J.W., 2013. Fabrication and characterization of metal-doped TiO₂ nanofibers for photocatalytic reactions. *Materials Letters*, 97, 64-66.
- [15] Jing, L., Xin, B., Yuan, F., Xue, L., Wang, B. and Fu, H., 2006. Effect of surface oxygen vacancy on photochemical and photochemical processes of Zn-doped TiO₂ nanoparticles and their relationships. *Journal of Physical Chemistry B*, 110, 17860-17865.
- [16] Devi, L G., Kottam, N., Murthy, B. N. and Kumar, S. G., 2010. Enhanced photocatalytic activity of transition metal ions Mn²⁺, Ni²⁺ and Zn²⁺ doped polycrystalline titania for the degradation of Aniline Blue under UV/solar light. *Journal of Molecular Catalysis A: Chemical*, 328, 44-52.
- [17] Nagaveni, K. K., Hegde, M.S. and Madras, G., 2004. Structural and photocatalytic activity of Ti_{1-x}M_xO_{2+/-delta} (M=W, V, Ce, Zr, Fe, and Cu) synthesized by solution combustion method. *The Journal of Physical Chemistry B*, 108, 20204-20212.
- [18] Tan, B. J., Klabunde, K.J., and Peter, M. A., 1991. XPS studies of solvated metal atom dispersed catalysts. evidence for layered cobalt-manganese particles on alumina and silica. *Journal of the American Chemical Society*, 113, 855-581.
- [19] Pirbazari, A.E., Monazzam, P.P. and Kisomi, B.F., 2017. Co/TiO₂ nanoparticles: preparation, characterization and its application for photocatalytic degradation of methylene blue. *Desalination and Water Treatment*, 63, 283-292.
- [20] Lee, H., Park, Y.K., Kim, S.J., Kim, B.H. and Jung, S.C., 2015. Titanium dioxide modification with cobalt oxide nanoparticles for photocatalysis. *Journal of Industrial and Engineering Chemistry*, 32, 259 -263.
- [21] Jiang, P., Xiang, W., Kuang, J., Liu, W. and Cao, W., 2015. Effect of cobalt doping on the electronic, optical and photocatalytic properties of TiO₂. *Solid State Sciences*, 46, 27-32.

Effects of Seven Plant Essential Oils on Mortalities of Chicken Lice (*Lipeurus caponis* L.) Adult

Jarongsak Pumnuan*, Ammorn Insung and Ampon Klompanya

Faculty of Agricultural Technology, King Mongkut's Institute of Technology
Ladkrabang, Bangkok, Thailand

Received: 9 August 2019, Revised: 16 October 2019, Accepted: 17 October 2019

Abstract

Chicken lice (*Lipeurus caponis* L.) are external parasite of chicken and farmers often use malathion and carbaryl insecticides to control this parasite. However, the use of chemical insecticides may result in direct toxicity to chicken or contamination in chicken meats. Thus, this study investigated the effect of seven plant essential oils (EOs) against adult chicken lice. Contact bioassay was performed by laying 10 adult chicken lice on treated filter paper added with EOs at concentrations of 0 (95% ethanol as a control), 0.079, 0.157, 0.236 and 0.314 $\mu\text{l}\cdot\text{cm}^{-2}$. Mortality percentages were observed at 3, 6 and 12 h intervals after the treatments. Clove, cinnamon, turmeric and star anise EOs were able to eliminate the lice completely (100% mortalities) at 12 h exposure which were higher than lemon grass, citronella grass and piper EOs. Clove EO was the most effective oil with LC_{50} of 0.132, 0.085 and 0.039 $\mu\text{l}\cdot\text{cm}^{-2}$ at 3, 6 and 12 h, respectively. Furthermore, clove EO at the 0.157 $\mu\text{l}\cdot\text{cm}^{-2}$ showed the highest mortalities with LT_{50} at 1.438 h. Our study suggests that clove EO could be used as an alternative medicinal insecticide to control chicken lice in farms.

Keywords: clove, cinnamon, star anise, contact method, insecticide, chicken lice
DOI 10.14456/cast.1477.5

1. Introduction

Poultry lice are important external parasite of poultry [1] that consume host tissues, secretions of quill feathers, etc. Their biting is usually irritating and painful and poultry will become restless resulting in decrease of feed intake [2]. Chicken lice (*Lipeurus caponis* L.), parasitic wing lice of chicken, may pierce the pulp of feathers or the skin which may be extremely dangerous especially to young poultry, even if they only feed by nibbling along the feather surface and/or eat epidermal debris [3]. Invasion of these lice are often found in many countries, including Bangladesh [4], Ethiopia [5], Malawi [6], Turkeys [7], Philippines [8], Nigeria [9], California [10] and Thailand [11].

In Thailand, the initial survey found that farmers often used malathion and carbaryl insecticides to control this parasite. Report from Turkey revealed that synthetic pyrethroid insecticides were applied for controlling chicken lice [12]. The use of organophosphate, pyrethroid and spinosyns insecticides to prevent lice and mite of poultry was recommended [13]. However, louse control can cause an intense growth of resistances against long-used insecticides [14]. The use of chemical pesticides may cause contamination in the chicken meats because animals intended for

* Corresponding author: Tel.: +66 02-329-8499 Fax: +66 02-329-8499
E-mail: jarongsak.pu@kmitl.ac.th

human food may absorb residual pesticides in their feed, water or during direct/indirect exposure in the course of pest control [15] and may cause direct toxic effect to chicken.

Nowadays, none of these methods are efficient for complete protection. Consequently, control method of high effectiveness against insects with non-toxic effect, non-residue toxicity in meat, environmentally friendly has focused on alternative bio-pesticides which specifically entails the property of natural degradability. Especially, essential oils (EOs) are good candidates for safer control agents that may provide good anti-lice activity and low levels of evolved resistance [16]. Essential oils were extensively studied and used against some insects and mites [17-20]. Plant EO s of clove, cinnamon, turmeric, star anise, black piper, citronella grass and lemon grass were previously reported as high potential against insect and mite pests [21].

The objective of this study was to evaluate the effectiveness of seven plant essential oils, namely clove (*Syzygium aromaticum*), cinnamon (*Cinnamomum bejolghota*), turmeric (*Curcuma longa*), star anise (*Illicium verum*), black piper (*Piper nigrum*), citronella grass (*Cymbopogon nardus*) and lemon grass (*Cymbopogon citratus*) against adult of chicken lice (*L. caponis*) by residue filter paper contact method in laboratory conditions.

2. Materials and Methods

2.1 Essential oil preparation

Essential oils from dried bud of clove (*S. aromaticum*), dried flower of star anise (*I. verum*), dried seed of black piper (*P. nigrum*), fresh rhizome of turmeric (*C. longa*), and fresh leaf of cinnamon (*C. bejolghota*), citronella grass (*C. nardus*) and lemon grass (*C. citratus*) which has been reported to contain insecticidal properties against adult of chicken lice (*L. caponis*) [22] are used in this study. All EO s were purchased from Thai-China Flavours and Fragrances Industry Co., Ltd., Bangkok, Thailand. The concentration of EO s at 0.1, 0.15 and 0.2% as well as the control group with the application of 0.2% of Tween-20 in water were applied.

2.2 Insect samples

An adult colony of chicken lice (*L. caponis*) was collected from native chickens at Learning Center and Management System Integrated with Urban Livestock Farm Learning, Faculty of Agricultural Technology, King Mongkut's Institute of Technology Ladkrabang (KMITL), Thailand.

2.3 Experimental treatments

The insecticidal activity test of the plant EO s against chicken lice was evaluated by using residue filter paper contact method. One ml of each plant EO s at concentrations of 0.2% in 95% ethanol was separately dropped on each filter paper (Whatman® No. 1) and placed onto Petri dish (with size of 90 mm in dia). By this application, the EO concentration was equal to $0.314 \mu\text{l}\cdot\text{cm}^{-2}$. The treated filter papers were air-dried for 5 min and 10 chicken lice adults were put into the petri dish. Mortality observations were recorded at 6 and 12 h after treatment. The plant EO s showing high effectiveness against chicken lice were selected for further experiments.

For further insecticidal activity test, those EO s at the concentrations of 0.05, 0.10, 0.15, 0.20 and 0.25% in 95% ethanol or $0.079, 0.157, 0.236, 0.314$ and $0.393 \mu\text{l}\cdot\text{cm}^{-2}$, respectively were applied by using as the same method as described previously. Mortality observations were recorded at 2, 4, 6, 8, 10 and 12 h after treatment.

The experiment was replicated three times and statistically designed by completely randomized replication design (CRD). The actual death rates were calculated via Abbot's formula [23]. The data obtained were statistically analyzed by applying analysis of variance (ANOVA) and Duncan's multiple range tests (DMRT). Lethal concentrations of EOs needed to kill 50 and 90% of the insects (LC_{50} and LC_{90} , respectively) and lethal time of EOs needed to kill 50 of the insects (LT_{50}) were calculated via probit analysis.

3. Results and Discussion

The efficacy in terms of insecticidal properties of seven plant EOs against the adult of chicken lice (*L. caponis*) conducted by residue filter paper contact method in laboratory conditions showed that plant EOs of clove, turmeric, cinnamon and star anise were able to eliminate the lice completely (100% mortalities) at 12 h exposure which were higher than those of lemon grass, citronella grass and black piper EOs, respectively (Figure 1). At 6 h after treatment, the plant EO of clove showed to be the most effective insecticidal activity against the lice with completely 100% mortalities followed by turmeric and cinnamon EOs with mortality rate of 76.7 and 73.9%, respectively. The star anise EO caused only 39.5% mortality whereas plant EOs of black piper, lemon grass and citronella grass were the lowest group to control chicken lice with 1.7%, 6.1% and 11.9% mortality. Thus, the plant EOs with high effectiveness against the lice, including clove, turmeric and cinnamon were selected for further experiments to obtain the toxicity level. The insecticidal activity test by residue filter paper contact bioassay showed that clove EO was the most effective candidate with LC_{50} (at 3, 6 and 12 h) of 0.132, 0.085 and 0.039 $\mu\text{l}\cdot\text{cm}^{-2}$, respectively and LC_{90} of 0.168, 0.112 and 0.108 $\mu\text{l}\cdot\text{cm}^{-2}$ followed by EOs of cinnamon and turmeric with LC_{50} of 0.220, 0.090 and 0.038 $\mu\text{l}\cdot\text{cm}^{-2}$ and 0.256, 0.148 and 0.106 $\mu\text{l}\cdot\text{cm}^{-2}$, respectively (Table 1). Furthermore, clove EO at 0.157 $\mu\text{l}\cdot\text{cm}^{-2}$ showed the highest mortalities with LT_{50} at 1.438 h and was able to eliminate the lice completely (100% mortalities) at 4 h exposure (Table 2).

There were many reports regarding the effectiveness of extract and EO of plants against insect and mite pests of poultry. Aquatic and ethanolic leaf extracts of *Conocarpus erectus* had some toxic effects (acaricidal and repellent properties) on poultry red mite, *Dermanyssus gallinae* in Iran [24]. *Thuja occidentalis* arborvitae and *Juniper* spp. (*Juniperus*) leaf EOs were also found to be effective against the poultry red mite (*D. gallinae*) [25]. Lans and Turner [26] reported nineteen species of plants conducted for parasite control in poultry farm of British Columbia, Canada. Our study showed that EO of clove was effective to control chicken lice and this EO has been reported for insecticidal property against insect and mites pests, including fruit fly (*Ceratitis capitata*) [27], head louse (*Pediculus humanus capititis*) [28], maize weed (*Sitophilus zeamais*) [29], thrips (*Frankliniella schultzei*) [20], mealybug (*Pseudococcus jackbeardsleyi*) [20], rice weevil (*Sitophilus oryzae*) [30], pear psyllid (*Cacopsylla chinensis*) [31], aphid (*Aphid gossypii*), whitefly (*Bemisia tabaci*) [32], red spider mite (*Oligonychus coffeae*) [33], house dust mite (*Dermatophagooides farina* and *Dermatophagooides pteronyssinus*) [34]. Our study suggests that clove EO or maybe the combination of clove EO with cinnamon and turmeric EOs as mixture could be used as a new alternative medicinal insecticide to control chicken lice. Combination of EOs are a combination of chemical compounds in these EOs together, which will encourage the EOs mixture to be more effective in pest eradication. The combination of chemical compounds from plant were also reported to enhance EO efficacy. Koul *et al.* [35] reported that the combination of anethole and 1,8-cineole demonstrated reduction in the population of red flour beetle (*Tribolium castaneum*). Synergism or additive effects of monoterpenoid binary mixtures against tobacco cutworm larvae (*Spodoptera litura*) was also reported [36].

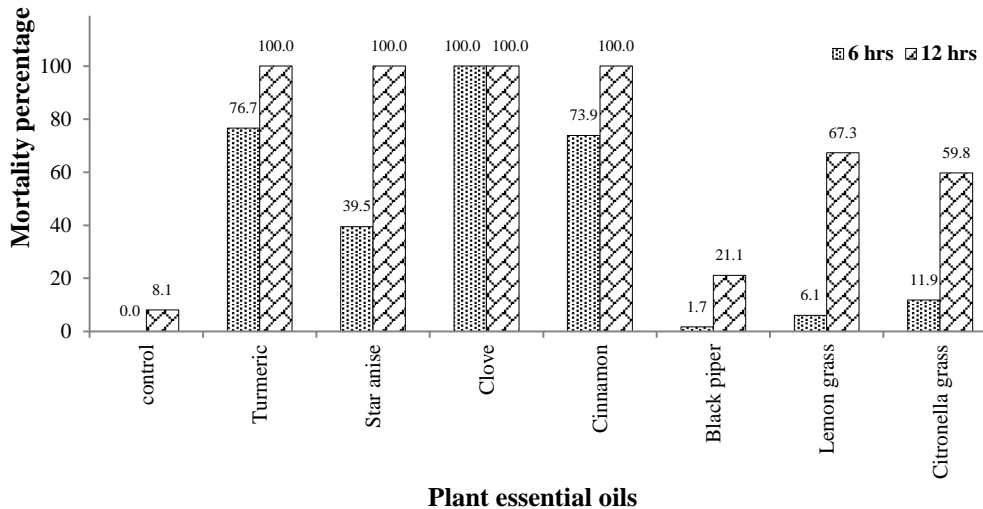


Figure 1. Mortality percentage of the adults of chicken lice (*Lipeurus caponis* L.) at 6 and 12 h after residue filter paper contact test with plant essential oils at the concentration of $0.314 \mu\text{l}\cdot\text{cm}^{-2}$

Table 1. Mortality percentage of the adults of chicken lice (*Lipeurus caponis* L.) at 6 and 12 h after residue filter paper contact test with plant essential oils at various concentrations

Plant essential oils	% Mortality ^{1/} (Means±S.D.)					LC ₅₀ ($\mu\text{l}\cdot\text{cm}^{-2}$)	LC ₉₀ ($\mu\text{l}\cdot\text{cm}^{-2}$)
	Concentration ($\mu\text{l}\cdot\text{cm}^{-2}$)						
	control	0.079	0.157	0.236	0.314	0.393	
3 h							
Turmeric	0.0±0.0 ^{Db}	0.0±0.0 ^{Dd}	0.0±0.0 ^{Dd}	52.2±13.5 ^{Cb}	74.3±14.8 ^{Bb}	100.0±0.0 ^{Aa}	0.256
Cinnamon	0.0±0.0 ^{Db}	5.1±8.9 ^{CDd}	12.5±6.5 ^{Cd}	48.8±5.8 ^{Bb}	100.0±0.0 ^{Aa}	100.0±0.0 ^{Aa}	0.220
Clove	0.0±0.0 ^{Cb}	3.3±5.8 ^{Cd}	81.2±17.1 ^{Bb}	100.0±0.0 ^{Aa}	100.0±0.0 ^{Aa}	100.0±0.0 ^{Aa}	0.132
6 h							
Turmeric	0.0±0.0 ^{Cb}	8.3±9.2 ^{Cd}	51.6±13.2 ^{Bc}	100.0±0.0 ^{Aa}	100.0±0.0 ^{Aa}	100.0±0.0 ^{Aa}	0.148
Cinnamon	0.0±0.0 ^{Db}	59.9±16.3 ^{Cb}	77.9±11.4 ^{Bb}	100.0±0.0 ^{Aa}	100.0±0.0 ^{Aa}	100.0±0.0 ^{Aa}	0.090
Clove	0.0±0.0 ^{Cb}	38.8±10.2 ^{Bc}	100.0±0.0 ^{Aa}	100.0±0.0 ^{Aa}	100.0±0.0 ^{Aa}	100.0±0.0 ^{Aa}	0.085
12 h							
Turmeric	8.6±2.4 ^{Da}	29.3±6.1 ^{Cc}	75.7±10.5 ^{Bb}	100.0±0.0 ^{Aa}	100.0±0.0 ^{Aa}	100.0±0.0 ^{Aa}	0.106
Cinnamon	8.6±2.4 ^{Ba}	97.4±4.4 ^{Aa}	100.0±0.0 ^{Aa}	100.0±0.0 ^{Aa}	100.0±0.0 ^{Aa}	100.0±0.0 ^{Aa}	0.038
Clove	8.6±2.4 ^{Ba}	97.0±5.2 ^{Aa}	100.0±0.0 ^{Aa}	100.0±0.0 ^{Aa}	100.0±0.0 ^{Aa}	100.0±0.0 ^{Aa}	0.039

^{1/} Means in each column followed by the same common letter and means in row followed by the same capital letter were not significantly different ($P < 0.05$) according to DMRT.

Table 2. Mortality percentage of the adults of chicken lice (*Lipeurus caponis* L.) at the various concentrations after residue filter paper contact test with plant essential oils at the 2-12 h

Plant essential oils	% Mortality ^{1/} (Means±S.D.)						LT ₅₀ (h)	LT ₉₀ (h)		
	Times (h)									
	2	4	6	8	10	12				
0.157 $\mu\text{l}\cdot\text{cm}^{-2}$										
Turmeric	0.0±0.0 ^{De}	3.3±5.8 ^{Dd}	51.6±13.2 ^{Cc}	57.4±10.8 ^{BCc}	72.5±10.5 ^{ABb}	75.5±10.5 ^{Ab}	7.284	10.526		
Cinnamon	2.8±4.8 ^{Dde}	21.8±4.8 ^{Cc}	77.9±11.4 ^{Bb}	80.9±10.5 ^{Bb}	100.0±0.0 ^{Aa}	100.0±0.0 ^{Aa}	5.368	7.933		
Clove	72.7±15.2 ^{Bb}	100.0±0.0 ^{Aa}	100.0±0.0 ^{Aa}	100.0±0.0 ^{Aa}	100.0±0.0 ^{Aa}	100.0±0.0 ^{Aa}	1.438	2.663		
0.236 $\mu\text{l}\cdot\text{cm}^{-2}$										
Turmeric	12.2±6.7 ^{Cd}	72.8±16.7 ^{Bb}	100.0±0.0 ^{Aa}	100.0±0.0 ^{Aa}	100.0±0.0 ^{Aa}	100.0±0.0 ^{Aa}	3.290	4.658		
Cinnamon	0.0±0.0 ^{Ce}	67.2±19.5 ^{Bb}	100.0±0.0 ^{Aa}	100.0±0.0 ^{Aa}	100.0±0.0 ^{Aa}	100.0±0.0 ^{Aa}	3.745	4.438		
Clove	100.0±0.0 ^{Aa}	100.0±0.0 ^{Aa}	100.0±0.0 ^{Aa}	100.0±0.0 ^{Aa}	100.0±0.0 ^{Aa}	100.0±0.0 ^{Aa}	-	-		
0.314 $\mu\text{l}\cdot\text{cm}^{-2}$										
Turmeric	26.9±3.3 ^{Bc}	100.0±0.0 ^{Aa}	100.0±0.0 ^{Aa}	100.0±0.0 ^{Aa}	100.0±0.0 ^{Aa}	100.0±0.0 ^{Aa}	2.337	3.036		
Cinnamon	90.3±0.5 ^{Ba}	100.0±0.0 ^{Aa}	100.0±0.0 ^{Aa}	100.0±0.0 ^{Aa}	100.0±0.0 ^{Aa}	100.0±0.0 ^{Aa}	0.661	1.986		
Clove	100.0±0.0 ^{Aa}	100.0±0.0 ^{Aa}	100.0±0.0 ^{Aa}	100.0±0.0 ^{Aa}	100.0±0.0 ^{Aa}	100.0±0.0 ^{Aa}	-	-		

^{1/} Means in each column concentration followed by the same common letter and means in row followed by the same capital letter were not significantly different ($P< 0.05$) according to DMRT.

Non-toxic alternative options are hence needed for control of insect pest and natural products from plants especially EOs are good candidates for safer control agents that may provide good insecticidal activity and low levels of evolved resistance [15]. Our study suggests that clove EO could be used as an alternative medicinal insecticide to control chicken lice in the farm.

4. Conclusions

Insecticidal properties of plant EOs against the adult of chicken lice (*L. caponis*) by residue filter paper contact method in laboratory conditions revealed that clove EO was the most effective candidate with the LC₅₀ at 3, 6 and 12 h of 0.132, 0.085 and 0.039 $\mu\text{l}\cdot\text{cm}^{-2}$, respectively. Furthermore, the clove EO at 0.157 $\mu\text{l}\cdot\text{cm}^{-2}$ showed the highest mortalities of chicken lice with LT₅₀ at 1.438 h, and this clove EO was able to eliminate the lice completely (100% mortalities) within 4 h exposure while the clove EO at the concentration of 0.236 $\mu\text{l}\cdot\text{cm}^{-2}$ was effective to kill the lice completely at 2 h. Our study suggests that clove EO or maybe the combination with cinnamon and turmeric EOs as the mixture could be used as an alternative medicinal insecticide to control chicken lice in farm.

References

- [1] Khan, M.N., Nadeem, M., Iqbal, Zafar., Sajid, M.S., and Abbas, R.Z., 2003. Lice infestation in poultry. *International Journal of Agriculture & Biology*, 2, 213-216.
- [2] Islam, M.K., Mondal, M.M.H., Rahman, M.M., Haque, A.K.M.F. and Chowdhury, M.A.A., 1999. Effects of *Lipeurus caponis*, Linnaeus, 1758, (*Mallophaga: Philopteridae*) on laying hens. *Veterinary Review Kathmandu*, 14, 32-33.

- [3] Al-Quraishy, S., Abdel-Ghaffar, F., Al-Rasheid, K.A.S., Mehlhorn, J. and Mehlhorn, H., 2011. Effects of a neem seed extract (MiteStop®) on mallophages (featherlings) of chicken: *in vivo* and *in vitro* studies. *Parasitology Research*, 110, 617-622.
- [4] Shanta, I.S., Begum, N., Anisuzzaman, A., Bari, A.S.M. and Karim, M.J., 2006. Prevalence and clinico-pathological effects of ectoparasites in backyard poultry. *Bangladesh Journal of Veterinary Medicine*, 4(1), 19-26.
- [5] Firaol, T., Daghmawit, A., Askale, G., Solomon, S., Morka, D. and Waktole, T., 2014. Prevalence of ectoparasite infestation in chicken in and around ambo town, Ethiopia. *Journal of Veterinary Science and Technology*, 5(4). Doi:10.4172/2157-7579.1000189.
- [6] Njunga, G.R. 2003. *Ecto and Haemoparasites of Chickens in Malawi with Emphasis on the Effect of Chicken Louse, Menacanthus cornutus*. Frederiksberg: The Royal Veterinary and Agriculture University, 173-195.
- [7] Zarith, Z. M., Suhaila, A. H., Izzauddin, N. and Khadijah, S., 2017. Parasites prevalence in poultry: focusing on free range turkeys (*Meleagris gallopavo*). *Malaysian Journal of Veterinary Research*, 8(1), 1-9.
- [8] Portugaliza, H. P and Bagot, M.A., 2015. Different species of lice (Phthiraptera), fleas (Siphonaptera) and ticks (Ixodida) collected from livestock, poultry, reptile and companion animal in Leyte Island, Philippines. *Livestock Research for Rural Development*, 27(8), 1-10.
- [9] Lawal, J.R., Yusuf, Z.B., Dauda, J., Gazali, Y.A. and Biu, A.A., 2017. Ectoparasites infestation and its associated risk factors in village chickens (*Gallus gallus domesticus*) in and around Potiskum, Yobe State, Nigeria. *Journal of Animal Husbandry and Dairy Science*, 1(1), 8-19.
- [10] Murillo, A.C. and Mullens, B.A., 2016. Diversity and prevalence of ectoparasites on backyard chicken flocks in California. *Journal of Medical Entomology*, 53(3), 707-711.
- [11] Sangvaranond, A., 1992. Study on incidence and outbreak of ectoparasites of native chickens in Nonthaburi province Thailand. *KKU Veterinary Journal*. 1(2), 68-75. (in Thai)
- [12] Diki, B., Erciyas- Yavuz, K. and Per, E., 2017. Chewing lice (Phthiraptera: Amblycera, Ischnocera) on birds in the Kızılırmak delta, Turkey. *Revue de Médecine Vétérinaire*, 167(1-2), 53-62.
- [13] College of Agriculture, Food and Environment, University of Kentucky. 2017. *Common External Parasites of Poultry*. [Online] Available at: <http://www2.ca.uky.edu/agcomm/pubs/asc/asc206/asc206.pdf>.
- [14] Kristensen, M., Knorr, M., Rasmussen, A.M. and Jespersen, J.B., 2006. Survey of permethrin and malathion resistance in human head lice populations from Denmark. *Journal of Medical Entomology*, 43, 533-538.
- [15] Aulakh, R. S., Gill, J. P. S., Bedi, J. S., Sharma, J. K., Joia, B. S. and Ockerman, H. W., 2006. Organochlorine pesticide residues in poultry feed, chicken muscle and eggs at a poultry farm in Punjab, India. *Journal of the Science of Food and Agriculture*, 86, 741-744.
- [16] Rossini, C., Castillo, L. and Gonzalez, A., 2008. Plant extracts and their components as potential control agents against human head lice. *Phytochemistry Reviews*, 7, 51-63.
- [17] Ayvaz, A., Sagdic, O., Karaborklu, S. and Ozturk, I., 2008. Insecticidal activity of the essential oils from different plants against three stored- product insects. *Journal of Insect Science*, 10(21), 1-10.
- [18] Pumnuan, J. and Insung, A., 2011. Effectiveness of essential oils of medicinal plants against stored product mite, *Suidasia pontifica* Oudemans. *ISHS Acta Horticulturae*, 945, 79-85.
- [19] Benelli, G., Flamini, G., Canale, A., Cioni, P.L. and Conti, B., 2012. Toxicity of some essential oil formulations against the mediterranean fruit fly, *Ceratitis capitata* (Wiedemann) (Diptera: Tephritidae). *Crop Protection*, 42, 223-229.
- [20] Pumnuan, J. and Insung, A., 2016. Fumigant toxicity of plant essential oils in controlling thrips, *Frankliniella schultzei* (Thysanoptera: Thripidae) and mealybug, *Pseudococcus jackbeardsleyi* (Hemiptera: Pseudococcidae). *Journal of Entomological Research*, 40(1), 1-10.

- [21] Pumnuan, J., Insung, A. and Chandrapatya, A., 2008. Acaricidal effects of herb extracts on the mushroom mites, *Luciaphorus perniciosus* Rack and *Formicomotes heteromorphus* Magowski. *Systematic & Applied Acarology*, 13(1), 33-38.
- [22] Chantawee, A., Pumnuan, J. and Insung, A., 2012. Effectiveness of essential oils of medicinal plants against brown planthopper (*Nilaparvata lugens* (Stål)). *Proceedings of the 10th International Symposium on Biocontrol and Biotechnology*, Harbin Institute of Technology, Harbin, P.R. China, December 27-30, 2012. 54-58.
- [23] Abbott, W.S., 1987. A method of computing the effectiveness of an insecticide. 1925. *Journal of the American Mosquito Control Association*. 3(2), 302-303.
- [24] Rajabpour, A., Mashhadi, A. R. A. and Ghorbani, M. R., 2018. Acaricidal and repellent properties of some plant extracts against poultry red mite, *Dermanyssus gallinae* (Mesostigmata: Dermanyssidae). *Persian Journal of Acarology*, 7(1), 85–91.
- [25] Maurer, V., Perler, E. and Heckendorf, F., 2009. *In vitro* efficacies of oils, silicas and plant preparations against the poultry red mite *Dermanyssus gallinae*. *Experimental and Applied Acarology*, 48, 31-41.
- [26] Lans, C. and Turner, N., 2011. Organic parasite control for poultry and rabbits in British Columbia, Canada. *Journal of Ethnobiology and Ethnomedicine*, 7(1), 1-10.
- [27] Arancibia, M., Rabossi, A., Bochicchio, P.A., Moreno, S., López-Caballero, M.E., Gómez-Guillén, M.C. and Montero, P., 2013. Biodegradable films containing clove or citronella essential oils against the Mediterranean fruit fly *Ceratitis capitata* (Diptera: Tephritidae). *Journal of Agricultural and Food Chemistry*, 3(3), 1-7.
- [28] Choi, H. Y., Yang, Y.C., Lee, S.H., Clark, J.M. and Ahn, Y.J., 2010. Efficacy of spray formulations containing binary mixtures of clove and eucalyptus oils against susceptible and pyrethroid/malathion-resistant head lice (Anoplura: Pediculidae). *Journal of Medical Entomology*, 47(3), 387-391.
- [29] Pumnuan, J., Teerarak, M. and Insung, A., 2012. Fumigant toxicity of essential oils of medical plants against maize weevil, *Sitophilus zeamais* Motsch. (Coleoptera: Curculionidae). *Proceeding of 2nd International Symposium of Biopesticides and Ecotoxicology Network (2nd IS-BIOPEN)*. Bangkok, Thailand, September 24-26, 2012, 177-183.
- [30] Ahmed, M. E. and Salam, A. E., 2010. Fumigant toxicity of seven essential oils against the cowpea weevil, *Callosobruch maculatus* (F.) and the rice weevil, *Sitophilus oryzae* (L.). *Egyptian Academic Journal of Biological Sciences*, 2(1), 1-6.
- [31] Tian, B., Liu, Q., Liu, Z., Li, P. and Wang, J., 2015. Insecticidal potential of clove essential oil and its constituents on *Cacopsylla chinensis* (Hemiptera: Psyllidae) in laboratory and field. *Journal of Economic Entomology*, 108(3), 957-961.
- [32] Pumnuan, J., Khurnpoon, L. and Insung, A., 2017. Insecticidal activity of essential oil formulas and their physiological effects on eggplant. *Journal of Applied Horticulture*, 19(2), 152-158.
- [33] Barua, A., Roy, S., Handique, G., Bora, F.R., Rahman, A., Pujari, D. and Muraleedharan, N., 2015. Clove oil efficacy on the red spider mite, *Oligonychus coffeae* Nietner (Acari: Tetranychidae) infesting tea plants. *Proceedings of the Zoological Society*, doi: 10.1007/s12595-015-0147-6.
- [34] Kim, E. H., Kim, H. K. and Ahn, Y. J., 2003. Acaricidal activity of clove bud oil compounds against *Dermatophagoides farinae* and *Dermatophagoides pteronyssinus* (Acari: Pyroglyphidae). *Journal of Agricultural and Food Chemistry*, 51, 885-889.
- [35] Koul, O., Walia, S. and Dhaliwal G.S., 2008. Essential oils as green pesticides: potential and constraints. *Biopesticides International*, 4(1), 63-84.
- [36] Hummelbrunner, L.A. and Isman, M.B., 2001. Acute sublethal, antifeedant and synergistic effects of monoterpenoid essential oil compounds on the tobacco cutworm, *Spodoptera litura* (Lep., Noctuidae). *Journal of Agricultural and Food Chemistry*, 49(2), 715-720.

Geographic Information System-based Analysis to Identify the Spatiotemporal Patterns of Road Accidents in Sri Racha, Chon Buri, Thailand

Narong Pleerux

Faculty of Geoinformatics, Burapha University, Chon Buri, Thailand

Received: 13 July 2019, Revised: 6 October 2019, Accepted: 22 October 2019

Abstract

The road accident rate has been growing in recent years; therefore, an analysis of the road accident hotspots is essential to reduce the number of accidents occurring in high-accident-density areas. Sri Racha district in Chon Buri province was selected as the study area for this research. The accident data of 2012-2017 was collected from the Road Accident Data Center (ThaiRSC). The spatiotemporal pattern of road accidents was clustered into various scales: accidents occurring on weekdays, weekends, daytime, nighttime and those involving fatality and injury. Spatial statistical methods, kernel density estimation (KDE), and Ripley's K-function in geographic information system (GIS) were applied to identify patterns and the distribution of road accidents. The findings showed that a high density of road accidents was found in three main areas: Sri Racha municipality, Laem Chabang City municipality and Bowin subdistrict. The spatial distribution of all types of road accidents was clustered at various distances. Several agencies can use the results for planning and managing road accident reduction strategies. Furthermore, GIS and spatial statistical methods are effective tools that are quite widely used for accident analysis.

Keywords: Kernel density estimation, Ripley's K-function, hotspot, spatial pattern, GIS
DOI 10.14456/cast.1477.6

1. Introduction

Road systems are important for transportation since they are cheap and rapid. However, it is associated with a high risk of accidents in comparison with other modes of transportation [1]. A lack of transportation infrastructure development has caused an increase in the number of road accidents [2]. Injuries, fatalities, and damaged properties are consequences of road accidents around the world [3-5], particularly in developing countries [6, 7]. Additionally, road accidents cause economic losses to victims, their families, and the nation [8]. Most road accidents result from human mistakes, such as inattentiveness of the drivers or pedestrians [9]. Hence, road accidents can be reduced through the analysis of the incident scenarios and spatial analysis [2, 8, 10].

The World Health Organization stated that 1.25 million people were killed in road accidents in 2013, with high fatality rates in low and middle income countries. In Thailand, the fatality rates of road accidents were estimated at 24,237 people, i.e. 36.2 per 100,000 [11].

*Corresponding author: Tel.: +66 82-231-3386 Fax: +66 38-102-379
E-mail: narong_p@buu.ac.th

According to statistics recorded by the Road Accident Data Center (ThaiRSC), 522 fatalities and 51,841 injuries were reported in Chon Buri province, the city with the second largest economy in Thailand, following Bangkok [12]. The effect of road accidents has been investigated for many years by studying the relationship between real-time traffic and road safety [13-15], detecting accident hotspots [16, 17], and analyzing the spatiotemporal pattern of road accidents [18, 19].

The geographic information system (GIS) is a powerful tool for spatiotemporal analysis. It has been used for analyzing and visualizing road accidents [20], identifying the spatial pattern and hotspot of accidents [21] and determining the density and distribution in the accident area [6, 15, 22]. Furthermore, the GIS facilitates researchers' understanding of the relationship between accidents and their contributing factors, such as accident data that include socioeconomic information, land use and travel information [16]. At present, GIS with spatial statistical techniques has been developed. Kernel density estimation (KDE) is one of the most popular methods used for analyzing the distribution and accident hotspot [21, 23-26]. Another method, the network kernel density estimation (NetKDE), was developed to evaluate the density of road accidents over a network space [5, 27-29]. Other methods of spatial point pattern analyses, such as Moran's I, Getis-Ord Gi* [30, 31] and Ripley's K- function [2, 19, 32, 33], have been presented.

Using ArcGIS 10.0, the density and distribution of road accidents were analyzed using KDE and Ripley's K- function within a particular period. The spatiotemporal analysis of road accidents can help transportation agencies improve road safety in Sri Racha district, Chon Buri province. The rest of the paper is organized as follows. Section 2 describes the study area, the data, and methods. Section 3 reveals the results and discussion of the analysis of road accident density and distribution and section 4 presents the conclusions.

2. Materials and Methods

2.1 Study area

Sri Racha district, Chon Buri province, located on the east coast of Thailand, was selected as the study area. According to the Department of Provincial Administration [34], Sri Racha has a population of approximately 51,197. Sri Racha district, an industrial zone comprising manufacturing and shipping industries, covers approximately 616.40 km². The district was supported by the port of Laem Chabang, the 20th largest port in the world. Furthermore, it contributes to the economic development of the eastern seaboard of Thailand. Rapid economic growth and development and an increase in the number of vehicles may lead to an increase in the number of road accidents, as shown in Figure 1.

2.2 Road accident database

The road accident data used in this study were acquired from the ThaiRSC. However, not all road accidents were recorded in the ThaiRSC database. ThaiRSC only recorded the data of the victims who petitioned for indemnification or payment in accordance with the Protection for Motor Vehicle Accident Victims Act, 1992. Figure 1 shows that 20,003 accidents occurred between 2012 and 2017 in Sri Racha. Details of these accidents such as date, time, road type and accident location were recorded and save as a GIS shape file. Spatiotemporal analyses were presented at various scales: weekdays (Monday-Friday), weekends (Saturday-Sunday), daytime (06.00-17.59), nighttime (18.00-05.59) and accidents involving fatality and injury. Later on, these six categories of spatiotemporal road accidents were combined to new four groups: fatality during daytime on weekdays, fatality

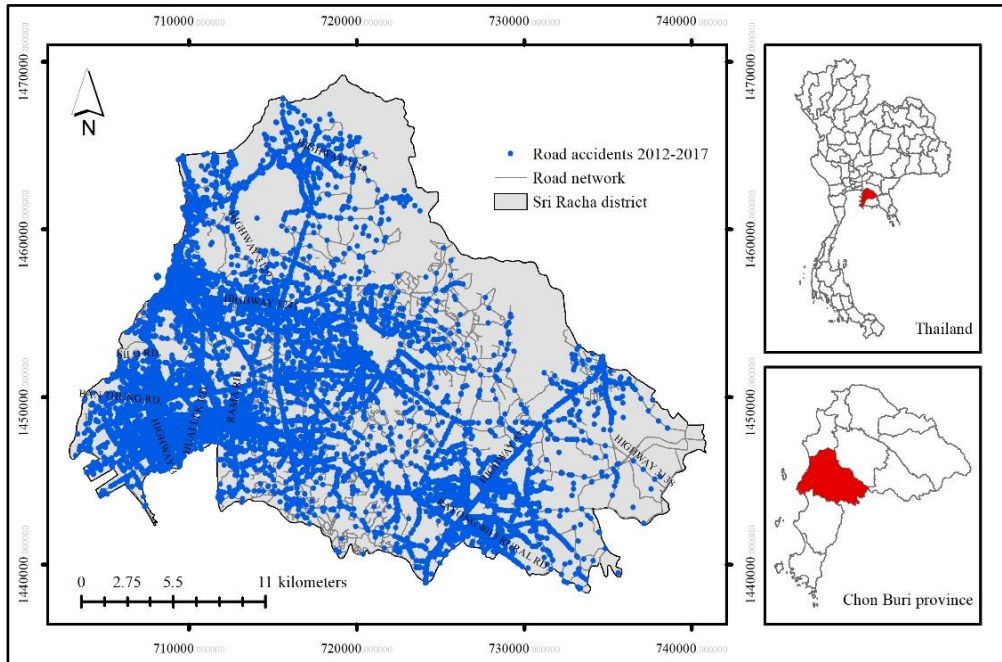


Figure 1. Study area, Sri Racha district, Chon Buri province, and spatial pattern of road accident points (2012-2017)

during nighttime on weekdays, fatality during daytime on weekends and fatality during nighttime on weekends.

2.3 KDE

KDE may be used to efficiently identify the point pattern of road accidents [22]. This method is used to create a density map based on a non-parametric approach. Furthermore, it distinguishes the areas by placing a plane-symmetry over each point. Afterwards, the distances between the center point and locations of accidents within the surface area are assessed. KDE repeats successive points and provides possibilities of using kernel functions for each observation. These kernels furnish density analysis of the distribution of accident points [35]. The density estimation function is as follows:

$$f(x, y) = \frac{1}{nh^2} \sum_{i=1}^n K\left(\frac{d_i}{h}\right) \quad (1)$$

Where $f(x, y)$ represents the density estimate of the location (x, y) , n refers to the number of observations, h is the bandwidth, K is the kernel function, and d_i indicates the distance between the location (x, y) and the location of the i^{th} observation ($i = 1, 2, 3, \dots, n$).

The bandwidth shows a strong effect on density estimation. A large bandwidth will produce over smoothed density estimation and a small bandwidth creates inadequate smoothing [19]. The

selection of the cell size is another parameter. In this study, a 300-m bandwidth and a 50-m cell size were applied for road accidents during 2012-2017 of all spatiotemporal scales using ArcGIS 10.0.

2.4 Ripley's K-function

Ripley's K-function is used to evaluate the spatial pattern of the point data and was successfully applied in spatial estimation of accidents [36]. The method summarizes spatial dependence over a range of distances. When the neighborhood size changes, it demonstrates the spatial clustering or dispersion of feature changes at a different distance [37]. In this regard, the K-function $L(d)$ is employed as follows:

$$L(d) = \sqrt{\frac{A \sum_{i=1}^n \sum_{j=1, j \neq i}^n k_{i,j}}{\pi n(n-1)}} \quad (2)$$

Where $L(d)$ is the difference between the observed and expected K-function values below a complete spatial randomness hypothesis (CPSR), d represents the distance, A represents the total area feature, n is equal to the total of features and $k_{i,j}$ is a weight.

ArcGIS 10.0, Ripley's K-function tool was used to estimate the road accident distribution in this study. This statistical test consolidates a normally used transformation ($L(d)$) with Monte-Carlo simulation to create a confidence envelope based on the results of the simulations [32]. At the specified distance of analysis, if the observed values are greater than the expected values and the upper confidence envelope is created from the simulation, the data are clustered in a statistically significant way. Similarly, if the observed values are lower than the expected values and the low confidence envelope, the data are dispersed in a statistically significant manner. However, if the observed values are within the lower and upper boundaries created by the confidence envelopes, the distribution does not randomly vary in a statistically significant manner [19, 32]. In this study, 99 permutations were run using the Ripley's K-function tool, and the corresponding results yield a 99% confidence level. The outcomes are presented using the unit m.

3. Results and Discussion

3.1 Number of road accidents

Figure 2 illustrates a distribution of hourly road accidents during 2012-2017 in Sri Racha, revealing 20,003 accidents points. During the time brackets of 20.00-20.59, 19.00-19.59, and 07.00-07.59, the number of accidents were 1,570 with 33 fatalities, 1,558 and 1,542. In addition, the highest number of fatalities, 48, was observed during 21.00-21.59. After midnight, the number of road accidents declined; the lowest number of accidents was recorded during 04.00-04.59 because people were sleeping at this time, resulting in less traffic. However, the number of accidents began to increase from 05.00 onwards, as people began their commutes to work at this time, particularly during 07.00-07.59. After 08.00, most people were at work, school and home; therefore, traffic reduced, resulting in a decline in the number of road accidents. During 16.00-20.59, the number of accidents was likely to increase because factory workers began to leave from or arrive at their workplaces, trucks travelled to Laem Chabang Port, and many people commuted during this time period.

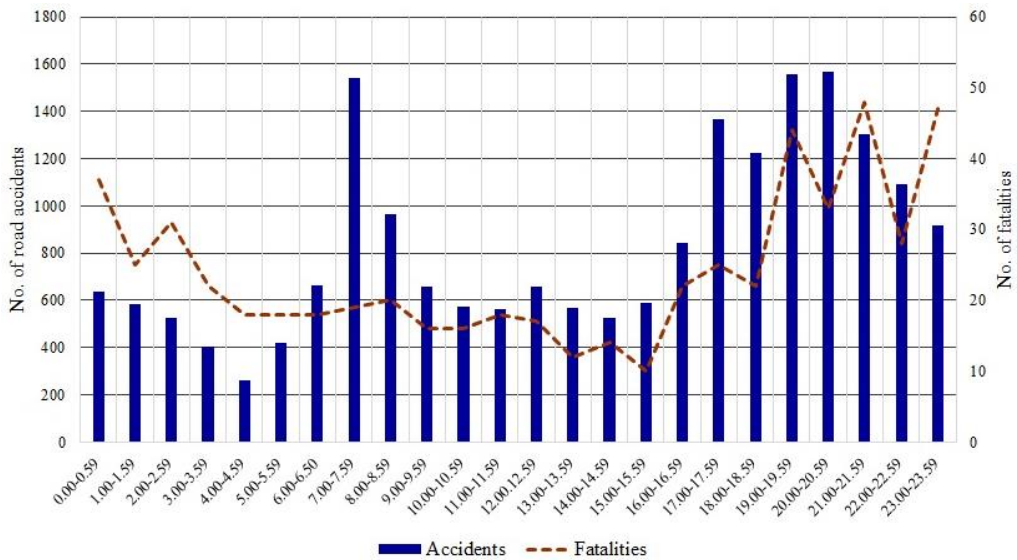


Figure 2. The number of road accidents and fatalities in 24 h

3.2 KDE

Road accidents during 2012-2017 were classified into six groups: (a) weekdays ($n = 13,461$), (b) weekends ($n = 6,542$), (c) daytime ($n = 9,862$), (d) nighttime ($n = 10,141$), (e) fatality ($n = 580$) and (f) injury ($n = 19,423$); fatality during daytime on weekdays ($n = 135$), fatality during nighttime on weekdays ($n = 238$), fatality during daytime on weekends ($n = 68$) and fatality during nighttime on weekends ($n = 139$). Based on the KDE analysis, the bandwidth value was 300 m with a grid size of 50 m. Figure 3 illustrates three areas with high KDE value: Sri Racha municipality, Laem Chabang City municipality and Bowin subdistrict. These areas are considered to be the economic, industrial, and transportation center of Sri Racha district. Sri Racha municipality is located at the center of Sri Racha district and it is an important commercial area with shops, department stores, hotels, hospitals and government agencies. However, this area faces heavy traffic congestion, particularly on Saturdays and Sundays from the morning to the evening when tourists visited Sri Racha, Pattaya, and Koh Larn, which are the famous tourist centers in Chon Buri. Moreover, the highest KDE value was recorded at the clock tower intersection along highway No. 3 (Sukhumvit Road).

Laem Chabang municipality, which is located at the south of Sri Racha municipality, is the location of Laem Chabang Port, the main seaport used by the international sea freight and transportation industry. The presence of many shipping and logistics companies and a large population in this area lead to traffic congestion during daytime and nighttime. In particular, the highest KDE value of all the areas within Sri Racha was recorded at Highway No. 3 (Sukhumvit Road), in front of Laem Chabang Port.

The Bowin subdistrict is a large area with a very dense population. Owing to its proximity to many large industrial estates such as WHH Chon Buri Industrial Estate 1, Eastern Seaboard Industrial Estate, Rojana Industrial Estate, Bowin Industrial Estate, Hemaraj Eastern Seaboard Industrial Estate 2 and Amata City Industrial Estate Rayong, the area is congested owing to the transportation of goods, raw materials and workers throughout the day. As a result, frequent

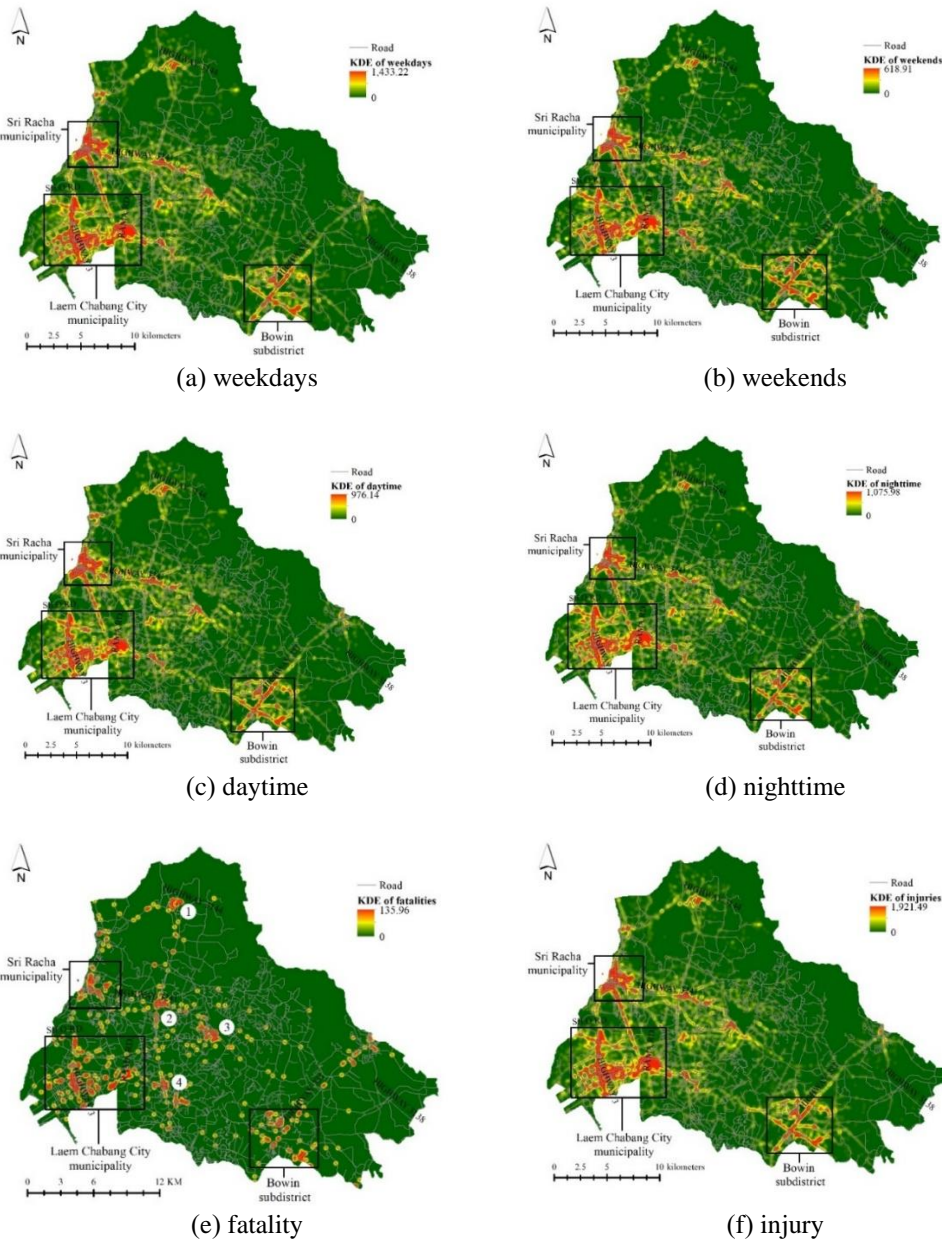


Figure 3. KDE of road accidents in Sri Racha district: (a) on weekdays, (b) weekends, (c) daytime, and (d) nighttime, (e) involving fatality and (f) injury

accidents occur at the intersection of Highway No. 331 in WHH Chon Buri Industrial Estate 1, recording the highest KDE value in this area.

Considering the KDE map of fatalities as shown in Figure 3(e), Sri Racha municipality, Laem Chabang City municipality and Bowin subdistrict have a high KDE value. In addition, other areas with a high KDE value are (1) Highway No. 3144 in the upper part of Sri Racha district, (2) the intersection between National Highway No. 7 (motorway road) and Highway No. 3241, (3) Highway No. 3241 at Nong Kham subdistrict near Nong Kho Reservoir and (4) National Highway No. 7 (motorway road) in the south of the district.

The number of fatalities during daytime, nighttime, weekdays and weekends were identified and it was found that the number of fatalities during nighttime was greater than during daytime on weekdays. Similarly, the highest number of fatalities was recorded during nighttime on weekends. Figure 4(a)-(d) illustrates the results based on KDE analysis in four spatiotemporal

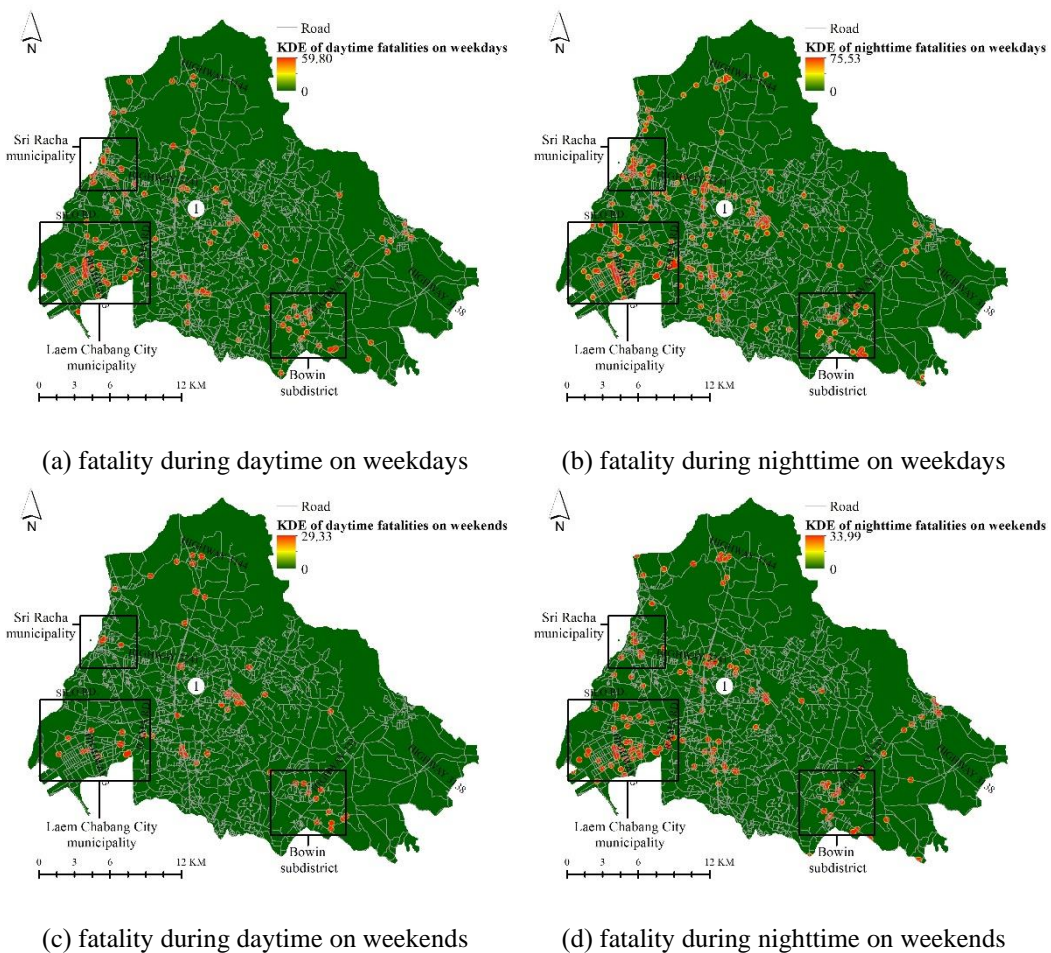


Figure 4. KDE of (a) fatality during daytime on weekdays, (b) fatality during nighttime on weekdays, (c) fatality during daytime on weekends and (d) fatality during nighttime on weekends

scales; fatality during daytime on weekdays, fatality during nighttime on weekdays, fatality during daytime on weekends and fatality during nighttime on weekends. Sri Racha Municipality, Laem Chabang City Municipality and Bowin Subdistrict have a high KDE value. Apart from three aforementioned areas, some other areas have also been found to have high KDE, especially (1) the center of the district which is a large community with many housing estates and the location of Pinthong Industrial Estate 3. Therefore, during nighttime on weekdays (Figure 4(b)), there have been more fatalities than on weekends, particularly along National Highway No. 7 (motorway road) and Highway No. 3241 because many people and workers commuted during this time period and these routes.

3.3 Ripley's K-function

Ripley's K-function was used to analyze the distribution of road accidents at all scales, which include accidents that occurred on weekdays, weekends, daytime and nighttime and those that involve fatality or injury. The confidence envelope value was set to 99 times and the statistical significance at 0.01 level.

Figures 5(a)-(f), the road accidents in all groups showed a clear distribution pattern. When the observed K values were based on the expected K values and higher than the confidence envelope values, the road accidents were clustered and distributed in the distance range of less than 10,300-13,800 m. Clustered distributions of road accidents occurring on weekdays, weekends, daytime and nighttime and those involving a fatality or injury were at distances of less than 13,700, 13,400, 13,600, 13,500, 10,300 and 13,800 m, respectively.

4. Conclusions

Road accidents are a major problem in many countries globally. One of the countries suffering the greatest impact of and damage caused by road accidents is Thailand. The characteristics, locations and periods of road accidents offer important information that can be used to solve and reduce the problems associated with road accidents. GIS tools have been employed to effectively study road accidents and in particular, the accident data that can be used to identify the location and time of the accident. This improves the accuracy and precision of studies. Sri Racha district in the Chon Buri province was chosen as the study area in this research because it is the economic center of transportation, industry and tourism. Furthermore, road accidents occur at an alarming rate within this area.

In this study, data were divided into ten spatiotemporal scales: accidents on weekdays, weekends, daytime and nighttime, accidents involving fatality and injury, fatality during daytime on weekdays and weekends and fatality during nighttime on weekdays and weekends. GIS was used for the analysis. First, KDE was used to analyze the density of the accidents. The corresponding results following three, important, high-density areas: Sri Racha municipality, Laem Chabang City municipality and Bowin subdistrict. Sri Racha municipality is the center of Sri Racha district; it is an important commercial area and has shops, hospitals, and government agencies. Laem Chabang City municipality is located at the Laem Chabang Port. Many shipping and logistics companies are located in the area. Bowin subdistrict is densely populated owing to its proximity to many large industrial estates. Second, Ripley's K-function was used to analyze the distribution of road accidents, revealing the following three road accident distribution patterns: clustered, dispersed and random. The results demonstrated that the distribution pattern of each group was clustered in distances of less than 10.30-13.80 km.

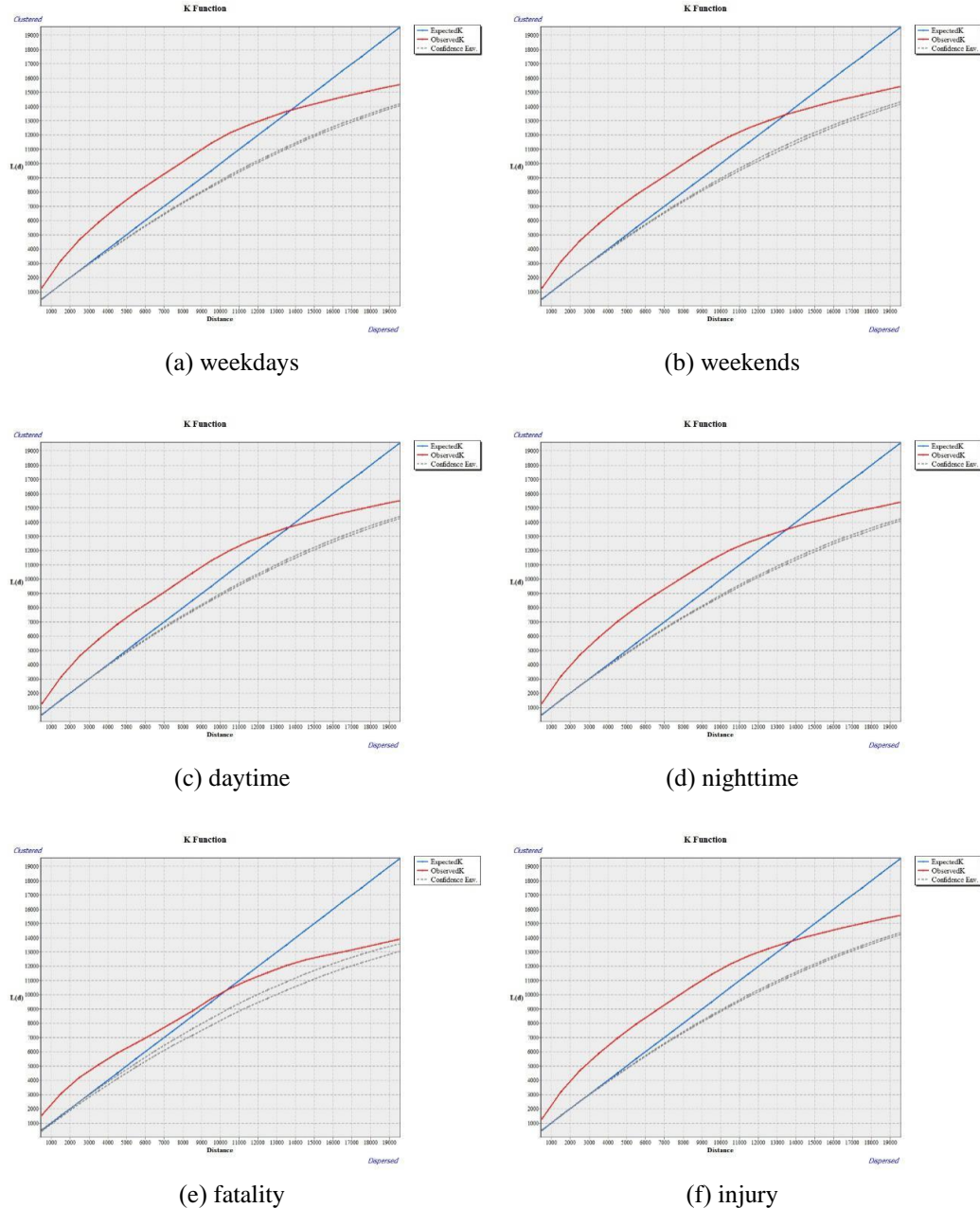


Figure 5. Ripley's K-function results for accidents: (a) occurring on weekdays, (b) weekends, (c) daytime and (d) nighttime, (e) involving fatality and (f) injury

The results of this research comprise important information that shows the trends, densities and distribution patterns of road accidents in the studied areas within each period of time. This information can be used for planning and setting measures to reduce road accidents. The accident information is categorized temporally as follows: accidents occurring on weekdays and weekends and during daytime and nighttime. Transport agencies and traffic police can use this information for monitoring accidents and increasing traffic safety during the aforementioned times.

The limitations of this research are as follows: first, the road accident data used for the study are only a part of insured accident data obtained from ThaiRSC, not all the accident data. Second, the published accident data lack important information such as the gender and age of the victims and causes of accidents. This important information could increase the integrity of this research. However, despite the aforementioned limitations, the finding of this research can be used to solve the problems associated with road accidents in Sri Racha district.

References

- [1] Dereli, M.A. and Erdogan S., 2017. A new model for determining the traffic accident black spots using GIS-aided spatial statistical models. *Transport Research Part A*, 103, 106-107.
- [2] Shafabakhsh, G., Famili, A. and Bahadori, M.S., 2017. GIS-based spatial analysis of urban traffic accidents: case study in Mashhad, Iran. *Journal of Traffic and Transport Engineering*, 4(3), 290-299.
- [3] Anderson, T.K., 2009. Kernel density estimation and K-means clustering to profile road accident hotspots. *Accident Analysis and Prevention*, 41, 359-364.
- [4] Indian Council of Medical Research (ICMR), 2009. Development of a feasibility module for road traffic injuries surveillance. *JCMR Bulletin*, 39(10-12), 41-50.
- [5] Xie, Z. and Yan J., 2013. Detecting traffic accident clusters with network kernel density estimation and local spatial statistics: an integrated approach. *Journal of Transport Geography*, 31, 64-71.
- [6] Satria, R. and Castro, M., 2016. GIS tools for analyzing accidents and road design: a review. *Transportation Research Procedia*, 18, 242-247.
- [7] Soltani, A. and Askari, S., 2017. Exploring spatial autocorrelation of traffic crashes based on severity. *Injury*, 48, 637-647.
- [8] Aghajania, M.A., Dezfoulian, R.S., Arjroodyb, A.R. and Rezaeid, M., 2017. Applying GIS to identify the spatial and temporal patterns of road accidents using spatial statistics (case study: Ilam province, Iran). *Transportation Research Procedia*, 25, 2126-2138.
- [9] Prasannakumar, V., Vijitha, H., Charuthaa, R. and Geetha N., 2011. Spatio-temporal clustering of road accidents: GIS based analysis and assessment. *Procedia Social and Behavioral Sciences*, 21, 317-325.
- [10] Rhee, K.A., Kim, J.K., Lee, Y.I. and Ulfarsson, G.F., 2016. Spatial regression analysis of traffic crashes in Seoul. *Accident Analysis and Prevention*, 91, 190-199.
- [11] World Health Organization (WHO), 2018. *Road Traffic Deaths: Data by Country 2013*. [online] Available at: http://www.who.int/gho/road_safety/mortality/traffic_deaths_number/en/
- [12] Road Accident Data Center (ThaiRSC), 2018. *Statistic of Injuries and Deaths All Provinces 2017*. [online] Available at: <http://www.thairsc.com/>
- [13] Xu, C., Tarko, A.P., Wang, W. and Lui, P., 2013. Predicting crash likelihood and severity on freeways with real-time loop detector data. *Accident Analysis and Prevention*, 57, 30-39.

- [14] Yu, R. and Abdel-Aty, M., 2014. Using hierarchical bayesian binary probit models to analyze crash injury severity on high speed facilities with real-time traffic data. *Accident Analysis and Prevention*, 62, 161-167.
- [15] Zheng, Z., Ahn, S. and Monsere, C.M., 2010. Impact of traffic oscillations on freeway crash occurrences. *Accident Analysis and Prevention*, 42, 626-636.
- [16] Li, L., Zhu, L. and Sui, D.Z., 2007. A GIS-based bayesian approach for analyzing spatial-temporal patterns of intra-city motor vehicle crashes. *Journal of Transport Geography*, 15, 274-285.
- [17] Harirforoush, H. and Bellalite, L., 2019. A new integrated GIS-based analysis to detect hotspots: a case study of the city of Sherbrooke. *Accident Analysis and Prevention*, 130, 62-74.
- [18] Yu, H., Liu, P., Chen, J. and Wang, H., 2014. Comparative Analysis of the spatial analysis methods for hotspot identification. *Accident Analysis and Prevention*, 66, 80-88.
- [19] Ouni, F. and Belloumi, M., 2018. Spatio-temporal pattern of vulnerable road user's collisions hot spots and related risk factors for injury severity in Tunisia. *Transportation Research Part F*, 56, 477-495.
- [20] Deepthi, J.K. and Ganeshkumar, B., 2010. Identification of accident hot spots: a GIS based implementation for Kannur district, Kerala. *International Journal of Geomatics and Geoscience*, 1(1), 51-59.
- [21] Benedek, J., Ciobanub, S.M. and Man, T.C., 2016. Hotspots and social background of urban traffic crashes: A case study in Cluj-Napoca (Romania). *Accident Analysis and Prevention*, 87, 117-126.
- [22] Mohaymany, A.S., Shahri, M. and Mirbagheri, B., 2013. GIS-based method for detecting high-crash-risk road segments using network kernel density estimation. *Journal Geo-Spatial Information Science*, 16(2), 113-119.
- [23] Pulugurtha, S.S., Krishnakumar, V.K. and Nambisan, S.S., 2007. New methods to identify and rank high pedestrian crash zones: An illustration. *Accident Analysis and Prevention*, 39, 800-811.
- [24] Plug, C., Xia, J.C. and Caulfield, C., 2011. Spatial and temporal visualisation techniques for crash analysis. *Accident Analysis and Prevention*, 43, 1937-1946.
- [25] Bíl, M., Andrásik, R. and Janoska, Z., 2013. Identification of hazardous road locations of traffic accidents by means of kernel density estimation and cluster significance evaluation. *Accident Analysis and Prevention*, 55, 265-273.
- [26] Hashimoto, S., Yoshiki, S., Saeki, R., Mimura, Y., Ando, R. and Nanba, S., 2016. Development and application of traffic accident density estimation models using dernel density estimation. *Journal of Traffic and Transportation Engineering*, 3(3), 262-270.
- [27] Xie, Z. and Yan, J., 2008. Kernel density estimation of traffic accidents in a network space. *Computers, Environment and Urban Systems*, 32, 396-406.
- [28] Matkan, A.A., Mohaymany, A.S., Mirbagheri, B., Shahri, M. and Mirzaie, M., 2012. Detecting the accident hazardous segments along Arakkhomein rural road using network kernel density estimation. *Proceeding of the International Geomatics Conference and Exhibition on Mapping and Spatial Information*, Tehran, Iran, May 7-9, 2012, 1-10.
- [29] Delso, J., Martín, B. and Ortega, E., 2018. A new procedure using network analysis and kernel density estimations to evaluate the effect of urban configurations on pedestrian mobility. The case study of Vitoria-Gasteiz. *Journal of Transport Geography*, 67, 61-72.
- [30] Ord, J.K. and Getis, A., 1995. Local spatial autocorrelation statistics: Distributional Issues and an Application. *Geographical Analysis*, 27(4), 286-306.
- [31] Soltani, A. and Askari, S., 2017. Exploring spatial autocorrelation of traffic crashes based on severity. *Injury*, 48, 637-647.

- [32] Thacher, D., Milne, S.B. and Park, R., 2017. Applying GIS and statistical analysis to assess the correlation of human behaviour and ephemeral architectural features among Palaeo-Eskimo sites on southern Baffin island, Nunavut. *Journal of Archaeological Science: Reports*, 14, 21-30.
- [33] Keskina, F., Yenilmezb, F., Çolakc, M., Yavuzerc, I. and Düzgün, H.S., 2011. Analysis of traffic incidents in METU campus. *Procedia Social and Behavioral Sciences*, 19, 61-70.
- [34] Department of Provincial Administration, 2018. *Statistic of Population and Residents in 2017*. [online] Available at: <http://stat.dopa.go.th>
- [35] Fotheringham, A.S., Brunsdon, C. and Charlton, M., 2000. *Quantitative Geography: Perspectives on Spatial Data Analysis*. First ed. Sage: Thousand Oaks.
- [36] Dixon, P.M., 2002. Ripley's K Function. In: El-Shaarawi A. H. , Piegorsch W. W. , ed. *Encyclopedia of Environmetrics*, pp.1796-1803.
- [37] ESRI, 2019. Multi-distance spatial cluster analysis (Ripley's K-function). [online] Available at: <http://desktop.arcgis.com>

Effect of Surface Treatment on Electrical Properties of Polydimethylsiloxane Based Triboelectric Nanogenerator

Parinya Panprom¹, Naratip Vittayakorn^{2,3,4} and Chanisa Nawanol^{1,2*}

¹Program of Physics, Faculty of Science, Udon Thani Rajabhat University,
Udon Thani, Thailand

²Advanced Materials Research Unit, Faculty of Science, King Mongkut's Institute of
Technology Ladkrabang, Thailand

³College of Nanotechnology, King Mongkut's Institute of Technology Ladkrabang,
Bangkok, Thailand

⁴Department of Chemistry, Faculty of Science, King Mongkut's Institute of Technology
Ladkrabang, Bangkok, Thailand

Received : 27 September 2019, Revised : 14 November 2019, Accepted : 20 November 2019

Abstract

This research investigated the effect of surface treatment on electrical properties of flexible triboelectric nanogenerator (TENG). Polydimethylsiloxane (PDMS) was used as triboelectric layer. The PDMS pads were prepared by simple casting method and the effect of surface treatments by heat and acid was examined. Physical morphology of treated samples were investigated by scanning electron microscope (SEM). Electrical properties were measured under continuous periodic knocking. The results revealed that the heat-treated PDMS-based TENG showed the outstanding output voltage. The maximum output voltage of heat-treated based TENG reached approximately 9 V, which was over 4 times larger than those of normal PDMS based TENG. The research demonstrated the feasibility to utilize PDMS-based TENG as an energy harvesting device and presented a cost-effective method for producing high-efficiency PDMS based TENG.

Keywords: triboelectric, surface treatment, polydimethylsiloxane, nanogenerator
DOI 10.14456/cast.1477.7

1. Introduction

Environmental mechanical energy is one of the most attractive energy sources for powering small electronics. Recently, the triboelectric nanogenerator (TENG) has attracted considerable attention, which can harvest mechanical energy caused by mechanical motion in our daily life including wind, rain, vehicle and human movement. It has potential applications in wireless systems [1, 2], portable electronics [3-5] and active sensors [6-8]. The principle of the TENG is based on triboelectrification and electrostatic induction [7]. The triboelectrification is the phenomenon that material becomes electrically charged when two different materials are pressed and rubbed together [7].

*Corresponding author: Tel.: +66 84-669-4115
E-mail: c.nawanol@gmail.com

Nowadays, flexible electronic devices have become a novel trend and more attention has been paid to this area to support the revolution of wearable devices. Polydimethylsiloxane (PDMS) elastomer has been considered as one of the most appropriate materials for TENG applications due to its flexibility, transparency, lightweight, non-toxicity, easy fabrication and high electronegativity [9-11].

In the past few years, much work has been done to improve the conversion efficiency of TENG, including optimizing its structure and material [10, 12-14]. Recently, Chen *et al.* [10] reported an enhancing performance of TENG by filling high dielectric nanoparticles into sponge PDMS film, which gives over 5-fold power enhancement compared with the nanogenerator based on the pure PDMS film. However, there have been a few related studies on surface treatment. The interface could significantly influence the electric performance of the triboelectric materials [11, 15]. For example, Yun *et al.* [11] reported the base-treated PDMS surfaces by sprinkling of NaOH solution. The resulting TENG generated voltage of 10.4 V and current of 179 nA is almost 3-fold larger than those of fresh PDMS.

In this work, we demonstrated a cost-effective method for producing high-efficiency PDMS based TENG. This research investigated the influence of chemical and physical treatment on electrical properties of PDMS-based TENG. The PDMS pad was chemically modified by acetic acid to create carboxyl groups on the surface. These chemical treatments devoted to enhance the charge density on the surface while the physical treatment is exposed by heat during the curing process to create an elastic porous PDMS. This research presented the simple preparation process of the TENG, which makes it easy to be upgraded for large-scale production and cost savings.

2. Materials and Methods

Electric properties of PDMS-based TENG was improved by employing chemical and physical treatments. The PDMS pads were prepared by a simple casting method. First, 10 ml PDMS solution (Sylgard 184, Dow Corning) was mixed with 1 ml curing agent. Then, the mixture was cast on plastic substrates and kept under room temperature for 24 h. For chemical treatment, the prepared PDMS pads were immersed in concentrated acetic acid for 24 h. After acetic acid treatment, the sample was rinsed several times with DI water. In the preparation of physical treated PDMS, a mixed PDMS solution was cast onto substrates and then cured at 100 °C for 2 h. After drying, the elastic porous PDMS was formed. Finally, the prepared PDMS pads were collected for the test. The effective surface area of the PDMS pads was 3 cm x 3 cm and 1 mm thickness. The chemical bonds of treated PDMS were examined using Fourier transform infrared spectroscopy (FT-IR, Perkin Elmer Spectrum GX FT-IR spectrometer). The morphology of PDMS was characterized by scanning electron microscope (SEM, Zeiss EVO MA1).

In this experiment, the TENG was fabricated with PDMS pad and aluminium (Al) tape. For electrical characterization, a conductive Al tape was applied as both common electrodes and another tribo-material to produce opposite sign mobile charges. The dynamic tester was used to control the cyclic contact of the two plates of the TENG. The PDMS and Al parts of a TENG were attached to the lower fixed part and upper movable part of the dynamic tester, respectively. The output voltage was characterized using an oscilloscope (Trektronix) during the continuous periodic knocking.

3. Results and Discussion

The digital photographs of all samples are presented in Figure 1. From the digital photographs, it was found that all PDMS pads have a smooth surface. All samples are very flexible and stretchable [see the inset of Figure 1(a-c)]. As representatively shown for the heat-treated PDMS [Figure 1(c)], an elastic porous structure was formed.

The morphology of all samples was revealed by scanning electron microscope (SEM). Figure 2(a-c) shows top-view of SEM micrographs from normal PDMS, acid-treated PDMS, and heat-treated PDMS, respectively. Figure 2(b) reveals that dipping of PDMS into acetic acid would result in dramatic changes in the surface morphology of PDMS. The surface of the PDMS has become rough and swollen in a circle as seen in Figure 2(b). The average diameter of the swelling area was $3.35 \pm 1.14 \mu\text{m}$. According to Figure 2(c), it could be seen that the heat-treated PDMS presents a wrinkled surface structure. From a cross-section of SEM image from the heat-treated PDMS [Figure 2(f)], it reveals that the pores are well-formed inside the sample. The average diameter of pores was $2.02 \pm 0.47 \mu\text{m}$. The formation of this porous structure was probably caused by the boiling effect during the curing process at high temperature above the boiling point of PDMS ($>100^\circ\text{C}$).

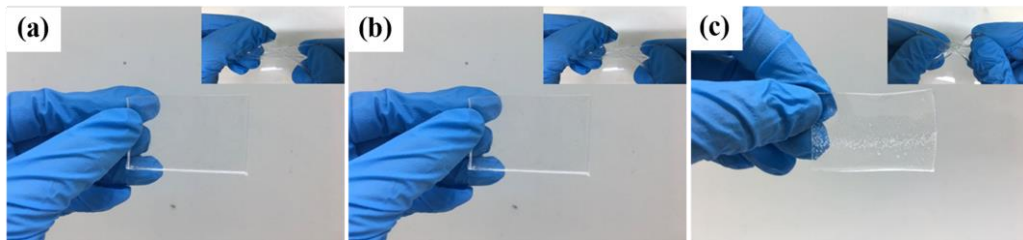


Figure 1. Digital images of (a) normal PDMS, (b) acid-treated PDMS and (c) heat-treated PDMS
An inset shows the digital image of PDMS stretched by hand

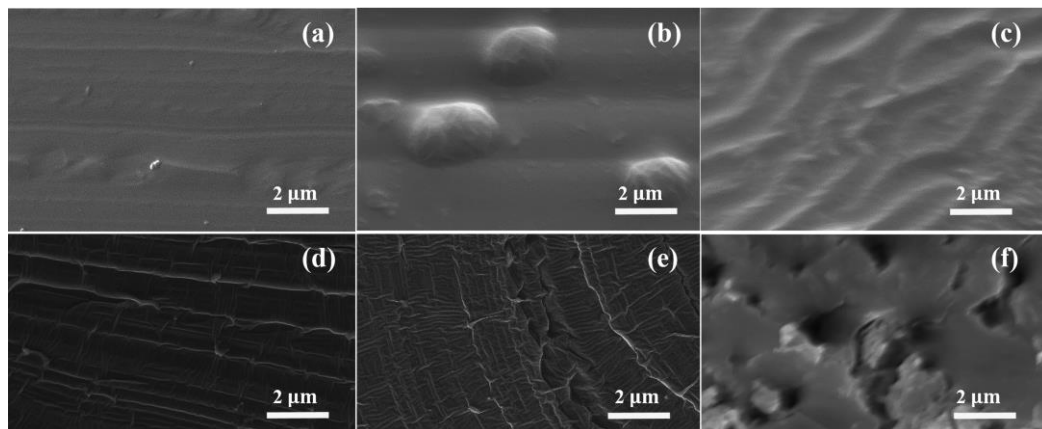


Figure 2. Top and cross-section views of SEM images: (a), (d) normal PDMS; (b), (e) acid-treated PDMS; (c), (f) heat-treated PDMS

FTIR is used to verify the effect of surface treatment of the PDMS as shown in Figure 3. For all samples, the spectrums showed multiple peaks in the range of 1000 to 4000 cm^{-1} , which correspond to the vibrations of PDMS functional groups. The absorption bands around 1400 and 1200 cm^{-1} correspond to the vibration of $-\text{CH}_3$ and the C-H stretching vibration was detected at 2950 cm^{-1} [16]. Peaks of around 700 and 1250 cm^{-1} indicated the Si- CH_3 stretching vibration [17]. A peak at 875 cm^{-1} corresponds to the Si-OH stretching vibration [17]. The multicomponent peaks of Si-O-Si stretching vibration were detected in a range of 930-1200 cm^{-1} [16]. Peaks of around 1100 cm^{-1} indicated the Si-O stretching vibration [17]. The Si-C and Si-(CH_3)₂ peaks were evidenced in the region of 825-865 cm^{-1} and 785-815 cm^{-1} , respectively [16]. After acetic acid treatment, the C=O stretching vibration of carboxyl (-COOH) functional groups was detected at around 1500 [18]. Moreover, the peak intensities of the CH_3 around 2800 cm^{-1} became more obvious, which correspond to the vibrations of acetic acid functional groups. These results revealed that the COOH functional groups were introduced onto the PDMS surface after surface treatment. Carboxylic groups were attached to the PDMS surface by formed H-bond, as shown in Figure 4. In another set of experiments, the heat-treated PDMS was investigated. The IR spectrum revealed that the spectrum has not been changed after heat treatment. The spectrum exhibited multiple absorption peaks in the region of 1000 to 4000 cm^{-1} , which corresponds to the vibrations of PDMS functional groups.

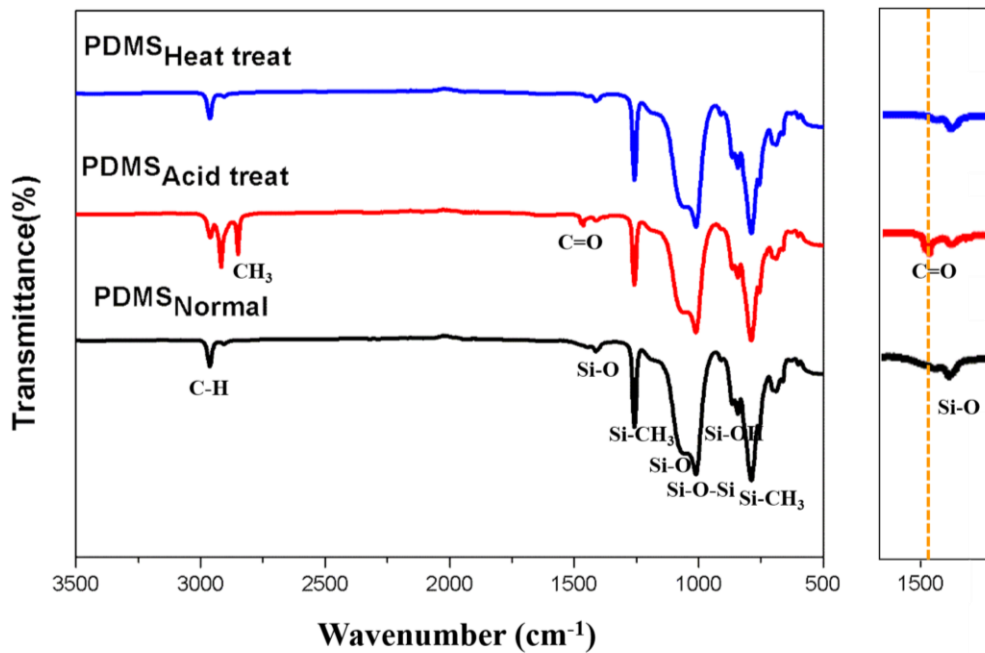


Figure 3. FT-IR spectra of the normal PDMS, acid-treated PDMS and heat-treated PDMS. Insets show FTIR spectra at high magnification.

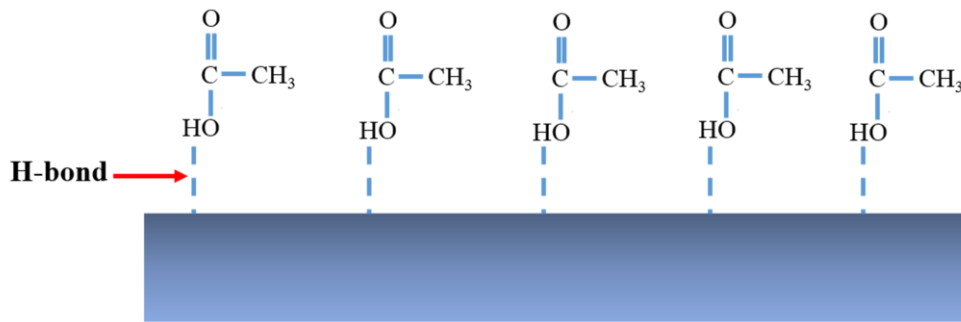


Figure 4. Schematic diagram of the effect of acid treatment which introduce the functional COOH groups onto the surface of PDMS

For electrical characterization, a conductive aluminium (Al) tape was applied as both electrodes and opposite tribo-material. When PDMS and Al come into contact with an external force, the Al is positively charged and the PDMS is negatively charged owing to its intrinsically different triboelectricity tendency [19]. Figure 5 compares the triboelectric power generation of untreated, acid-treated, and heat-treated PDMS-based TENGs. The output voltage signals were detected in both positive and negative side when the substrate was pressed and released, respectively. The formation of a negative signaled after removing external load due to the reverse-flowing carriers. During periodic contact and separation, the normal PDMS-based TENG generated an output voltage of about 2 V [Figure 5(a)]. After surface treatment with acetic acid for 24 h, the PDMS-based TENG exhibited a significantly enhanced triboelectric voltage [Figure 5(b)]. The output voltage of the acid-treated PDMS reached approximately 5 V, which was over two times larger than those of normal PDMS based TENG. This result can be attributed to two reasons. The first reason is the effect of surface roughness, resulting in larger contact areas compared with the normal PDMS. This result leads to an increase in surface charge density and directly enhances the output signals of the TENG. Another possible reason could be the presence of carboxyl groups on the PDMS surface. This could increase the polar components on the surface of PDMS, which affects the surface charge density. The increasing of surface charge density could enhance the output signals of TENG. Yun *et al.* [11] reported the significantly enhanced triboelectric surface charge of PDMS by sprinkling of NaOH solution. It reveals that the enhanced triboelectric charge is related with an increase of polar bonds in PDMS. Therefore, the acid-treated PDMS could greatly enhance the electric output of TENG when combined with the larger contact areas.

In another set of experiments, the heat-treated PDMS-based TENG showed outstanding output voltage [Figure 5(c)]. The maximum output voltage can reach 9 V, which was almost 4.5 times as high as that in the untreated samples. This result may be due to the pores forming in the PDMS pads that could effectively minimize its thickness [10]. The elastic porous PDMS can

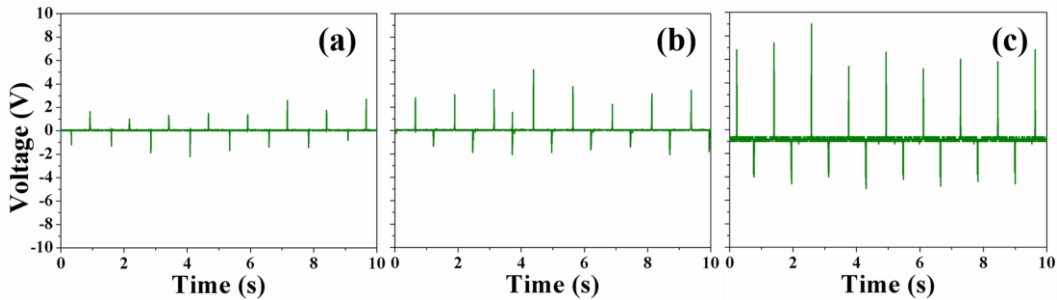


Figure 5. Output voltage of (a) normal, (b) acid-treated and (c) heat-treated PDMS-based TENGs measured with respect to time under an impulsive loading

shrink into minimum thickness which is lower than normal one after an external force was applied. This result leads to an increase in capacitance and the capacitance affects the surface charge density [10]. Therefore, the output signals of the TENG was increased. Moreover, based on the SEM images, the heat-treated sample showed the roughest surface that resulting in larger contact areas. This result also leads to an increase in surface charge density and directly enhance the output signals of the TENG. The triboelectric voltage of heat-treated PDMS-based TENG is higher than those of untreated and acid-treated PDMS-based TENGs.

4. Conclusions

In summary, this research reported the improving electric properties of polydimethylsiloxane based triboelectric nanogenerator by employing physical and chemical treatment. The PDMS pad was chemically modified by acetic acid. The acid-treated PDMS-based TENG revealed a significantly enhanced triboelectric voltage. This improvement corresponded to the increase of surface charge density, which was induced by the carboxyl groups on the sample surface and increase of surface area. While physical treatment is exposed by heat during the curing process. After drying, the elastic porous PDMS was formed. The heat-treated PDMS-based TENG showed better TENG performance than both the normal and the acid-treated PDMS-based TENGs. This result can be attributed to the pores forming in the PDMS pads by heat treatment which could effectively reduce its thickness. This result leads to an increase in capacitance and affects the surface charge density. Therefore, the output signals of the TENG was increased. The output voltage of the heat-treated PDMS-based TENG reached approximately 9 V, which was over 4 times larger than those of normal PDMS-based TENG.

5. Acknowledgements

This research was supported by National Nanotechnology Center (NANOTEC), NSTDA, Ministry of Science and Technology, Thailand, through its program of Center of Excellence Network and National Research Council of Thailand (NRCT).

References

- [1] Cheng, X., Song, Y., Han, M., Meng, B., Su, Z., Miao, L. and Zhang, H., 2016. A flexible large-area triboelectric generator by low-cost roll-to-roll process for location-based monitoring. *Sensors and Actuators A*, 247, 206-214.
- [2] Khan, A.A., Mahmud, A., Zhang, S., Islam, S., Voss, P. and Ban, D., 2019. A self-powered multi-broadcasting wireless sensing system realized with an all-in-one triboelectric nanogenerator. *Nano Energy*, DOI: 10.1016/j.nanoen.2019.05.073.
- [3] Xing, F., Jie, Y., Cao, X., Li, T. and Wang, N., 2017. Natural triboelectric nanogenerator based on soles for harvesting low frequency walking energy. *Nano Energy*, 42, 138–142.
- [4] Tian, Z., He, J., Chen, X., Zhang, Z., Wen, T., Zhai, C., Han, J., Mu, J., Hou, X., Chou., X and Xue, C., 2017. Performance-boosted triboelectric textile for harvesting human motion energy. *Nano Energy*, 39, 562-570.
- [5] Wang, X., Yin, Y., Yi, F., Dai, K., Niu, S., Han, Y., Zhang, Y. and You, Z., 2017. Bioinspired stretchable triboelectric nanogenerator as energy-harvesting skin for self-powered electronics. *Nano Energy*, 39, 429-436.
- [6] Xiang, C., Liu, C., Hao, C., Wang, Z., Chea, L. and Zhou, X., 2017. A self-powered acceleration sensor with flexible materials based on triboelectric effect. *Nano Energy*, 31, 469-477.
- [7] Wang, Z.L., Chen, J. and Lin, L., 2015. Progress in triboelectric nanogenerators as a new energy technology and self-powered sensors. *Energy and Environmental Science*, 8(8), 2250-2282.
- [8] Rasel, M.S., Cho, H.O., Kim, J.W. and Park, J.Y., 2018. A self-powered triboelectric sensor for wide-range pressure detection in wearable application. *Journal of Physics: Conference Series*, 1052, 012029.
- [9] Zhu, D., Handschuh-Wang, S. and Zhou, X., 2017. Recent progress in fabrication and application of polydimethylsiloxane Sponges. *Journal of Materials Chemistry A*, 5(32), 16467-16497.
- [10] Chen, J., Guo, H., He, X., Liu, G., Xi, Y., Shi, G. and Hu, C., 2016. Enhancing performance of triboelectric nanogenerator by filling high dielectric nanoparticles into sponge PDMS film. *ACS Applied Materials and Interfaces*, 8(1), 736-744.
- [11] Yun, B.K., Kim, J.W., Kim, H.S., Jung, K.W., Yi, Y., Jeong, M.S., Ko, J.H. and Jung, J.H., 2015. Base-treated polydimethylsiloxane surfaces as enhanced triboelectric nanogenerators, *Nano Energy*, 15, 523-529.
- [12] Park, S.J., Seol, M.L., Jeon, S.B., Kim, D., Lee, D. and Choi, Y.K., 2015. Surface engineering of triboelectric nanogenerator with an electrodeposited gold nanoflower structure. *Scientific Reports*, 5(1), 1-7. doi: 10.1038/srep13866.
- [13] Guo, T., Liu, G., Pang, Y., Wu, B., Xi, F., Zhao, J., Bu, T., Fu, X., Li, X., Zhang, C. and Wang, Z.L., 2018. Compressible hexagonal-structured triboelectric nanogenerators for harvesting tire rotation energy. *Extreme Mechanics Letters*, 18, 1-8.
- [14] Dong, Y., Mallineni, S.S.K., Maleski, K., Behlow, H., Mochalin, V.N., Rao, A.M., Gogotsi, Y. and Podila, R., 2018. Metallic MXenes: A new family of materials for flexible triboelectric Nanogenerators. *Nano Energy*, 44, 103-110.
- [15] Yu, Y. and Wang, X., 2016. Chemical modification of polymer surfaces for advanced triboelectric nanogenerator development. *Extreme Mechanics Letters*, 9, 514-530.

- [16] Nour, M., Berean, K., Balendhran, S., Ou, J.Z., Plessis, J.D., McSweeney, C., Bhaskaran, M., Sriram, S. and Kalantar-zadeh, K., 2013. CNT/PDMS composite membranes for H₂ and CH₄ gas separation. *International Journal of Hydrogen Energy*, 38(25), 10494-10501.
- [17] Kuo, A.C.M., 1999. Poly(dimethylsiloxane). In: J.E. Mark, ed. 1999. *Polymer Data Handbook*. Oxford University Press Inc, New York, pp. 411-435.
- [18] Shao, L., Tobias, G., Salzmann, C.G., Ballesteros, B. and Hong, S.Y., Crossley, A., Davis, B.G. and Green, M.L.H., 2007. Removal of amorphous carbon for the efficient sidewall functionalisation of single-walled carbon nanotubes. *Chemical Communications*, 47, 5090-5092.
- [19] Pan, S. and Zhang, Z., 2018. Fundamental theories and basic principles of triboelectric effect: A review. *Friction*, 7(1), 2-17.

Resistance to Quinone-outside Inhibitor (QoI) Fungicides in *Colletotrichum* Species Isolated from Anthracnose Disease Occurring in Thailand

Pornprapa Kongtragoul^{1*}, Kazuumi Imamoto² and Hideo Ishii^{2,3}

¹King Mongkut's Institute of Technology Ladkrabang, Prince of Chumphon, Thailand

²School of Agriculture, Kibi International University, Minami-awaji, Hyogo, Japan

³University of Tsukuba, Tsukuba, Ibaraki, Japan

Received: 30 August 2019, Revised: 25 November 2019, Accepted: 29 November 2019

Abstract

Colletotrichum species are plant pathogens causing anthracnose diseases in many crops that result in significant reduction of quality and quantity of the crop products. Management of these diseases has become increasingly difficult recently due to the development of fungicide resistance in pathogens. Thus, monitoring for fungicide sensitivity in the pathogen is important to manage these diseases. The isolates of *Colletotrichum* species were isolated from anthracnose disease on various crops collected during 2016-2017 in central and southern Thailand. They were tested for their mycelium growth sensitivity to azoxystrobin, a quinone-outside inhibitor (QoI) fungicide and their internal transcribed spacer (ITS) and 5.8S regions of rDNA were analyzed. The results showed that eleven out of twenty four isolates of *Colletotrichum* species were resistant to azoxystrobin. They were able to grow on PDA amended with 100 mg/l azoxystrobin in the presence of salicylhydroxamic acid (SHAM) at 100 mg/l. Moreover, two isolates of azoxystrobin-resistant *Colletotrichum* spp. produced much larger lesions than azoxystrobin-sensitive isolates on mango fruits after treatment with 100 mg/l azoxystrobin. This is the first report on the occurrence of azoxystrobin resistance in *Colletotrichum* species present in Thailand and will contribute to the management of these important diseases in the future.

Keywords: anthracnose, azoxystrobin, *Colletotrichum*, fungicide resistance, mango, QoIs

DOI 10.14456/cast.1477.8

1. Introduction

Anthracnose diseases, caused by *Colletotrichum* species are major diseases of many crops in Thailand because the weather conditions in this country are favorable to disease development. They destroy both pre- and post-harvest products of economic crops such as chili [1], coffee [2], orchid [3], banana and mango [4]. The management of anthracnose diseases has relied largely on various As a result, QoI fungicides, which inhibit mitochondrial respiration at the ubiquinol oxidation center of the cytochrome *bc1* enzyme complex (complex III) have been introduced to control groups of

*Corresponding author: Tel.: +66 89-728-9459 Fax: +66 7-750-6425
E-mail: kkpornpr@gmail.com

chemical fungicides such as quinone-outside inhibitor (QoI), sterol demethylation inhibitor (DMI), methyl benzimidazole carbamate (MBC) fungicides during the growing season for a long time [5, 6]. They are systemic fungicides with single-site mode of actions which have high risk for the development of resistance in fungal populations [7]. In fact, resistance of *Colletotrichum* species, the cause of mango anthracnose, to the benzimidazole fungicide carbendazim has been reported formerly in Thailand [8, 9].

As a result, QoI fungicides, which inhibit mitochondrial respiration at the ubiquinol oxidation center of the cytochrome *bc1* enzyme complex (complex III), have been introduced to control anthracnose [10-12]. These fungicides inhibit electron transfer which leads to preventing the production of ATP in fungal cells [10-12].

Currently, azoxystrobin and trifloxystrobin, members of the QoI fungicides, are recommended for the control of mango and chili anthracnose as alternative fungicides of carbendazim in Thailand [5, 6]. They were imported into Thailand with the cost of approx. 5,264,773 US dollars a year which was ranging the top ten fungicides by value in 2017 [13]. Furthermore, the QoI fungicide resistance in several *Colletotrichum* species has been reported on various crops from many countries such as *C. graminicola* from creeping bent grass in Japan and annual bluegrass in the United States [14], *C. gloeosporioides* from strawberry anthracnose in Japan [15], *C. cereale* causing turfgrass anthracnose in California and the southern United States [16, 17], *C. siamense* from peach and blueberry anthracnose in South Carolina [18], *C. acutatum* from strawberry anthracnose in Florida [19], *C. gloeosporioides* causing orange anthracnose in Italy [20], *C. truncatum* from physic nut, papaya, and pepper in Mexico [21] and *C. acutatum* and *C. gloeosporioides* from boxthorn and apple in Korea [22]. However, it has never been reported in Thailand. Consequently, the monitoring of QoI fungicide resistance development in *Colletotrichum* species is necessary for anthracnose disease management.

The objectives of this research were to (i) collect isolates of *Colletotrichum* species causing anthracnose from naturally infected crops, (ii) evaluate their sensitivity to azoxystrobin and (iii) analyze their internal transcribed spacer (ITS) and 5.8S regions of rDNA to identify species complex. The overall impact of this research is expected to help determining the management strategies for anthracnose diseases in the future.

2. Materials and Methods

2.1 Fungicides and Pathogen collection

Commercial formulation of azoxystrobin (Amistar®, 25% active ingredient (a.i.) SC) was used in this study. The diluted suspensions of azoxystrobin were prepared in sterile distilled water and added to the medium after autoclaving. It is well known that an alternative respiration pathway is activated in fungal cells after treatment with QoI fungicides and isolates are able to grow on fungicide amended culture medium [14-17]. Therefore, it is a common practice to include salicylhydroxamic acid (SHAM) as alternative oxidase (AOX) inhibitors in the medium to suppress alternative respiration [15]. SHAM was dissolved in methanol and added to azoxystrobin amended potato dextrose agar (PDA).

Chili fruits, orange fruits, mango fruits inflorescences, and leaves, crinum lily leaves and orchid leaves showing symptoms of anthracnose disease naturally infected were selected from local markets, orchards and private houses in Chumphon, Saraburi, Prachuap Khiri Khan, Bangkok, Cha Choeng Sao, Samut Prakarn and Chon Buri provinces during 2016-2017. Fungal isolation was made by cutting a small section of anthracnose infected portion, which was surface sterilized with 10% Clorox® (8.25% a.i. sodium hypochlorite) for 1-2 min, rinsed in sterilized distilled water, and blotted

dry on sterile paper towels in a laminar flow hood. The dried tissues were then placed on the plates of water agar, and incubated at room temperature of approx. 28-30°C. The pure culture of isolates was maintained on PDA slants. All isolates used in this study are listed in Table 1.

Table 1. Source list of *Colletotrichum* isolates used in this study.

Year of isolation	Isolate code	Host	Location
2016	CC004	chili_fruits	Local market, Chumphon
	CC005	chili_fruits	Local market, Chumphon
	CC007	chili_fruits	Local market, Chumphon
	CO010	orange_fruits	Local market, Chumphon
2017	CM_S013	mango_fruits	Orchard, Saraburi
	CM_C019	mango_fruits	Local market, Prachuap Khiri Khan
	CM_C020	mango_fruits	Local market, Prachuap Khiri Khan
	CM_002	mango_fruits	Local market, Bangkok
	C1_m02	mango_inflorescences	Orchard, Cha Choeng Sao
	C1_m05	mango_fruits	Local market, Bangkok
	C1_m06	mango_fruits	Orchard, Samut Prakarn
	C1_m07	mango_fruits	Orchard, Samut Prakarn
	C1_m08	mango_fruits	Orchard, Samut Prakarn
	C1_m10	mango_fruits	Orchard, Samut Prakarn
	C1_m31	mango_fruits	Orchard, Bangkok
	C1_m32	mango_fruits	Orchard, Bangkok
	C1_m33	mango_fruits	Orchard, Bangkok
	C1_m34	mango_fruits	Orchard, Bangkok
	C1_m35	mango_fruits	Local market, Bangkok
	C1_m36	mango_fruits	Local market, Bangkok
	C1_m37	mango leaves	Orchard, Bangkok
	C1_m38	mango leaves	Orchard, Bangkok
	C1_cl39	crinum lily leaves	Private house, Bangkok
	C1_or40	orchid leaves	Private house, Chon buri

2.2 Sensitivity of *Colletotrichum* isolates to azoxystrobin in mycelial growth assay

The sensitivity of 24 *Colletotrichum* isolates to azoxystrobin was assessed by mycelial growth assay. Each isolate of *Colletotrichum* spp. was previously grown on PDA plates at 25°C for 3 days. Mycelial discs (4 mm in diameter) were cut from actively growing colony margins and transferred onto PDA amended with azoxystrobin at 0, and 100 mg (a.i.)/l and SHAM at 100 mg/l (3 replications). After incubation at 25°C for 3 days, the diameter of colony was recorded and the percentage of mycelial growth inhibition by fungicide treatment was calculated as follows: [(mean of colony diameter on the control medium – mean of colony diameter on the medium with fungicide)/(mean of colony diameter on the control medium) × 100].

2.3 Azoxystrobin sensitivity on inoculated mango fruits

Azoxystrobin sensitivity of the isolates was determined on mango fruits. Thirty six mango fruits were washed thoroughly using sterilized water before being surface sterilized with 10% Clorox®

and air-dried. Two 1×1.5 mm (diameter \times depth) wounded inoculation sites were marked on the top (4 cm from stalk) and the bottom (4 cm from apex) of the fruits with a sterile needle. The wounded mango fruits were soaked with 100 mg/l azoxystrobin or sterilized water for 5 min. All tested isolates were previously cultured on PDA at 25°C for 4 days. The mycelial discs of 5 mm diameter were cut with a sterilized cork borer and transferred upside down onto the wounded site of mango fruits (3 replications). The inoculated mango fruits were incubated in a moist plastic box at room temperature (28-30°C) for 4 days. The lesion zone appeared as brown rot around the wounded site was measured after 4 days of incubation and the percentage of disease control was calculated from $[(\text{mean lesion diameter on water treated mango fruits} - \text{mean lesion diameter on azoxystrobin treated mango fruits}) / \text{mean lesion diameter on water treated mango fruits}] \times 100$. For statistical analysis, one-way ANOVA was performed and followed by least significant difference test. Probability values ($P < 0.05$) were considered statistically significant.

2.4 Isolation of total DNA

The isolates of *Colletotrichum* were grown on PDA at 25°C for 5 days. The total DNA of each isolate was extracted from mycelia as described by Saitoh *et al.* [23] with slight modifications [24]. A small piece about 1 cm² in size of agar medium with actively growing mycelia was transferred in an Eppendorf tube (1.5 ml size) containing 500 μ l of lysis buffer (50 mM of ethylenediaminetetraacetic acid (EDTA), 200 mM of NaCl, 200 mM of Tris-HCl, 1% *n*-lauroylsarcosine sodium salt, pH 8.0). They were homogenized using a plastic pestle and an electric drill. The mixture was incubated for 10 min at room temperature and then centrifuged at 13,000 rpm at 4°C for 5 min. The 300 μ l of supernatant was transferred to a fresh tube. After mixing with 750 μ l of ethanol, the DNA was precipitated by centrifugation at 13,000 rpm at 4°C for 2 min. The pellet was washed with 70% ethanol and then air dried in a laminar floor bench. The dried pellet was dissolved in 50 μ l of Tris-EDTA (TE) buffer containing 1 mM of EDTA (pH 8.0) and 10 mM of Tris-HCl.

2.5 PCR experiments and sequencing

To amplify the rDNA-ITS (ITS1-5.8S rDNA-ITS2) regions from total DNA, the PCR primers ITS5 and ITS4 [25] were used. A total volume of 50 μ l of PCR reaction mixtures contained a set of forward and reverse primers (0.2 μ M for each), premixed Go Taq Green Master Mix (Promega, Madison, WI) and 1 μ l of total DNA. PCR reactions were performed in a Mastercycler nexus gradient (Eppendorf, Hamburg, Germany) programmed at 94°C for 1 min, followed by 35 cycles at 94°C for 1 min, 52°C for 1 min, 72°C for 2 min, a final extension at 72°C for 10 min and holding at 10°C.

The PCR products were separated by electrophoresis on a 1.5% agarose gel in 2 mM EDTA + 89 mM Tris-borate (TBE) buffer (pH 8.0) and stained with GelRed™ (Biotium, Hayward, CA). They were cleaned up using ExoSAP-IT (Affymetrix, Santa Clara, CA) according to the manufacturer's instructions. Sequencing in both directions was conducted at Macrogen Japan Corp. (Kyoto, Japan) using the same primers employed for PCR. The nucleotide sequences were analysed with the database of National Center for Biotechnology Information (NCBI)/GenBank using basic local alignment search tools (BLAST).

3. Results and Discussion

3.1 Azoxytropin sensitivity of mycelial growth

Azoxytropin sensitivity was examined based on mycelial growth inhibition on fungicide amended PDA plates. As shown in Table 2, ten isolates (C1_m02, C1_m10, C1_m31, C1_m32, C1_m33, C1_m34, C1_m35, C1_m36, C1_m37, and C1_m38) of *Colletotrichum* spp. from mango anthracnose and one isolate (C1_cl39) from crinum lily anthracnose grew on the plate containing azoxytropin at 100 mg/l in the presence of SHAM at 100 mg/l and they were determined as resistant (R) according to Avila-Adame *et al.* [14] and Torres-Calzada *et al.* [21]. In contrast, three isolates from chili anthracnose (CC004, CC005, and CC007), eight isolates from mango anthracnose (CM_S013, CM_C019, CM_C020, CM_002, C1_m05, C1_m06, C1_m07 and C1_m08) and two isolates from orange and orchid anthracnose (CO010 and C1_or40) were sensitive (S) to azoxytropin because their growth was completely inhibited at 100 mg/l azoxytropin with 100 mg/l SHAM [14]. To our knowledge, this is the first documentation of azoxytropin resistance in *Colletotrichum* species in Thailand. Historically, azoxytropin was used as an alternative control agent to manage anthracnose diseases in commercial chili farms and mango orchards because these diseases were poorly controlled by other fungicides. As a result, the use of this fungicide has also caused a problem in disease control. The same problem of anthracnose disease control has occurred in many other countries on various crops [14-22].

3.2 Azoxytropin sensitivity on inoculated mango fruits

Based on the differential azoxytropin sensitivity of mycelial growth in the presence of SHAM, two groups of isolates were used for inoculation onto detached mango fruits. Two azoxytropin-resistant isolates, C1m02 and C1m10, produced brown lesions on mango fruits pretreated with 100 mg/l azoxytropin with no significant differences in their diameter from those in non-treated control (disease control: -5.41 and 8.37%, respectively). However, four azoxytropin-sensitive isolates, C1m05, C1m06, C1m07, and C1m08, significantly differed in lesion diameter when compared with the non-treated control, which showed the disease control of 55.38% - 87.31% (Table 3 and Figure 1). It was thus confirmed that azoxytropin was not effective at 100 mg/l against resistant isolates on mango fruits. A similar QoI resistance was found in other reports on anthracnose in strawberry [15], annual bluegrass and creeping bent grass [17]. These results indicated that QoI fungicides will not successfully control anthracnose if azoxytropin-resistant isolates are widely distributed in the field.

3.3 rDNA-ITS sequence analysis

The PCR products from each isolate (except the isolate C1_m34) amplified using the ITS5 and ITS4 primers were sequenced directly and analysed with the NCBI database. The results showed that the nucleotide sequences of all isolates indicated that the causal agent of anthracnose diseases in chili, mango, crinum lily-leaf, and orchid-leaf identified as *Colletotrichum* species. The chili isolates CC004 was *C. acutatum* with 99% identity, CC005 was associated with *C. acutatum* and *C. scovillei* with 100% identity, and CC007 was associated with *C. aeschynomenes*, *C. acutatum*, *C. boninense*, *C. fructicola*, *C. gloeosporioides*, *C. siamense*, *C. nupharicola*, and *C. viniferum* with 99-100% identity [Table 4]. Three species, *C. capsici*, *C. gloeosporioides* and *C. acutatum* were the major causal agents of chili anthracnose in Thailand and other countries in Southeast Asia [1]. Some species including in our results, such as *C. scovillei* and *C. siamense* have been shown to cause

Table 2. Mycelial growth inhibition of *Colletotrichum* species on potato dextrose agar plates at 100 mg/l azoxystrobin amended with 100 mg/l SHAM and phenotype classification.

Isolate code	Growth inhibition of azoxystrobin at 100 mg/l (%)	Phenotype
CC004	100	S
CC005	100	S
CC007	100	S
CO010	100	S
CM_S013	100	S
CM_C019	100	S
CM_C020	100	S
CM_002	100	S
C1_m02	57	R
C1_m05	100	S
C1_m06	100	S
C1_m07	100	S
C1_m08	100	S
C1_m10	55.2	R
C1_m31	65	R
C1_m32	75.6	R
C1_m33	77.8	R
C1_m34	70.0	R
C1_m35	68.3	R
C1_m36	62.2	R
C1_m37	63.4	R
C1_m38	70.8	R
C1_cl39	60.4	R
C1_or40	100	S

R = resistant (the mycelia were able to grow on 100 mg/l azoxystrobin with 100 mg/l SHAM)

S = sensitive (the mycelia were not able to grow on 100 mg/l azoxystrobin with 100 mg/l SHAM)

Table 3. Anthracnose lesion diameter and disease control on detached mango fruits after treatment with azoxystrobin prior to pathogen inoculation.

Response to azoxystrobin	Isolate code	Lesion diameter (mm)*		Disease control (%)
		Control	Azoxystrobin at 100 mg/l	
Resistant	C1m02	18.5a	19.5a	-5.41
	C1m10	21.5a	19.7a	8.37
Sensitive	C1m05	19.7a	2.5b	87.31
	C1m06	19.5a	8.7b	55.38
	C1m07	23.5a	5.2b	77.87
	C1m08	17.7a	3.5b	80.23

*Values expressed are means with 3 replications. The different letters in the same row are significantly different as determined by least significant difference test at $P<0.05$.

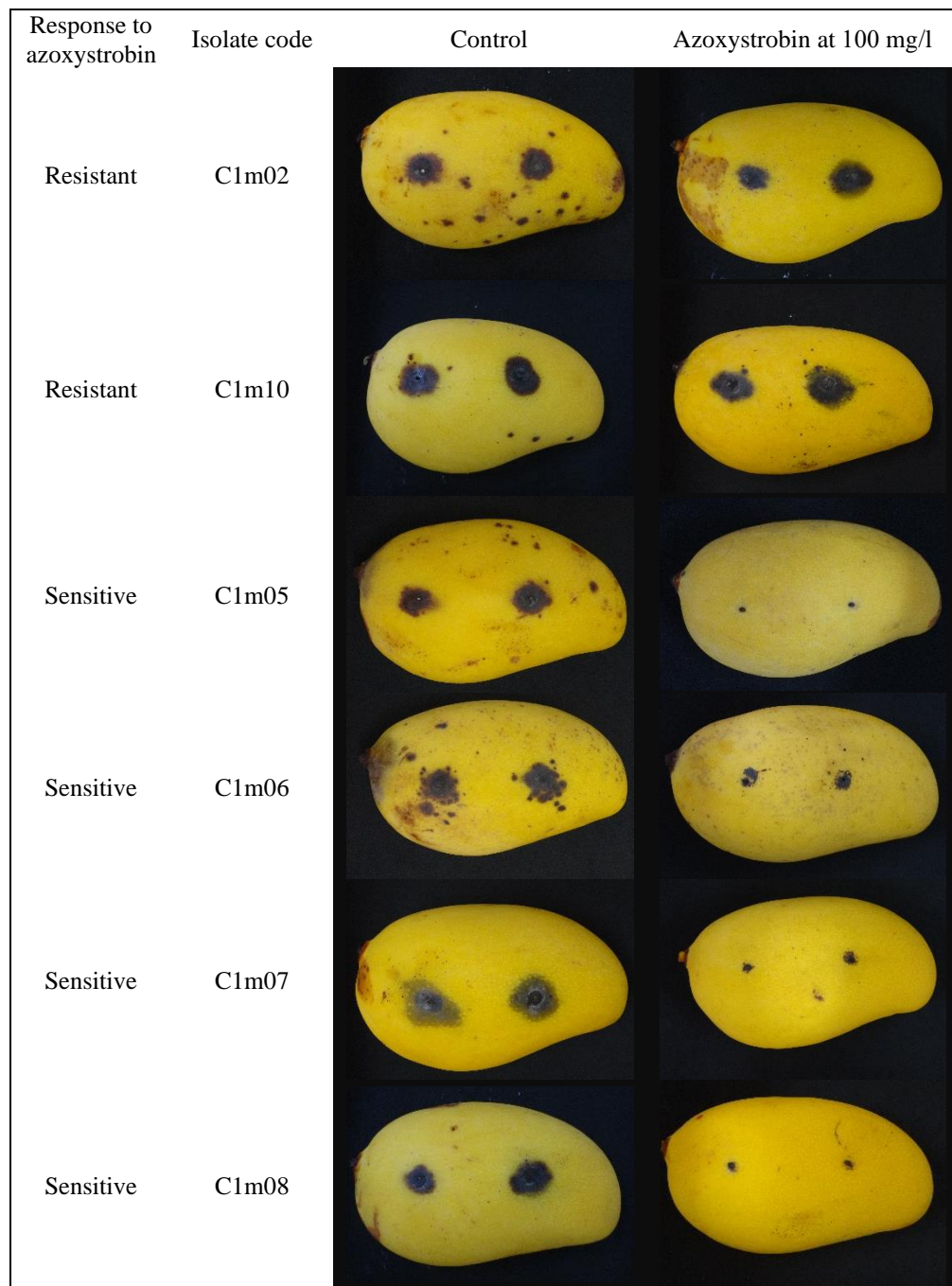


Figure 1. Comparative development of anthracnose lesion on detached mango fruits pretreated with 100 mg/l azoxystrobin or untreated 5 days after inoculation with *Colletotrichum* isolates

Table 4 Percentage of identity of rDNA-ITS nucleotide sequence after NCBI BLAST analysis.

Host	Plant organ	Isolate code	Identity (%)	Species
chili	fruits	CC004	99	<i>C. acutatum</i>
		CC005	100	<i>C. acutatum, C. scovillei</i>
		CC007	99-100	<i>C. acutatum, C. aescynomene, C. boninense, C. fructicola, C. gloeosporioides, C. nupharicola, C. siamense, C. viniferum</i>
mango	fruits	CM_S013	99-100	<i>C. gloeosporioides</i>
		CM_C019	99	<i>C. asianum C. gloeosporioides</i>
		CM_C020	99	<i>C. asianum C. gloeosporioides</i>
		CM_002	99-100	<i>C. gloeosporioides</i>
		C1_m05	99-100	<i>C. asianum, C. fructicola, C. gloeosporioides</i>
		C1_m06	100	<i>C. asianum, C. gloeosporioides</i>
		C1_m07	99-100	<i>C. asianum, C. gloeosporioides</i>
		C1_m08	99-100	<i>C. asianum, C. boninense, C. gloeosporioides</i>
		C1_m10	99-100	<i>C. gloeosporioides C. queenslandicum, C. siamense, C. tropicale,</i>
		C1_m31	99-100	<i>C. alatae, C. gloeosporioides, C. siamense, C. tropicale, Glomerella cingulata,</i>
		C1_m32	99-100	<i>C. alatae, C. gloeosporioides, C. siamense, C. tropicale G. cingulata</i>
		C1_m33	99	<i>C. gloeosporioides, C. siamense, C. tropicale</i>
		C1_m35	99-100	<i>C. queenslandicum, G. cingulata</i>
		C1_m36	99-100	<i>C. gloeosporioides, C. siamense</i>
leaves	leaves	C1_m37	99-100	<i>C. gloeosporioides, C. musae</i>
		C1_m38	100	<i>C. gloeosporioides, C. musae</i>
		C1_m02	99-100	<i>C. asianum, C. gloeosporioides</i>
Crinum lily	leaves	C1_cl39	99-100	<i>C. alienum, C. endomangiferae C. gloeosporioides, C. siamense, G. cingulata</i>
		CO010	99	<i>C. siamense, C. queenslandicum, C. gloeosporioides</i>
orange	fruits	CO010	99	<i>C. siamense, C. queenslandicum, C. gloeosporioides</i>
orchid	leaves	C1_or40	98-99	<i>C. coelogynes, C. cordylinicola, C. tropicicola</i>

anthracnose of chili in Thailand, Brazil, China and Malaysia [26, 27]. *C. fructicola* was reported to be associated with chili anthracnose in China, India, and Malaysia [26, 27] and *C. viniferum* associated with chili anthracnose in China [26, 27]. However, 24 *Colletotrichum* species have been identified as the pathogen of chili anthracnose from different countries and regions [26, 27].

In mango anthracnose, the isolates CM_S013 and CM_002 were *C. gloeosporioides* with 99-100% identity. Moreover, five isolates (CM_C019, CM_C020, C1_m02, C1_m06, and C1_m07) were associated with *C. asianum* and *C. gloeosporioides* with 99-100% identity. Moreover, other species were identified with 99-100% identity including *C. alatae*, *C. boninense*, *C. fructicola*, *C. musae*, *C. queenslandicum*, *C. siamense*, and *C. tropicale* [Table 4]. Several *Colletotrichum* species such as *C. gloeosporioides* and *C. asianum* are well known as the pathogen of a mango anthracnose in Thailand and many countries of mango producers [29-33]. Moreover, *C. siamense* and *C.*

fructicola were reported from mango, too [29, 34, 35]. In this study, eleven isolates with azoxystrobin resistance were associated with several *Colletotrichum* species. High level of genetic variability among the *Colletotrichum* isolates from mango was reported by de Souza *et al.* [31]. However, comparison of the rDNA-ITS sequence alone is not always satisfactory to separate *Colletotrichum* species [36]. Therefore, the precise identification of *Colletotrichum* species needs to be conducted using multi locus phylogenetic analysis [28, 37] in the future.

4. Conclusions

The present study first revealed the development of QoI resistance in *Colletotrichum* species isolated from anthracnose-infected mango fruits and crinum lily in Thailand. The detection of resistant phenotypes in pathogen populations is the first step for effective disease control. The use of QoIs in mango should be carefully reconsidered in the management of anthracnose. It could contribute to prevent the further development of QoI-resistant pathogen populations by altering fungicide application programmes. Future studies should be focused on the wide-range of QoI resistance monitoring and identification of *Colletotrichum* species.

5. Acknowledgements

The authors express the sincere appreciation to Dr. Dusanee Thanaboripat, Mr. Sakrin Boonlum, and Ms. Wasinee Thamsatit, Faculty of Science and Prince of Chumphon Campus, King Mongkut's Institute of Technology Ladkrabang, Thailand for supporting this study.

References

- [1] Than, P.P., Prihastuti, H., Phoulivong, S., Taylor, P.W.J. and Hyde, K.D., 2008. Chilli anthracnose disease caused by *Colletotrichum* species. *Journal of Zhejiang University, Science B*, 9, 764-778.
- [2] Prihastuti, H., Cai, L., Chen, H., McKenzie, E.H.C. and Hyde, K.D., 2009. Characterization of *Colletotrichum* species associated with coffee berries in northern Thailand. *Fungal Diversity*, 39, 89-109.
- [3] Kuenpech, W. and Akarapisan, A., 2014. Biological control of anthracnose disease in Lady's Slipper using *Bacillus subtilis* isolate B6. *Journal of Agricultural Technology*, 10, 449-457.
- [4] Photita, W., Taylor, P.W.J., Ford, R., Hyde, K.D. and Lumyong, S., 2005. Morphological and molecular characterization of *Colletotrichum* species from herbaceous plants in Thailand. *Fungal Diversity*, 18, 117-133.
- [5] Chantrasri, P., 2019. *Control of Anthracnose Disease in Mango Orchard*. Science and Technology Research Institute. [online] Available at: https://stri.cmu.ac.th/article_detail.php?id=11.
- [6] Plant Protection Group, Nakhon Si Thammarat Provincial Agricultural Extension Office, 2013. *Dried Chili Disease or Anthracnose*. News of forecasting epidemics and pests. [online] Available at: <http://www.nakhonsri.doea.go.th/web/files/antrac.pdf>.
- [7] Fungicide Resistance Action Committee, 2018. *FRAC Code List ©*2018: Fungicides sorted by mode of action*. [online] Available at: <http://www.phi-base.org/images/fracCodeList.pdf>.

- [8] Kongtragoul, P., Nalumpang, S., Miyamoto, Y., Izumi, Y. and Akimitsu, K., 2011. Mutation at codon 198 of *Tub2* gene for carbendazim resistance in *Colletotrichum gloeosporioides* causing mango anthracnose in Thailand. *Journal of Plant Protection Research*, 51, 377-384.
- [9] Nalumpang, S., Miyamoto, Y., Miyake, C., Izumi, Y., Akitmitsu, K. and Kongtragoul, P., 2010. Point mutations in the beta-tubulin gene conferred carbendazim-resistant phenotypes of *Colletotrichum gloeosporioides* causing 'Nam Dok Mai' mango anthracnose. *International Journal of Agricultural Technology*, 6, 365-378.
- [10] Fernández-Ortuño, D., Torés, J.A., de Vicente, A. and Pérez-García, A., 2008. Mechanisms of resistance to QoI fungicides in phytopathogenic fungi. *International Microbiology*, 11, 1-9.
- [11] Gisi, U., Sierotzki, H., Cook, A. and McCaffery, A., 2002. Mechanisms influencing the evolution of resistance to Qo inhibitor fungicides. *Pest Management Science*, 58, 859-867.
- [12] Sierotzki, H., Wullschleger, J. and Gisi, U., 2000. Point mutation in cytochrome b gene conferring resistance to strobilurin fungicides in *Erysiphe graminis* f sp. *tritici* field isolates. *Pesticide Biochemistry and Physiology*, 68, 107-112.
- [13] Office of Agricultural Economics, 2018. *Quantity and value of imports of agricultural hazardous substances in 2011-2017*. [online] Available at: <http://oldweb.oae.go.th/economicdata/pesticides.html>.
- [14] Avila-Adame, C., Olaya, G. and Köller, W., 2003. Characterization of *Colletotrichum graminicola* isolates resistant to strobilurin-related QoI fungicides. *Plant Disease*, 87, 1426-1432.
- [15] Inada, M., Ishii, H., Chung, W.H., Yamada, T., Yamaguchi, J. and Furuta, A., 2008. Occurrence of strobilurin resistant strains of *Colletotrichum gloeosporioides* (*Glomerella cingulata*), the causal fungus of strawberry anthracnose. *Japanese Journal of Phytopathology*, 74, 114-117.
- [16] Wong, F.P., Midland, S.L. and Karla, A.C., 2007. Occurrence and distribution of QoI-resistant isolates of *Colletotrichum cereale* from annual bluegrass in California. *Plant Disease*, 91, 1536-1546.
- [17] Young, J.R., Tomaso-Peterson, M., Tredway, L.P. and Cerdá, K., 2010. Occurrence and molecular identification of azoxystrobin resistant *Colletotrichum cereale* isolates from golf course putting greens in the southern United States. *Plant Disease*, 94, 751-757.
- [18] Hu, M.J., Grabke, A., Dowling, M.E., Holstein, H.J. and Schnabel, G., 2015. Resistance in *Colletotrichum siamense* from peach and blueberry to thiophanate-methyl and azoxystrobin. *Plant Disease*, 99, 806-814.
- [19] Forcelini, B.B., Seijo, T.E., Amiri, A. and Peres, N.A., 2016. Resistance in strawberry isolates of *Colletotrichum acutatum* from Florida to quinone-outside inhibitor fungicides. *Plant Disease*, 100, 2050-2056.
- [20] Piccirillo, G., Carrieria, R., Polizzib, G., Azzaroc, A., Lahoza, E., Fernández-Ortuño, D. and Vitaleb, A., 2018. *In vitro* and *in vivo* activity of QoI fungicides against *Colletotrichum gloeosporioides* causing fruit anthracnose in *Citrus sinensis*. *Scientia Horticulturae*, 236, 90-95.
- [21] Torres-Calzada, C., Tapia-Tussell, R., Higuera-Ciapara, I., Martin-Mex, R., Nexticapan-Garcez, A. and Perez-Brito, D., 2015. Sensitivity of *Colletotrichum truncatum* to four fungicides and molecular characterization of thiabendazole-resistant isolates. *Plant Disease*, 99, 1590-1595.
- [22] Kim, S., Min, J., Back, D., Kim, H., Lee, S. and Kim, K., 2016. Assessment of QoI resistance in *Colletotrichum* spp. isolated from boxthorn and apple in Korea. *Phytopathology*, 106 (Suppl. 12), 71.
- [23] Saitoh, K., Togashi, K., Arie, T. and Teraoka, T., 2006. A simple method for a mini-preparation of fungal DNA. *Journal of General Plant Pathology*, 72, 348-350.

- [24] Ishii, H., Zhen, F., Hu, M., Li, X. and Schnabel, G., 2016. Efficacy of SDHI fungicides, including benzovindiflupyr, against *Colletotrichum* species. *Pest Management Science*, 72, 1844-1853.
- [25] White, T.J., Bruns, T., Lee, S. and Taylor, J., 1990. Amplification and direct sequencing of fungal ribosomal RNA genes for phylogenetics. In: Innis, M.A., Gelfand, D.H., Sninsky, J.J. and White, T.J. eds. *PCR Protocols: A Guide to Methods and Applications*. Academic Press, New York, pp. 315-322.
- [26] Mongkolporn, O. and Taylor, P.W.J., 2018. Chili anthracnose: *Colletotrichum* taxonomy and pathogenicity. *Plant Pathology*, 67, 1255-1263.
- [27] De Silva, D.D., Ades, P.K., Crous, P.W. and Taylor, P.W.J., 2016. *Colletotrichum* species associated with chili anthracnose in Australia. *Plant Pathology*, 66, 254-267.
- [28] Noor, N.M. and Zakaria, L., 2018. Identification and characterization of *Colletotrichum* spp. associated with chili anthracnose in peninsular Malaysia. *European Journal Plant Pathology*, 151, 961-973.
- [29] Phoulivong, S., Cai, L., Chen, H., McKenzie, H.E.H.C., Abdelsalam, K., Chukeatirote, E. and Hyde, K. D., 2010. *Colletotrichum gloeosporioides* is not a common pathogen on tropical fruits. *Fungal Diversity*, 44, 33-43.
- [30] Sharma, G., Gryzenhout, M., Hyde, K.D., Pinnaka, A.K. and Shenoy, B.D., 2015. First report of *Colletotrichum asianum* causing mango anthracnose in South Africa. *Plant Disease*, 99, 725.
- [31] de Souza, A., Delphino Carboni, R.C., Wickert, E., de Macedo Lemos, E.G. and de Goes, A., 2013. Lack of host specificity of *Colletotrichum* spp. isolates associated with anthracnose symptoms on mango in Brazil. *Plant Pathology*, 62, 1038-1047.
- [32] Rakesh, P.K. and Singh, R., 2017. Anthracnose of mango incited by *Colletotrichum gloeosporioides*: A comprehensive review. *International Journal of Pure & Applied Bioscience*, 5, 48-56.
- [33] Krishnapillai, N. and Wilson Wijeratnam, R.S., 2014. First Report of *Colletotrichum asianum* causing anthracnose on Willard mangoes in Sri Lanka. *New Disease Reports*, 29, 1.
- [34] Mo, J., Zhao, G., Li, Q., Solangi, G.S., Tang, L., Guo, Tangxun and Huang, S., 2018. Identification and characterization of *Colletotrichum* species associated with mango anthracnose in Guangxi, China. *Plant Disease*, 102, 1283-1289.
- [35] Lima, N.B., Batista, M.V.D.A., De Moraes Jr, M.A., Barbosa, M.A.G., Michereff, S.J., Hyde, K.D. and Câmara, M.P.S., 2013. Five *Colletotrichum* species are responsible for mango anthracnose in northeastern Brazil. *Fungal Diversity*, 61, 75-88.
- [36] Cannon, P.F., Damm, U., Johnston, P.R. and Weir, B.S., 2012. *Colletotrichum* - current status and future directions. *Studies in Mycology*, 73, 181-213.
- [37] He, L., Li, X., Gao, Y., Li, B., Mu, W. and Liu, F., 2019. Characterization and fungicide sensitivity of *Colletotrichum* spp. from different hosts in Shandong, China. *Plant Disease*, 103, 34-43.

Semi-Automated Method to Extract Urban Areas from Barren Land/ Bare Soil, Case Study: Idku, Nile Delta Coast, Egypt

Hanady H. Khalil* and Mahmoud Hassaan

Institute of Graduate Studies and Research, Alexandria University, Alexandria, Egypt

Received: 8 July 2019, Revised: 26 November 2019, Accepted: 3 December 2019

Abstract

Optical remote sensing offers a time and cost-effective manner to monitor urban-form expansion over time. The availability of recent and historical remote sensing data together with the wide coverage of these data make remote sensing application further favorable for the purpose. However, urban areas surrounded by barren land/ bare soil tend to be overestimated due to the similar spectral behavior of both urban areas and their surroundings. This paper aims to develop a methodology that overcomes the interference between urban areas and barren land/ bare soil and thus enhances the urban areas' extraction in a semi-automated manner. For this purpose, SAVI, NDBI and MNDWI indices, PCA and thermal band were employed to extract urban areas from their surroundings in two Landsat images for the years 1998 and 2016. The developed methodology was applied to extract urban form of Idku Town, one of the coastal urban centers of the Nile Delta, with an overall accuracy of 96.48% and 93.39% for the images of 1998 and 2016, respectively. The results have revealed that the urban form of Idku Town was tripled over the last two decades with an annual growth rate of about 12%.

Keywords: urban-form, Barren land, bare soil, remote sensing
DOI 10.14456/cast.1477.9

1. Introduction

Unplanned rapid urban expansion and its associated change in land use/land cover pattern place a heavy burden on environmental resources and have serious environmental consequences, for example, urban expansion usually alters local climate (usually referred to as microclimate), creates heat island effect and accordingly increases energy demand and costs of new infrastructure [1-10]. Therefore, regular and continued monitoring of urban-form expansion is required [11-13] to predict urban growth, to understand its dynamics, to define energy needs and to learn about changes in microclimate. Monitoring urban-form expansion starts with delineating urban areas out of their surroundings in a fast and cost-effective manner. Delineating urban areas is a basic step in many researches especially those related to heat islands, microclimate and climate change [7].

*Corresponding author: Tel.: +203 424-9290 Fax: +203 424-9290
E-mail: hanady.h.khalil@gmail.com

Optical remote sensing provides a reliable mapping of urban areas through many techniques including automated and semi-automated techniques [14, 15]. Due to the dynamic nature of urban areas expansion, applying conventional approaches in monitoring urban expansion such as aerial photography, surveys and/or cartography is questionable. This is because they are usually time, money and effort consuming in addition to their unavailability over long time span in many cases [11, 12]. Instead, remotely-sensed data provides a powerful source of knowledge in monitoring rapid urban expansion over long periods of time. For this reason, remote sensing imagery has been used repeatedly in monitoring and assessing urban expansion and consequent changes in land use/land cover through discriminating urban land from non-urban land in a fast and cost-effective manner [16, 17].

Delineating urban areas from remote sensing imagery depends mainly on their spectral behavior that, in turn, determined by their physical characteristics and chemical composition. Thus, it is important to understand the physical characteristics of urban areas that govern their spectral behavior in order to distinguish them as a first step towards identifying their spatial extent and quantifying their development through remotely sensed data [12].

There are two distinguished approaches to extract urban areas from remote sensing data which are classification techniques [18, 19] and spectral indices [20, 21]. Both of these approaches depend on the spectral behavior of different land covers, but they work differently. Both have their advantages and limitations but indices have a virtue over classification in terms of time needed to generate them [22]. Classification techniques are laborious, time-consuming and expert-dependent techniques. Moreover, there is a problem in differentiating urban areas and barren land/ bare soil under classification techniques as both have similar response at some places leading to overestimation of urban lands [7]. Spectral indices are favorable and frequently employed to enhance a desired land cover in order to detect its changes over time. The powerful point about indices is that they are selective, fast and easy to implement and totally automated. Indices use the spectral response of a certain land cover to enhance and manifest it on the expense of other land covers. Normal Difference Water Index (NDWI) and Modified Normal Difference Water Index (MNDWI) [17, 23] are examples of these selective indices as they make water bodies much more remarkable on the expense of vegetation and land. The same goes for other indices such as Normal Difference Vegetation Index (NDVI) [24], Soil-Adjusted Vegetation Index (SAVI) [25] and Normal Difference Built-up Index (NDBI) [17, 20, 21]. Each of these indices focus on the desired land cover and make it easier to be extracted and make it possible to identify different classes related to this particular land cover in a relatively higher accuracy.

Many indices, such as NDBI, have been developed to enhance built-up areas in order to extract them in an automated manner. Although NDBI enhances the urban areas in a notable manner, it has its limitations when the scene contains barren land/ bare soil, dry vegetation and/or water of high-suspended matter. Urban areas tend to mix up with barren land/ bare soil leading to overestimation of built-up areas [3, 7, 9, 14, 15]. Likewise, some vegetation and water surfaces under certain conditions may give positive value in the NDBI and hence misclassified as urban areas [17].

Despite the limitations of NDBI, it still works well to separate built-up and barren land from other land covers (water and vegetation). Yet, mapping urban areas out of barren lands through such an index is challenging due to the similarity in spectral behavior of both [3, 7, 9, 14, 15] especially in Mediterranean cities as they have very low vegetation cover in rural areas, scarce rains and land covers lacking moisture [7]. Therefore, there is always a need for improved techniques considering the similarity of urban areas spectral response with their adjoining barren land/ bare soil. Several studies suggested that NDBI should not be used alone but in a combination with NDVI and NDWI [15, 17, 26] to enhance its performance.

The purpose of this paper is to develop a systematic, semi-automated methodology to extract urban areas out of barren land/ bare soil areas using remote sensing data and to detect the

long-term change in urban-form. The developed methodology is applied to one of the Nile Delta coastal urban areas; Idku Town, Egypt.

2. Materials and Methods

2.1 Study area

Idku Town is one of the Egyptian urban centers located in the coastal zone of the Nile Delta. As many of the Mediterranean coastal towns [7], it undergoes rapid population growth and rapid expansion of urban areas in an undersigned manner mostly. The urban environment in Idku is characterized by high densities in the south adjacent to the road and moderate to low densities and mixed land-uses as approaching the Mediterranean coastal barren land/ bare soil. The town has been expanding rapidly during the last two decades. Such rapid expansion was largely motivated by transportation network development and population growth. The physical setting of the surrounding landscape is mostly barren land/bare soil (Figure 1).



Figure 1. Situation of Idku Town

2.2 Data source

To detect changes in the urban areas in Idku, two multi-temporal Landsat images are used with a time span of 18 years (Table 1). The Idku Town is covered by the scenes of path 177 and row 38. Both scenes are cloud-free and high quality. No atmospheric correction has been performed for the data. Sub-scenes covering the Idku Town and its surroundings are clipped from the original scenes for data analysis.

Table 1. Landset scene metadata

Year	Satellite	Sensor	Path	Row	Date
1998	Landsat 5	TM	177	38	11-04-1998
2016	Landsat 8	OLI/TIRS	177	38	18-04-2016

2.3 Methodology

The developed methodology is based on separating urban areas from their surrounding barren land and bare soil through utilizing the thermal band. It is well-known that urban areas can cause land surface temperature (LST) to increase in a phenomenon known as “heat island” [2, 9]. Such urban heat island can be used to better separate built-up areas from other land covers [22] such as water and vegetation. But barren land and bare soil emit more energy in the thermal band compared to the built-up areas. Therefore, applying a careful threshold can separate both. The difference in emitted heat between both of them is not huge but it is sufficient to define a threshold.

The extraction process of the built-up areas can be performed according to the following steps which are illustrated in Figure 2:

Step 1: Generate the indices images

There are three general land covers in the sub-scene image which are vegetation, land and water. These land covers are enhanced using specified indices which depend mostly on the spectral properties of these land covers (Figure 3). Three indices were used to reduce the redundancy of multispectral data and maximize the difference among different land covers. These indices are: Soil-Adjusted Vegetation Index (SAVI), Normal Difference Built-up Index (NDBI) Modified Normal Difference Water Index (MNDWI). The multispectral bands of each image are used to generate the three indices: SAVI, NDBI and MNDWI using the equations given in Table 2. Therefore, each multispectral image would generate three images each of which represented one of the up mentioned indices. SAVI was used to discriminate vegetation from soil. It is considered to be a better replacement for the well-known Normal Difference Vegetation Index (NDVI) because it is more sensible for the low plant cover as in built up areas [17] and in low vegetated agricultural land. SAVI can discriminate vegetation in an area of plant cover as low as 15%, whereas NDVI can only discriminate vegetation effectively in an area when the plant cover is higher than 30% [25]. SAVI has more advantage of the remarkable reflection of vegetation in the near infrared (NIR) region of the spectrum when compared to the red one. In the used sub-scenes, the vegetation cover is moderate, therefore, a value of 0.5 was assigned to the “I” term in the SAVI equation. NDBI has the advantage of the unique response of the built-up areas in which they have higher response in the middle infrared (MIR) than in the NIR [20] to discriminate them from their surroundings. This would hold true in areas of healthy vegetation and water bodies. However, some vegetation under certain circumstances of dryness would have high values in MIR and sometimes even higher than in the NIR resulting in positive values under the NDBI [27, 28] and get confused for the urban areas. The same goes for barren land/bare soil and accordingly they are misclassified as built-up areas, which is the case in our case study. MNDWI developed by Xu [29], was employed to enhance the NDWI to better discriminate between water and built-up areas as both reflect green light more than reflect NIR light [17]. MNDWI used the MIR instead of the NIR in the NDWI (Table 2).

Step 2: Replace the multispectral image by the different indices' images

The multispectral data with their high redundancy is replaced by indices so that the differences among the major land covers are maximized.

Step 3: Apply principal component analysis (PCA) to the indices' images

Principal Component Analysis (PCA) is used to reduce the interference among different land covers produced by the three indices. The three indices' images represent the input for the PCA

to generate three principal components (PCs). The first principal component (PC1) contains most of the data (about 90% of the data) then followed by the second and third principal components (PC2 and PC3). The amount of data contained in each PC is given in Table 3.

Step 4: Choose the PC in which the land is most discriminated from other features

Out of the three PCs, there is one PC image in which the land features are more discriminated than both water and vegetation. This would appear in one of the PCs as areas of either remarkable brightness or darkness according to the sign of its value (if the sign is positive, land features would appear as bright areas while negative value means dark areas). The PC that reveals the land sharply either in positive or negative values (bright or dark features, respectively) was selected. Determining the suitable PC could be attained by analyzing the Eigen vectors and Eigen values for each date. In the chosen PC, land features would have an Eigen vector with a sign that is opposite to those of both water and vegetation.

Step 5: Separation of land

The chosen PC was then employed to extract the built-up areas in an automated manner by the means of applying a threshold [17]. By applying a careful threshold on the chosen PC image, the land areas which contain both built-up areas and barren land/bare soil, are separated from both water and vegetation. The resulting image would be a land-only image.

Step 6: Generate a mask image out of the land-only image

The land-only image was converted into a binary image in which all values of land are given as a value of 1 and elsewhere as a value of 0.

Step 7: Extract the thermal values corresponding to the land

The generated mask was multiplied by the thermal band of the original data (band 6 for 1998 image and band 10 for 2016 TIRS image) to generate an image which contains the thermal range of land. In the land-thermal-range image, the built-up areas would appear darker than the barren land/bare soil areas.

Step 8: Extract the built-up areas

By applying a careful threshold on the thermal values of land, land class is separated into two subclasses: built-up areas and barren land/bare soil areas. The difference between the thermal values of the built-up areas and the barren land/bare soil is not huge but it is enough to differentiate between them. The threshold choice in this step is crucial and requires a great deal of attention. The built-up areas are given a value of 1 and elsewhere in the image is given the value of 0. The resulting image represents the built-up areas with a minimal noise from barren land/bare soil.

Finally, the accuracy of the resulted thematic images was assessed using 256 randomly distributed points. The same exact points have been employed for both images. Visual interpretation has been applied to check on the points using False Color Composite (30 m) of RGB 7, 5, 2 for the L5, 1998 image and a High Pass Filter (HPF) panchromatic sharpened image (15 m) with RGB 7, 5, 2 for the L8, 2016 image.

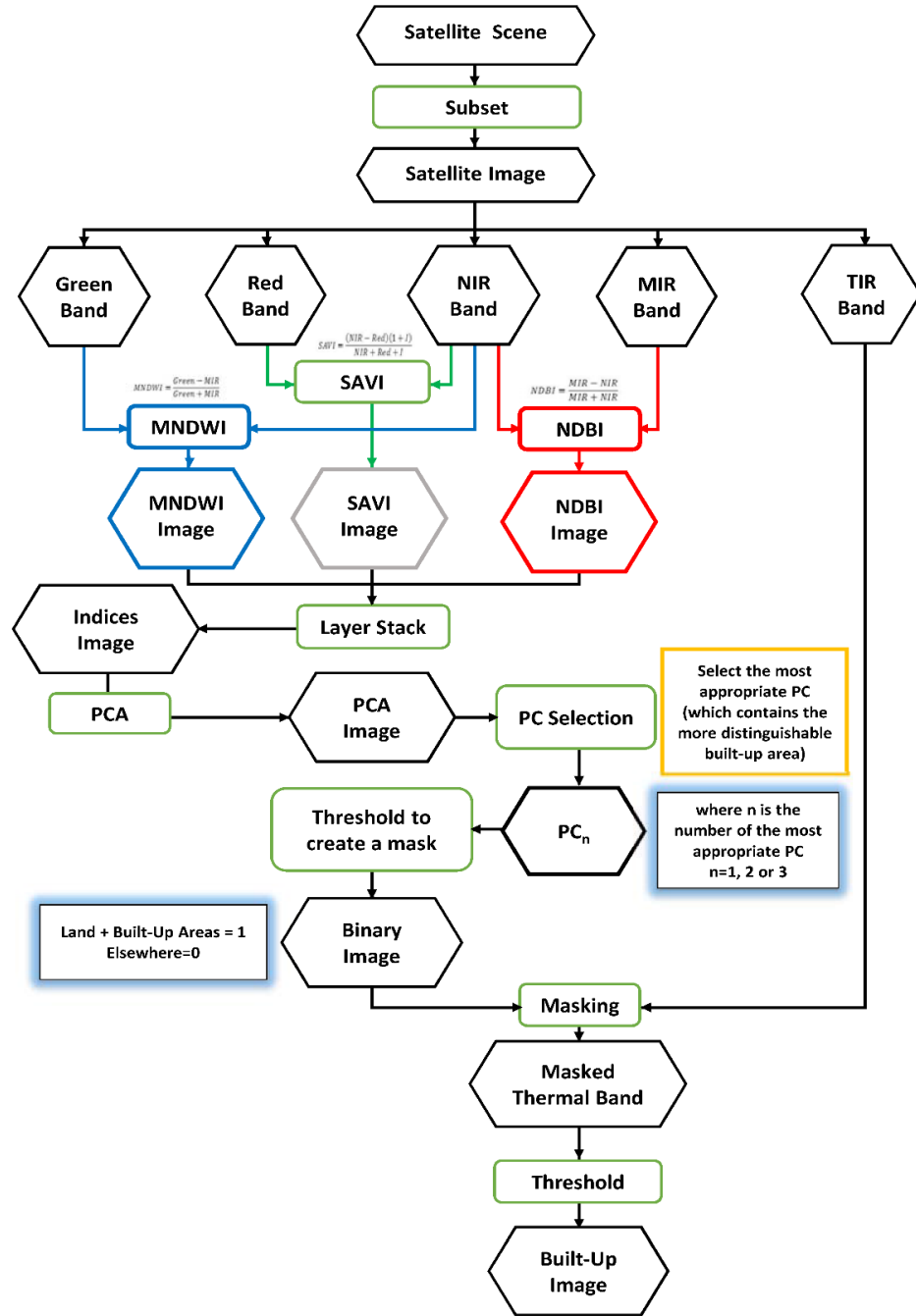


Figure 2. Methodology for semi-automated built-up area extraction

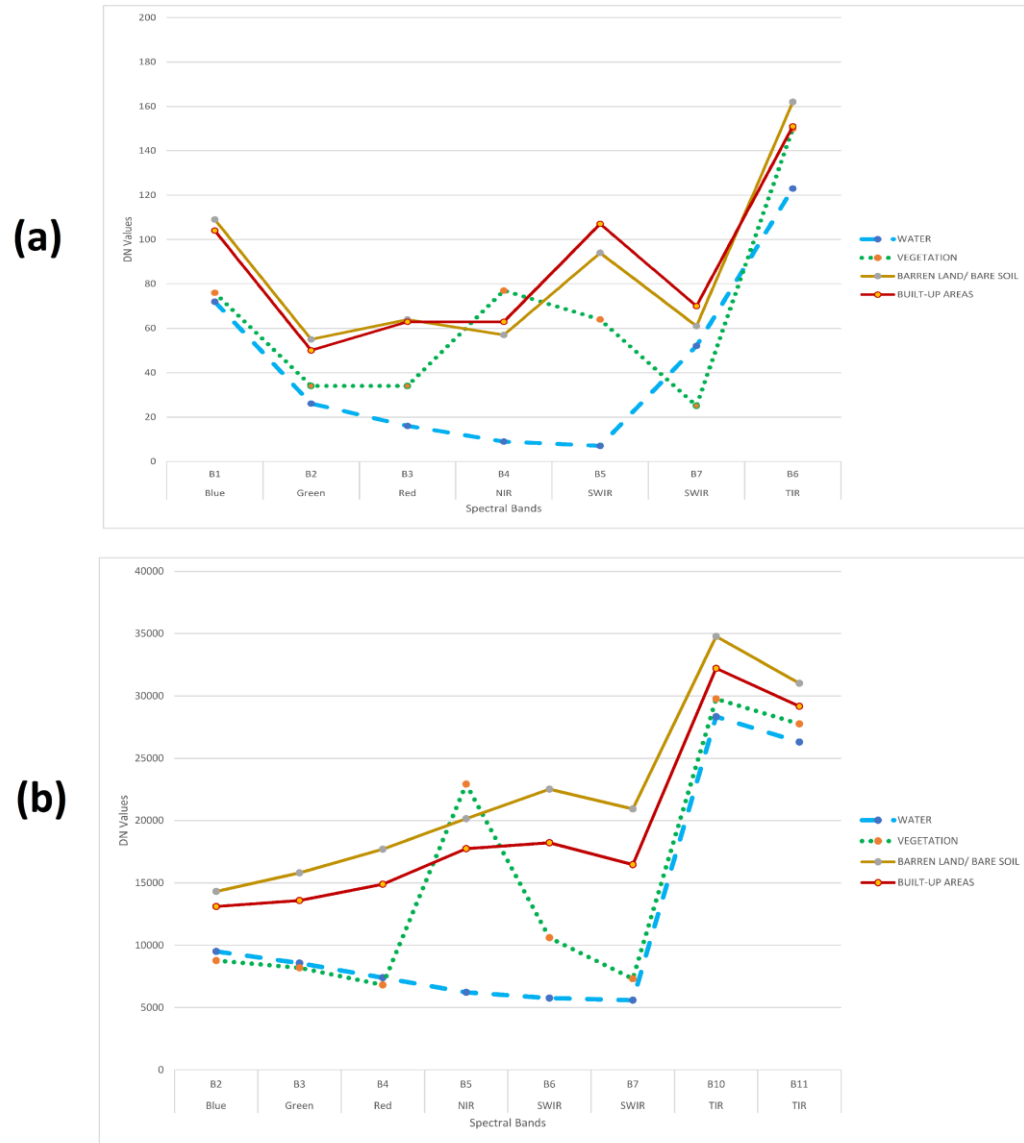


Figure 3. Spectral signatures of different land covers for (a) L5 TM image for the year 1998 and (b) L8 OLI/TIRS image for the year 2016

Table 2. Different indices and the formulae used to generate them

Indices	Formulae	Reference
SAVI	$SAVI = \frac{(NIR - Red)(1 + I)}{NIR + Red + I}$	[25]
	Where I is a correction factor that ranges from 0 (in case of dense vegetation cover) to 1 (in case of lack of vegetation or a very low vegetation cover).	
NDBI	$NDBI = \frac{MIR - NIR}{MIR + NIR}$	[20]
MNDWI	$MNDWI = \frac{Green - MIR}{Green + MIR}$	[27]

3. Results and Discussion

The three-indices images for the years 1998 and 2016 are illustrated in Figure 4 whereas Table 3 shows the Eigen vector and Eigen values of the principal component analysis of the multi-temporal indices. The second principle component (PC2) is the one in which built-up areas are most distinguished from water and vegetation as the different sign indicates. The positive sign of the NDBI Eigen vector indicates areas of brightness in the PC 2 whereas negative values of SAVI and MNDWI Eigen vectors indicate areas of darkness (Figure 5).

Table 3. Eigen vector and eigen values of the principal component analysis of the multi-temporal indices

	INDICES IMAGES	1998			2016		
		PC1	PC 2	PC 3	PC1	PC 2	PC 3
Eigen Vectors	SAVI	0.74	-0.53	0.42	0.89	-0.18	0.43
	NDBI	0.07	0.68	0.73	-0.24	0.60	0.76
	MNDWI	-0.67	-0.51	0.54	-0.40	-0.77	0.49
% Eigen Values		90.9	8.8	0.3	92.9	6.9	0.2

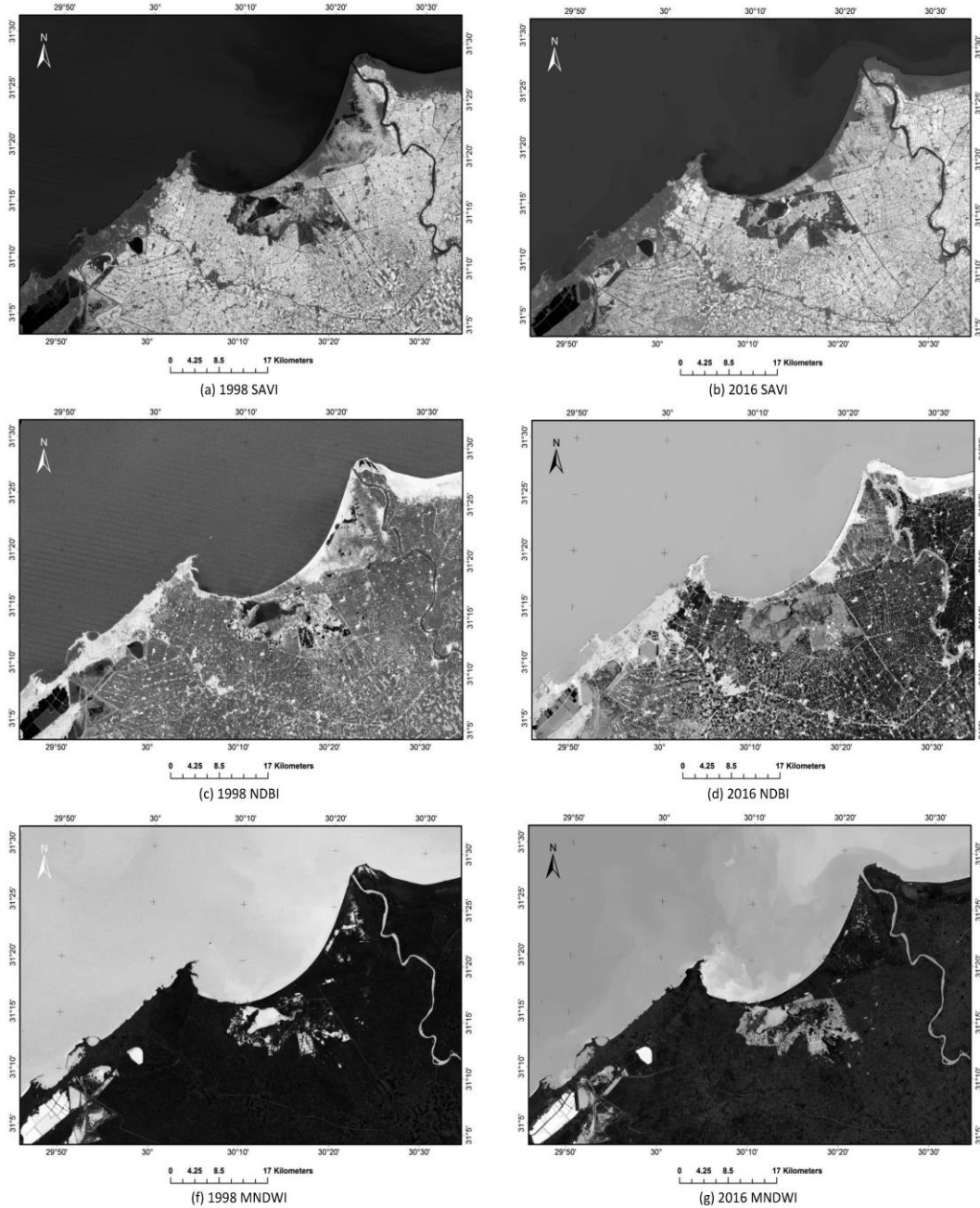


Figure 4. Indices images for multi-temporal sub-scenes

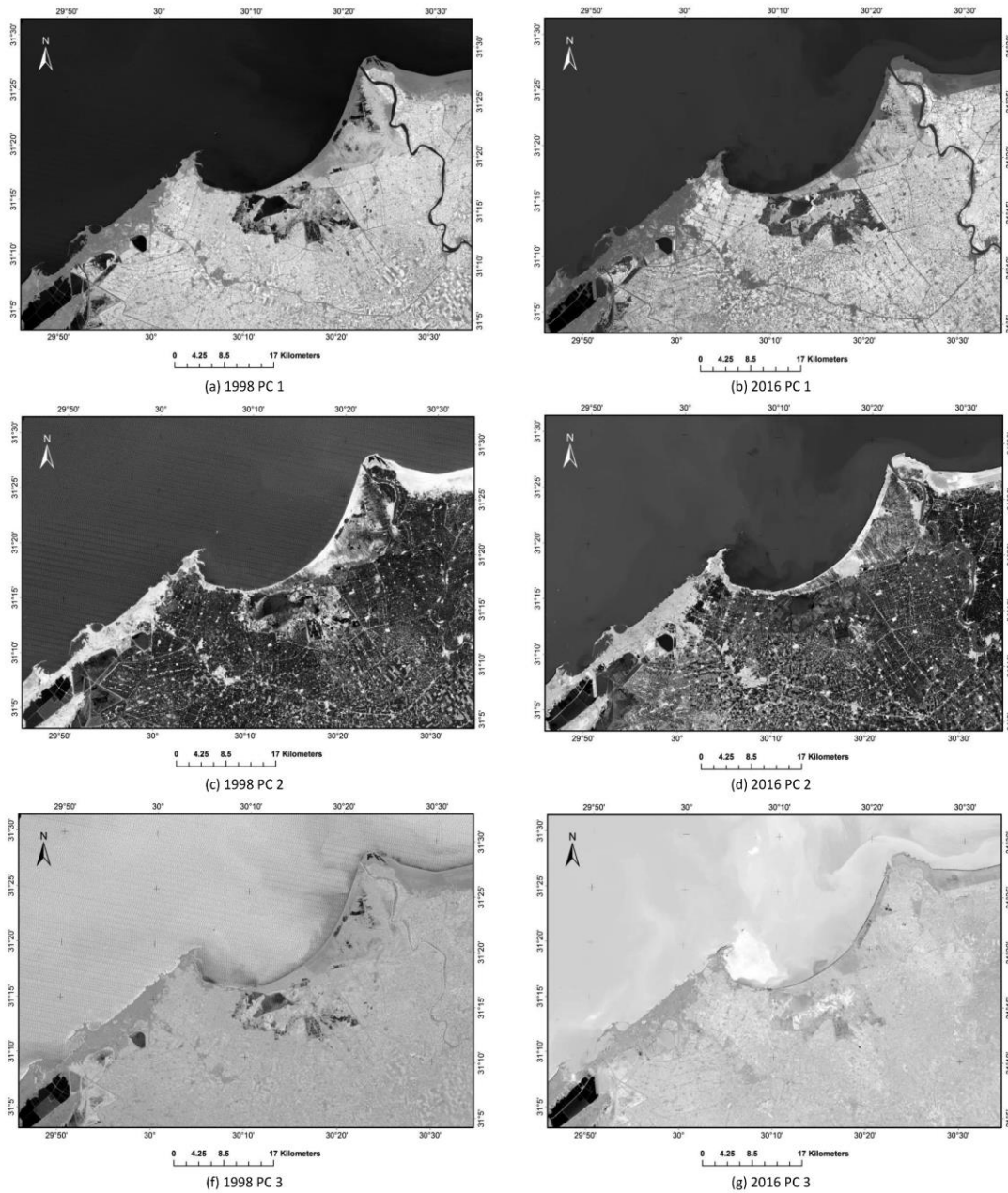


Figure 5. Principal component analysis (PCA) for the multi-temporal index images

Figure 6 shows the histograms of the second principal components (PC2s) of the indices' images for the years 1998 (a) and 2016 (b). The x-axis of the histogram represents the PC2 values while the y-axis refers to the frequency which means how many pixels are belonging to a certain value. The last peak of the histogram represents the values of the land as these values are the highest values of the image. The low frequency of the peak is due to the land that is not the dominating feature in the image. Applying a threshold to separate the values of the last peak would result in the separation of land values from the image. A threshold of 0.2 and a double threshold of 0.05 and 0.15 for the PC 2 of the 1998 and 2016 images, is applied to extract the land features as shown in Figure 6. Figure 7 shows the extracted land features for the multi-temporal sub-scenes. This method is successful in regard to extracting land features from water and vegetation. However, it can not differentiate between built-up areas and their adjoining barren land and bare soil. Therefore, the need for the thermal band integration arose.

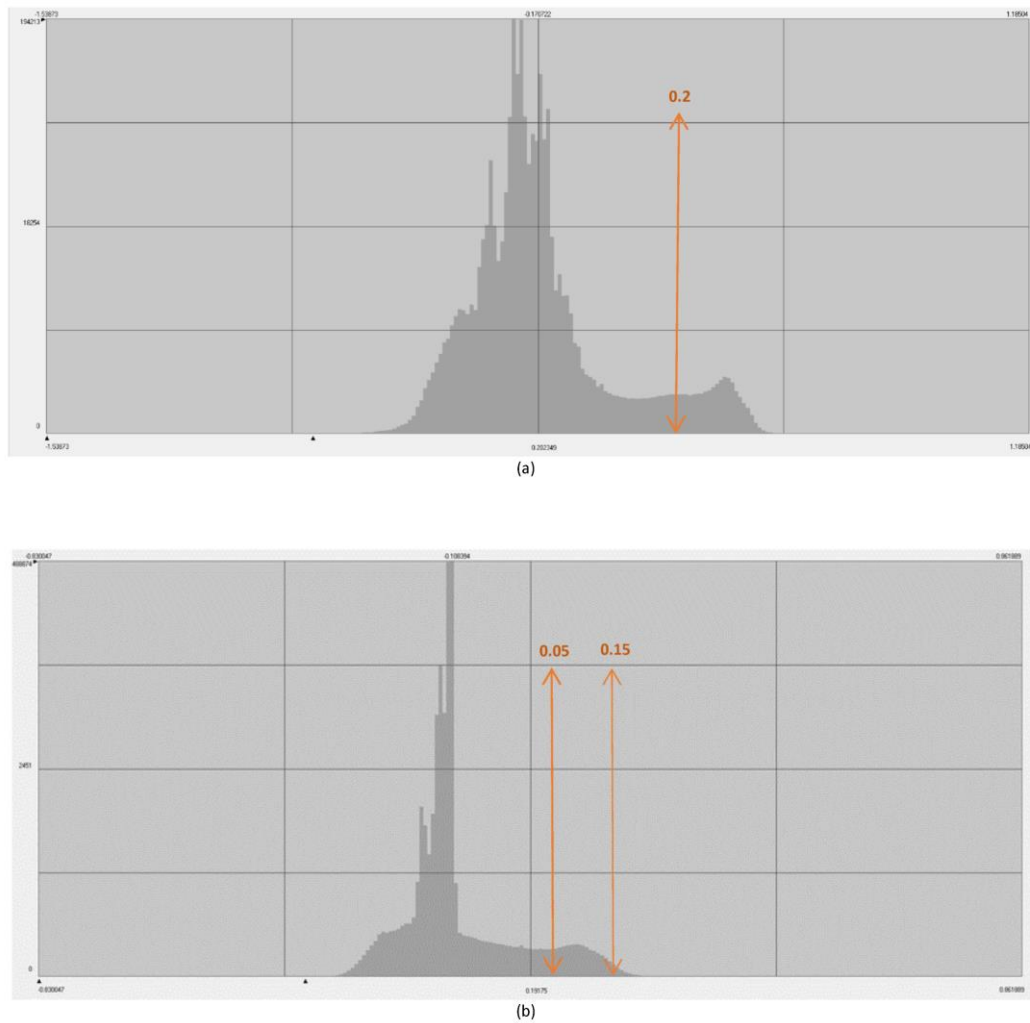


Figure 6. Histogram of the PC 2 with the threshold(s) for the years (a) 1998 and (b) 2016

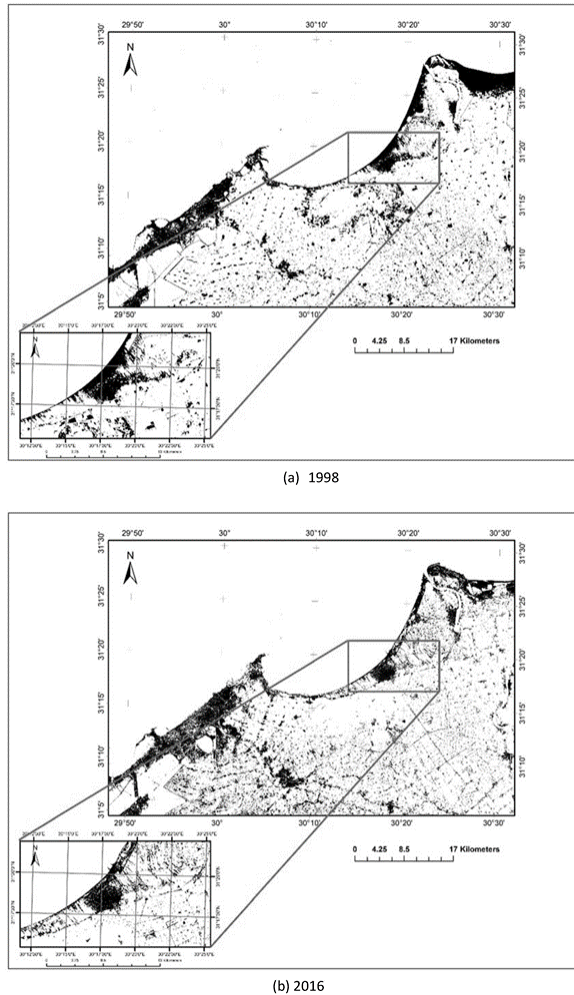


Figure 7. Extracted land features from the multi-temporal indices PC2 images for the years (a) 1998 and (b) 2016 and the Town of Idku is zoomed-in

The thermal values for the land features were separated in a new image (land-only thermal image). Then a threshold was applied to separate built-up areas and barren land/ bare soil. A double threshold has been assigned to extract thermal ranges of 152 to 157 and 29400 to 33800 out of the land thermal values of the years 1998 and 2016, respectively. These ranges have been found to be corresponding to built-up areas. The built-up areas' separation is thus much enhanced and the borders of the town is much more realistic (Figure 8). The idea behind the thermal band integration in differentiating built-up areas from barren land/bare soil is that built-up areas are coarse textured-areas reflecting more light than the smooth-natured barren land/ bare soil does. As built-up areas reflect more light, they are expected to emit less light. This is always the case; good reflectors are bad emitters and vice versa [28]. Although the proposed methodology is able to improve the extraction of the built-up areas, it can not totally eliminate barren land/bare soil from the scene, none of the methodologies does [7, 15, 17, 22]. But this methodology reduced the interference significantly and increased the accuracy of extraction remarkably.

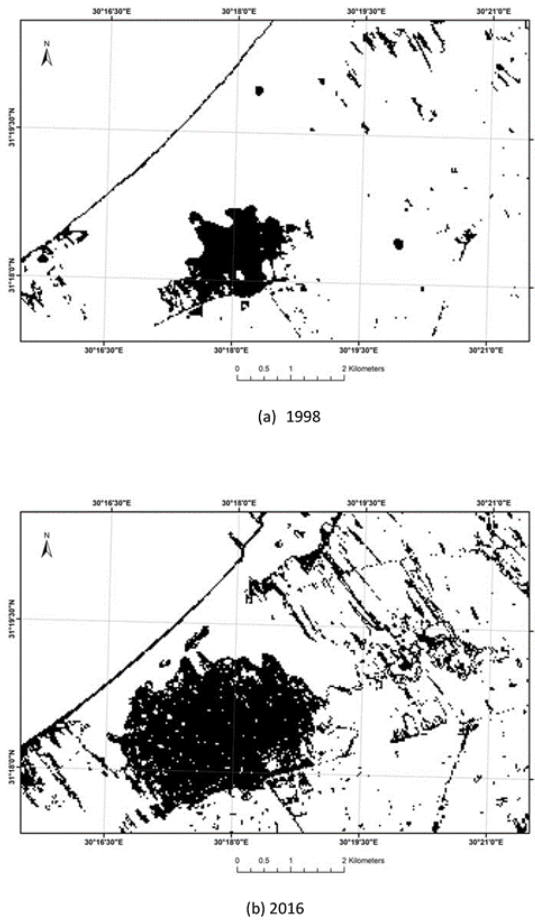


Figure 8. Idku Town as extracted by integrating the thermal band for the years (a) 1998 and (b) 2016

The overall accuracies were found to be 96.48% and 93.39% with overall Kappa statistics of 0.6488 and 0.7305 for the images of the years 1998 and 2016, respectively (Table 4). For the image of L8, 2016, the panchromatic sharpened image allowed better error avoidance during the accuracy assessment due to the relative easiness of visual interpretation compared to the unsharpened RGB image. Unfortunately, this was not the case for the L5, 1998 image due to the absence of the panchromatic band.

The coarse resolution of the thermal band compared to other multispectral bands (60 m for ETM+ and 100 m for TIRS) does not much affect the accuracy of estimation in this study as it is concerned with the urban form expansion of Idku Town. Therefore, the border of the town is what matters. Mixed pixels of concern would be restricted only to those on the margin of the town. These mixed pixels could be a source of error together with the different resolution of both L5 and L8 thermal bands but compared to the bulk urban area of the town, it would be much like applying a

filter to smooth its appearance. In case of using the same sensor, the error would be distributed evenly through different scenes and the changes in urban areas would still hold true.

Spatial analysis of urban form extracted from remotely-sensed data showed that the built-up area of Idku Town has expanded from 2502 km² in 1998 to 8003 km² in 2016. This means that the built-up area has enlarged three times its original area in 1998 with an annual expansion rate of about 12% during almost 20 years. Such rapid expansion can be related mainly to demographic deriving forces as well as the construction of new road infrastructure. For instance, the population size of Idku Town increased from 87,848 in 1996 to 97,168 in 2006 [29, 30]. In addition, it was noted that the town expansion during this time span was directed towards the northern parts of the town. This is mainly due to two reasons, i.e. the construction of the International Coastal Highway in the north of the town in 2002 and the existence of Idku lake in the south of the town which acts as a natural barrier that hinders town expansion southward (Figure 9).

Table 4. Summary of accuracy assessment results

Class Name	1998					2016				
	Urban	Non-Urban	Total	Overall Accuracy	Kappa	Urban	Non-Urban	Total	Overall accuracy	Kappa
Urban	9	7	16	96.48%	0.6488	28	16	44	93.39%	0.7305
Non-Urban	2	238	240			1	212	213		
Total	11	245	256			29	228	257		

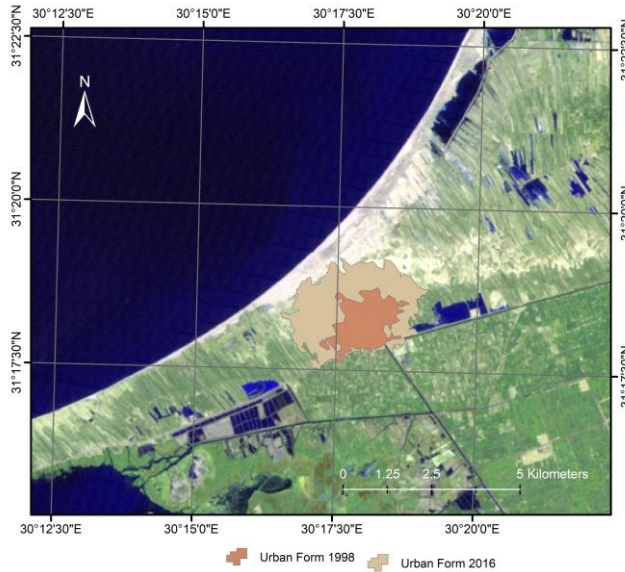


Figure 9. Urban Form Expansion from 1998 to 2016

4. Conclusions

It was revealed that the proposed methodology for delineating urban areas within barren land/ bare soil background in a semi-automated manner yielded satisfactory results. This developed methodology was capable of decreasing the high interference between the urban areas and their adjoining barren land/bare soil. The use of the thermal band to differentiate between these two classes was successful and increased the accuracy of the extraction in a remarkable manner. Furthermore, it was found that the coarse resolution of the thermal band compared to other multispectral bands (60 m for ETM+ and 100 m for TIRS) has marginal impact on the accuracy of estimation.

5. Acknowledgements

This research work is part of a research project sponsored by the IDRC-Canada for establishing Alexandria Research Center for Adaptation to Climate Change (ARCA) at Alexandria University, Egypt.

References

- [1] Bernstein, J.D., 1994. Land use considerations in urban environmental management In: Urban management programme discussion paper, UMPP no. 12. Washington D.C.: World Bank, pp. 9-26.
- [2] Gartland, L., 2008. Heat islands: understanding and mitigating heat in urban areas [e-book] London: Earthscan. [online]. Available at: <https://books.google.com.eg/books?id=wokqNDknbLIC>.
- [3] Jusuf, S.K., Wong, N.H., Hagen, E., Anggoro, R., and Hong, Y., 2007. The influence of land use on the urban heat island in Singapore. *Habitat International*, 31(2), 232-242.
- [4] Kim, H.H., 1992. Urban heat island. *International Journal of Remote Sensing*, 13(12), 2319-2336.
- [5] Lo, C.P., 2004. Testing urban theories using remote sensing. *GiScience & Remote Sensing*, 41(2), 95-115.
- [6] Oke, T.R., 1973. City size and the urban heat island. *Atmospheric Environment* (1967), 7(8), 769-779.
- [7] Polydoros, A. and Cartalis, C., 2015. Use of earth observation based indices for the monitoring of built-up area features and dynamics in support of urban energy studies. *Energy and Buildings*, 98, 92-99.
- [8] Weng, Q., Lu, D., and Schubring, J., 2004. Estimation of land surface temperature-vegetation abundance relationship for urban heat island studies. *Remote Sensing of Environment*, 89(4), 467-483.
- [9] Yuan, F. and Bauer, M.E., 2007. Comparison of impervious surface area and normalized difference vegetation index as indicators of surface urban heat island effects in Landsat imagery. *Remote Sensing of Environment*, 106(3), 375-386.
- [10] Zhao, S., Da, L., Tang, Z., Fang, H., Song, K., and Fang, J., 2006. Ecological consequences of rapid urban expansion: Shanghai, China. *Frontiers in Ecology and the Environment*, 4(7), 341-346.

- [11] Fazal, S., 2000. Urban expansion and loss of agricultural land-a GIS based study of Saharanpur City, India. *Environment and Urbanization*, 12(2), 133-149.
- [12] Villa, P., 2012. Mapping urban growth using soil and vegetation index and Landsat data: The Milan (Italy) city area case study. *Landscape and Urban Planning*, 107, 245-254.
- [13] Weber, C. and Puissant, A., 2003. Urbanization pressure and modeling of urban growth: example of the Tunis Metropolitan Area. *Remote Sensing of Environment*, 86, 341-352.
- [14] Waqar, M., Mirza, J., Mumtaz, R., and Hussain, E., 2012. *Development of new indices for extraction of built-up area and bare soil from landsat*. [Online] Available at: <https://www.researchgate.net/publication/284816904>.
- [15] Xu, H., 2008. A new index for delineating built-up land features in satellite imagery. *International Journal of Remote Sensing*, 29, 4269-4276.
- [16] Ma, Y. and Xu, R., 2010. Remote sensing monitoring and driving force analysis of urban expansion in Guangzhou City, China. *Habitat International*, 34, 228-235.
- [17] Xu, H., 2007. Extraction of urban built-up land features from Landsat Imagery using a thematic oriented index combination technique. *Photogrammetric Engineering & Remote Sensing*, 73(12), 1381-1391.
- [18] Cleve, C., Kelly, M., Kearns, F.R., and Moritz, M., 2008. Classification of the wildland-urban interface: A comparison of pixel- and object-based classifications using high-resolution aerial photography. *Computers, Environment and Urban Systems*, 32(4), 317-326.
- [19] Guindon, B., Zhang, Y., and Dillabaugh, C., 2004. Landsat urban mapping based on a combined spectral-spatial methodology. *Remote Sensing of Environment*, 92(2), 218-232.
- [20] Zha, Y., Gao, J., and Ni, S., 2003. Use of normalized difference built-up index in automatically mapping urban areas from TM imagery. *International Journal of Remote Sensing*, 24(3), 583-594.
- [21] Zhang, Q., Pavlic, G., Chen, W., Fraser, R., Leblanc, S., and Cihlar, J., 2005. A semi-automatic segmentation procedure for feature extraction in remotely sensed imagery. *Computers & Geosciences*, 31(3), 289-296.
- [22] Bhatti, S.S. and Tripathi, N.K., 2014. Built-up area extraction using Landsat 8 OLI imagery. *GIScience & Remote Sensing*, 51(4), 445-467.
- [23] Xu, H., 2006. Modification of normalised difference water index (NDWI) to enhance open water features in remotely sensed imagery. *International Journal of Remote Sensing*, 27(14), 3025-3033.
- [24] Sader, S.A., Hayes, D.J., Hepinstall, J.A., Coan, M., and Soza, C., 2001. Forest change monitoring of a remote biosphere reserve. *International Journal of Remote Sensing*, 22 (10), 1937-1950.
- [25] Ray, T.W., 1994. *Vegetation in remote sensing FAQs*. [online]. Available at: http://www.remote-sensing.info/wp-content/uploads/2012/07/A_FAQ_on_Vegetation_in_Remote_Sensing.pdf.
- [26] Varshney, A., 2013. Improved NDBI differencing algorithm for built-up regions change detection from remote-sensing data: an automated approach. *Remote Sensing Letters*, 4(5), 504-512.
- [27] Xu, H., 2005. A study on information extraction of water body with the Modified Normalized Difference Water Index (MNDWI). *Journal of Remote Sensing*, 9(5), 511-517.
- [28] Schowengerdt, R.A., 2007. *Remote Sensing: Models and Methods for Image Processing*. 3rd ed. USA: Elsevier Inc.
- [29] CAPMAS, 1996. Population Census 1996 In. Cairo: Central Agency for Public Mobilization and Statistics, pp. 4.
- [30] CAPMAS, 2006. Population Census 2006 In. Cairo: Central Agency for Public Mobilization and Statistics, pp. 4.

Physiological and Metabolic Modifications in Response to Nanocarbon in Callus of Indica Rice Cultivar

Thanawat Sutjaritvorakul¹ and Suttee Chutipaijit^{2*}

¹Faculty of Science and Technology, Pathumwan Institute of Technology,
Bangkok, Thailand

²College of Nanotechnology, King Mongkut's Institute of Technology Ladkrabang,
Bangkok, Thailand

Received: 5 September 2019, Revised: 11 November 2019, Accepted: 19 December 2019

Abstract

Nanocarbon has been shown to be implicated in the response of plants to an assortment of positive or negative impacts. In the present research, the effects of nanocarbon on cell growth and secondary metabolite production on rice callus were studied. Different concentrations of nanocarbon (0-1000 mg l⁻¹) were added into callus induction media to investigate the effects on the growth of callus, and secondary metabolite production in indica rice callus (*Oryza sativa* L. cv. Pathumthani1). The growth of callus was measured in terms of the size and weight of callus, and secondary metabolite production was determined based on the levels of total phenolic compounds and flavonoid production. The results showed that the callus induction, the callus growth and the secondary metabolite production in rice callus after treatment with nanocarbon were significantly different when compared to control (without treatment with nanocarbon). The rice callus treated with low (100 and 200 mg l⁻¹) and moderate (400 and 600 mg l⁻¹) level of nanocarbon displayed an enhancement in callus growth, total phenolic compounds and flavonoid production. However, the induction of callus, cell growth, and secondary metabolite production were decreased when rice callus was treated with high concentrations of nanocarbon (800 and 1000 mg l⁻¹). The results of this research showed that the nanocarbon application of 400-600 mg l⁻¹ had potential to induce the cell growth and secondary metabolite production. This research suggests further investigation in using different concentrations of nanocarbon on other plant species for potential pharmaceutical application.

Keywords: callus, growth, metabolite, nanocarbon, rice

DOI 10.14456/cast.1477.10

*Corresponding author: Tel.: +66 86-667-7036 Fax: +66 2-329-8265
E-mail: natadee24@hotmail.com

1. Introduction

The level of response in plant cells is motivated by various elicitors such as microorganisms, climates, metals and so on. Elicitors from biotic and abiotic stresses are able to activate morphological, physiological and biochemical responses in plant cells [1, 2]. The levels of biochemical responses and secondary metabolite generation and accumulation in plant cells are affected by several elicitors [3, 4]. Generally, the plant cells encompass secondary metabolites such as phenolics and flavonoids which have been considered as the alternative substances for pharmaceuticals, medicinal and supplementary food properties [5]. In recent years, the various types of biotic and abiotic elicitors have been advanced as an application scheme of plant cells that can trigger the generation and accumulation of secondary metabolites [6, 7]. Nanotechnology has gained an increasing attention in agricultural science and attracted remarkable consideration because of the positive and negative effects from the unique properties of nanomaterials and nanoparticles [8-10]. The synthesis and development of nanoparticles could open up the various applications in the field of biological and agricultural science. Several types of nanoparticles have been attracted noteworthy consideration and they have been studied in different organisms to investigate morphological, physiological and biochemical responses [11, 12]. Nanocarbon is one of the comprehensively used nanoparticles for various applications. In recent years, many studies have shown the effects of nanocarbon on plant responses such as micropropagation, plant growth, seed germination and plant metabolites. Positive or negative effects of nanocarbon on plant cells that are diverse among plant species, growth stages, concentrations, size and specific shapes of nanocarbon are also reported. The impacts of nanocarbon on plant response and development have been studied in different plant species such as maize, wheat, tomato and so on. [13-15].

Rice (*Oryza sativa* L.) is the world's important food crop and a model crop for research. Moreover, rice is a main food for more than 50% of the world's population, especially indica rice cultivars which is suitable for studying the impact of nanoparticles in plant responses [16]. The applications of nanoscience and nanotechnology in agricultural technology are an increasingly numerous incidence and enormous challenges that need to be supported for plant productions [17, 18].

The main emphasis of this research was to investigate the impact of nanocarbon on the callus formations (size, fresh weight, dry weight, relative growth rate and callus induction) and the accumulation of secondary metabolites, including total phenolic compound and flavonoid contents, and to evaluate the antioxidant activities of the callus extracts.

2. Materials and Methods

2.1 Plant materials, explants preparation and culture conditions

Mature seeds of indica rice cultivar Pathumthani 1 were obtained from Pathumthani Rice Research Center, Ministry of Agriculture and Cooperatives, Thailand. Mature seeds were dehusked by hand and surface sterilized by immersion in 70% (v/v) ethanol for 2-3 min, followed by immersion in 5% (v/v) commercial bleach (5.25% sodium hypochlorite) for 30 min and followed by immersion in 30% (v/v) commercial bleach (5.25% sodium hypochlorite) for 30 min. The mature seeds were then rinsed 5-6 times with sterile distilled water. The sterilized seeds were placed on sterilized filter papers in a petri dish and cultured on NB basal medium [19] supplemented with 500 mg l⁻¹ glutamine, 300 mg l⁻¹ casein hydrolysate, 30 g l⁻¹ sucrose, 1.5 mg l⁻¹ 2,4-D (2,4-Dichlorophenoxy-acetic acid), and 8 g l⁻¹ agar for callus induction medium. In order to study the effect of nanocarbon on callus induction and physiological responses, the seeds of indica rice cultivar Pathumthani 1 were

cultured on callus induction medium supplemented with different concentrations (0-1,000 mg l⁻¹) of nanocarbon. The seed cultures were maintained under the experimental conditions at 25 ± 2 °C under 16/8 h light/dark photoperiod with light intensity of 1,000 lux provided by cool white fluorescent lights.

2.2 Determination of callus induction performances

Plant samples were taken 4 weeks after cultivation for callus growth measurement and metabolite analysis because this period was the log phase or growth phase for appropriate growth and metabolite production. After 4 weeks in culture, the number, size, fresh weight and dry weight of embryogenic calli were recorded. The relative growth rate was measured and calculated according to the protocol of Hoffmann and Poorter [20].

2.3 Determination of secondary metabolite accumulations

Four-week-old biomass of callus induction from different concentrations of nanocarbon treatments was used for estimation of secondary metabolites (total phenolic compounds and total flavonoid contents) and antioxidant activities. The biomass of callus from each treatment was extracted with acidic-methanol (methanol:HCl; 99:1) at room temperature for 2 h on a rotary shaker (250 rpm). The homogenates were centrifuged at 8,000 rpm at 4 °C for 20 min. The supernatant was collected and investigated for the total phenolic compound contents, the total flavonoid contents and the total antioxidant activities.

The total phenolic compound contents of the callus extractions were determined by the Folin and Ciocalteu assay according to the protocol of Alothman *et al.* [21]. The total phenolic compound contents were expressed as milligrams of gallic acid equivalents (GAE) per g of sample.

The total flavonoid contents of the callus extractions were determined by the Aluminium-chloride (AlCl₃) colorimetric method according to the protocol of Pedro *et al.* [22]. The total flavonoid contents were expressed as milligrams of flavonoids per gram of sample.

The total antioxidant activities of the callus extractions were determined by DPPH method according to the protocol of Brand-Williams *et al.* [23]. The total antioxidant capacities were expressed as % inhibition and micromolar (μM) of Trolox equivalents per gram of sample.

2.4 Statistical analysis

Data were expressed as mean ± SD from five replicates. The experiments were set up in a completely random design (CRD). Data of experimental investigations were analyzed by analysis of variance (ANOVA) and compared by Duncan's New Multiple Range Test (DMRT) ($P \leq 0.05$) using SPSS statistics (SPSS for Windows version 15, SPSS Inc., Chicago, USA).

3. Results and Discussion

3.1 Callus induction performances

The results from this research showed that different concentrations of nanocarbon influenced the performances of callus induction, size, fresh weight, dry weight, relative growth rate in indica rice callus cultivar Pathumthani 1. The mature seeds cultured on callus induction medium supplemented with and without nanocarbon exhibited callus formation after 2 weeks of culture and the data of

these parameters were recorded after 4 weeks of culture. The percentage of callus induction and growth performances (size, fresh weight, dry weight and relative growth rate) induced by nanocarbon at various concentrations after 4 weeks was shown in Figure 1 and Table 1, respectively.

The treatment of 600 mg l^{-1} nanocarbon showed the highest percentage of callus induction ($93.33 \pm 2.35\%$) when compared to the other treatments (Figure 1). Callus induction medium containing 600 mg l^{-1} nanocarbon induced the highest size ($1.28 \pm 0.08 \text{ cm}$), fresh weight ($80.34 \pm 0.65 \text{ mg}$), dry weight ($49.56 \pm 1.52 \text{ mg}$) and relative growth rate ($0.0570 \pm 0.0026 \text{ mg d}^{-1}$) (Table 1). At high concentrations of nanocarbon (800 and $1,000 \text{ mg l}^{-1}$), size, fresh weight, dry weight, and relative growth rate as well as the percentage of callus induction were drastically reduced.

The size, fresh weight, dry weight and relative growth rate of callus were recorded at a regular interval to determine the growth performances for plant growth index [24-26]. Nanocarbon has been used to induce callus tissues and cell culture in many plant species. It had a significant positive effect of nanocarbon on plant germination and growth performances could also be noticed [27-29]. The previous research has reported that the production of biomass and relative growth rate were enhanced by the stimulated process of water uptake in plant cells when exposed to nanocarbon [30]. Nanocarbon has possibly been associated with the motivation of genes and proteins expressions that are related to the plant growth and development [31]. The present research reveals that the use of nanocarbon on callus induction medium was beneficial for callus culture of indica rice cultivar Pathumthani 1. The efficiency of nanocarbon for plant responses was supported by previous studies in various plants [32-34].

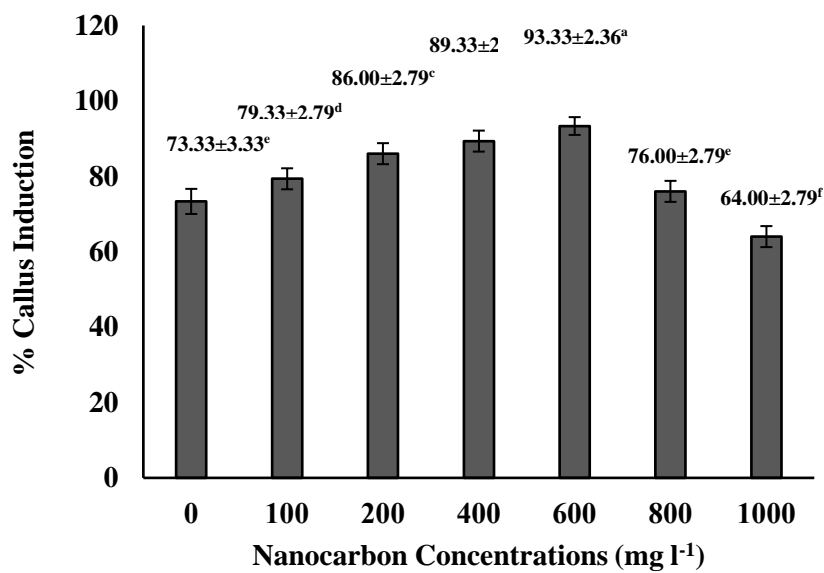


Figure 1. Effect of different concentrations of nanocarbon (0, 100, 200, 400, 600, 800 and $1,000 \text{ mg l}^{-1}$ nanocarbon) on the percentage of callus induction from indica rice cultivar Pathumthani 1. Data show means $\pm \text{SD}$ ($n = 5$). Different letters on bars represent statistically significant effects of different concentrations of nanocarbon ($P \leq 0.05$).

Table 1. Effect of different concentrations of nanocarbon (0, 100, 200, 400, 600, 800 and 1,000 mg l⁻¹ nanocarbon) on size, fresh weight, dry weight and relative growth rate of callus formations from indica rice cultivar Pathumthani1

Treatments (mg l ⁻¹ Nanocarbon)	Growth Performances				Relative Growth Rate (mg d ⁻¹)
	Size (cm)	Fresh weight (mg)	Dry weight (mg)		
0	0.60 ±0.07 ^d	66.52 ±1.45 ^d	30.66 ±1.44 ^e		0.0524 ±0.0019 ^{bc}
100	0.76 ±0.05 ^c	72.82 ±1.40 ^c	35.26 ±0.63 ^d		0.0534 ±0.0031 ^b
200	0.86 ±0.09 ^c	75.66 ±0.65 ^b	39.44 ±1.06 ^c		0.0541 ±0.0037 ^b
400	1.02 ±0.08 ^b	76.44 ±1.39 ^b	44.08 ±1.17 ^b		0.0555 ±0.0021 ^b
600	1.28 ±0.08 ^a	80.34 ±0.65 ^a	49.56 ±1.52 ^a		0.0570 ±0.0026 ^a 0.0524
800	0.64 ±0.05 ^d	66.88 ±1.12 ^d	30.80 ±1.04 ^e		±0.0015 ^{bc}
1000	0.48 ±0.08 ^e	64.06 ±1.02 ^e	25.92 ±1.27 ^f		0.0514 ±0.0056 ^c

Note: Data show means ± SD (n = 5) and different superscripts in the same column mean significant difference (P ≤ 0.05).

3.2 Secondary metabolite accumulations

After 4 weeks of culture, the application of nanocarbon was tested to determine the effects on the accumulation of total phenolic compound contents, total flavonoid contents and its antioxidant activities in callus extractions of indica rice cultivar Pathumthani 1 (Figures 2-4). The callus extraction of indica rice cultivar Pathumthani 1 showed a significant increase in the total phenolic compound contents and total flavonoid contents as well as antioxidant activities as a response to nanocarbon treatments.

The total phenolic compound and flavonoid contents of acidic-methanol extracts were achieved from the callus formations. Maximum contents of the total phenolic compounds (122.77 ±3.23 mg GAE g⁻¹) and total flavonoids (0.0052 ±0.0001 mg g⁻¹) were obtained from the extracts of callus cultured on callus induction medium supplemented with 600 mg l⁻¹ nanocarbon (Figures 2 and 3).

The maximum percentage of radical scavenging activity (% inhibition) and antioxidant activities (μM Trolox g⁻¹) was found in the extract of callus cultured on callus induction medium supplemented with 600 mg l⁻¹ nanocarbon. The callus extracts from the treatment of 600 mg l⁻¹ nanocarbon also showed the percentage of inhibition and antioxidant activities which were 41.38 ±0.90 % and 6.85 ±0.24 μM Trolox g⁻¹, respectively. These were more than the extract from the other treatments (Figure 4).

Callus extracts have been used effectively for the production of plant secondary metabolites for several applications [35-37]. In this research, nanocarbon treated callus at optimum concentrations could induce higher total phenolic compound and flavonoid contents than untreated callus. Under abiotic conditions such as nanomaterials and nanoparticles, this stress could trigger a sequence of modifications in physiological and biological processes and products in the accumulation of reactive oxygen species (ROS) in plant cells. Non-enzymatic antioxidant compounds including phenolic compounds and flavonoids contribute in ROS scavenging to defend

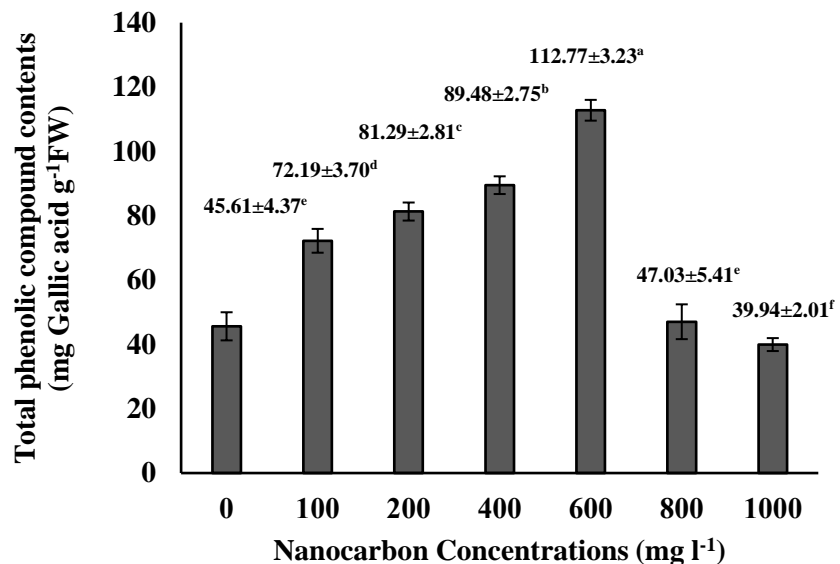


Figure 2. Effects of different concentrations of nanocarbon (0, 100, 200, 400, 600, 800 and 1,000 mg l⁻¹ nanocarbon) on the contents of total phenolic compounds from callus extraction in indica rice cultivar Pathumthani 1. Data show means ± SD (n = 5). Different letters on bars represent statistically significant effects of different concentrations of nanocarbon ($P \leq 0.05$).

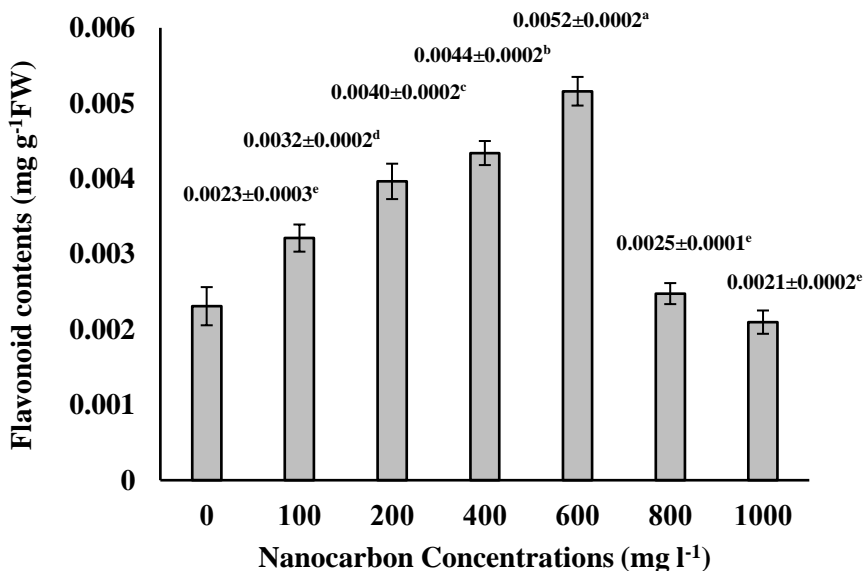


Figure 3. Effects of different concentrations of nanocarbon (0, 100, 200, 400, 600, 800 and 1,000 mg l⁻¹ nanocarbon) on the contents of total flavonoids from callus extraction in indica rice cultivar Pathumthani 1. Data show means ± SD (n = 5). Different letters on bars represent statistically significant effects of different concentrations of nanocarbon ($P \leq 0.05$).

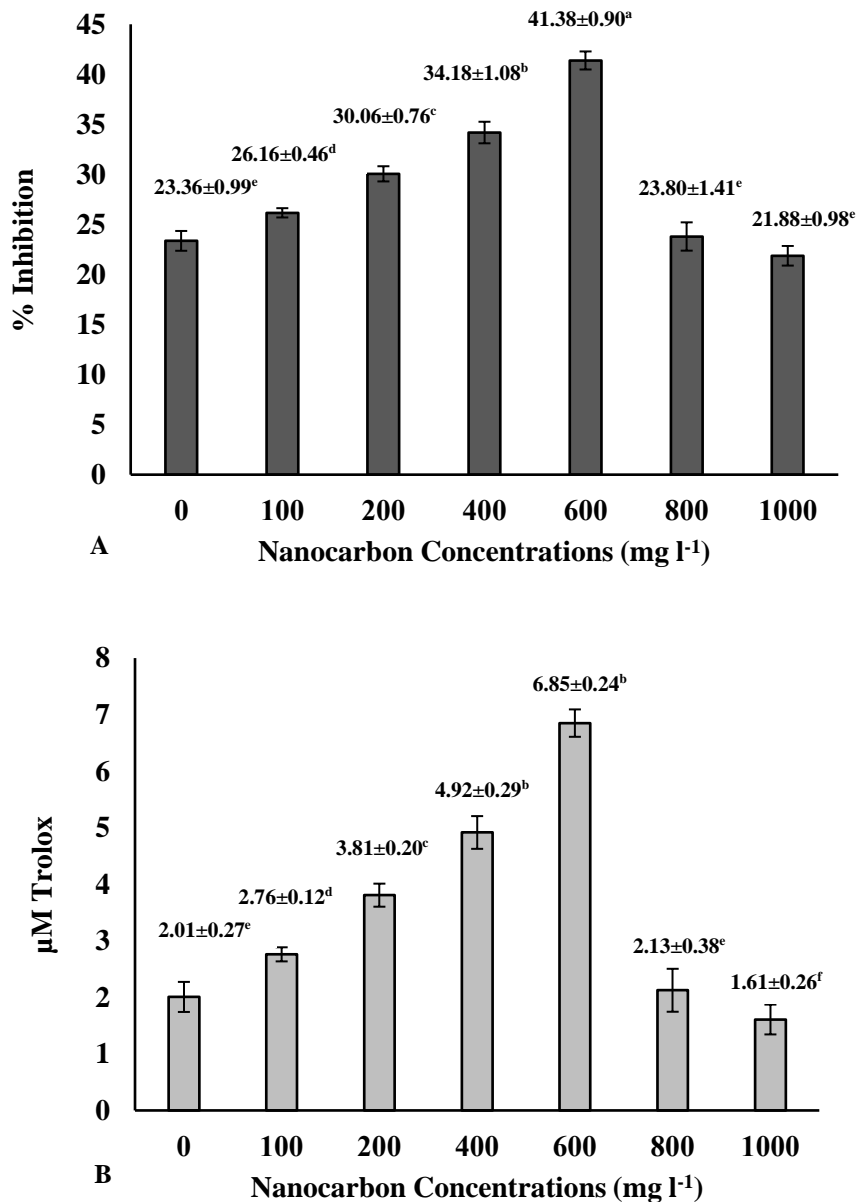


Figure 4. Effects of different concentrations of nanocarbon (0, 100, 200, 400, 600, 800 and 1,000 mg l^{-1} nanocarbon) on the percentages of inhibition (A) and Trolox equivalent antioxidant capacities (B) from callus extraction in indica rice cultivar Pathumthani 1. Data show means \pm SD ($n = 5$). Different letters on bars represent statistically significant effects of different concentrations of nanocarbon ($P \leq 0.05$).

plant cells from stress conditions [38-40]. Phenolic compounds and flavonoids are essential for plant growth, development and plant protection [41]. Previous studies reported that application of nanomaterials and nanoparticles at appropriate concentrations could act as elicitors to induce plant metabolic responses, in particular the secondary metabolite induction by plant tissue culture for various plant species [42-48]. The phenolic compounds and flavonoids are quintessential components because of their antibacterial, anti-inflammatory, antiviral and free radical scavenging activities which have attracted considerable attention by various researchers [49-51].

4. Conclusions

The results of this research indicated that the induction of callus formation, total phenolic compound contents, total flavonoid contents and antioxidant activities from indica rice cultivar Pathumthani 1 could be enhanced when cultured on media supplemented with suitable concentrations of nanocarbon. The results substantiated the presence of nanocarbon substance in indica rice, which may be used as an alternative for plant metabolites production. The influence of nanocarbon significantly changed the growth performance and metabolite response of the callus. The results obviously demonstrated that nanocarbon enhanced the callus formations as well as secondary metabolite accumulations of indica rice cultivar Pathumthani 1. The synergistic effect of nanocarbon was found to be the optimal concentrations for the induction of the total phenolic compounds and flavonoids. It is interesting to characterize a reliable application of nanocarbon for the production of potential secondary metabolites (total phenolic compounds and flavonoids) through the callus culture of indica rice cultivar Pathumthani 1.

5. Acknowledgements

This work was supported by King Mongkut's Institute of Technology Ladkrabang (Grant Number A118-0361-055 and KREF046105), Office of the National Research Council of Thailand (NRCT) and plant materials were supplied by Pathumthani Rice Research Center, Office of Grain Rice Department, Ministry of Agriculture and Cooperatives, Thailand.

References

- [1] Mandal, C., Bera, S., Dey, N. and Adak, M., 2016. Physiological alterations of *Salvinia natans* L. exposed to aluminium stress and its interaction with polyamine. *Plant Science Today*, 3, 195-206.
- [2] Wang, W., Yang, C., Tang, X., Gu, X., Zhu, Q., Pan, K. and Ma, D., 2014. Effects of high ammonium level on biomass accumulation of common duckweed *Lemna minor* L. *Environmental Science and Pollution Research*, 21, 14202-14210.
- [3] Ardebili, N.O., Saadatmand, S., Niknam, V. and Khavari-Nejad, R.A., 2014. The alleviating effects of selenium and salicylic acid in salinity exposed soybean. *Acta Physiologiae Plantarum*, 36, 3199-3205.
- [4] Habibi, G., 2013. Effect of drought stress and selenium spraying on photosynthesis and antioxidant activity of spring barley. *Acta agriculturae Slovenica*, 101, 31-39.

- [5] Ozkan, G., Sagdic, O., Gokturk, R.S., Unal, O. and Albayrak, S., 2010. Study on chemical composition and biological activities of essential oil and extract from *Salvia pisisidica*. *LWT-Food Science and Technology*, 43, 186-190.
- [6] Shaw, A.K., Ghosh, S., Kalaji, H.M., Bosa, K., Breistic, M., Zivcak, M. and Hossain, Z., 2014. Nano-CuO stress induced modulation of antioxidative defense and photosynthetic performance of Syrian barley (*Hordeum vulgare* L.). *Environmental and Experimental Botany*, 102, 37-47.
- [7] Asgari-Targhi, G., Iranbakhsh, A. and Ardebili, Z.O., 2018. Potential benefits and phytotoxicity of bulk and nano-chitosan on the growth, morphogenesis, physiology, and micropropagation of *Capsicum annuum*. *Plant Physiology and Biochemistry*, 127, 393-402.
- [8] Gogos, A., Knauer, K. and Bucheli, T.D., 2012. Nanomaterials in plant protection and fertilization, current state, foreseen applications, and research priorities. *Journal of Agricultural and Food Chemistry*, 60, 9781-9792.
- [9] Pandey, A.C., Sanjay, S.S. and Yadav, R.S., 2010. Application of ZnO nanoparticles in influencing the growth rate of *Cicer arietinum*. *Journal of Experimental Nanoscience*, 5, 488-497.
- [10] Dimkpa, C.O., Latta, D.E., McLean, J.E., Britt, D.W., Boyanov, M.I. and Anderson, A.J., 2013. Fate of CuO and ZnO nano and micro particles in the plant environment. *Environmental Science and Technology*, 47, 4734-4742.
- [11] Adhikari, T., Kundu, S., Biswas, A.K., Tarafdar, J.C. and Rao, A.S., 2012. Effect of copper oxide nano particle on seed germination of selected crops. *Journal of Agricultural Science and Technology*, 2, 815-823.
- [12] Rahmani, F., Peymani, A., Daneshvand, E. and Biparva, P., 2016. Impact of zinc oxide and copper oxide nano-particles on physiological and molecular processes in *Brassica napus*. *Indian Journal of Plant Physiology*, 21, 122-128.
- [13] Zaytseva, O. and Neumann, G., 2016. Carbon nanomaterials: production, impact on plant development, agricultural and environmental applications. *Chemical and Biological Technologies in Agriculture*, 3, 17.
- [14] Peng, Q., Dearden, A.K., Crean, J., Han, L., Liu, S., Wen, X. and De, S., 2014. New materials graphyne, graphdiyne, graphene, and graphane: review of properties, synthesis, and application in nanotechnology. *Nanotechnology, Science and Applications*, 7, 1-29.
- [15] Chutipaijit, S. and Sutjaritvorakul, T., 2018. Application of activated charcoal and nanocarbon to callus induction and plant regeneration in aromatic rice (*Oryza sativa* L.). *Chemical Speciation and Bioavailability*, 30, 1-8.
- [16] Ata-Ul-Karim, S.T., Liu, X.J., Lu, Z.Z., Yuan, Z.F., Zhu, Y. and Cao, W.X., 2016. In-season estimation of rice grain yield using critical nitrogen dilution curve. *Field Crops Research*, 195, 1-8.
- [17] Adams, J., Wright, M., Wagner, H., Valiente, J., Britt, D. and Anderson, A., 2017. Cu from dissolution of CuO nanoparticles signals changes in root morphology. *Plant Physiology and Biochemistry*, 110, 108-117.
- [18] Yang, Z., Chen, J., Dou, R., Gao, X., Mao, C. and Wang, L., 2015. Assessment of the phytotoxicity of metal oxide nanoparticles on two crop plants, maize (*Zea mays* L.) and rice (*Oryza sativa* L.). *International Journal of Environmental Research and Public Health*, 12, 15100-15109.
- [19] Li, L., Qu, R., De Kochko, A., Frauquet, C. and Beachy, R.N., 1993. An improved rice transformation method using the biolistic method. *Plant Cell Reports*, 12, 250-255.
- [20] Hoffmann, A. and Poorter, H., 2002. Avoiding bias in calculations of relative growth rate. *Annals of Botany*, 80, 37-42.

- [21] Alothman, M., Bhat, R. and Karim, A.A., 2009. Antioxidant capacity and phenolic content of selected tropical fruits from Malaysia, extracted with different solvents. *Food Chemistry*, 115, 785-788.
- [22] Pedro, A.C., Granato, D. and Rosso, N.D., 2016. Extraction of anthocyanins and polyphenols from black rice (*Oryza sativa* L.) by modeling and assessing their reversibility and stability. *Food Chemistry*, 191, 12-20.
- [23] Brand-Williams, W., Cuvelier, M.E. and Berset. C., 1995. Use of a free radical method to evaluate antioxidant activity. *LWT-Food Science and Technology*, 28, 25-30.
- [24] Ivanova, K., Dimitrova, V., Georgieva, T. and Markovska, Y., 2015. Effect of soil salinity on growth, gas exchange and antioxidant defence of two *Paulownia* lines. *Genetics and Plant Physiology*, 4, 163-173
- [25] Gupta, S.D. and Jatooth, B., 2013. Fundamentals and applications of light emitting diodes (LEDs) in *in vitro* plant growth and morphogenesis. *Plant Biotechnology Reports*, 7, 211-220.
- [26] Samart, S. and Chutipaijit, S., 2018. Modifications of morphological and physiological characteristics of pigmented-rice seedlings by application of titanium dioxide nanoparticles. *AIP Conference Proceedings*, 2010, 020003.
- [27] Wang, X., Han, H., Liu, X., Gu, X., Chen, K. and Lu, D., 2012. Multi-walled carbon nanotubes can enhance root elongation of wheat (*Triticum aestivum*) plants. *Journal of Nanoparticle Research*, 14, 1-10.
- [28] Tiwari, D.K., Dasgupta-Schubert, N., Villasenor Cendejas, L.M., Villegas, J., Carreto Montoya, L. and Borjas Garcia, S.E., 2014. Interfacing carbon nanotubes (CNT) with plants: enhancement of growth, water and ionic nutrient uptake in maize (*Zea mays*) and implications for nanoagriculture. *Applied Nanoscience*, 4, 577-591.
- [29] Husen, A. and Siddiqi, K.S., 2014. Carbon and fullerene nanomaterials in plant system. *Journal of Nanotechnology*, 12, 1-10.
- [30] Khodakovskaya, M., Dervishi, E., Mahmood, M., Xu, Y., Li, Z., Watanabe, F. and Biris, A.S., 2009. Carbon nanotubes are able to penetrate plant seed coat and dramatically affect seed germination and plant growth. *ACS Nano*, 3, 3221-3227.
- [31] Villagarcia, H., Dervishi, E., de Silva, K., Biris, A.S. and Khodakovskaya, M.V., 2012. Surface chemistry of carbon nanotubes impacts the growth and expression of water channel protein in tomato plants. *Small*, 8, 2328-2334.
- [32] Canas, J.E., Long, M., Nations, S., Vadan, R., Dai, L., Luo, M., Ambikapathi, R., Lee, E.H. and Olszyk, D., 2008. Effects of functionalized and nonfunctionalized single-walled carbon nanotubes on root elongation of select crop species. *Environmental Toxicology and Chemistry*, 27, 1922-1931.
- [33] Flores, D., Chacón, R., Alvarado, L., Schmidt, A., Alvarado, C. and Chaves, J., 2014. Effect of using two different types of carbon nanotubes for blackberry (*Rubus adenotrichos*) *in vitro* plant rooting, growth and histology. *American Journal of Plant Sciences*, 5, 3510-3518.
- [34] Khodakovskaya, M.V., Kim, B.S., Kim, J.N., Alimohammadi, M., Dervishi, E., Mustafa, T. and Cerniglia, C.E., 2013. Carbon nanotubes as plant growth regulators: effects on tomato growth, reproductive system, and soil microbial community. *Small*, 9, 115-123.
- [35] Kumari, A., Baskaran, P. and Van Staden, J., 2016. *In vitro* propagation and antibacterial activity in *Cotyledon orbiculata*: a valuable medicinal plant. *Plant Cell, Tissue and Organ Culture*, 124, 97-104.
- [36] Liao, D.Y., Chai, Y.C., Wang, S.H., Chen, C.W. and Tsai, M.S., 2015. Antioxidant activities and contents of flavonoids and phenolic acids of *Talinum triangulare* extracts and their immunomodulatory effects. *Journal of Food and Drug Analysis*, 23, 294-302.
- [37] Mahboubi, A., Kamalinejad, M., Ayatollahi, A.M. and Babaeian, M., 2014. Total phenolic content and antibacterial activity of five plants of *Labiatae* against four foodborne and some other bacteria. *Iranian Journal of Pharmaceutical Research*, 3, 559-566.

- [38] Sergeant, K., Kieffer, P., Dommes, J., Hausman, J.F. and Renaut, J., 2014. Proteomic changes in leaves of poplar exposed to both cadmium and low-temperature. *Environmental and Experimental Botany*, 106, 112-123.
- [39] Song, S.Y., Chen, Y., Chen, J., Dai, X.Y. and Zhang, W.H., 2011. Physiological mechanisms underlying *OsNAC5*-dependent tolerance of rice plants to abiotic stress. *Planta*, 234, 331-345.
- [40] Chutipaijit, S., 2016. Changes in physiological and antioxidant activity of *indica* rice seedlings in response to mannitol-induced osmotic stress. *Chilean Journal of Agricultural Research*, 76, 455-462.
- [41] Ghorbanpour, M., 2015. Major essential oil constituents, total phenolics and flavonoids content and antioxidant activity of *Salvia officinalis* plant in response to nano-titanium dioxide. *Indian Journal of Plant Physiology*, 20, 249-256.
- [42] Aghajani, Z., Pourmeidani, A. and Ekhtiyari, R., 2013. Effect of nano-silver on stages of plant growth and yield and composition of essential of *Thymus kotschyani* Boiss. & Hohen. *African Journal of Agricultural Research*, 8, 707-710.
- [43] Hatami, M., Ghorbanpour, M. and Salehiarjomand, H., 2014. Nanoanatase TiO₂ modulates the germination behavior and seedling vigor of the five commercially important medicinal and aromatic plants. *Journal of Biological and Environmental Sciences*, 8, 53-59.
- [44] Ghorbanpour, M. and Hatami, M., 2015. Changes in growth, antioxidant defense system and major essential oils constituents of *Pelargonium graveolens* plant exposed to nano-scale silver and thidiazuron. *Indian Journal of Plant Physiology*, 20, 116-123.
- [45] Yang, H., Liu, C., Yang, D., Zhang, H. and Xi, Z., 2009. Comparative study of cytotoxicity, oxidative stress and genotoxicity induced by four typical nanomaterials: the role of particle size, shape and composition. *Journal of Applied Toxicology*, 29, 69-78.
- [46] Remya, N., Saino, H.V., Baiju, G.N., Maekawa, T., Yoshida, Y. and Sakthi, K.D., 2010. Nanoparticulate material delivery to plants. *Plant Science*, 179, 154-163.
- [47] Oloumi, H., Soltaninejad, R. and Baghizadeh, A., 2015. The comparative effects of nano and bulk size particles of CuO and ZnO on glycyrrhizin and phenolic compounds contents in *Glycyrrhiza glabra* L. seedlings. *Indian Journal of Plant Physiology*, 20, 157-161.
- [48] Mohammadia, R., Maali-Amiria, R. and Mantri, N.L., 2014. Effect of TiO₂ nanoparticles on oxidative damage and antioxidant defense systems in chickpea seedlings during cold stress. *Russian Journal of Plant Physiology*, 61, 768-775.
- [49] Nagarajan, A., Arivalagan, U. and Rajagurua, P., 2011. *In vitro* root induction and studies on antibacterial activity of root extract of *Costusigneus* on clinically important human pathogens. *Journal of Microbiology and Biotechnology Research*, 1, 67-76.
- [50] El-Bakry, A.A., Mostafa, H.A.M. and Alam Eman, A., 2014. Antioxidant and antibacterial activity of callus and adventitious root extracts from *Rumex vesicarius* L. *Journal of Medicinal Plants Research*, 8, 479-488.
- [51] Baskaran, P., Kumari, A., Naidoo, D. and Van Staden, J., 2015. *In vitro* propagation and biochemical changes in *Aloe pruinosa*. *Industrial Crops and Products*, 77, 51-58.

Genotypic Variation of Seed Oil Content in Twelve Genotypes of *Citrullus colocynthis* from Morocco

Saïd El Madidi* and Abedlhamid Benmoumou

BVRN Laboratory, Faculty of Sciences, Ibn Zohr University, Agadir, Morocco

Received: 11 October 2019, Revised: 22 November 2019, Accepted: 2 January 2020

Abstract

Citrullus colocynthis (L.) Schrad ($2n = 22$) is a perennial herbaceous species of the family Cucurbitaceae. It has natural tolerance to drought with a deep root system and is widespread in the arid and semi-arid zones of Africa and the Mediterranean region. This plant can be considered as a new potential source of vegetable oil. Twelve accessions of *C. Colocynthis*, collected from different regions of Morocco, were studied for seed and oil yields. The average yields obtained under non-optimal growing conditions are 479 kg/ha for seed yield and 99 kg/ha for oil yield. Significant genotypic variability was observed for seed oil content, seeds yields and oil yields. Heritability and genotypic advance are moderate to high for the characters measured. The exploitation of this variability could be used for the selection of accessions that have good oil yields in limited growing conditions.

Keywords: *Citrullus colocynthis*, seeds yield, oil yield, oil content, oil composition

DOI 10.14456/cast.2020.1

1. Introduction

Citrullus colocynthis (L.) Schrad ($2n = 22$), is a related species of domesticated watermelon (*Citrullus lanatus* var. *Lanatus*) [1], it is a perennial herbaceous species of the family Cucurbitaceae that is well adapted to arid zones through its tolerance to drought with a deep root system. It is widespread in the Sahara Desert in Africa and in the Mediterranean region where it grows spontaneously [2, 3]. *Citrullus colocynthis* is widely used for therapeutic purposes in Mediterranean countries and contains many bioactive compounds that are of functional importance. Its fruits are used for the treatment of many diseases, including diabetes, rheumatism, ulcers and cancer [4, 5]. In addition to these therapeutic uses, this plant can potentially be used as a source of biodiesel feedstock [6, 7]. It has also been shown that the seeds of this plant are nutritionally valuable with high protein and mineral content, and the seed oil is edible and has comparable characteristics to most conventional vegetable oils [5, 6, 8]. In recent years, the development of new oil seed crops that can be used as alternatives to conventional plants has generated a lot of interest and *C. colocynthis* is one of the plants that is able to adapt to arid conditions. Thus, its natural variability should be evaluated in order to select the best accessions. Several authors have already shown the existence of a great variability for agro-morphological characters and for the molecular polymorphism [9, 10]. The level of variability and heritability needed to aid selection of cultivars with improving traits and yield is scanty. The present study was undertaken to evaluate the level of genotypic variability and heritability for traits associated with seed yield for selection of high yielded accessions for production of seeds and oil.

*Corresponding author: Tel.: +212 52-822-0957 Fax: +212 52-822-0100

E-mail: s.elmadidi@uiz.ac.ma

2. Materials and Methods

The plant material includes several accessions that are collected from 12 different localities in Morocco (Figure 1). The experimental design was the randomized complete block design with three repetitions. For each plot, 3 plants were randomly selected and 5 fruits per plant were analysed with a total of 45 fruits analyzed for each genotype. The seeds were planted at 75 cm between the plants and 150 cm spacing between the lines. Each plot received a limited amount of water equivalent to 100 mm of irrigation water and no fertilizer or insecticide spraying was applied at any time for the duration of the trial. The measured traits were including fruit weight per plant (FW), seed weight per plant (SW), seed number per plant (SN), weight of 100 seeds per plant (W100) and oil content of seed (OC). For the extraction of the lipid components, the seeds were crushed and then extracted with n-hexane (200 ml) at 40-60°C in a soxhlet apparatus. The total extraction time was 6 h for each repetition. The composition of the oil in fatty acids was determined by Chromatography coupled with Mass Spectrometry [11, 12]. The phenotypic variance in each trial was estimated by:

$$\hat{\sigma}_P^2 = \hat{\sigma}_G^2 + \frac{\hat{\sigma}_E^2}{n} \text{ and the Broad-sense heritability was estimated by: } \hat{\sigma}_G^2 / \hat{\sigma}_P^2.$$

$\hat{\sigma}_P^2$ = phenotypic variance, $\hat{\sigma}_G^2$ = genotypic variance, $\hat{\sigma}_E^2$ = environmental variance (error mean square from the analysis of variance) and n = number of replications. The estimate of the genotypic gain was calculated by: $\Delta G_i = i \hat{H}^2 \hat{\sigma}_P$ where i= selection differential, the value is 1.40 at 20 % selection intensity. The relative genotypic gain ($R\Delta G_i$) was obtained by dividing the genotype gain by the average of the analyzed character. All statistical analyzes were performed using SAS version 9.3 software [13].

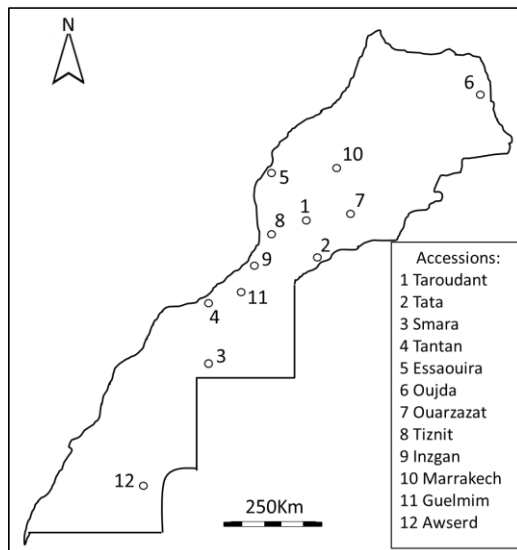


Figure 1. Origin of accessions of *Citrullus colocynthis* (L.) Schrad collected in several localities in Morocco

3. Results and Discussion

The data recorded for morphological and agronomic characteristics showed considerable variability among the accessions (Table 1). The fruits weight, seed number and seed weight per plant varied between 79 to 482, 37 to 682 and 1.94 to 38.25 g, respectively and seed oil content varied between 16.94% to 34.85% of seed weight. The coefficient of variation (CV) estimates ranged from 6.21% to 42.81%. Figure 2 shows the variability observed between the accessions for the seeds weight where accession 11 has the highest average value and accession 8 the lowest value.

Table 1. Descriptive statistics for the measured characters

Characters	Mean	Min	Max	SD	CV (%)
FW (kg/plant)	178.50	79.00	482.00	63.92	35.81
SN	222.15	37.00	682.00	90.68	40.82
SW(g/plant)	11.97	1.94	38.25	5.12	42.81
W100	5.32	0.00	9.40	0.80	15.12
OC (%)	24.75	16.94	34.85	1.78	6.21

FW: fruit weight, SN: seed number, SW: seed weight, W100: weight of 100 seeds, OC: oil content, SD: Standard deviation and CV: Coefficient of variation

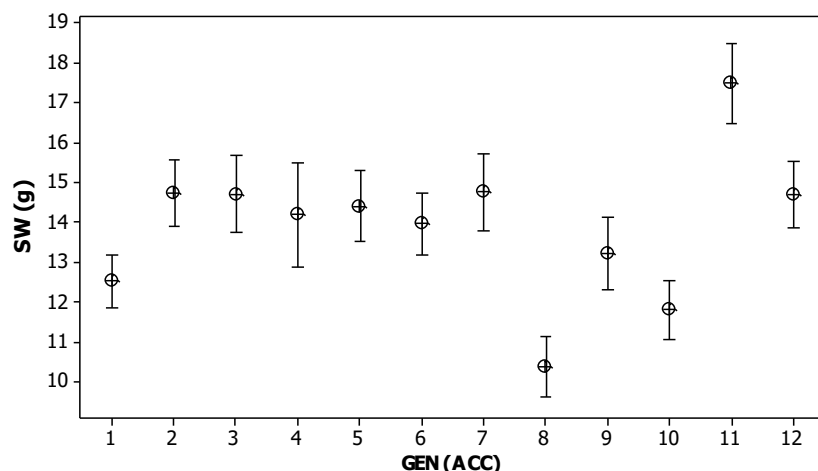


Figure 2. Variation of *C. colocynthis* seeds weight (sw, g) for different accessions (95% CI for the mean)

Heritability in the broad sense refers to the part of the genotype variance in the phenotypic variance of a trait and it is a statistical datum allowing an estimation by genetic factors in the expression of the character [14, 15]. The estimation of heritability is a first step in establishing a genetic evaluation for a given trait and the knowledge of this parameter is particularly important for the objective of selection. The \hat{H}^2 estimates ranged from 0.33 to 0.62 and the relative genotypic gain ranged from 10.23 to 24.68% (Table 2). These results indicated that the genotypic component played a relatively important role in the expression of these traits and its significant genetic progress could be obtained by selection based on phenotypic performance.

The comparison of accessions means showed highly significant differences (Table 3). The p-values were respectively equal to 0.0032 and 0.0065 for the seed yield and the oil yield respectively. For seed yield, average values were grouped into 3 homogeneous groups and ranged from 301.95 kg/ha (accession 4) to 673.68 kg/ha (accession 11). For oil yield, the average values were arranged into 4 homogeneous groups and varied between 63.85 kg/ha (accession 10) and 151.69 kg/ha (accession 11).

Table 2. The Broad-sense heritability and relative genotypic gain

Characters	\hat{H}^2	$R\Delta G_i$
Fruit weight	0.41	24.68%
Seed number	0.45	12.60%
Seed weight	0.43	10.23%
Weight of 100 seeds	0.33	14.73%
Oil content	0.62	18.23 %

Table 3. Means of seed and oil yields from 12 accessions of *Citrullus colocynthis* (L.) Schrad

Accessions	Seeds yield (Kg/ha)	Oil yield (Kg/ha)
4	301.95 ^a	64.57 ^a
10	342.95 ^a	63.85 ^a
7	345.37 ^a	67.93 ^a
8	361.82 ^a	77.10 ^{ab}
3	368.57 ^a	85.48 ^{abc}
1	465.70 ^{ab}	95.86 ^{bc}
5	485.28 ^{ab}	97.75 ^c
9	493.46 ^{ab}	114.60 ^{cd}
6	513.82 ^b	104.20 ^{cd}
2	629.46 ^{bc}	127.70 ^{cd}
12	642.94 ^c	132.10 ^d
11	673.68 ^c	151.69 ^d

Means within columns with different superscript are significantly different ($p < 0.01$) using the Duncan New Multiple Range Test (DMRT).

The fatty acid profiles of the seed oil showed an unsaturated fatty acid content of 74.10 % and the predominant fatty acid was linoleic acid (C18.2) in 60.06 %, followed by oleic acid (C18.1) (14.4%), palmitic acid (C16.0) (11.14%) and stearic acid (C18.0) (8.36%). The oil content and fatty acid compositions of the seed oil found in this study are in agreement with the results observed in other studies which showed a predominance of unsaturated fatty acids [6, 7, 16].

As indicated in Table 3, the analysis of the data revealed important differences between accessions, with seed yields ranging from the lowest value of 220.28 to the highest value of 815.76 kg per hectare and seed oil yield from 45.12 to 171.71 kg/ha (Table 4). The results of these yield observed in semi-arid conditions in this study without any fertilizer and in conditions of limited irrigation, remain relatively low compared to those potentially obtained under optimal growing conditions. Mertia and Gupta [17] reported the production of 4,400 kg of seed and 1,000 to 1,175 L/ha of colocynth vegetable oil in rainfed conditions. With plant density of four plants per m², the extrapolated annual seed yield among the accessions of *Citrullus colocynthis* ranged from 0.47 to 14.95 tons/ha with an overall mean of 5.17 tons/ha [18]. In the desert in Pakistan, some accessions of *C. colocynthis* developed an extensive root system despite of receiving only 35-40 mm of rainfall, yield can be as much as 1-1.5 t of seed/ha, but as much as 40-fold more if rainfall is higher [19].

Table 4. Descriptive statistics for the yield attributes

Yield	Mean	Min	Max	SD	CV (%)
Seed yield (kg/ha)	468.75	220.28	815.76	63.92	35.81
Oil yield (kg/ha)	98.57	45.12	171.71	29.81	36.29

Min: Minimum, Max: Maximum, SD: Standard Deviation, CV: Coefficient of Variation

4. Conclusions

All these results showed that the cultivation of *C. colocynthis* could be an important asset for the production of edible oil, especially under challenging conditions in arid and semi-arid lands. High yields can be achieved by finding the best growing conditions for proper production and selecting the best accessions selected for seed and oil yield with good tolerance to different abiotic stresses.

5. Acknowledgements

This work has received financial support from Ibn Zohr University and the valuable assistance of the management and technicians of the Sidi Bibi experimental center for the installation and monitoring of the field experience.

References

- [1] Chomicki, G. and Renner, S.S., 2015. Watermelon origin solved with molecular phylogenetics including Linnean material: another example of museomics. *New Phytologist*, 205, 526-532.
- [2] Si, Y., Dane, F., Rashotte, A., Kang, K. and Singh, N.K., 2010. Cloning and expression analysis of the Ccrboh gene encoding respiratory burst oxidase in *Citrullus colocynthis* and grafting onto *Citrullus lanatus* (watermelon). *Journal of Experimental Botany*, 61 (6), 1635-1642.
- [3] Wang, Z., Hu, H., Goertzen, L.R., McElroy, J.S. and Dane, F., 2014. Analysis of the *Citrullus colocynthis* transcriptome during water deficit stress. *PLoS ONE*, 9(8), e104657.
- [4] Hussain, A.I., Rathore, H.A., Sattar, M.Z.A., Chatha, S.A.S., Sarker, S.D. and Gilani A.H., 2014. *Citrullus colocynthis* (L.) Schrad (bitter apple fruit): A review of its phytochemistry, pharmacology, traditional uses and nutritional potential. *Journal of Ethnopharmacology*, 155, 54-66.
- [5] Marzouk, B., Marzouk, Z., Haloui, E., Fenina, N., Bouraoui, A. and Aouni, M., 2010. Screening of analgesic and anti-inflammatory activities of *Citrullus colocynthis* from southern Tunisia. *Journal of Ethnopharmacology*, 128 (1), 15-19.
- [6] Giwa, S., Abdullah, L.C. and Adam, N.M., 2010. Investigating “Egusi” (*Citrullus colocynthis* L.) seed oil as potential biodiesel feedstock. *Energy*, 3(4), 607-618.
- [7] Bello, E.I. and Makanju, A., 2011. Performance evaluation of Egusi melon (*Citrullus colocynthis* L.) seeds oil biodiesel. *Journal of Emerging Trends in Engineering and Applied Sciences*, 2(5), 741-745.
- [8] Mabaleha, M.B., Mitei, Y.C. and Yeboah, S.O., 2007. A comparative study of the properties of selected melon seed oils as potential candidates for development into commercial edible vegetable oils. *Journal of the American Oil Chemists' Society*, 84 (1), 31-36.
- [9] Shahid, M. and Rao, N. K., 2014. Diversity of *Citrullus colocynthis* (L.) Schrad.(Cucurbitaceae) in the United Arab Emirates. *Journal on New Biological Reports*, 3, 145-150.
- [10] Avval, S. E., 2017. Assessing polymorphism information content (PIC) using SSR molecular markers on local species of *Citrullus colocynthis*. Case study: Iran, Sistan-Baluchestan province. *Journal of Molecular Biology Research*, 7(1), 42-49.
- [11] Sparkman, O.D., 2005. Identification of essential oil components by gas chromatography/quadrupole mass spectroscopy Robert P. Adams. *Journal of the American Society for Mass Spectrometry*, 16(11), 1902-1903.
- [12] Roberts, L. D., McCombie, G., Titman, C. M. and Griffin, J. L., 2008. A matter of fat: an introduction to lipidomic profiling methods. *Journal of Chromatography B*, 871(2), 174-181.
- [13] SAS Institute, 2010. *Statistical Analysis Software Version 9.3 User's Manual.*, Cary, NC: SAS Institute Inc. USA.
- [14] Nyquist, W.E., 1991. Estimation of heritability and prediction of selection response in plant population. *Critical Review in Plant Sciences*, 10, 235-322.
- [15] Falconer, D.S. and Mackay, T.F.C., 1996. *Introduction to Quantitative Genetics*. 4th ed., London: Benjamin Cummings.
- [16] Gurudeeban, S., Satyavani, K. and Ramanathan, T., 2010. Bitter apple (*Citrullus colocynthis*): An overview of chemical composition and biomedical potentials. *Asian Journal of Plant Sciences*, 9(7), 394.
- [17] Mertia, R.S. and Gupta, I.C., 1994. Cultivate the colocynth in waste lands. *Indian Horticulture*, April-June, 40-41.

- [18] Menon, K., Sood, N. and Rao, N. K., 2016. Study of morpho-agronomic diversity and oil content in desert gourd (*Citrullus colocynthis* (L.) Schrad.). *Australian Journal of Crop Science*, 10 (7), 1000.
- [19] Mahajan, S.S. and Kumawat, R.N., 2013. Study of seed dormancy in colocynth (*Citrullus colocynthis* L.) with after-ripening of fruits, seed extraction procedures and period of seed storage. *National Academy Science Letters*, 36, 373-378.

Fabrication of Activated Carbon Pouch Cell Supercapacitor: Effects of Calendering and Selection of Separator-Solvent Combination

Gladis Aros Safitri¹, Khanin Nueangnoraj¹, Paiboon Sreearunothai¹ and
Jedsada Manyam^{2*}

¹School of Bio-Chemical Engineering and Technology, Sirindhorn International Institute
of Technology (SIIT), Pathum Thani, Thailand

²National Nanotechnology Center (NANOTEC), National Science and Technology
Development Agency (NSTDA), Pathum Thani, Thailand

Received: 11 September 2019, Revised: 8 December 2019, Accepted: 9 January 2020

Abstract

Most published articles reported characterization of a supercapacitor utilizing a coin cell or a Swagelok cell design, while the higher capacity format such as a pouch or cylindrical cell is needed to predict the performance of a supercapacitor for a practical application. In this work, the guideline to produce a pouch cell supercapacitor is given. The three-component electrode is based on a commercially available activated carbon, carbon black, and a polyvinylidene fluoride binder, which is formed a layer on a conductive-carbon coated aluminum foil current collector. The roles and optimization of a calendering process and selection of a separator-solvent combination are highlighted. The symmetric electric double-layer capacitor (EDLC) pouch cell using organic salt electrolyte is rated at 2.5 Volt. The pouch cell has the maximum capacitance of 32.6 F with a specific capacitance of 25.6-29.4 F/g.

Keywords: supercapacitor, pouch cell, electric double-layer capacitor (EDLC), activated carbon, organic electrolyte

DOI 10.14456/cast.2020.2

1. Introduction

The foreseeable limit of fossil fuel reserves, accompanied with an increasing concern about environmental impacts, initiates the development of alternative technologies that promote the efficient use of energy and renewable sources. However, the implementation of grid-scale electricity generated from renewable sources requires grid balancing to compensate for an intermittency issue in which energy storage technologies could play a crucial role [1]. In addition, a recent trend in the penetration of electric vehicles (EV) is another driver of growing demand on the advancement of high energy and power density storage devices [2]. Li-ion batteries and supercapacitors are among the potential storage technologies which have received increasing attention in the past few years for both stationary and transportation applications [2-5].

*Corresponding author: E-mail: jedsada@nanotec.or.th

Although a Li-ion battery is preferable as a primary power source in mainstream design due to its high energy density (~200 Wh/kg) and cost effectiveness, supercapacitor which possesses relatively high power density (~10 kW/kg) and extremely long life cycle can find its niche applications such as a power source for the EV regenerative breaking and a blade pitch control in wind turbine generator [2, 6, 7]. In addition, a battery and a supercapacitor could be integrated to provide robust energy management [2, 8].

A supercapacitor electrode stores polarization energy in an electric double-layer built up by the accumulation of ions and electric charges near the interface between a highly porous electrode and an electrolyte solution without having an electron transfer reaction, providing the fast charge-discharge rate. It is also widely known as an electric double-layer capacitor (EDLC). The design of EDLC involves the selection of electrode materials, electrolytes and separators. The selection of components can be the first consideration to minimize the trade-off between the electrode performance and the material cost. A commercially available EDLC uses activated carbon as an electrode material because of its high specific surface area (up to 3,000 m²/g), good electrical conductivity, excellent chemical stability and low cost [9]. In a typical electrode formulation, carbon black and a thermoplastic binder are added to improve electrical conductivity and adhesion, respectively [10, 11]. An organic electrolyte such as tetraethylammonium tetrafluoroborate (TEABF₄) in an organic solvent is commonly used in a commercial cell because it provides moderate ionic conductivity and relatively high voltage rating, typically 2.7 V, and the larger amount of energy stored in comparison to an aqueous electrolyte system [12]. A separator, commonly made of a porous sheet of polyolefins, glass, or cellulose, serves as an insulating layer to prevent electrical contact between a negative electrode and a positive electrode. It must possess high porosity and good wettability to be able to absorb and retain electrolyte which supports sufficient ionic conductivity and interfacial contact to electrode surface [13, 14].

Apart from a material aspect, the performance of a supercapacitor cell indicated by capacitance and internal resistance can be significantly varied by a number of factors regarding electrode processing conditions and a cell assembly such as thickness [15] and density [16, 17] of an electrode, cell pressure [18], and pre-conditioning process [19]. A brief fabrication process for a supercapacitor includes (1) preparation of a homogeneous mixture of ingredients, (2) forming an electrode layer on a sheet of a current collector, (3) cell assembling, and (4) packaging. In a laboratory, a pair of small electrodes, a few cm² area or mF capacity, are normally packed in a coin cell or other derivatives such as a Swagelok cell in order to characterize an electrode material in a full cell configuration. However, demonstration of a large capacity cell is needed to evaluate the cell performance in a practical aspect and it is also the step toward commercialization. A high capacity cell, 10s-1000s F, requires packaging in a cylindrical or pouch cell. Unfortunately, the guideline to produce a cell in such large package is proprietary in the industrial domain and a little information is provided in the published research. An attempt to scale up the size of a supercapacitor coin cell to a larger format, specifically a pouch cell, has been recently reported, pointing out a challenge on electrode preparation and processing [17, 19-21]. The pouch cell packaging seems the preferable format in literature because of its simplicity, affordable processing, industrial compatibility as well as design of the minimum footprint.

In this paper, we report prototyping of a 30-farad EDLC pouch cell made of commercially available materials. The basic instructions for the preparation of a carbon-based electrode and a pouch cell package are described. The roles of the calendaring process, which governs the thickness and density of an electrode and the selection of a separator-solvent system to the electrode performance is highlighted and discussed. The process optimization and the characterization of the as-fabricated pouch cells are reported.

2. Materials and Methods

2.1 Electrode preparation

All chemicals were commercially available and reagent grade, unless otherwise stated. A supercapacitor-grade activated carbon powder was purchased from TOB (China) having a Brunauer-Emmett-Telle (BET) specific surface area of 1,894 m²/g. A carbon black Super-P (TOB, China) was used as a conductive agent. A binder was polyvinylidene fluoride (PVdF; Sigma Aldrich, Germany). Three different separators were tested in this study: (1) A 180- μ m thick cellulose Whatman filter paper (grade 1) was used only for an aqueous electrolyte system in a Swagelok test cell, (2) A 35- μ m thick cellulose NKK TF4035 separator (Nippon Kodoshi, Japan), having 75% porosity [22] and (3) A 25- μ m thick polypropylene (PP) separator (TOB, China). The porosity of a PP separator is specified to be 43.5% [23]. A current collector was 15- μ m-thick aluminum foil having a thin layer of conductive coating (TOB, China), which promotes adhesion and electrical conductivity between aluminum foil and activated carbon film.

The procedure for electrode preparation is shown in Figure 1(a). First, the electrode paste was prepared by mixing activated carbon powders, conductive agent, and binder at the weight ratio of 90: 5: 5 in 1-methyl-2-pyrrolidinone (NMP). NMP was carefully added to adjust solid contents to be between 20 and 25 % by weight. A mixture was mixed using a vortex mixer for 15-30 min to achieve a homogeneously mixed carbon slurry. It can be noticed that a slurry flows similarly to thick honey. We report the viscosity test of our routinely formulated sample to be in the range of 3,000-5,000 cP (at the shear rate of 10 s⁻¹), and suggest the suitable viscosity range of 3,000-5,000 cP. It was noticed that if the viscosity value is over or under the proper range, it can cause peeling off or pinholes in an electrode. The carbon slurry was spread onto a sheet of current collector with a doctor blade device producing carbon film with the wet thickness of 250 μ m. A conductive-carbon coated aluminum foil was dried in an oven at 100 °C for 1 h. The dried electrode was transferred through a gap of calendering rollers to achieve a dense and uniform-thickness electrode. Calendering process was performed at room temperature with the determined gap size between 100 μ m and 20 μ m.

2.2 Pouch cell assembly

The process diagram for pouch cell assembly is shown in Figure 1 (b) and the layout showing components of a supercapacitor pouch cell is illustrated in Figure 2. The capacitor consisted of two symmetric electrodes and a sheet of separators, in Figures 2(a) and 2(b), respectively. Single-side coated electrodes were cut to the predetermined size. A separator was placed between two electrodes and on the top of the upper electrode to prevent a short circuit. Two electrodes were aligned to maximize the overlapping area of carbon coating. A stack of electrode-separator, in Figure 2(c), was folded to minimize its size, as shown in Figure 2(d). Each electrode was attached with an aluminum strip to be utilized as an electrical terminal. Firm electrical contact can be achieved by welding or mounting two parts with a metal eyelet. The assembly of electrodes and separators was inserted into a pouch bag, as shown in Figure 2(e). A pouch was constructed from a 100- μ m-thick aluminum laminated foil. It is noted that the thickness of a battery-grade laminated foil is typically 150 μ m or thicker, in order to provide packaging toughness and durability. A cell contained pouch was heat sealed, leaving another end opened for electrolyte injection. It is suggested that hot melt adhesive must be applied to promote leak-free bonding between an aluminum terminal and laminated foil. The pouch cell was further dried in a vacuum oven at 100 °C for 1 h before transferred to a glove box for electrolyte injection. This drying step is to prevent contamination of moisture,

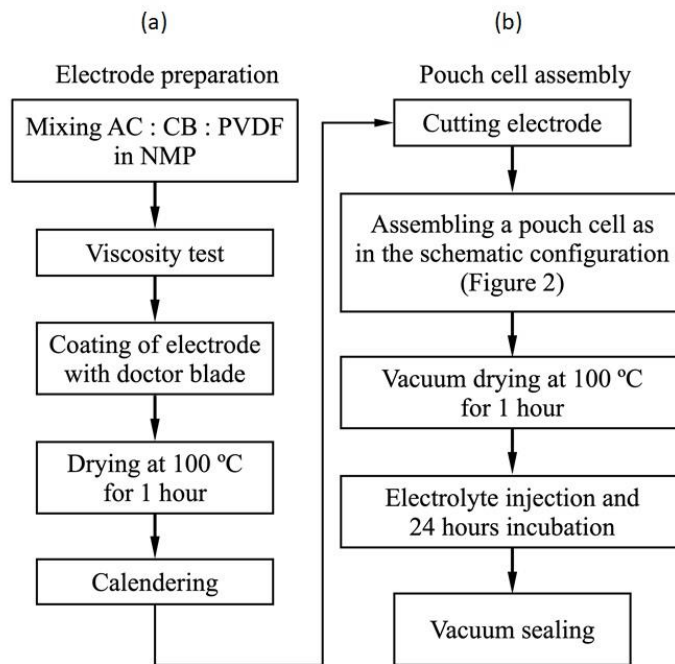


Figure 1. The flow chart of pouch cell supercapacitor fabrication: (a) electrode preparation and (b) pouch cell assembly

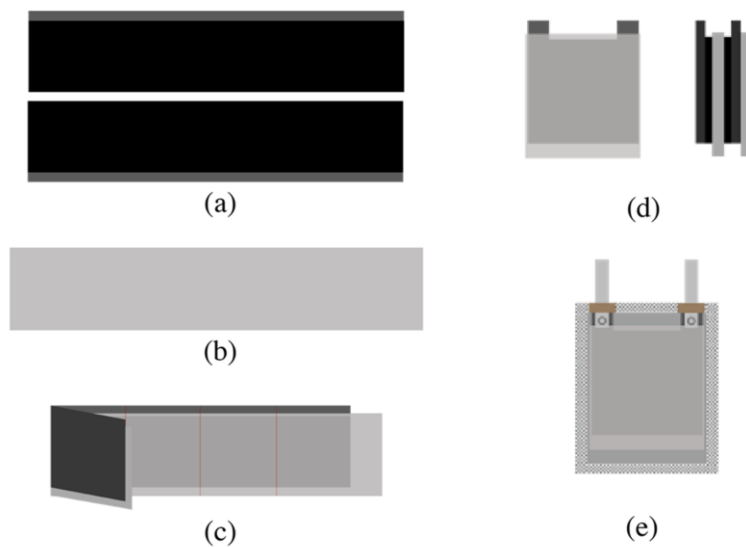


Figure 2. Layout showing components of a pouch cell supercapacitor: (a) carbon-coated electrodes, (b) a separator, (c) a stack of electrodes and separators, (d) front-view (left) and side-view (right) of a rolled cell, and (e) an assembled pouch cell

which typically causes electrolysis and deterioration of an electrode [13, 24]. In a glove box with a moisture level of less than 0.5 ppm, a pouch cell was then filled with an excess amount of electrolyte, approximately 5 ml, and sealed. In this study, 1M tetraethylammonium tetrafluoroborate (TEABF₄) in acetonitrile (ACN) or propylene carbonate (PC) was examined as organic electrolytes for a pouch cell supercapacitor. The sealed pouch cell was then incubated at room temperature for 24 h to allow impregnation of electrolyte. The pouch cell was finally vacuum sealed using a compact vacuum sealer and transferred out of a glove box for characterization.

2.3 Characterizations

Viscosity of a carbon slurry was measured in dynamic mode at the shear rate of 10 s⁻¹ and 19 °C using a Brookfield DV II+ viscometer with a SC4-29 spindle. Morphology of an electrode was investigated by using a Hitachi S3400N scanning electron microscope. For wettability test, a 5- μ l droplet of solvent, PC or ACN, was deposited on a sheet of separator, NKK or PP and observed by using a digital microscope, Dino-Lite Edge AM4815ZT, in order to measure the contact angle and estimate the capability of solvent absorption. In a study on calendering condition, a Swagelok test cell was assembled from a pair of 10-mm diameter electrodes, a Whatman filter paper separator, and 1 M Na₂SO₄ aqueous electrolyte solution to evaluate the performance of a calendered electrode. All electrochemical measurements were performed using Autolab PGSTAT204 (Metrohm Autolab B.V., Switzerland). Cyclic voltammetry (CV) was performed at 3 mV/s within the potential range of 0 and 2.5 Volt. Galvanostatic charge-discharge (GCD) was performed in the same potential range at a charge-discharging current of 0.1 A/g. Capacitance and specific capacitance were calculated from the discharging curve of GCD. Cell resistance was calculated from voltage (IR) drop feature in GCD curve.

3. Results and Discussion

3.1 Pouch cell

Photographs in Figure 3 summarize fabrication of a pouch cell made of a 210-cm² supercapacitor electrode which contains the active material of approximately 1.2 g. Carbon electrode can be casted on an Al current collector manually using a doctor blade device, in Figure 3(a). The device is capable of coating the largest area of 7.5 cm × 28 cm per batch, as shown in Figure 3(b). In order to make the electrode-separator stack more compact, the zig-zag folding is applied, as shown in Figure 3(c). After aluminum terminals are mounted to the electrodes using iron eyelets, a pre-fabricated cell is ready for pouch packaging, as shown in Figure 3(d). The complete pouch cell is shown in Figure 3(e). The pouch dimension was typically 7.5 × 9 × 0.25 cm³, while the size of stacked electrodes was 5.6 cm × 3.8 cm. Some pouch cells may be swollen after long charge-discharge cycles, as shown in Figure 3(f). It is because moisture residue in a pouch provokes generation of gases or electrolysis products. Drying an assembly before loading into a glove box and vacuum sealing a pouch cell after electrolyte injection can reduce the remaining air and moisture inside a pouch cell. Therefore, these procedures must be applied to ensure a healthy pouch cell.

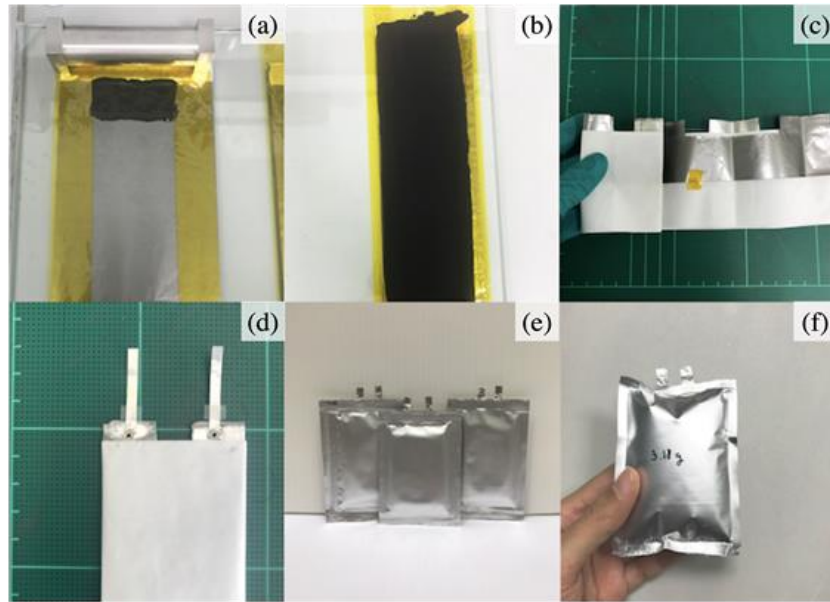


Figure 3. Photographs of an electrode (a) before and (b) after doctor blade coating of carbon slurry, (c) a stack of electrodes and a separator, (d) a rolled electrode assembly with aluminum terminals attached, (e) a sealed pouch cell, and (f) a swollen pouch cell.

3.2 Effects of calendering

Calendering, in principle, is a process to compress an electrode by passing a thick sheet of electrode through a slit of drum rollers, typically at elevated temperature. The compaction produces a flat surface, uniform thickness, and relatively dense carbon film. It promotes electrical contact between the electrode and current collector as well as activated carbon granules, which enhance conduction and accessibility of electrons throughout an electrode [16, 25]. Firm electrical contact results in increasing capacitance and reducing resistance.

In this study different calendering conditions were tested on a sheet of supercapacitor electrode to determine the suitable electrode processing. The as-coated electrode was typically non-uniform thickness. After rolling pressed using the gap comparable to the electrode thickness, 80–100 μm , it appeared partially squeezed. Complete coverage of film compaction achieved at 60 μm gap and below. The cross-section SEM images of the electrode processed without calendering, and calendering with 60 μm or 50 μm gap are shown in Figures 4(a-c), respectively. The calendered electrodes exhibited uniform thickness and significant reduction in cavity compared with the as-coated electrode. Further calendering with the smaller gap size showed no significant change in film morphology, and damages such as wrinkle on aluminum foil or peeled film started to be obviously seen. It was noticed that the thickness of the calendered electrode was greater than the gap size. The 60 μm and 50 μm calendered electrodes were measured to be 75 μm and 65 μm , respectively. It seems that the carbon electrode possesses spongy characteristic and there exists the saturated value density which may differ upon electrode materials and formulation. In the present work, the saturated density of the 90% activated carbon contained electrode is calculated to be approximately 0.7 g/cm^3 , while the thickness can vary with material loading.

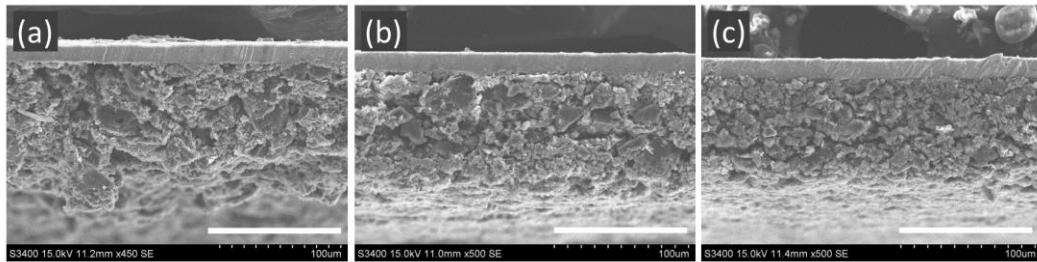


Figure 4. Cross-section SEM images of an electrode layer on aluminum foil (a) without calendaring and received calendaring with (b) 60 μm and (c) 50 μm gap; scale bars are 100 μm .

The aforementioned electrodes were further evaluated for capacitance using an aqueous electrolyte in a Swaglok test cell. Comparison of GCD of three test cells is shown in Figure 5. The specific capacitance of the control electrode, without calendaring, is 3.9 F/g. The IR drop was 70 mV, corresponding to the cell resistance of 30 Ω . For the calendered electrodes, the specific capacitance values were almost three times higher than the control electrode. They were 11.3 and 12.5 F/g for the 60 μm and 50 μm calendered electrodes, respectively. In addition, the IR drop of the calendered electrode was also relatively small. The IR drop values were 55 mV (21.5 Ω) and 42 mV (22 Ω) for the 60 μm and 50 μm calendered electrodes, respectively. There was a slight improvement in the capacitance with further calendaring. The maximum capacitance of 13.5 F/g was achieved for the case of 30 μm calendaring. The results suggest that adequate film compaction is crucial for the optimization of the electrode performance. Empirically, the 60 μm or 50 μm calendaring condition, which produces film compression of approximately 50% or greater, seems sufficient to take effect without the risk of electrode damage. As a consequence, we adopted 50 μm calendaring in procedure to make a pouch cell.

3.3 Selection of separators and solvents

Selection of separators and solvents was preliminary examined by wettability test. Images of a solvent droplet on a separator for four solvent-separator combinations are illustrated in Figure 6. The PC droplet seems to stand on a PP sheet without being adsorbed, as shown in Figure 6(a). The contact angle was measured to be 75°. The result suggests that PC performs poor wetting on the PP separator. As a result, this solvent-separator combination was rejected from further investigation. The ACN initially formed a droplet on a PP sheet with the contact angle of 50°, in Figure 6(b). It was observed that ACN was gradually absorbed into a PP substrate, suggesting the moderate wettability of PP by ACN. In the case of the cellulose separator, both PC and ACN droplets were readily absorbed into the substrate, in Figures 6(c) and 6(d), indicating the excellent wettability of the cellulose separator by both solvents. Therefore, pouch cells based on the latter three solvent-separator system were fabricated to evaluate in the next step for electrochemical performance.

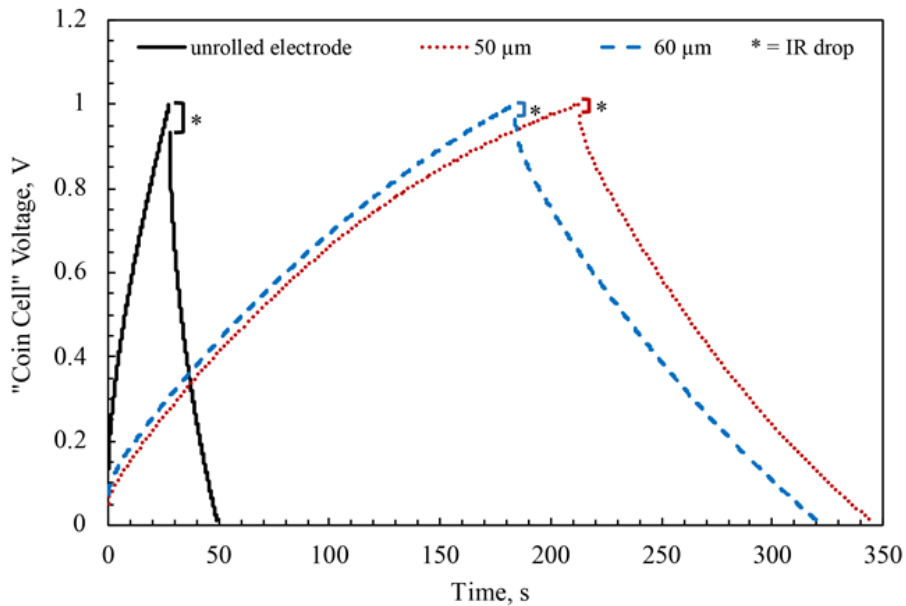


Figure 5. Comparison of GCD curves of coin cells fabricated without calendering (unrolled), calendering through 50 μm and 60 μm gaps; data were taken from the last charge-discharge curve of 5 cycles.

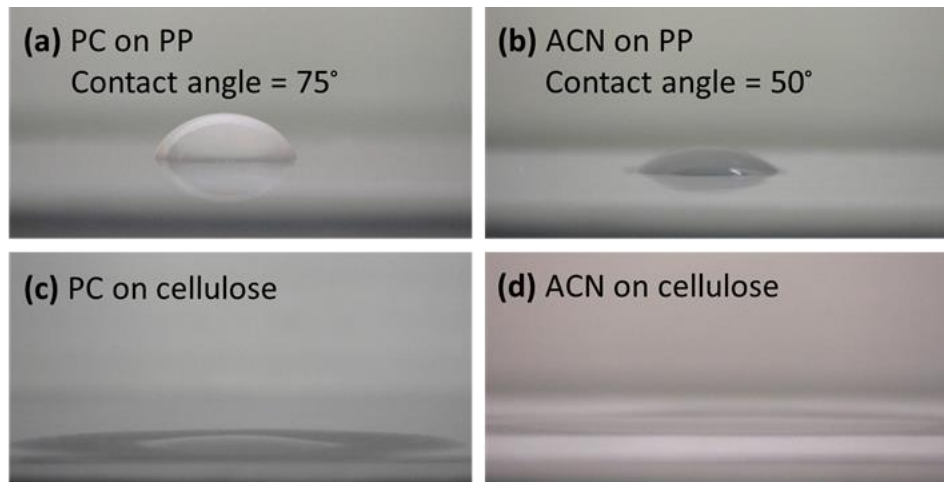


Figure 6. Photographs of a 5- μl droplet of (a) PC on PP, (b) ACN on PP, (c) PC on NKK cellulose, and (d) PC on NKK cellulose accompanied with the value of contact angle. A photograph was immediately captured after deposition of a droplet.

GCD curves of three pouch cells: a PP separator and 1M TEABF₄/ACN electrolyte (ACN-PP), an NKK cellulose separator and 1M TEABF₄/PC (PC-cellulose), and an NKK cellulose separator and 1M TEABF₄/ACN (ACN-cellulose) are presented in Figure 7. The ACN-PP shows the largest specific capacitances of 29.4 F/g and the smallest IR drop of 0.07 V, which is equivalent to the internal resistance of 0.3 Ω. The specific capacitance of the PC-cellulose and ACN-cellulose cells are 21.7 F/g and 26.3 F/g while the IR drop (internal resistance) values are 0.17 V (0.7 Ω) and 0.22 V (0.9 Ω), respectively. Although the cellulose possesses high porosity and the excellent wettability by the selected solvents which could promote ionic conductivity [13], it is found that the supercapacitor using the NKK cellulose separator tends to have less capacitance and relatively high internal resistance. As in our case the PP is thinner than the cellulose separator, one explanation could be the contribution from the thickness of a separator in which the thinner the separator is, the lower ionic resistance would be [12, 13]. Another explanation is that the hydrophilic nature and the high porosity of cellulose separator could provide rich interaction with the electrolyte solvent. Such interaction leads to swelling of the separator and a decline of cellulose mechanical strength after immersion in the electrolyte which may induce poor interfacial contact between an electrode and a separator, thus an increase in cell resistance [26]. In addition, ACN has a higher solvent reorganization energy compared to PC, which could cause additional ionic resistance in the case of the cellulose-solvent system.

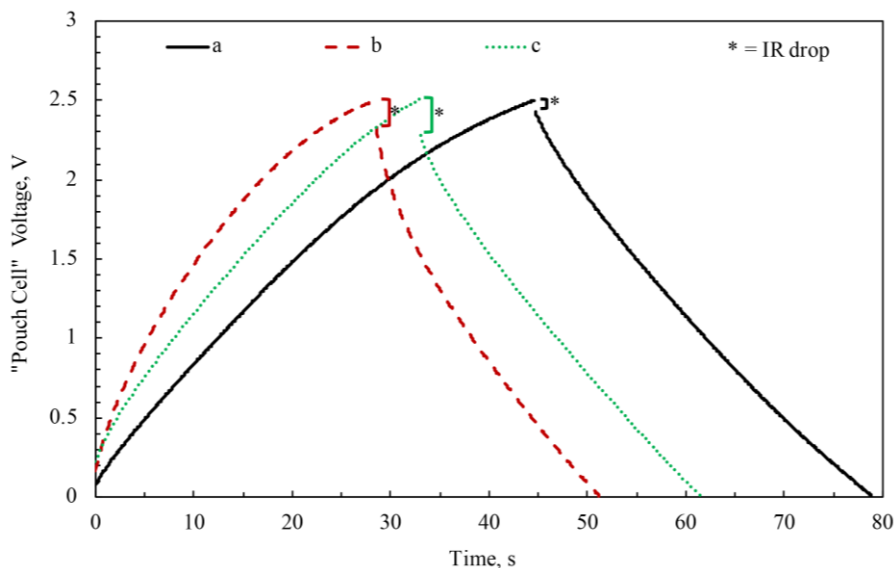
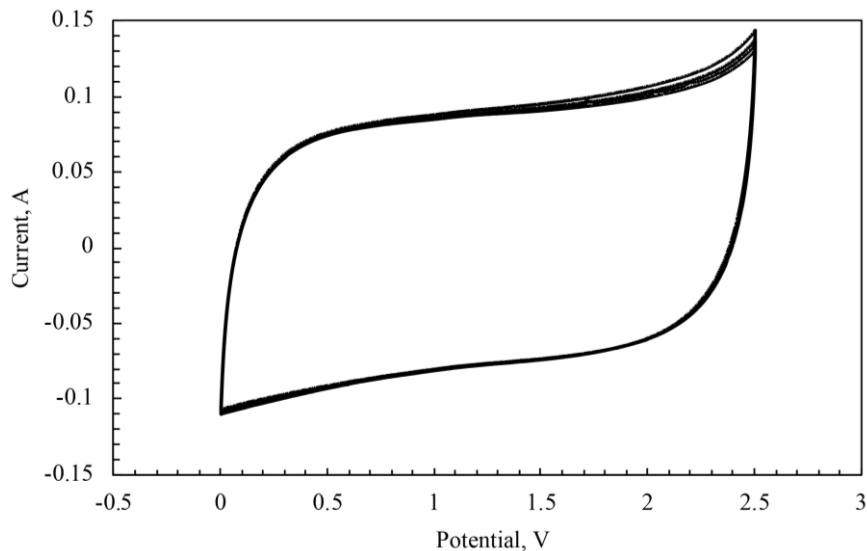


Figure 7. GCD curves of pouch cells with (a) PP separator in 1M TEABF₄/ACN, (b) cellulose separator in 1M TEABF₄/PC, and (c) cellulose separator in 1M TEABF₄/ACN

Under the scope of this study, it is suggested that ACN-PP is the best solvent-separator system for high capacitance application. The highest capacitance of 32.6 F was achieved in our optimized pouch cell. Summary of the optimized formulation and specification for the supercapacitor electrode are given in Table 1. The CV curve of a corresponding pouch cell supercapacitor is shown in Figure 8. The shape of the CV curve is almost rectangular which corresponds to the ideal EDLC in a potential range of 0 - 2.5 V. The steep tail at the upper-end potential suggests that the value of the rated voltage is limited to 2.5 V. This potential limit, rather than 2.7 V for a commercial cell, could be originated from the presence of moisture impurity.

Table 1. Formulation and specifications of an EDLC electrode in a pouch cell

Item	Both positive and negative electrode specification
Active material	90 wt.% activated carbon (TOB)
Conductive material	5 wt.% carbon black super-P (TOB)
Binder	5 wt.% polyvinylidene fluoride (PVdF: Sigma Aldrich)
Current collector	Conductive carbon coated aluminum foil (TOB)
Separator	Polypropylene (PP)
Electrolyte	1M TEABF ₄ /ACN
Electrode density	0.7 g/cm ³
Electrode porosity	65%

**Figure 8.** CV curve of pouch cell supercapacitor using electrode specified in Table 1

4. Conclusions

In this article, basic procedures to fabricate a pouch cell for a symmetric EDLC are described. Key material components and process steps are revealed, especially, the calendaring condition and the selection of separator-solvent combination have been highlighted. Detailed information provided here is aimed to encourage research community in the area of energy storage, to be capable of prototyping a large scale device and to close a gap between material research and application.

5. Acknowledgements

This project is supported by Energy Policy and Planning Office (EPPO), Ministry of Energy (Contract no. P-17-50509). Financial support from the Research Fund for DPST Graduate with First Placement (Grant no.27/2014) is also acknowledge. The authors would like to acknowledge EFS

scholarship from SIIT and the Center of Excellence in Materials and Plasma Technology, Thammasat University. Thanks to Dr. Prayoon Songsiriritthigul of the Suranaree University of Technology for helpful discussion and the Physical Characterization Laboratory, MTEC, for the support on viscosity measurement.

References

- [1] Al-Hallaj, S., Wilke, S. and Schweitzer, B., 2017. Energy storage systems for smart grid applications. In: A. Badran, S. Murad, E. Baydoun and N. Daghir, eds. *Water, Energy & Food Sustainability in the Middle East*. Cham, Switzerland: Springer.
- [2] Vazquez, S., Lukic, S.M., Galvan, E., Franquelo, L.G. and Carrasco, J.M., 2010. Energy storage systems for transport and grid applications. *IEEE Transactions on Industrial Electronics*, 57(12), 3881-3895.
- [3] Hannan, M.A., Hoque, M.M., Mohamed, A. and Ayob, A., 2017. Review of energy storage systems for electric vehicle applications: Issues and challenges. *Renewable and Sustainable Energy Reviews*, 69, 771-789.
- [4] Horn, M., MacLeod, J., Liu, M., Webb, J. and Motta, N., 2019. Supercapacitors: A new source of power for electric cars?. *Economic Analysis and Policy*, 61, 93-103.
- [5] Mejdoubi, A.E., Chaoui, H., Gualous, H., Oukaour, A., Slamani, Y. and Sabor, J., 2016. Supercapacitors state-of-health diagnosis for electric vehicle applications. *World Electric Vehicle Journal*, 8(2), 379-387.
- [6] Muyeen, S.M., Shishido, S., Ali, M.H., Takahashi, R., Murata T. and Tamura, J., 2007. Application of energy capacitor system to wind power generation. *Wind Energy*, 11(4), 335-350.
- [7] Maxwell Technologies. *Document number: 3000615-EN.2*. [online] Available at: https://www.maxwell.com/images/documents/Ultracapacitors_Overview_Flyer_3000615-2EN.pdf
- [8] Soltani, M., Ronsmans, J., Kakihara, S., Jaguemont, J., Bossche, P.V., Mierlo, J. and Omar, N., 2018. Hybrid battery/lithium-ion capacitor energy storage system for a pure electric bus for an urban transportation application. *Applied Sciences*, 8, 1176.
- [9] Iro, S.Z., Subramani, C. and Dash, S.S., 2016. A brief review on electrode materials for supercapacitor. *International Journal of Electrochemical Science*, 11, 10628-10643.
- [10] Pandolfo, A.G., Wilson, G.J., Huynh, T.D. and Hollenkamp, A.F., 2010. The influence of conductive additives and inter-particle voids in carbon EDLC electrodes. *Fuel Cells*, 10(5), 856-864.
- [11] Böckenfeld, N., Jeong, S.S., Winter, M., Passerini, S. and Balducci, A., 2013. Natural, cheap and environmentally friendly binder for supercapacitors. *Journal of Power Sources*, 221, 14-20.
- [12] Zhong, C., Deng, Y., Hu, W., Qiao, J., Zhang, L. and Zhang, J., 2015. A review of electrolyte materials and compositions for electrochemical supercapacitors. *Chemical Society Reviews*, 44, 7484-7539.
- [13] Zhong, C., Deng, Y., Hu, W., Sun, D., Han, X., Qiao, J. and Zhang, J., 2016. Compatibility of Electrolytes with Inactive Components of Electrochemical Supercapacitors. In: *Electrolytes for Electrochemical Supercapacitors*. [online] Available at: <https://www.routledgehandbooks.com/doi/10.1201/b21497-4>
- [14] Arora, P. and Zhang, Z., 2004. Battery separators. *Chemical Reviews*, 104, 4419-4462.
- [15] Liu, X., Dai, X., Wei, G., Xi, Y., Pang, M., Izotov, V., Klyui, N., Havrykov, D., Ji, Y., Guo, Q. and Han, W., 2017. Experimental and theoretical studies of nonlinear dependence of the

internal resistance and electrode thickness for high performance supercapacitor. *Scientific Reports*, 7, 45934.

[16] Dsoke, S., Tian, X., Täubert, C., Schlüter, S. and Wohlfahrt-Mehrens, M., 2013. Strategies to reduce the resistance sources on electrochemical double layer capacitor electrodes. *Journal of Power Sources*, 238, 422-429.

[17] Bhattacharjya, D., Carriazo D, Ajuria, J. and Villaverde, A., 2019, Study of electrode processing and cell assembly for the optimized performance of supercapacitor in pouch cell configuration. *Journal of Power Sources*, 439, 227106.

[18] Masarapu, C., Wang, L.P., Li, X. and Wei, B., 2012. Tailoring electrode/electrolyte interfacial properties in flexible supercapacitors by applying pressure. *Advanced Energy Materials*, 2, 546-552.

[19] Roberts, A.J., 2019. Effect of time, temperature and potential on pre-conditioning of supercapacitors. In: *ECS Meeting Abstract*, The Electrochemical Society, p. 116.

[20] Robertsa, A.J., Rubioa, I., Gonzalezb, D. and Bhagata, R., 2016. Supercapacitors: From coin cell to 800 F pouch cell. In: *ECS Meeting Abstract*, The Electrochemical Society, p. 1029.

[21] Rubioa, I., Gonzaleza, D., Stoevab, Z., Lowa, J.C.T. and Robertsa, A.J., 2017. Development and Testing of Large Format Graphene Supercapacitors, in: *Meeting Abstract*, The Electrochemical Society, p. 595.

[22] Azais, P., Tamic, L., Huitric, A., Paulais, F. and Rohel, X., 2016. *Separator Film, Its Fabrication Method, Supercapacitor, Battery and Capacitor Provided with Said Film*, US. Pat. 9,461,288.

[23] Xiamen Tob New Energy Technology Co., Ltd. *Specifications: 25um PP Film Battery Separator for Lithium Battery Research*. [online] Available at: <https://tob.en.alibaba.com>

[24] Morita, M., Noguchi, Y., Tokita, M., Yoshimoto, N., Fujii, K. and Utsunomiya, T., 2016. Influences of residual water in high specific surface area carbon on the capacitor performances in an organic electrolyte solution. *Electrochimica Acta*, 206, 427-431.

[25] Haselrieder, W., Ivanov, S., Christen, D.K., Bockholt, H. and Kwade, A., 2012. Impact of the calendering process on the interfacial structure and the related electrochemical performance of secondary lithium-ion batteries. *ECS Transactions*, 50(26), 59-70.

[26] Liu, W., Dang, Y., Xie, W. and Tang, A., 2019. Weakening of mechanical properties of cellulose separator caused by electrolyte immersion and elevated temperature. *Polymer Composites*, 40(10), 3857-3865.

Adsorbents Based on Keratin for Lead and Cadmium Removal

Viktoria Havryliak^{1*}, Vasylyna Mykhaliuk², Romana Petrina¹, Olena Fedorova¹,
Vira Lubenets¹ and Volodymyr Novikov¹

¹Department of Technology of Biologically Active Substances, Pharmacy and Biotechnology,
Institute of Chemistry and Chemical Technology, Lviv Polytechnic National University,
Lviv, Ukraine
²Laboratory of Animal Nutrition and Biosynthesis of Products,
Institute of Animal Biology NAAS, Lviv, Ukraine

Received: 15 October 2019, Revised: 27 December 2019, Accepted: 16 January 2020

Abstract

Keratins are an important source of biopolymers with high potential for application in various areas of biotechnology and biomedicine. Due to the presence of different functional groups in the structure of keratins, it can be used to bind the metal ions from aqueous solutions. Every year, tons of keratinous wastes are produced in the world especially in the wool textile industry. Therefore, the application of keratin biomaterial for the elimination of heavy metals from water is important for the environment. Our results have shown that the adsorption capacity of chemically modified keratin for Pb (II) and Cd (II) is higher than the untreated keratin and depends on pH. The highest adsorption efficiency for Pb (II) and Cd (II) was determined for sodium bisulfite-treated keratin at pH 6.0 (68.7 and 38.5% respectively). Under these conditions, Pb (II) and Cd (II) were much less adsorbed from solution by hydrogen peroxide-treated keratin (53.3 and 28.2% respectively). It is noteworthy that in the same model systems, the adsorption efficiency for Pb (II) is higher than for Cd (II). Our study showed that chemically treated keratin is a promising adsorbent for removing Pb (II) and Cd (II) ions from water solution, and would expand the application of keratin wastes.

Keywords: adsorption, cadmium, chemical treatment, keratin, lead
DOI 10.14456/cast.2020.3

1. Introduction

Anthropogenic pollution of the environment by heavy metals is becoming a priority threat to living organisms, including humans. Functioning chemical, metallurgical enterprises, and transport networks are the main factors that significantly increase the risk of heavy metal concentrations in ecosystems [1]. It is known that heavy metals can accumulate at all levels of the environmental pyramid and can be transmitted throughout the food chains. Their exposure leads to several adverse effect such as carcinogenesis, mutagenic impact, as well as toxic effect on the gastrointestinal tract, cardiovascular, endocrine, nervous, reproductive systems with the increasing risk of infertility [2].

*Corresponding author: Tel.: +38 050-431-6582
E-mail: vitahavryliak@gmail.com

Lead and cadmium are some of the biggest pollutants in the environment and their levels are constantly increasing. These heavy metals are generated into the environment mainly as a result of industrial activity and pose a serious threat to ecosystems. Thus, bioaccumulation of lead can cause impaired function of all systems in the body, especially renal, reproductive and nervous systems [3]. According to the information of the Institute for Health Metrics and Evaluation (USA) in 2017, lead exposure is the cause of 1.06 million deaths due to long-term effects on health, mainly in low- and middle-income countries [4].

Cadmium belongs to toxic ultramicroelements and its harmful effect on living organisms is manifested in very low concentrations. Bioaccumulation of cadmium in trophic chains leads to acute and chronic intoxication of living organisms, which can be accompanied by the impaired renal, central nervous system, immune system, psychological problems, etc [5]. Therefore, the urgent task is to search for an appropriate technique that can remove heavy metal ions from water with economical advantages.

There are various approaches for removing heavy metal ions from aqueous solutions such as chemical precipitation, ion exchange, reverse osmosis, filtration through semi-liquid membranes, adsorption [6]. However, their uses are often limited due to the high cost, energy costs, reagent requirements and incomplete removal of metal ions. Research data indicate that many substances of natural origin have sorbent properties [7-12]. From this point of view, biomaterials are considered as an alternative of new biosorbents when the price/efficiency ratio as well as the high adsorption capacity are taken into account. Thus, wool is characterized by the similar features. Significant advantages of keratin-based biosorbents are their availability, biodegradability, ability to regenerate [13-15].

Keratins differ from other structural proteins by the number of cysteine residues in the molecule (7-20% of the total amount). The presence of a large number of disulfide bonds is the basis for many chemical modifications of keratin that affect its physicochemical properties. Moreover, keratin contains a large number of ionized groups, in which the isoelectric point is 4-5 [16]. This characteristic provides the ability to bind heavy metals, cationic dyes, oil products from water, and some volatile substances. However, adsorption of the pollutants by keratin depends on several factors, in particular, composition of the sorbent, surface area, pH of the solution, initial concentration of the pollutants, temperature, etc [16].

It is well known that keratin is able to remove contaminants through physisorption and chemisorption. Physisorption refers to the binding of metal ions on the surface or in the pores of keratin, whereas chemisorption is related to the ability of the main functional groups to form active chemical sites for the binding of metal ions. Natural keratin is highly ordered on the molecular level mainly due to its disulfide bonds which can limit the availability of reactive sites [13]. Therefore, various treatment can provide structural changes in the molecular organization of keratin. It is known that modification of wool fibers by chemical and physical agents can significantly increase its adsorption capacity [17-19].

The simplest methods of the chemical reorganization of keratin are oxidation and reduction. Hydrogen peroxide treatment of wool caused oxidation of disulfide bonds mainly to cysteic acid residues. The advantages of hydrogen peroxide application are its efficiency, low cost, and little toxicity. At the same time, bisulfite treatment provides the reconstruction of disulfide bonds with the formation of thiol and sulfonate residues. In the current study, the adsorption of Pb (II) and Cd (II) ions from aqueous solutions by keratin-based material was determined.

2. Materials and Methods

2.1 Materials

Raw wool was selected from a farm that belongs to the Institute of Animal Breeding in Steppe regions named by M. F. Ivanov, "Askania-Nova" (Ukraine). In experiments, the samples of low quality raw wool with a mean diameter of 30 μm were used. Wool fibers were washed with neutral detergent solution, rinsed many times with deionized water and dried at $22\pm1^\circ\text{C}$. Then lipids were removed from wool surface in the Soxhlet apparatus with carbon tetrachloride for 6 h.

2.2 Preparation of keratin-based biosorbent

For improving sorption capacity, wool was treated with 10% hydrogen peroxide and 0.2 M sodium bisulfite and placed into solutions at a ratio of 1:20 (w/V) for 3 h in a thermostat at 37°C . After treatment, the fibers were washed several times with deionized water and dried at room temperature. Then, chemically modified wool was ground and the resulting powder was used as a biosorbent for removal of heavy metals from their aqueous solutions. Chemically untreated keratin served as control

2.3 Experimental setup

Stock solutions of lead and cadmium ions were prepared by dissolving lead acetate and cadmium nitrate, respectively, in deionized water. Then, working metal solutions at 100 mg/l were obtained by dilution with DI water. The pH of the solutions was adjusted with 0.1 N HCl or 0.1 N NaOH and pH was varied between 5 and 7.

Keratin biosorbent (0.5 g) was placed in plastic flasks and 50 ml of the solution with a corresponding concentration of heavy metal was added. The flasks were shaken on a rotary shaker for one h and maintained for equilibrium for 24 h. The solutions were then filtered through filter paper and the concentration of Pb (II) and Cd (II) in the filtrates were determined by atomic absorption spectrophotometry.

2.4 Analytical methods

Biosorption efficiency was estimated by the equation [20]:

$$\% = \frac{C_i - C_e}{C_i} \cdot 100\%$$

where C_i and C_e are the initial and the final concentration of Pb (II) and Cd (II) ions in the aqueous solutions.

The adsorption capacity of keratin (mg/g) was calculated using the equation [20]:

$$q = \frac{q_0 - q_1 \cdot V}{m}$$

where

q_0 - the amount of metal ions in solution before adsorption;

q_1 - the amount of metal ions in solution after adsorption;

V - a volume of solution, L;

m - a mass of biosorbent, g.

For all experiments, analytical grade chemicals were used. The obtained data were analyzed by using ANOVA test. All results are expressed as means of five measurements \pm standard error ($x \pm SE$). For all statistical calculations, the significance was considered as the value of $P < 0.05$.

3. Results and Discussion

3.1 Pb (II) removal by keratin-based adsorbents

Keratinous biomaterials were used as a sorbent for the removal of lead from aqueous solutions. The adsorption capacity of Pb (II) by keratin-based biosorbent was studied in the pH range from 5.0 to 7.0. The higher adsorption capacity for these ions was observed for chemically treated keratin in our model systems (Figure 1). Keratin treated with sodium bisulfite was characterized by the highest adsorption of Pb (II) ions from aqueous solution in all experimental series. After the treatment of keratin with hydrogen peroxide, their adsorption capacity of Pb (II) ions increased compared to the untreated keratin, but was lower than for keratin treated with sodium bisulfite.

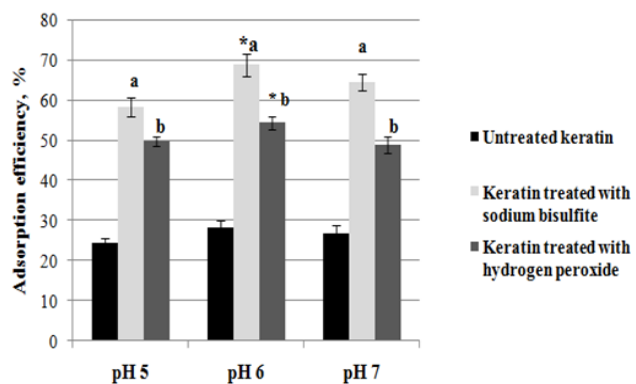


Figure 1. Adsorption efficiency of Pb (II) by keratin-based biosorbent

* - statistically significant differences between chemically treated keratin at pH 5 and pH 6;
 a - statistically significant differences between untreated keratin and keratin treated with sodium bisulfite at pH 5 – pH 7;
 b - statistically significant differences between untreated keratin and keratin treated with hydrogen peroxide at pH 5 – pH 7

When pH value was increased to 6.0, the adsorption efficiency of keratin-based sorbents also increased. It is noteworthy that under these conditions the adsorption efficiency of functionalized keratin was higher on 10.5 % for bisulfite treated keratin and on 5 % for keratin treated with hydrogen peroxide ($P < 0.05$) compared with those at pH 5.0. However, it was reported that about 88% of Pb (II) was eliminated by precipitation with a keratin solution at pH 5 and the maximum absorption of Pb(II) was 43.3 mg/g and the removal of heavy metal ions also depends on the initial concentrations in solution [21]. Our results have shown that the adsorption efficiency of untreated keratin for Pb (II) ions practically did not exceed 30%. The chemical treatment of keratin was accompanied by a significant increase in the efficiency of the removal of Pb (II) ions

from their solutions. These results indicate the increase of available functional groups on the keratin surface after treatment [22]. The better sorption properties of bisulfite-modified keratin can be explained by the formation of new thiol and sulfonate groups [23]. Some researchers believe that among different functional groups, the sulfur atoms can more readily coordinate to the heavy metal ions [24]. At the same time the lower sorption capacity of hydrogen peroxide treated keratin is obvious because of the products of cystine oxidation in the form of cysteic acid, cystine monoxide, cystine dioxide form less reactive groups [22].

Zhang *et al.* [22] have shown that chemical modification of human hair enhanced biosorption of heavy metals from solution due to the increase of surface area and the forming of new metal-binding site in the surface of keratin. According to the experimental data, the highest adsorption efficiency for Pb (II) was found for sodium bisulfite treated keratin at pH 6.0 whereas keratin treated with 10% hydrogen peroxide was slightly less bound to the Pb (II) ions. However, these results were significantly higher than untreated keratin. Similar results were observed in the study of adsorption of Pb (II) at pH 5.0 and 7.0. The data revealed that there were no significant differences between the adsorption efficiency of chemically treated keratin-based biosorbent at pH 6.0 and 7.0. Our data showed that pH is significantly influenced the adsorption processes. It is known that there is the competition of H⁺ ion adsorption with metal ions, therefore, the adsorption capacity at low pH is relatively small [25]. Our findings are consistent with the finding of Mahdavian [14] that the optimum pH at 5.8 is effective for biosorption of lead by human hair.

3.2 Cd (II) removal by keratin-based adsorbents

As can be seen in Figure 2, the adsorption capacity of Cd (II) ions by untreated keratin is quite low. After the chemical treatment with sodium bisulfite and hydrogen peroxide, the adsorption capacity of the biosorbent increases, but it significantly depends on the pH of the solution. The sorption performance of novel wool powders was studied and the optimum pH for Cu (I) and Cd (II) ions was found to be in the range of 6.0-7.0 [26].

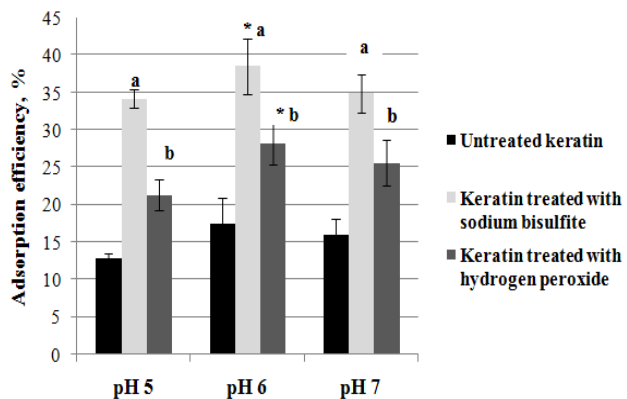


Figure 2. Adsorption efficiency of Cd (II) by keratin-based biosorbent

* - statistically significant differences between chemically treated keratin at pH 5 and pH 6;

a - statistically significant differences between untreated keratin and keratin treated with sodium bisulfite at pH 5 – pH 7;

b - statistically significant differences between untreated keratin and keratin treated with hydrogen peroxide at pH 5 – pH 7

Our study found that the adsorption efficiency of chemically-modified keratin increased at the pH 5.0 when compared with untreated keratin ($P<0.05$). With increasing pH to 6.0 the adsorption efficiency of keratin-based biosorbents increased. It is noteworthy that, as in the case of Pb (II), keratin treated with hydrogen peroxide binds Cd (II) ions less than keratin treated with sodium bisulfite. The lower adsorption efficiency of Cd (II) than Pb (II) can be explained that the size of ions influences the removal of metal ions from aqueous solution. With increasing atomic size of the metal, the adsorption becomes higher. In general, the outer shell of metals with a large atomic radius interacts more readily with proteins, including keratin [27]. It seems that with increasing pH to 6.0, the major functional groups on the keratin surface became deprotonated. As a result, the surface negative charge is increased, facilitating the binding of heavy metals [22].

According to the data presented in Figure 2, the adsorption capacity of chemically treated biosorbents did not differ at pH 5.0 and 7.0. But as in all previous results, the untreated keratin was characterized by significantly worse sorption properties compared to the modified ones. The similar results were observed for Cd (II) ions by using untreated human hair and other biofibers [22]. The adsorption efficiency of Cd (II) by untreated keratin-based biosorbent varied from 12.8 to 15.5% depending on the pH of the solution. At pH 6.0, the adsorption efficiency increased to 28.2% for keratin treated with hydrogen peroxide and 38.5% for keratin chemically modified by sodium bisulfite. Our results are in agreement with the finding that chemical treatment increases the affinity of keratin to heavy metal ions [22, 28]. Therefore, the maximum adsorption efficiencies for both Cd (II) and Pb (II) ions were observed for biosorbent based on keratin treated with sodium bisulfite. It is known that many functional groups (carboxyl, hydroxyl, amide, thiol/disulfide) were present in the structure of keratin [29]. It is obvious that the chemical treatment of keratin could lead to an increase in the functional groups on its surface. The thiol and sulfonate groups are formed as a result of the sulfitolysis enhancing the biosorption of heavy metals from solution [22].

In general, the affinity of keratin for lead ions was higher than for cadmium ions, which was due to stronger interactions between the functional groups with metal ions. On the other hand, the greater adsorption of Pb (II) can be related to its higher potential binding capacity and stability, especially of the Pb-S interaction, and, perhaps, to the greater electrostatic interactions between Pb (II) and reactive sites of chemically treated keratin. According to the Hard and Soft Acid Base Principale such ions as Pb (II) form strong bond with CN^- , R-S^- , $-\text{SH}^-$, NH_2^- , which are groups containing sulfur and nitrogen atoms, whereas Cd (II) ions could form stable bonds mainly with SO_3^{2-} , O_2^- ligands [30]. Therefore, the differences in the adsorption capacity of Pb (II) and Cd (II) by the chemically modified keratin can be explained by the competition between protons and metal ions for specific binding sites on the surface of the keratin [22, 25].

4. Conclusions

The adsorption efficiency of heavy metals by keratin-based biosorbent depends on the pH of aqueous solutions. Maximum adsorption efficiency was observed at pH 6.0 for both Cd (II) and Pb (II) ions. Chemical treatment increased the adsorption capacity of keratin-based biosorbents. The best sorption properties for Cd (II) and Pb (II) have been found for keratin treated with sodium bisulfite. Under the same conditions in model systems, the adsorption efficiency of Pb (II) ions by keratin-based biosorbents was significantly higher than for Cd (II) ions due to the stronger interactions between Pb (II) ions and reactive sites of chemically treated keratin. The current study showed that increasing the adsorption capacity of biosorbents is possible by chemical modification of keratin and optimizing the corresponding parameters of the model systems.

References

- [1] Ali, H., Khan, E. and Illahi, I., 2019. Environmental chemistry and ecotoxicology of hazardous heavy metals: Environmental persistence, toxicity, and bioaccumulation. *Journal of Chemistry*, 2019, Article ID 6730305, 1-14. <https://doi.org/10.1155/2019/6730305>.
- [2] Masindi, V. and Muedi, K.L., 2018. *Environmental Contamination by Heavy Metals*. [e-book] London: IntechOpen. Available through: <<https://www.intechopen.com/books/heavy-metals/environmental-contamination-by-heavy-metals>>.
- [3] Wani, A.L., Ara, A. and Usmani, J.A., 2015. Lead toxicity. *Interdisciplinary Toxicology*, 8 (2), 55-64.
- [4] World Health Organization, 2019. *International Lead Poisoning Prevention Week of Action*. [online] Available at: https://www.who.int/ipcs/lead_campaign/en/
- [5] Sharma, H., Rawal, N. and Mathew, B., 2015. The characteristics, toxicity and effects of cadmium. *International Journal of Nanotechnology and Nanoscience*, 3, 1-9.
- [6] Song, J., Kong, H. and Jang, J., 2011. Adsorption of heavy metal ions from aqueous solution on by polyrhodanine-encapsulated magnetic nanoparticles. *Journal of Colloid and Interface Science*, 359 (2), 505-511.
- [7] Ngwenya, S., Guyo, U., Zinyama, N.P., Chigondo, F., Nyamunda, B.C. and Muchanyereyi, N., 2019. Response surface methodology for optimization of Cd (II) adsorption from wastewaters by fabricated tartaric acid-maize tassel magnetic hybrid sorbent. *Biointerface Research in Applied Chemistry*, 9 (4), 3996-4005.
- [8] Fadillah, G., Putri, E.N.K., Febrianastuti, S., Maylinda, E.V. and Purnawan, C., 2018. Adsorption of Fe Ions from Aqueous Solution Using α -Keratin-Coated Alginate Biosorbent. *International Journal of Environmental Science and Development*, 9 (3), 82-85.
- [9] El-Gendy, M.M.A.A., Hassanein, N.M., Abd El-Hay, I.H.A. and Abd El-Baky, D.H., 2017. Heavy Metals Biosorption from Aqueous Solution by Endophytic *Drechslera hawaiiensis* of *Morus alba* L. derived from Heavy Metals Habitats. *Mycobiology*, 45 (2), 73-83.
- [10] Poonam, Bharti, S.K. and Kumar, N., 2018. Kinetic study of lead (Pb^{2+}) removal from battery manufacturing wastewater using bagasse biochar as biosorbent. *Applied Water Science*, 8, 119. <https://doi.org/10.1007/s13201-018-0765-z>
- [11] Mondal, N.K. and Basu, S., 2019. Potentiability of waste human hair towards removal of chromium (VI) from solution: kinetic and equilibrium studies. *Applied Water Science*, 9, 49. <https://doi.org/10.1007/s13201-019-0929-5>
- [12] Nodoushan, M.H., Ehrampoush, M.H., Rafati, L., Farzi, M. and Barzegar, K., 2015. Study of Co (II) adsorption from aqueous solution using protein granules produced from chicken feather. *Environmental Health Engineering and Management Journal*, 2 (4), 193-197.
- [13] Ghosh, A. and Collie, S.R., 2014. Keratinous materials as novel absorbent systems for toxic pollutants. *Defence Science Journal*, 64 (3), 209-221.
- [14] Mahdavian, L., 2012. Effects of magnetic field, pH and retention time on the lead (Pb^{2+}) adsorption by modified human hair, goat hair and sheep wool. *African Journal of Microbiology Research*, 6 (1), 183-189.
- [15] Mousavia, S.Z., Manteghiana, M., Shojaosadatib, S.A. and Pahlavazadeha, H., 2018. Keratin nanoparticles: synthesis and application for Cu (II) removal. *Advances in Environmental Technology*, 2, 83-93.
- [16] Shavandi, A., Silva, T.H., Bekhit, A.A. and Bekhit, A.E., 2017. Keratin: dissolution, extraction and biomedical application. *Biomaterials Sciences*, 5(9), 1699-1735.

- [17] Hanzlikova, S., Branisa, J., Hybler, P., Sprinclova, I., Jomova, K. and Porubska, M., 2016. Sorption properties of sheep wool irradiated by accelerated electron beam. *Chemical Papers*, 70 (9), 1299-1308.
- [18] Aluigi, A., Tonetti, C., Vineis, C., Varesano, A., Tonin, C. and Casasola, R., 2012. Study on the adsorption of Chromium (VI) by hydrolyzed keratin/polyamide 6 blend nanofibres. *Journal of Nanoscience and Nanotechnology*, 12(9), 7250-7259.
- [19] Aluigi, A., Corbellini, A., Rombaldoni, F. and Mazzuchetti, G., 2012. Wool-derived keratin nanofiber membranes for dynamic adsorption of heavy-metal ions from aqueous solutions. *Textile Research Journal*, 83(15), 1574-1586.
- [20] Khosa, M. A. and Ullah, A., 2014. In-situ modification, regeneration, and application of keratin biopolymer for arsenic removal. *Journal of Hazardous Materials*, 78, 360-371.
- [21] Sekimoto, Y., Okiharu, T., Nakajima, H., Fudjii, T., Shirai, K. and Moriwaki, H., 2013. Removal of Pb (II) from water using keratin colloidal solution obtained from wool. *Environmental Sciences and Pollution Research*, 20 (9), 6531-6538.
- [22] Zhang, H., Carillo, F., Lopes-Mesas, M. and Palet, C., 2019. Valorization of keratin biofibers for removing heavy metals from aqueous solutions. *Textile Research Journal*, 89 (7), 1153-1165.
- [23] Sinkiewicz, I., Sliwinska, A., Staroszczyk, H. and Kołodziejska, I., 2017. Alternative methods of preparation of soluble keratin from chicken feathers. *Waste Biomass Valorization*, 8, 1043-1048.
- [24] Dabrowski, A., Hubicki, Z., Podkoscielny, P. and Robens, E., 2004. Selective removal of the heavy metal ions from waters and industrial wasterwaters by ion-exchange method. *Chemosphere*, 56 (2), 91-106.
- [25] Homagai, P.L., Paudyal, H. and Ghimire, K. N., 2008. Adsorption kinetics of Pb(II), Cd(II), Zn(II) and Fe(III) onto saponified apple waste. *Journal of Nepal Chemical Society*, 23, 102-105.
- [26] Naik, R., Wen, G., Ms, D., Hureau, S., Uedono, A., Wang, X., Liu, X., Cookson, P.G. and Smith, S.V., 2010. Metal ion binding properties of novel wool powders. *Journal of Applied Polymer Science*, 115 (3), 1642-1650.
- [27] Kar, P. and Misra, M., 2004. Use of keratin fiber for the separation of heavy metal from water. *Journal of Chemical Technology and Biotechnology*, 79 (11), 1313-1319.
- [28] Khosa, M. A., Wu, J., and Ullah, A., 2013. Chemical modification, characterization, and application of chicken feathers as novel biosorbents. *RSC Advances*, 3, 20800-20810.
- [29] Zahn, H., Wortmann, F. J., Wortmann, G., Schaefer, K., Hoffmann, R. and Finch, R., 2003. Wool. In: *Ullmann's Encyclopedia of Industrial Chemistry*. Vol. 39. 6th ed. Weinheim, Germany: Wiley-VCH Verlag, pp. 525-555.
- [30] Wang, J. and Chen, C., 2009. Biosorbents for heavy metals removal and their future. *Biotechnology Advances*, 27 (2), 195-226.

Application of TOPSIS Method to Green Supplier Selection for a Thai OTOP Producer

Walailak Atthirawong

Department of Statistics, Faculty of Science, King Mongkut's Institute of Technology
Ladkrabang, Bangkok, Thailand

Received: 26 December 2019, Revised: 7 January 2020, Accepted: 23 January 2020

Abstract

In recent years, the level of consciousness and awareness of environmental problems is increasingly concerned by society, businesses and governments globally. In order to decrease hazardous environment effects, a number of organizations have been forced to improve and diminish the harmful impact of business activities in terms of production, consumption and purchasing behavior which may affect the environment. Despite environmental concern, several consumers are also willing to pay more for environmental benefits. Supplier selection is one of the most crucial parts in the decision-making process by which the companies classify, assess and select the suppliers of their required raw materials. The appropriate supplier selection will lead to environmental performance which affect the quality of final product. Thus, this paper presents an approach for evaluating and ranking suppliers with respect to traditional and environmental criteria. Such problem is regarded as multi-criteria decision making (MCMD) in nature that both qualitative and quantitative criteria have to be considered. In this study, TOPSIS method was applied to rank the green suppliers. An illustrate example in herbal cosmetics and personal care products from a Thai OTOP producer, is conducted to demonstrate how to select the most suitable supplier. A set of criteria were identified from literature review and then confirmed by the case company. The decision was made on the basis of observation of three suppliers with ten criteria. The proposed model helps the case company in finding the suitable supplier according to the operating conditions and market performance of those potential suppliers. The findings of this study could contribute a noteworthy tool to help a small enterprise in the supplier evaluation more precisely and reduce the subjective bias to some extent.

Keywords: green supplier selection, multi criteria decision making (MCMD), technique for order of preference by similarity to ideal solution (TOPSIS), Thai OTOP producer
DOI 10.14456/cast.2020.4

1. Introduction

In recent years, the world has suffered from environmental destruction, resource depletion, pollution problems and global warming everywhere. The sources of pollution vary from small unit of natural sources to large volume of emission from industrial activities [1, 2].

*Corresponding author: Tel.: +66 9-675-0621 Fax: +66 2-329-8426
E-mail: walailaknoi@gmail.com

These issues have forced manufacturing companies to protect the environment by improving their environmental performance [3]. The growing awareness and consciousness of environmental pressures has led to the emergence of sustainable development, minimizing negative impact on nature, ecology and society. In order to decrease hazardous environmental effects, it is necessary to shift from traditional practices to a more sustainable practice across sectors. As a consequence of this effort, companies today have begun to incorporate green practices in their business activities [4] with all members in the supply chain to make their products universally accepted. It is quite clear that nowadays those companies have also realized the value arising from sustainable actions from markets such as cost reduction due to a consequence of waste reduction [5], as well as competitive advantage over competitors and so forth.

Supplier selection is one of the most crucial parts in the decision-making process by which the companies classify, assess and select the suppliers of their required raw materials. The appearances of those raw materials will be the dominant factor in forming final products' features [6] which is a significant role in meeting greater customers' satisfaction, stakeholders and government [6]. Appropriate supplier selection affects the total supply chain performance and the quality of the final product [7]. As such, it is almost impossible to magnificently produce high quality products without satisfactory supplier selection, especially in today's competitive marketplace. Nevertheless, this task is very complex due to the variety of factors that must be considered during the selection process. Moreover, those factors may vary from time to time and industry to industry.

Supplier selection is a part of any business; however, selecting suitable suppliers are complicated tasks by the fact that several steps and various criteria are involved in decision making process [7]. Such criteria are both quantitative (e.g. cost) and qualitative (e.g. delivery) aspects. This kind of problem is considered as a multi-criteria decision making (MCMD) problem in nature [8]. The increasing complexity of economic and social systems also results in an increase in the complexity of the related decision problems. In relation to the literature, a number of evaluation models for supplier selection were examined and investigated. Traditional model is usually considered economy aspects as a single objective [9]. Some example models are linear programming method and total cost ownership with main emphasis on minimizing costs of production. Recently, several supplier selection problems are addressed in the literature as multiple criteria decision-making (MCMD) problems [10]. These approaches enable the simultaneous assessment of numerous measurable and non-measurable strategic and operational factors, and also allow relevant decision-makers (DMs) in the decision-making process. Analytical Hierarchy Process (AHP), Analytical Network Process (ANP), Decision-making Trail and Evaluation Laboratory (DEMATEL), VIKOR, TOPSIS, PROMOTHEE are some of examples of these approaches which have been applied in supplier selection [11].

Selection of suppliers is confronted by various criteria, as well as alternatives for the final outcome. As such, applying the right supplier selection criteria play a critical role in helping companies reach an effective result. Conventionally, price, quality and delivery are the dominant factors when considering any suppliers [12, 13]. Over the last two decades, the sustainable supplier selection has gained attention from industry practices [14, 15] by taking into account the supplier's environmental responsibility due to the competitive market and global warming concerns. Selecting green supplier is the key process of finding a sustainable partnership that will be able to provide customers with lower prices, higher quality, on-time delivery, flexibility, as well as consideration on minimizing the environmental effects [16].

The green supplier selection problem and suitable criteria selection are very important for operations and can directly affect the success of businesses [17]. On basis of the literature

analysis, there are various publications concerning supplier selection and evaluation. However, Akman and Piskin [3] claimed that most studies employed in this area are relatively limited attention on large companies such as petrochemical [18], textile industries [19] and so forth. Nielsen *et al.* [17] argued that finding specific green supplier selection criteria in specific products or different industries are important areas for investigation. Hence, in this paper multi-criteria decision making (MCDM) is employed to implement and analyze for selecting the most efficient supplier among a set of alternatives in green suppliers using a case study of One Tumbon One Product (OTOP) in Thailand. This paper investigates on the application of the proposed model that is a major contributor for a community enterprise to effectively select the best possible sustainable supplier in the global warming and the competitive environment.

2. Materials and Methods

2.1 TOPSIS method

TOPSIS (Technique for Order Preference by Similarity to Ideal Solution) was first introduced by Yoon [20] and further extended by Hwang and Yoon [21]. It is one of the multi-criteria decision making methods which attempts to rank different alternatives through numerical evaluations by the decision maker's performance with respect to certain criteria. The method tries to indicate the best alternative that simultaneously has the shortest distance from the positive ideal solution and the farthest distance from the negative ideal solution. The positive ideal solution is a solution that attempts to maximize the profit criteria and minimize the cost criteria, while the negative ideal solution is just opposed to previous one. An alternative with the maximum similarity to the ideal solution will then be selected [22].

This method is relatively simple to understand. Furthermore, it does not have strict assumptions compared to the other MCDM models such as AHP and ANP [23]. One of the benefits of TOPSIS over AHP and ANP is that the method avoids pair-wise comparison process or a consistency check. Moreover, it is simple and quick to apply and a measurable assessment accounts for both the ideal and non-ideal choices at the same time [24]. TOPSIS has been successfully applied to a wide range of application areas and industrial fields, including supply chain management and logistics, engineering and manufacturing systems, and business and marketing management [25]. Accordingly, in this paper TOPSIS method is employed to evaluate suppliers of a community enterprise based on their performance towards criteria. The steps of TOPSIS can be summarized as follows:

Step 1: Construct normalized decision matrix $R = (r_{ij})_{m \times n}$.

This step transforms various attribute dimensions into non-dimensional attributes, which allows comparisons across criteria. Vector normalization is the most frequently used methods for calculating the normalized value [26]. The procedure depends on the type of attribute.

For benefit attribute,

$$r_{ij} = x_{ij} / \sqrt{\sum_{i=1}^m x_{ij}^2} \quad (1)$$

For cost attribute,

$$r_{ij} = 1 - (x_{ij} / \sqrt{\sum_{i=1}^m x_{ij}^2}) \quad (2)$$

where $i = 1, \dots, m$; $j = 1, \dots, n$, m is the number of attribute value in each criterion, n is the number of criteria and x_{ij} is original score of decision matrix, respectively.

Step 2: Construct the weighted normalized decision matrix.

Here w_j represents a weight of each criterion for $j = 1, \dots, n$. Given $w_j \in [0,1]$ with $w_1 + w_2 + \dots + w_n = 1$. Then multiply each column of the normalized decision matrix by its associated weight to get v_{ij} . The weighted normalized decision matrix is written as equation (3):

$$v_{ij} = w_j r_{ij} \quad (3)$$

These weights can be directly determined by the decision maker or using other methods such as ROC and AHP.

Step 3: Determine the positive ideal A^* (PIS) and negative ideal solutions A' (NIS).

$$A^* = \{v_1^*, \dots, v_n^*\} = \{(\max_i(v_{ij}), j \in J) (\min_i(v_{ij}), j \in J')\} \quad i = 1, \dots, m \quad (4)$$

$$A' = \{v_1', \dots, v_n'\} = \{(\min_i(v_{ij}), j \in J) (\max_i(v_{ij}), j \in J')\} \quad i = 1, \dots, m \quad (5)$$

where J is associated with “the more, the better” or “benefit” criteria and J' is associated with “the less, the better” or “cost” criteria.

Step 4: Calculate the separation measures for each alternative from A^* and A' .

The separation measured from the ideal alternative is calculated using the m -dimensional Euclidean distance. The distance of each alternative from A^* and A' is calculated using the following formulas:

$$S_i^* = [\sum (v_j^* - v_{ij})^2]^{1/2} \quad i = 1, \dots, m \quad (6)$$

$$S_i' = [\sum (v_j' - v_{ij})^2]^{1/2} \quad i = 1, \dots, m \quad (7)$$

Step 5: Calculate the relative closeness to the ideal solution C_i^* .

$$C_i^* = S_i' / (S_i^* + S_i') \quad 0 < C_i^* < 1 \quad (8)$$

Step 6: Rank the preference order.

Rank the preference order and select the alternative with maximum C_i^* which is closest to 1 or rank alternatives according to C_i^* in descending order. The larger value of C_i^* indicates the better performance of the alternatives [25, 26].

2.2 Supplier criteria

Aforementioned studies reveal varieties of factors involving in supplier selection decisions factors. The pioneer work was done by Dickson [27] who conducted a survey with 273 US companies to identify the important factors for vendor selection. The study identified 23 criteria and revealed that product quality, on-time delivery and performance history of supplier and

warranties were the most significant factors for supplier selection. This study was re-examined by Weber *et al.* [13] via reviewing all seminal articles between 1996-1990. The results of their study illustrated that 23 criteria still remained but the ranking of those criteria had been changed.

In the last two decades, supplier selection based on environmental/green consideration has been attracted the attention of numerous researchers. For instance, Govindan *et al.* [23] studied 33 previous papers from 1996 to 2011 on green supplier selection. Later, Nielsen *et al.* [17] reviewed international journal articles from the appearance to 2013. Both studies revealed the growth of green criteria taking into consideration in supplier selection process. Some environmental aspects are green image, environmental management system, pollution control and so on.

In this study, green supplier selection criteria are summarized into ten criteria from reviewing twenty publish articles between 2010-2019 [3-4, 18, 23, 28-41]. These criteria can be grouped into two categories, i.e. economy and environmental aspects which are displayed in Table 1.

2.3 The empirical case of a Thai OTOP producer

An empirical case study of XYZ for a Thai OTOP producer, located in Samutprakarn province, is selected to illustrate the applicability of the proposed methodology. XYZ, a micro enterprise, produces herbal cosmetics and personal care products such as body cream, facial cream, hand cream, cleansing lotion, bath foam, shampoo, toothpaste and liquid soap. Products are sold to local markets though online and offline marketplace, as well as selling directly to other consumers through regional exhibitions and fairs organized by the government.

Due to the rising awareness in health and environment, it is a must for producers to provide trustfulness with high quality standard natural products to their consumers. Therefore, it is necessary that herbal in process and product from upstream to downstream has to be reassured. Selecting the right suppliers in relation to such production is very crucial. Such raw materials of XYZ are aloe, butterfly pea, purple rice, lemon-grass, peppermint oil and lime. Most local suppliers are found in the Eastern and Central parts of Thailand. Management team is responsible to plan when to produce each product as well as helping each other to find raw materials and select appropriate suppliers. Lately, XYZ considers 3 main suppliers (S_1, S_2, S_3) and also aims to develop supplier selection intensively with respect to environmentally friendly targets and natural based ingredients products.

However, at present there is no any tool to help the case company to select the proper suppliers as yet. Accordingly, development of the right supplier evaluation criteria and model is essential for this case enterprise. It will not only enable the producer to promptly deliver the quality goods, reduce its operating costs but will also take environmental issues into the consideration at the same time. The application of the proposed algorithm is divided into 5 steps i.e. 1) determination and evaluation criteria, 2) assigning weights criteria, 3) determining qualified suppliers, 4) evaluation of alternatives by implementing TOPSIS method and 5) obtaining the final rank.

Table 1. Summarization of common supplier selection criteria

Category	Criteria	Definition	References
Traditional aspects	(A) Cost	Cost of acquisitioning product including material, transportation, inventory, etc.	[18,28,29,30,31, 32,33,34, 35,36,37]
	(B) Delivery Reliability	Ability to fulfill shipping orders within the period of time promised	[18,29,33,34,35, 36, 37,38]
	(C) Quality	Meet the quality requirements	[18, 29,30,31, 32, 34,35,36,38,39,40]
	(D) Flexibility and responsiveness	Ability to tolerate the variability	[18,23,33,34]
	(E) Service capability	Ability to provide added service value	[18, 28, 29, 31,32, 33,35,36,37]
	(F) Strategic alliance	Willingness to share information, capability of building long term relationship	[33,36]
Environmental aspects	(G) Pollution control	The control of emissions and wastes into air, soil and water	[3,32,33,34,35,36,41]
	(H) Green competencies	The competencies of supplier in improving green production such as a use of environmentally friendly materials	[3, 32,33,34,35,36]
	(I) Environment Management System (EMS)	A set of systematic practices reducing environmental impacts	[3,4,18,23,31,32,34, 35,36]
	(J) Green image	Market share changes due to the adoption of environmentally friendly products or implementing green program	[3,18,32]

3. Results and Discussion

3.1 Determination and evaluation criteria

The first step is to determine criteria that will be used for the selection of alternatives or suppliers. An interview process is the important source to gain insight for the case practices. Regarding data collection of the case company through interviews and inquiries compared with those reported in the literature, the company owner was asked whether those attributes were appropriate for the company in the supplier selection. The case company has agreed with those 2 main categories with 10 criteria from the published literature, as mentioned in Table 1. However, some of those criteria are still at the beginning stage for implementation with suppliers.

3.2 Assigning weight criteria

First, five experts (three of them were management team of XYZ, one of them was a government officer who has responsibility to promote OTOP products in Thailand and the rest was a key customer of this company) were selected to involve in the process. They were asked to give their evaluation to those ten criteria according to their importance using score 1 to 10. One means that criteria were the least importance, whereas 10 means that criteria were the most importance. Then, Rank Order Centroid (ROC) technique [42] was employed to calculate weights of those criteria. ROC is simple, easy to follow and practical for determining criteria weight. According to Morais and de Almeida [43], it was found that ROC performed better than other approximate weights, i.e. Rank sum (RS), Rank reciprocal (RR) and Equal weight (EW) via testing with simulation study. Hence, it is widely applied in multi-criteria models in dealing with imprecise information [44].

Table 2 shows the results of important weights of the criteria provided by ROC and the ranking. It reveals that quality (C), cost/price (A) and pollution control (G) are the top three important criteria in the supplier selection process identified by ROC technique for this community enterprise.

Table 2. Weight and rank criteria

Criteria	Weight	Rank
(A) Cost/Price	0.192897	2
(B) Delivery reliability	0.109563	4
(C) Quality	0.292897	1
(D) Flexibility and responsiveness	0.033611	8
(E) Service capability	0.021111	9
(F) Strategic alliance	0.047897	7
(G) Pollution control	0.142897	3
(H) Green competencies	0.064563	6
(I) Environment management system (EMS)	0.010000	10
(J) Green image	0.084563	5

3.3 Determining qualified suppliers

The XYZ examined three main suppliers which were labeled as S_1 , S_2 and S_3 . The assessment was conducted in form of 1-10 scale (1-lowest performance,..., 10-highest performance according to ten criteria mentioned herein with the evaluation criteria being recorded as A, B, C,...J. Three key decision-makers from XYZ producer, i.e. the owner (DM_1), a financial manager (DM_2) and a purchasing manager (DM_3), were involved in the decision making process [45]. Practically, they are only three people in this community enterprise who take a responsibility for material management due to the small size of business. The results of the assessment of each supplier with respect to the ten criteria are displayed in Table 3.

Table 3. Input values of the TOPSIS analysis

Criteria	DM ₁			DM ₂			DM ₃		
	S ₁	S ₂	S ₃	S ₁	S ₂	S ₃	S ₁	S ₂	S ₃
A	8	7	6	10	9	8	9	9	8
B	9	9	7	9	8	7	8	8	7
C	8	9	6	8	10	5	9	10	8
D	7	7	8	8	8	7	7	7	7
E	8	9	8	7	8	10	7	7	9
F	9	8	6	9	9	7	7	9	5
G	8	7	7	9	8	8	10	7	7
H	9	8	7	9	9	7	8	8	6
I	6	6	6	7	7	6	8	8	7
J	8	8	7	7	7	7	7	7	6

3.4 Evaluation of alternatives by implementing TOPSIS method

The first step is to construct a normalized decision matrix using equations (1) and (2). After that a weighted normalized decision matrix is calculated using equation (3). The results are provided in Table 4.

Table 4. Weighted normalized decision matrix

	S ₁	S ₂	S ₃	A*	A'
A	0.0714	0.0804	0.0939	0.0714	0.0939
B	0.0683	0.0656	0.0551	0.0683	0.0551
C	0.1713	0.1987	0.1302	0.1987	0.1302
D	0.0194	0.0194	0.0194	0.0194	0.0194
E	0.0110	0.0120	0.0135	0.0135	0.0110
F	0.0297	0.0309	0.0214	0.0309	0.0214
G	0.0937	0.0763	0.0763	0.0937	0.0763
H	0.0407	0.0391	0.0313	0.0407	0.0313
I	0.0060	0.0060	0.0054	0.0060	0.0054
J	0.0503	0.05023	0.0457	0.0503	0.0457

3.5 Obtaining the final rank

After determining the weighted normalized decision matrix, the ideal and negative ideal solutions are computed using equations (4) and (5). Then the Euclidean separation distance between the positive ideal solution (A*) and the negative ideal solution (A') for each alternative are calculated using equations (6) and (7) in order to find the relative closeness to the ideal solution (C_i^*), which is shown in Table 5. Lastly, the closeness coefficient of each supplier is estimated, as presented in Table 6.

Table 5. Euclidean separation distance

Supplier	S _i ^*			S _i '		
	S ₁	S ₂	S ₃	S ₁	S ₂	S ₃
Total	0.0276	0.0198	0.0767	0.0534	0.0719	0.0025

Table 6. Closeness coefficients and supplier ranking

Supplier	S ₁	S ₂	S ₃
C _i *	0.6596	0.7837	0.0315
Ranking	2	1	3

4. Conclusions

Green supplier selection problem is still relatively new concept in Thailand, especially for SMEs and micro enterprises. However, in recent years a number of companies have started to realize the importance of sustainability due to an increasing awareness in environmental production and its long term effect on businesses' performance and marketing issue [8]. It is obvious that the choice of green suppliers relates to the long term development of any business. This research proposes the TOPSIS method for solving a real world OTOP producer in the selection of supplier with the incorporation of environmental requirements. TOPSIS is a good management tool for handling both qualitative and qualitative assessments of such problems. The foundation of TOPSIS is grounded on the logic of defining the positive ideal solution and the negative ideal solution points.

The decision making process involves multiple and conflicting criteria. Those criteria for green supplier selection of XYZ were firstly identified based on the published literature. With the validation of key experts in the case company, possible green supplier selection criteria were identified and ranked. According to Rank Order Centroid (ROC) technique, it reveals that quality (C), cost/price (A) and pollution control (G) are major influencing criteria for the XYZ to evaluate green suppliers. It could be concluded that 'S₂' is the best alternative supplier, followed by 'S₁' and 'S₃', respectively. The research demonstrates that this method can objectively evaluate criteria of listed green suppliers in the herbal cosmetics and personal care products producer, which is a small scale enterprise. The study indicates that TOPSIS can be used as a decision support model for making effective choice and could reduce subjective bias from decision makers in some extend [25].

Also, this study has shown some limitations that can provide opportunity for further study in this area. One of the limitations is that only a real case study is demonstrated, which limited to three suppliers. Moreover, these suppliers were determined by three related management team according to ten criteria. With the development of sustainability supply chain management, a social performance aspect could be incorporated in supplier selection for future studies [32]. Furthermore, another technique such as Structural Equation Modeling (SEM) could be employed to identify criteria and their sub-criteria from a group of community enterprises around the country. Analytical Hierarchy Process (AHP) could also be further employed to weight the importance of those factors in order to observe the changing of the results with respect to the changing of weights criteria. In addition, the proposed model of this study could be extended by taking fuzzy environments into consideration in order to deal with the imprecise judgments, and the ambiguity of human being's judgment [36]. Consequently, the efficiency of the evaluation could precisely be increased.

5. Acknowledgements

The work was financially supported by the Faculty of Science, King Mongkut's Institute of Technology Ladkrabang (Small Project Funding 2562-01-05-33). The author is grateful to a case company who was kindly involved and provided valuable and fruitful information for this study.

References

- [1] Robinson, D.L., 2005. Air pollution in Australia: Review of costs, sources and potential solutions. *Health Promotion Journal of Australia*, 16, 213-220.
- [2] Habre, R., Coull, B., Moshier, E., Godbold, J., Grunin, A., Nath, A., Castro, W., Schachter, N., Rohr, A., Kattan, M., Spengler, J. and Koutrakis, P., 2014. Sources of indoor air pollution in New York city residences of asthmatic children. *Journal of Exposure Science and Environmental Epidemiology*, 24, 269-278.
- [3] Akman, G. and Piskin, H., 2013. Evaluating green performance of suppliers via analytic network process and TOPSIS. *Journal of Industrial Engineering*. [online] Available at: <http://dx.doi.org/10.1153/2013/915241>
- [4] Kannan, D., Jabbour, A.B.L. and Jabbour, C.J.C., 2014. Selecting green suppliers based on GSCM practices: using fuzzy TOPSIS applied to a Brazilian electronics company. *European Journal of Operations Research*, 233(2), 432-447.
- [5] Rao, P. and Holt, D., 2005. Do green supply chains lead to competitiveness and economic performance?. *International Journal of Operations and Production Management*, 25(9), 898-916.
- [6] Molamohamadi, Z., Ismail, N., Leman, Z. and Zulkifli, N., 2013. Supplier selection in a sustainable supply chain. *Journal of Advanced Management Science*, 1(3), 278-281.
- [7] Onder, E. and Dag, S., 2013. Combining analytical hierarchy process and TOPSIS approaches for supplier selection in a cable company. *Journal of Business & Finance*, 2(2), 56-74.
- [8] Grover, R., Rao, V.B. and Kejriwal, K., 2016. Supplier selection using sustainable criteria in sustainable supply chain management. *International Journal of Social, Behavioral, Educational, Economic, Business and Industrial Engineering*, 10(5), 1775-1779.
- [9] Luthra, S., Kumar, V., Kumar, S. and Haleem, A., 2011. Barriers to implement green supply chain management in automobile industry using interpretive structural modeling technique: an Indian perspective. *Journal of Industrial Engineering and Management*, 4(2), 231-257.
- [10] Zarbini-Sydani, A., Karbasi, A. and Atef-Yekta, E., 2011. Evaluating and selecting supplier in textile industry using hierarchical fuzzy TOPSIS. *Indian Journal Science and Technology*, 4(10), 1322-1334.
- [11] Lin, C. T., Chen, C. B. and Ting, Y. C., 2011. An ERP model for supplier selection in electronics industry. *Expert Systems with Applications*, 38, 1760-1765.
- [12] Cheraghi, S.H., Dadashzadeh, M. and Subramaniam, M., 2004. Critical success factors for supplier selection: An update. *Journal of Applied Business Research*, 20(2), 91-108.
- [13] Weber, C., Current, J. and Benton, W., 1991. Vendor selection criteria and methods. *European Journal of Operations Research*, 50, 2-18.
- [14] Esfahbodi, A., Zhang, Y. and Watson, G., 2016. Sustainable supply chain management in emerging economies: Trade-offs between environmental and cost performance. *International Journal of Production Economics*, 181, 350-366.

- [15] Schoenherr, T., Modi, S.B., Benton, W.C., Carter, C.R., Choi, T.Y., Larson, P.D., Leenders, M.R., Mabert, V.A., Narasimhan, R. and Wagner, S.M., 2012. Research opportunities in purchasing and supply management. *International Journal of Production Research*, 50(16), 4556-4579.
- [16] Lee, A.H.I., Kang, H.Y., Hsu, C.F. and Hung, H.C., 2009. A green supplier selection model for high-tech industry. *Expert System with Applications*, 36, 7917-7927.
- [17] Nielsen, I.E., Banaeian, N., Golin'ska, P. Mobli, H. and Omid, M., 2014. Green supplier selection criteria: From a literature review to a flexible framework for determination of suitable criteria. In : P. Golinska, ed. *Logistics Operations, Supply Chain Management and Sustainability*. Springer. Eco Production, pp. 79-100.
- [18] Sayfi, P. and Nikbakht, M., 2016. Identification and ranking green supplier selection criteria using one-sample T-test and FANP methods: A case study for petrochemical industry. *Journal of Modern Processes in Manufacturing and Production*, 5(1), 53-67.
- [19] Acar, E., Kilic, M. and Guner, M., 2015. Measurement of sustainability performance in textile industry by using a multi-criteria decision making method. *Tekstil ve Konfeksiyon*, 25(1), 1-8.
- [20] Yoon, K., 1980. *Systems selection by multiple attribute decision making*. Ph.D. Kansas State University.
- [21] Hwang, C.L. and Yoon, K.P., 1981. *Multiple Attribute Decision Making: Methods and Applications: A State-of-the Art Survey*. New York: Springer-Verlag.
- [22] Yoon, K.P. and Hwang, C.L., 1995. *Multiple Attribute Decision Making: An Introduction*. London: Sage Publication.
- [23] Govindan K., Khodaverdi, R. and Jafarian, A., 2013. A fuzzy multi criteria approach for measuring sustainability performance of a supplier based on triple bottom line approach. *Journal of Cleaner Production*, 47, 345-354.
- [24] Mohammed, A., Harris, I., Soroka, A., Mohamed, N. and Ramjaun, T., 2018. Evaluating Green and Resilient Supplier Performance: AHP-Fuzzy Topsis Decision-Making Approach. *Proceedings of the 7th International Conference on Operations Research and Enterprise Systems (ICORES 2018)*, 209-216.
- [25] Behzadian, M., Otaghsara, S. K., Yazdani, M. and Ignatius, J., 2012. A state-of-the-art survey of TOPSIS applications. *Expert Systems with Applications*, 39, 13051-13069.
- [26] Roszkowska, E., 2011. Multi-criteria decision making models by applying the topsis method to crisp and interval data. *Multiple Criteria Decision Making*, 6, 200-230.
- [27] Dickson, G.W., 1966. An analysis of vendor selection systems and decisions. *Journal of Purchasing*, 2(1), 5-17.
- [28] Awasthi, A., Chauhan, S.S. and Royal, S.K., 2010. A fuzzy multicriteria approach for evaluating environmental performance of suppliers. *International Journal of Production Economics*, 126, 370-378.
- [29] Ho, W., Xu, X. and Dey, P.K., 2010. Multi-criteria decision making approaches for supplier evaluation and selection: A literature review. *European Journal of Operational Research*, 202, 16-24.
- [30] Thiruchelvam, S. and Tookey, J.E., 2011. Evolving trends of supplier selection criteria and methods. *International Journal of Automotive and Mechanical Engineering*, 4, 437-454.
- [31] Gurel, O., Zafer, A., Onden, I. and Gumus, I., 2015. Determinants of the green supplier selection. *Procedia - Social and Behavioral Sciences*, 181, 131-139.
- [32] Sivaprakasam, R., Selladurai, V. and Sasikumar, P., 2015. Integrating environmental factors in the suppliers assessment using analytic hierarchy process as a decision making tool. *Journal of Materials Environmental Science*, 6 (8), 2097-2104.

- [33] Rabieh, M., Rafsanjani, A., Babaei, L. and Esmaeili, M., 2019. Sustainable supplier selection and order allocation: An integrated delphi method, fuzzy TOPSIS, and multi-objective programming model. *Scientia Iranica Transactions E: Industrial Engineering*, 6(4), 2524-2540.
- [34] Song, W., Chen, Z., Liu, A., Zhu, Q., Zhao, W., Tsai, S. and Lu, H., 2018. A Study on Green Supplier Selection in Dynamic Environment. *Sustainability*, 10 [online] Available at: <https://www.mdpi.com/journal/sustainability>
- [35] Quan, J., Zeng, B. and Liu, D., 2018. Green Supplier Selection for Process Industries Using Weighted Grey Incidence Decision Model, *Complexity*, 1-12. <https://doi.org/10.1155/2018/4631670>.
- [36] Uluta, G.A., Topal, A. and Bakhsh, R., 2019. An application of fuzzy integrated model in green supplier selection. *Mathematical Problems in Engineering*. <https://doi.org/10.1155/2019/4256359>.
- [37] Phumchusri, N. and Tangsiriwattanam S., 2019. Optimal supplier selection model with multiple criteria: A case study in the automotive parts industry. *Engineering Journal*, 23(1), 191-203.
- [38] Kuo, R., Wang, Y. and Tien, F., 2010. Integration of artificial neural network and MADA methods for green supplier selection. *Journal of Cleaner Production*, 8(12), 1161-1170.
- [39] Buyukozkan, G. and Cifci, G., 2012. A novel hybrid MCDM approach based on fuzzy DEMATEL, fuzzy ANP and fuzzy TOPSIS to evaluate green suppliers. *Expert System with Applications*, 39, 3000-3011.
- [40] Dai, J. and Blackhurst, J., 2012. A four-phase AHP-QFD approach for supplier assessment: a sustainability perspective. *International Journal of Production Research*, 50(19), 5474-5490.
- [41] Hashemi, S.H., Karimi, A. and Tavana, M., 2015. An integrated green supplier selection approach with analytic network process and improved Grey relational analysis. *International Journal of Production Economics*, 159, 178-191.
- [42] Roszkowska, E., 2013. Rank ordering criteria weighting methods-a comparative overview. *Optimum Studia Ekonomiczne*, 5(65), 14-33.
- [43] Morais, D.C. and de Almeida, A.T., 2007. Group decision-making for leakage management strategy of water network. *Resources, Conservation and Recycling*, 52(2), 441-459.
- [44] Hutton, B.F., 1992. Electing a best multiattribute alternative with partial information about attribute weights. *Acta Psychologica*, 80(1-3), 91-103.
- [45] Banaeian, N., Mobli, H., Nielsen, I.E. and Omid, M., 2015. Criteria definition and approaches in green supplier selection-a case study for raw material and packaging of food industry. *Production & Manufacturing Research*, 3(1), 149-168.

Recent Evaluations and Applications of a Cassava Model in Thailand: A Review

Benjamas Kumsueb* and Attachai Jintrawet

Center for Agricultural Resource System Research, Faculty of Agriculture,
Chiang Mai University, Chiang Mai, Thailand

Received: 6 August 2019, Revised: 8 September 2019, Accepted: 22 November 2019

Abstract

Cassava is an important economic crop in Thailand. The cassava simulation model, under the Crop Simulation Model of Decision Support System for Agrotechnology Transfer package (DSSAT-CSM), has been evaluated and widely applied to simulate, evaluate and predict cassava production systems and related policy scenarios. This is the first review on the system modeling and simulation approach on cassava studies in Thailand, with an emphasis on its applications and future research directions. Various research teams were also trying to explore the site-specific technology, but still in the early stage of development. Availability of reliable data sets for model calibration and evaluation is one of the main issue that users are facing with. Therefore, future needs on the development of reliable input data sets for model testing under diverse cassava production ecosystems in Thailand are required.

Keywords: DSSAT, CSM, CROPSIM-Cassava, simulation, model, Thailand
DOI 10.14456/cast.2020.5

1. Introduction

Agricultural systems are modified natural ecosystems with complex interactions of abiotic and biotic resources and researchers are generating technical knowledge and practical solutions to maintain positive interactions and to make informed agricultural decisions. Therefore, it is imperative and need to consider the interactions of agricultural production, natural resources and human factors [1] with reliable research and practice tools. Cassava is a valuable subsistence food crop for approximately 500 million farmers [2]. In Thailand, cassava is a crop for small-scale farmers. The main planted area is in Northeastern part of Thailand. In 2017, the total cassava planted area covered 1.39 million ha and produced 27.4 million tons of fresh storage root with an averaged fresh storage root yield of 21.4 ton per ha. In the same year, various cassava products generated an export value of 92,100 million Baht [3]. Thailand has utilized cassava for chips, pellets and high value-added products including tapioca pearls, modified starch, sweeteners, organic acid, sugar alcohols and alcohols, for well-developed industry and market. These products are supplied for both local and export markets and value-chains [3].

*Corresponding author: E-mail: bkumsueb@yahoo.com

The importance of improving cassava productivity and the welfare of small-scale farmers regarding sustainable agricultural development is unquestioned. However, there are threats to any effectiveness of effort resulting from the complexity matters. Thus, crop simulation models can be used to test the diverse suitability and to provide decisions at the farm level to the regional level for perceiving and forecasting overall agroecosystem performance [4-5].

2. Decision Support System for Agrotechnology Transfer Model

Decision Support System for Agrotechnology Transfer (DSSAT) is a set of the application programs that consists of dynamic crop growth simulation models for over 40 crops. It is based on various tools and ranges of crops for researchers to enable an experiment for all crop from diverse weather, soil, genetics, crop management and sets of experimental and example data. [6]. It has been used for many purposes from utilities for on-farm precision crop management to regional to assess various risks. Cassava is one of the crops included in the priority list for model development. The International Benchmark Sites Network for Agrotechnology Transfer (IBSNAT) has launched this crop module to improve the transfer of technology to less developed countries [7].

In 1983, the first crop modeling workshop was held in Venezuela for a common database of the model such as input standardization and output structure. The models (programmed in FORTRAN), databases (.dbf or dBASE format) and an application program (in BASIC) were combined into a computer software called the Decision Support System for Agrotechnology Transfer (DSSAT) [8]. The first version of cassava model was launched (v2.1) in 1989; additional releases were made in 1994 (v3.0) [9], 1998 (v3.5), 2002 and 2004 (v4B), 2005 (v4.02), 2008, 2010 and 2011 (v4.5B), 2012 (v4.6) and 2017 (v4.7) [7].

2.1 Primary component of DSSAT model

The model contains the main driver program, a land unit module and modules for the primary components that make up a land unit in the cropping system. The primary modules consist of: 1) Management module, 2) Soil module, 3) Weather module, 4) Soil-plant-atmosphere module, and 5) Plant module. In the plant module, there are sub-modules such as CROPGRO (for grain legumes, vegetables, and fiber crops), CROPGRO-Perennial Forage, CERES-Maize, Sweetcorn, Rice, Sorghum, Millet, Wheat and Sugar-beet, IXIM, SUBSTOR-Potato, AROID-Taro and Tuber, YUCA-Cassava, CROPSIM-Cassava, CANEGRO-sugarcane and ALOHA-pineapple [6, 10-12].

2.2 Modes of DSSAT model operation

Different types of applications are performed by using different modes using DSSAT-CSM model. The basic mode performs the interactive sensitivity analysis and the comparison of simulated and observed field data. A second mode of operation simulate crops to evaluate the effects of uncertain weather conditions and to provide information for decision by using a number of years of weather under the same soil initial conditions. A third mode operates the simulation of crop rotations over a number of years, and soil conditions for cropping system management. A fourth mode simulates for precision agriculture, land use management or other spatial-based applications [6]. It was consequently developed to generate plausible predictions for practical options to improve productivity and farm performance [11].

2.3 Minimum data set

A crop simulation model under DSSAT package needs the minimum data set for model calibration and evaluation, following the standard of input and output file structure such as data for site, weather, soil and crop management [5]. The calibration phase was based on time-series and end-of-season samplings of crop developmental stages, biomass of cassava plant parts collected from well-designed field experiments. Field observations required for this phase are the date of key cassava phenological stages, including branching dates and storage root yield. The genetic coefficients of a given cassava variety were derived using GENCALC or GLUE utilities. The evaluation phase requires four minimum data set, namely; 1) Weather data during the growing season, 2) Site soil profile and soil surface data, 3) Crop management data, and 4) Observed data from the field experiment [12]. Thus, these data sets should not have been used for the previous calibration but should represent the complete array of environments and crop sequences for which model has to be performed [6], for example, from different planting dates, years, water and nitrogen management practices.

2.4 Benefit of DSSAT model

All levels of agricultural decision making need the relevant information to collectively handle with the demands of agricultural products that are increasing rapidly. The traditional research methods and dissemination of information are not sufficient to generate new knowledge to meet these needs. The applications of crop simulation models under DSSAT package to a research program can provide a number of advantages such as identification of knowledge gaps, generation and testing of hypotheses and an aid to the specific experiments, determination of the sensitivity of a system, provision of a medium for better cooperation between researchers in different disciplines and bringing all stakeholders to solve common problems in a given situation [13].

3. Development of CROPSIM-Cassava application in Thailand

In Thailand, crop model has been used to develop for site-specific recommendations of fertilizer management for small holder farmers growing crops such as rice, cassava, maize and sugarcane. Cassava is an important economic crop that can adapt well in poor fertile soil, requires low inputs and it is a famous crop for smallholder farmers [6]. Improving crop productivity focuses on choosing suitable cassava cultivar and applying good cultural practices for a given site and area as well as to maintain the certain cassava production capacity have been done over time. The development of the cassava model has been applied in some key issues in Thailand. Here we presented three applications related to its applications.

3.1 Genetic coefficient (GC)

The application of DSSAT model on cassava has been used in both research institute and university such as Department of Agriculture, Kasetsart University, and Khon Kaen University. The DSSAT-cassava simulation model, called “GUMCAS” [14-15], was first used in Thailand. It was applied to study growth, phenology and the estimation of genetic coefficients in four cassava cultivars, namely; Rayong 1, Rayong 5, Rayong 90 and Kasetsart 50. Subsequently, the derived GCs were applied to calibrate and evaluate the model. The result showed that the model gave a reasonable prediction of phenology, the first branching date and storage root dry matter yield for Rayong 90 cassava variety. However, the model overestimated yield of Rayong 90 and Rayong 5 cassava variety. In the

application phase, the model provided site-specific variety recommendation. Rayong 90 is suitable to plant on Satuk and Korat soil series and Kasetsart 50 for Yasothon soil series [16-18, 8]. The modification of Mcol-1648GC data was set to evaluate growth and yield of three cassava cultivars, namely; Rayong 9, Kasetsart 50 and Huay Bong 80 in early and late dry season. The model provided good simulations of growth and yield. In addition, it provided a fair prediction for mid rainy planting dates [19].

3.2 Climate change

The DSSAT model and Geographic Information System (GIS) were applied to understand the impact of global warming on cassava production areas throughout the country during 1980-2099, using the CropDSS 1.0 shell. The result showed that cassava yield was decreased by 43% from 1980s (based year period). In addition, there was the fluctuation in temporal and spatial of the future climate system by 33%. Consequently, cassava yield was also much affected by climate change scenarios under the study [20].

3.3 Site-specific technology

The application of DSSAT-Gumcas model for the assessment of site-specific technology was done on seven cassava cultivars, namely; Rayong 5, Rayong 90, Rayong 7, Rayong 72, Rayong 9, Rayong 11 and Kasetsart 50. The model can predict the storage root yield of those cassava cultivars depending on the conditions of each tested site based on climate, soil series and planting season and the model can be used as a tool to provide information of site-specific production options [4, 21]. The calibration of Kasetsart 50 for selected Thai cassava production conditions to determine nitrogen requirements of cassava, and to evaluate the requirements, the minimum data set of GC was used. The model gave good estimation of first branching, top root weight, dry root yield, leaf area index (LAI) and harvested root N concentration. The model gave reasonable prediction of dry root yield in the range from 0 to 250 kg N ha⁻¹. The rate of nitrogen that greater than 300 kg N ha⁻¹ gave low yield, which was not adequately predicted from developed GC data set [22]. The determination of the optimum N fertilizer rate in representative soils of Thailand for cassava, namely; Satuk (Suk), Pak Chong (Pc), Ban Bueng (Bbg) and Don Chedi (DC) soil series, showed the maximum cassava storage root yield could be obtained with the application of urea at the rate of 187.5 kg ha⁻¹ and gave significant net revenue increased ranging from 54 to 211%. In addition, the prediction on the relationships of physiological characteristics and storage root yield of three cassava cultivars, namely; Rayong 9, Rayong 11 and Kasetsart 50 under three N fertilizer rates was 46.9, 90.0 and 133.2 kg N ha⁻¹, respectively. The result showed that higher N rates resulted in a higher positive effect of N fertilizer application on cassava growth [23-24]. The variation of soil properties and weather conditions in each region could result in the difference of response to N fertilizer application and maximum fresh root yield [19].

4. General Discussion

Crop simulation model can help researchers from various disciplines to co-develop hypotheses for improving crop management options by making appropriate decisions, developing improved cultural practices and management strategies. It can also be used to support the planning process to link the implementing agencies and policy levels for sustainable cassava consumption and production. There are needs for researcher to use modeling approach as an integrated research method of the mainstream methods to develop appropriate crop production technologies with cassava farmers in various production situations [2, 16-17].

The calibration and evaluation work of cassava model in Thailand was in the early stage. The genetic coefficients of major cassava varieties can be estimated from data sets generated from well-designed and well-equipped field experiments. The future development of application of the CSM-cassava model in Thailand requires careful and long-term policy to carry out model calibration and evaluation, which depends on the development of reliable data sets, following the DSSAT's field manuals, to improve model performances. In turn, these efforts facilitate the model's users to analyze various practices under diverse cassava ecosystems for optimizing practices, resources and profit [25-26]. However, budget allocation for long-term research strategy planning and implementation, research infrastructure and researcher networks are urgently required for driving the development and implementation of the cassava model in Thailand. In addition, farmer participatory research (FPR) approach, including all stakeholders in the cassava supply and demand value chain, should also be incorporated to provide opportunity for effective adoption of appropriate and economically technologies [27].

Recently, there is a requirement to predict the impacts and risks of various changes such as climate change, regional technologies changes, natural resources degradation and agriculture sustainability [28]. So, the need for policies to develop adaptive strategies for handling future risks under the Sufficiency Economy Philosophy (SEP) is required, which stresses the middle path of agricultural resource utilization as an overriding principle for all Thai people. SEP calls for national development and administration to temporally and spatially modernize in line with the forces of globalization for Sustainable Development Goals (SDGs) in 2030 [29]. Therefore, policy makers and implementing agencies should integrate the modeling approach and geographic information systems, which are essential tools for decision-makers to account for the spatial dimension of vast cassava production ecosystems in Thailand. These approaches allow greater number of production and consumption options at different levels to be evaluated and implemented for the improvement of cassava production and consumption systems as well as livelihood of communities.

5. Conclusions

The applications of crop simulation models in Thailand, especially cassava model, were expanding in various issues including (i) improve cassava productivity with site-specific recommendations, (ii) evaluate impacts, vulnerability and adaptation to climate change. The understandings of agricultural system situations and solving these concerns require integration and quantification of knowledge at the whole system level. There is a need to reorganize our research teams and resources to implement system simulation and modeling approach to develop the cassava model as an integral component of cassava research strategy in Thailand to support small-scale cassava farmers. This is crucial, considering that these tools are progressively needed to ensure that agricultural crop, in particular cassava, will reach the food demands and will environmentally and economically sustainable in the near future.

6. Acknowledgement

This review article was financially provided and supported by The Thailand Research Fund (TRF), grant number CMU-TRF-PHD/0231/2560. We acknowledge the Department of Agriculture (DOA) for providing opportunity to pursue the advanced study of the first author.

References

- [1] Jones, J.W., Hoogenboom, G., Porter, C.H., Boote, K.J., Batchelor, W.D., Hunt, L.A., Wilkens, P.W., Singh, U., Gijsman, A.J. and Ritchie, J.T., 2003. DSSAT cropping system model. *European Journal of Agronomy*, 18, 235-265.
- [2] Howeler, R.H., 2011. Recent trends in production and utilization of cassava in Asia. In: R. H. Howeler, ed. *The Cassava Handbook*. Colombia: CIAT, pp. 1-22.
- [3] Office of Agricultural Economic., 2017. *Agricultural Statistics of Thailand 2017*. Centre for Agricultural information, Bureau of Agricultural Economic Research, Bureau of Agricultural Development Policy and Planning, International Agricultural Economics Division.
- [4] Rattanasriwong, S., Sarawat, V., Sasiprapa, W., Wannasai, N. and Somkid, S. 2010. Application of cassava model for assessment of site specific technology. *Thai Agricultural Research Journal*, 28 (2), 144-156. [In Thai]
- [5] Hunt, L.A., Jones, J.W., Tsuji, G.Y. and Uehara, G., 1994. A minimum data set for field experiments. In: P.F. Uhlir and G.C. Carter, ed. *Crop Modelling and Related Environmental Data. A Focus on Applications for Arid and Semiarid Regions in Developing Countries*. Paris: CODATA, International Council of Scientific Unions, pp. 27-33.
- [6] Jones, J.W., Antle, J.M., Basso, B., Boote, K.J., Conant, R.T., Foster, I., Godfray, H.C.J., Herrero, M., Howitt, R.E., Janssen, S., Keating, B.A., Munoz-Carpena, R., Porter, C.H., Rosenzweig, C. and Wheeler, T.R., 2017. Brief history of agricultural systems modeling. *Agricultural Systems*, 155, 240-254.
- [7] Hoogenboom, G., Porter, C.H., Shelia, V., Boote, K.J., Singh, U., White, J.W., Hunt, L.A., Ogoshi, R., Lizaso, J.I., Koo, J., Asseng, S., Singels, A., Moreno, L.P. and Jones, J.W., 2017. *Decision Support System for Agrotechnology Transfer (DSSAT) Version 4.7*. Florida: DSSAT Foundation.
- [8] Sirichumphuan, V., Limpinit C. and Limsila, A., 2005. *Growth and Genetic Value of Cassava. Research Report (Volume 1)*. Khon Kaen: Khon Kaen Field Crops Research Center Bureau of Agricultural Research and Development, Region 3, Department of Agriculture.
- [9] Tsuji, G.Y., Uehara, G. and Balas, S., 1994. *Decision Support System for Agrotechnology Transfer (DSSAT) Version 3*. Hawaii: University of Hawaii.
- [10] Hoogenboom, G., Jones, J.W., Porter, C.H., Wilkens, P.W., Boote, K.J., Hunt, L.A. and Tsuji, G.Y. 2010. *Decision Support System for Agrotechnology Transfer Version 4.5. Vol. 1: Overview*. Hawaii: University of Hawaii.
- [11] Hoogenboom, G., Hunt, T., Jarvis, A., Cock, J., Fisher, M. and Ramirez, J., 2012. *Rethinking a cassava crop model*. CIAT Decision and Policy Analysis, Cali, Colombia. [Online]. Available at: <http://dapa.ciat.cgiar.org/rethinking-a-cassava-crop-model/>
- [12] Hoogenboom, G., Jones, J.W., Wilkens, P.W., Boote, C.H., Hunt, K.J., Singh, L.A., Lizaso, J.I., White, J.W., Uryasev, O., Ogoshi, R., Koo, J., Shelia, V. and Tsuji, G.Y., 2015. *Decision Support System for Agrotechnology Transfer (DSSAT) Version 4.6*. Washington: DSSAT Foundation.
- [13] Seligman, N.G., 1990. The Crop model record: promise or poor show?. In R. Rabbinge, J. Goudriaan, H. van Keulen, F.W.T.P. de Vries and H.H. van Laar, eds. *Theoretical Production Ecology: Reflection and Prospects. Simulation Monographs*. Pudoc: Wageningen, pp. 249-263.
- [14] Matthews, R.B. and Hunt, L.A., 1994. GUMCAS: a model describing the growth of cassava (*Manihot esculenta* L. Crantz). *Field Crops Research*, 36, 69-84.

- [15] Uehara, G. and Tsuji, G.Y. 1998. Overview of IBNSAT. In: Y.T. Gordon, G. Hoogenboom and P.K. Thornton, ed. *Understanding Options for Agricultural Production*. Dordrecht: Springer, pp. 1-7.
- [16] Sarawat, V., Rattanasriwong, S., Puangprakon, K. and Jintrawet, A., 2000. The development of a cassava growth model in Thailand. *Cassava Research and Development in Asia: Exploring New Opportunities for an Ancient Crop. Proceedings of the 7th Regional Workshop*, Bangkok, Thailand, October 28- November 1, 2002.
- [17] Sarawat, V., Rattanasriwong, S., Puangprakon, K., Sringsam, P. and Jintrawet, A., 2004. *MunThai DSS: A decision support system for cassava production*. AFTTA/WCCA Joint Congress on IT in Agriculture.
- [18] Sarawat, V., Pabsimma, W., Kongton, S. and Jintrawet, A., 2013. *A Calibration of CSM-Cropsim-cassava simulation model for site-specific nitrogen fertilizer implementation for integrated cassava production system*. Khon Kaen Field Crop Research Center. A Research Final Report. Chiang Mai: Center for Agricultural Resource System Research.
- [19] Hinthong, Y. and Banterng, P., 2013. Evaluation of the potential of the CSM-CSCRP-Cassava model. *Khon Kaen Agricultural Journal*, 41(4), 469-482. [In Thai]
- [20] Boonpradub, S., Rattanasriwong, S., Sarawat, V., Kapetch, P., Ek-un, K., Damrakhemtrakul, W., Buddhasimma, I. and Pannangpetch, K., 2009. Impact of global warming on three major field crops production of Thailand. *Khon Kean University Research Journal*, 14(7), 626-649. [In Thai]
- [21] Sasiprapa, W., Rattanasriwong, S., Sarawat, V., Somkid, S. and Wannasai, N., 2011. Using GUMCAS to identify site specific cassava (*Manihot esculenta* Crantz) cultivar and planting duration. *Thai Agricultural Research Journal*, 29(2), 147-160. [In Thai]
- [22] Kaweewong, J., Tawornpruek, S., Yampracha, S., Russell, Y., Kongton, S. and Kongkeaw, T., 2013. Cassava nitrogen requirements in Thailand and crop simulation model predictions. *Soil Science*, 178, 248-255.
- [23] Kaweewong, J., Kongkeaw, T., Tawornprek, S., Yampracha, S. and Yost, R., 2013. Nitrogen requirements of cassava in selected soils of Thailand. *Journal of Agriculture and Rural Development in the Tropics and Subtropics*, 11 (3), 13-19.
- [24] Phuntupan, K. and Banterng, P., 2017. Physiological determinants of storage root yield in three cassava genotypes under different nitrogen supply. *The Journal of Agricultural Science*, 155, 978-992.
- [25] Boote, K. J., Jones, J.W. and Pickering, N.B., 1996. Potential uses and limitation of crop models. *Agronomy Journal*, 88 (5), 704-716.
- [26] Jame, Y.W. and Cutforth, H.W., 1996. Crop growth models for decision support systems. *Canadian Journal of Plant Science*, 76, 9-19.
- [27] Howeler, R.H. 2011. Farmer participation in research and extension: The key to achieving adoption of more sustainable cassava production practices in Asia. In: R. H. Howeler, ed. *The Cassava Handbook*. Colombia: CIAT, pp. 566-587.
- [28] Rötter, R.P., Sehomí, F.L., Höhn, J.G., Niemi, J.K., and Marrit, V., 2016. On the use of agricultural system models for exploring technological innovations across scales in Africa: A critical review. *ZEF Discussion Papers on Development Policy*, No. 223, University of Bonn, Center for Development Research (ZEF).
- [29] Department of International Organizations., 2019. *Thailand's voluntary national review on implementation of the 2030 agenda for sustainable development*. [e-book] Ministry of Foreign Affairs of Thailand. Available through: Ministry of Foreign Affairs website <www.mfa.go.th>.

Instructions for Authors

Current Applied Science and Technology journal contains research reports, articles concerning development work, reviews of the literature and research activities. The objectives are to publish and promote research contributions and innovative work in fields associated with applied science and technology. An electronic journal is provided on the website (<https://www.tci-thaijo.org/index.php/cast/index>). The editors reserve the right to require revision of the submitted manuscript as a condition for final acceptance.

The institute and the editorial board claim no responsibility for the contents or views expressed by the authors of individual articles. Copying is allowed provided that acknowledgement is made. All articles submitted for publication will be assessed by a group of distinguished.

Ethics:

The journal is committed to maintaining the high level of integrity in the content published and has a Conflict of Interest policy in place. The journal uses plagiarism detection software to screen the submissions. If plagiarism is found, the COPE guidelines on plagiarism will be followed. For more details, please see https://www.tci-thaijo.org/index.php/cast/navigationMenu/view/Publication_Ethics.

Page Charge: Free

Submission of Manuscripts:

Manuscripts must be written in English and submitted online. Manuscripts are to be reviewed (double blinded) by at least 3 referees specializing in relevant fields. Revised manuscripts have to be sent online.

All manuscripts should be submitted to: <https://www.tci-thaijo.org/index.php/cast/index>

Contact:

Editor of Current Applied Science and Technology
King Mongkut's Institute of Technology Ladkrabang
1 Soi Chalongkrung 1, Ladkrabang District,
Bangkok 10520, Thailand
Tel: 662-329-8136
Fax: 662-329-8221
Email: cast@kmitl.ac.th

Manuscript Preparation Guide:

General: Manuscripts must be typewritten using *Microsoft Word for Windows*, single-spaced with margin set-up (in page set up menu) as follows (see also the document template):

Top Margin 1.5"
Left Margin 1.5"

Bottom Margin 1.5"
Right Margin 1.5"

Good quality printouts using A4 paper size are required. Format should be a single column. Times New Roman font type is required. Font sizes for various text functions are as follows:

Text functions	Size *	Typeface
Title	14 (CT)	Bold
Author and co-authors	11 (CT)	Normal
Address for correspondence	11 (CT)	Normal
Abstract and main text	10 (LJ)	Normal
Section heading and number including “Abstract”, “Acknowledgement”, “References”	12 (CT)	Bold
Subsection heading and number	11 (LJ)	Bold

* CT = Center Text, LJ = Left Justified.

The corresponding author should be noted (included a Fax number and E-mail address) and indicated with an asterisk. Full postal addresses must be given for all co-authors, keyed to names (if required) by superscripted Arabic numbers.

Paper Length: Should not normally exceed 10 pages including figures and tables

Spelling: American English

Abstract: Should not exceed 250 words

Keywords: Should not exceed 8 keywords

Text: Authors are requested to use the following order when typing:-

All research reports (Full Length or Short Reports): Title, Authors, Affiliations, Abstract, Keywords, Introduction (in research papers this must be confined to relevant matters, and must not be a general review of cognate literature), Materials and Methods, Results and Discussion, Conclusions, Acknowledgements, References.

Reviews and Discussion Papers will be considered in any format appropriate to the purposes of the authors, although adherence to the general guidelines described above is encouraged.

Line Art Figures: Figures can be drawn using several packages such as Win Draw®, Auto CAD®, Corel Draw®, VISIO® etc.

Photographs: Actual size photographs are acceptable. However, they can also be put into a text stream using a good-resolution scanner. All photographs must be clear when printed in monochrome.

Graphs: Several packages available today can produce attractive and professional graph presentation. Some also provide curve-fitting function, which can be useful. However, two-dimensional bar charts are preferred. All graphs must be clear in monochrome printing.
Equations and complex expressions: Math CAD®, Math Writer® and Equation Editor® (included in Microsoft Word®) are acceptable for presentation of this type of material.

Citations: Citations in the text should be denoted by numbers between square brackets (i.e. [1, 2], [1-3], [1, 3-8]...) *in the order of first appearance in the text.*

References: References should be numbered to correspond with the text citations. References must be arranged as follows:

Books

Authors, Initials., Year. *Title of Book*. Edition. (only include this if not the first edition) Place: Publisher.

Example:

[1] Barker, R., Kirk, J. and Munday, R.J., 1988. *Narrative Analysis*. 3rd ed. Bloomington: Indiana University Press.

Chapters of edited books

Chapter authors' surname(s), initials., Year of book. Title of chapter. In: Book editor(s) initials. surnames, ed. or eds. *Title of Book*. Place of publication: Publisher. Chapter number or first and last page numbers.

Example:

[2] Samson, C., 1970. Problems of information studies in history. In: S. Stone, ed. *Humanities Information Research*. Sheffield: CRUS, pp. 44-68.

E-books

Author, Year, *Title of Book*. [e-book] Place of publication: Publisher. Available through: include e-book source/database, web address or URL.

Example:

[3] Carlsen, J. and Charters, S., eds. 2007. *Global Wine Tourism*. [e-book] Wallingford: CABI Pub. Available through: Anglia Ruskin University Library website <www.libweb.anglia.ac.uk>.

Journal articles

Author, Initials., Year. Title of article. *Full Title of Journal*, Volume number (Issue number), Page numbers.

Example:

[4] Ross, A.B., Junyapoon, S., Jones, J.M., Williams, A. and Bartle, K.D., 2005. A study of different soots using pyrolysis-GC-MS and comparison with solvent extractable material. *Journal of Analytical and Applied Pyrolysis*, 74(1-2), 494-501.

In case of online journal articles without page number:

Author, Initials., Year. Title of article. *Full Title of Journal*, Volume number (Issue number), DOI-based link.

Example:

[5] Islam, A.K.M.M. and Kato-Noguchi, H., 2014. Phytotoxic activity of *Ocimum tenuiflorum* extracts on germination and seedling growth of different plant species *The Scientific World Journal*. <http://dx.doi.org/10.1155/2014/676242>.

Proceedings

Author, Initials., Year. Title of article. *Full Title of Proceedings*, Place of Conference, Date, page.

Example:

[6] Thanaboripat, D., Ruangrattanametee, V. and Srikitkademwat, K., 2010. Control of growth and aflatoxin production of aflatoxin producing fungi in corn by salts. *Proceeding of the 8th International Symposium on Biocontrol and Biotechnology*, Pattaya, Thailand, October 4-6, 2010, 283-289.

Patent

Inventor name, Initial(s)., Assignee., Year. *Title*. Place. Patent number (status, if an application).

Example:

[7] Leonard, Y., Super Sports Limited., 2008. *Tin Can Manufacture and Method of Sealing*. Canada. Pat. 12,789, 675.

Dissertation

Author, Year of publication. *Title of Dissertation*. Level. Official name of University.

Example:

[8] Richmond, J., 2005. *Customer Expectations in the World of Electronic Banking: a Case Study of the Bank of Britain*. Ph.D. Anglia Ruskin University.

Websites

Authorship or Source, Year. *Title of Document*. [online] Available at: include web site address/URL (Uniform Resource Locator).

Example:

[9] NHS Evidence, 2003. *National Library of Guidelines*. [online] Available at: <http://www.library.nhs.uk/guidelines>

Acknowledgements: These should be as brief as possible.

Proofs:

Proofs will be sent to the corresponding author and *must* be returned as soon as possible. Corrections should be restricted to typesetting errors.

Copyright:

The author(s) transfer(s) the copyright of the article to Current Applied Science and Technology effective if and when the article is accepted for publication.

Page Numbering:

All pages must be sequentially numbered, preferably by using the automatic page numbering function on your computer.

Copyright Material:

It is the authors' responsibility to obtain written permission from the copyright holder (usually the book or journal publisher) to use copyright material, and to send a copy of this consent with the manuscript. This consent is not normally denied but it is an international legal requirement that it be obtained.

Note:

Please note that authors are urged to check their proofs carefully before returning, since the inclusion of late corrections cannot be guaranteed.

Author(s) are responsible for ensuring that the submitted manuscript fully meets the requirements specified in the above Instructions. Manuscripts which fail to do so will be returned unedited to the Author(s) for correction in accordance with the above requirements, before they can be submitted to the processes of Referee evaluation.

1.5 "
TEMPLATE

Enter title here (14 PT type size, Title Case, Bold, Centered)

Author Information entered here:
Name (in full)

Affiliation
City
Country
(11 pt type size, upper and lower case, centered under the title)

How to Use This Document Template

Insert the information in your document in place of the text here. For the body of your document, use Times New Roman 10 pt. Font, upper and lower case, double-spaced. Allow an extra half space above a line containing superscripts and/or below a line containing subscripts. The whole text should be left-justified. The headings should be 12 pt size, uppercase, bold and centered.

1.5"

Abstract (12pt)

1.5"

Maximum 250 words here. (10 pt)

.....
.....
.....
.....
.....

Keywords: (10 pt)

Maximum of 8 words

1. Introduction (12 pt)

Clearly explain the nature of the problem, previous work, purpose, and contribution of the paper (10 pt).

.....
.....
.....
.....

*Corresponding author: Tel.: Fax:
E-mail:

2. Materials and Methods (12 pt)

.....
.....
.....
.....

3. Results and Discussion (12 pt)

.....
.....

4. Conclusions (12 pt)

Clearly indicate advantages, limitations and possible applications (10 pt).

.....
.....

5. Acknowledgements (12 pt)

A brief acknowledgement section may be included here (10 pt).

.....
.....

References (12 pt)

References must be numbered in the order cited in the manuscript and indicated in the text by a number in square brackets (e.g. [1, 2]) (10 pt).

Example of References must be arranged as follows:

- [1] Barker, R. Kirk, J. and Munday, R.J., 1988. *Narrative Analysis*. 3rd ed. Bloomington: Indiana University Press.
- [2] Samson, C., 1970. Problems of information studies in history. In: S. Stone, ed. *Humanities Information Research*. Sheffield: CRUS, pp. 44-68.
- [3] Carlsen, J. and Charters, S., 2007. *Global Wine Tourism*. [e-book] Wallingford: CABI Pub. Available through: Anglia Ruskin University Library website <www.libweb.anglia.ac.uk>.
- [4] Ross, A.B., Junyapoon, S., Jones, J.M., Williams, A. and Bartle, K.D., 2005. A study of different soots using pyrolysis-GC-MS and comparison with solvent extractable material. *Journal of Analytical and Applied Pyrolysis*, 74(1-2), 494-501.
- [5] Thanaboripat, D., Ruangrattanametee, V. and Srikitkademwat, K., 2010. Control of growth and aflatoxin production of aflatoxin producing fungi in corn by salts. *Proceeding of the 8th International Symposium on Biocontrol and Biotechnology*, Pattaya, Thailand, October 4-6, 2010, 283-289.

- [6] Leonard, Y., Super Sports Limited., 2008. *Tin Can Manufacture and Method of Sealing*. Canada. Pat. 12,789,675.
- [7] Richmond, J., 2005. *Customer Expectations in the World of Electronic Banking: a Case Study of the Bank of Britain*. Ph.D. Anglia Ruskin University.
- [8] NHS Evidence, 2003. *National Library of Guidelines*. [online] Available at: <http://www.library.nhs.uk/guidelines>

Note:

Tables and Graphs: Minimum of 10 pt type size, all captions should be upper and lower case, centered. Each table and figure must be on a separate page (or pages if required), **and must be embedded in the text**.

Illustrations and Photographs: Halftones, minimum of 10 pt type size, bold, captions should be in upper and lower case, centered. Images must be computer-designed with clearly visibility.

Contact

**Editor of Current Applied Science and Technology
King Mongkut's Institute of Technology Ladkrabang
1 Soi Chalongkrung 1, Ladkrabang District
Bangkok 10520, Thailand
Tel: 662-329-8136 Fax: 662-329-8221
E-mail: cast@kmit.ac.th
Website: <https://www.tci-thaijo.org/index.php/cast/index>**

KING MONGKUT'S INSTITUTE OF TECHNOLOGY LADKRABANG
1 Soi Chalongkrung 1, Ladkrabang District Bangkok 10520, Thailand
Tel: 662-329-8136 Fax: 662-329-8221
E-mail: cast@kmitl.ac.th
Website: <https://www.tci-thaijo.org/index.php/cast/index>